Control, Modelling, and Applications of Dynamic Wireless Power Transfer Systems for Electric Vehicles

Krzysztof Jakubiak

A thesis presented for the degree of
Doctor of Philosophy

Department of Engineering
Cardiff University
United Kingdom
December 2024

Acronyms

AC Alternating Current

ACD Automatic Connection Device

ACDU Automatic Connection Device for vehicle Under-body connection

BEV Battery Electric Vehicle

BMS Battery Management System

CO_2 Carbon Dioxide

CPT Capacitive Power Transfer

DC Direct Current

DWPT Dynamic Wireless Power Transfer

EMF Electromagnetic Field

EMI Electromagnetic Interference

EV Electric Vehicle

EVSE Electric Vehicle Support Equipment

FEA Finite Element Analysis

FOD Foreign Object Detection

G2V Grid-to-Vehicle

GHG Greenhouse Gas

IoV Internet of Vehicles

IPT Inductive Power Transfer

LOD Living Object Detection

MOD Metal Object Detection

OBC On-board Charger

OEM Original Equipment Manufacturer

PFC Power Factor Correction

PV Photovoltaics

PWM Pulse Width Modulation

SOC State-of-Charge, %

SWPT Static Wireless Power Transfer

THD Total Harmonic Distortion

UN United Nations

UNFCCC United Nations Framework Convention on Climate Change

V2B Vehicle-to-building

V2G Vehicle-to-grid

V2H Vehicle-to-home

V2P Vehicle-to-parking

V2V Vehicle-to-vehicle

V2X Vehicle-to-everything

WPT Wireless Power Transfer

Symbols and Variables

Symbol	Description
C_f	Filter Capacitance (F)
C_p, C_t	Primary (transmitter) compensation capacitor for resonant WPT (F)
C_s, C_r	Secondary (receiver) compensation capacitor for resonant WPT (F)
D	Duty cycle of a PWM signal
f	Frequency (Hz)
f_r, f_{opt}	Resonant (optimal) frequency (Hz)
h	Air gap (distance) between two coils (m)
i_s	Source current (A)
I_o	Output current (A)
k	Coupling factor between coils (dimensionless)
k_i	Integral gain of PI controller
k_p	Potential gain of PI controller
L_f	Filter inductance (H)
L_p, L_t	Primary (transmitter) coil inductance (H)
L_s, L_r	Secondary (receiver) coil inductance (H)
M	Mutual inductance between coils (H)
P	Active power (W)
PI	Potential, integral controller
Q	Reactive power (VAR)
R_b	Battery resistance (V)
R_p, R_t	Primary (transmitter) coil resistance (Ω)
R_s, R_r	Secondary (receiver) coil resistance (Ω)
$S_1, ...S_n$	Switching signal
s	Complex frequency variable in the Laplace domain (rad/s)
V_b	Battery voltage (V)
V_{dc}, V_C, V_{Rec}	DC bus voltage (V)
V_s	Source voltage (V)
x, y	Displacement of two coils when viewed from above (m)
ω	Angular frequency (rad/s)

Abstract

Reducing global carbon emissions is essential to addressing global warming, with multiple sectors requiring research into greener alternatives. The transport sector, as a significant contributor to net greenhouse gas emissions, has driven the development and deployment of Electric Vehicles (EVs) and their supporting technologies.

As the number of EVs grows, charging infrastructure must evolve. While charging technologies have advanced, distribution grid upgrades have lagged, limiting charger installations and falling short of public charging needs. As a result, home charging has become most common—but is not feasible for all users due to limited off-street parking, often leading to cables crossing sidewalks. To address this, alternative charging methods like wireless charging are being explored. Embedded systems in public parking could serve users without private driveways while keeping walkways clear.

Wireless charging offers promise for stationary vehicles—such as buses and taxis at stops—and extends to Dynamic Wireless Power Transfer (DWPT), enabling energy transfer while in motion. Still in early development, dynamic systems are an active research area, with modelling and control techniques continuing to mature.

Current wireless charging efforts have focused on static systems and limited dynamic testing, often lacking simulation comparisons and omitting power delivery fluctuations. Circuit design typically centres on inductive coils, neglecting interaction with distribution grids. DWPT simulations can help refine control strategies and improve future system design.

Power electronic systems usually target transient behaviour with simulation times of 1 μs to 1 ms. In contrast, DWPT simulations span 1–10 s to assess charging during vehicle motion. As future systems incorporate multiple primary and secondary coils to support longer roads and successive vehicles, system complexity and simulation time increase. Since total transferred power is more critical than microsecond-level detail, developing equivalent models becomes increasingly important.

This thesis explores the modelling and control of dynamic wireless charging by first developing system models and control schemes, then advancing modelling techniques to significantly reduce simulation times through average modelling. Initial circuit analysis is used to build a representative model, which is then expanded to implement dynamic charging. Lab results validate factors such as coil type (copper vs. Litz wire) and travel speed, highlighting dynamic effects not captured by static analysis. Average modelling techniques achieve accurate system dynamics with only a 6% error while reducing simulation time by a factor of 30.

Considering the potential impact of future charging technologies, Vehicle-to-grid (V2G) systems are examined to assess their potential for grid support and to minimize adverse effects on existing infrastructure. In parallel, the industrial development of an Automatic Connection Device for vehicle Under-body connection (ACDU) is undertaken in collaboration with IPFT to provide alternative charging methods.

Acknowledgments

I would like to express my sincere gratitude to Prof. Jun Liang and Prof. Liana Cipcigan for their invaluable guidance and supervision throughout my research. Their expertise, insights, and continuous support were instrumental in bringing this work to fruition. I am also immensely grateful to Dr. Chuanyue Li for helping me navigate technical challenges and for fostering my problem-solving and technical development skills. The knowledge and wisdom they imparted, particularly in research methods and problem-solving, will serve as a foundation for my future endeavours, both academic and professional.

A special thanks to IPFT Fuels for not only providing me the opportunity to pursue this academic research but also for offering practical industrial experience in developing and deploying charging technologies. The exposure to real-world applications allowed me to cultivate a wide range of skills that proved invaluable during the research and will continue benefit my career.

To my family and friends, your unwavering love and encouragement sustained me throughout this journey. Without your support, this accomplishment would not have been possible.

Contents

List of Figures

List of Tables

1 Introduction

1.1 Motivation

As a result of the existing climate related crises and the forecast future events, several legal agreements have been constructed for various nations to slowdown and reduce the effects of global warming by planning and implementation of various solutions as well as supporting other nations to do the same [1]. Aiming to keep global warming below 2℃ since 1850, the agreement requires countries to declare their contributions and future actions to reduce their Greenhouse Gas (GHG) which requires social, economical and technological planning and innovation which is reviewed every five years. The United Nations Framework Convention on Climate Change (UNFCCC) is the largest organisation driving this effort through the Paris agreement to keep global warming to 2℃ as well as the Race to Zero [2] which is a campaign to bring together large economy actors such as companies, financial institutions, cities, states, regions, educational and healthcare institutions. Recognising finance is a key factor to enabling the change and innovation to realise the UNFCCCs goal, the Net-zero asset owner alliance [3] (also stemming from the United Nations (UN)) is an initiative for finance investors to incrementally reduce their Carbon Dioxide (CO_2) emissions. As a result, general awareness of GHG emissions is rising and companies are more considerate with their purchases and increasingly more willing to allocate resources to reduce their carbon footprint, which in turn drives demand for eco-friendly technology and innovation. These global campaigns had a knock on effect sparking further agreements and initiatives such as the European Green Deal [4] which not only set a target of net-zero GHG emissions by 2050 but also invested €1.8 trillion following the COVID-19 pandemic to jump-start innovation and ensure these ambitious targets can be met on time. Further organizations such as the climate pledge have moved this net-zero target forward to 2040, requiring regular reports, elimination and mitigation of emissions to make progress toward the global net-zero target [5].

In order to tackle the global emissions problem, we must first analyse the key contributing factors to GHG emissions. Figure 1.1 shows the global emissions by sector, this figure effectively highlights the large contribution of the energy sector to GHG emission and in turn global warming, it is important to note almost all of these sectors need to change in some way to meet the UNFCCCs targets. As these sectors are linked in several factors, a whole system approach is required to tackle the problem and deliver various solutions based on sector and application. For example transport electrification requires access to electricity at both commercial and residential venues. The remainder of this chapter will cover the energy generation and distribution sector before moving onto the transport (specifically road transport) sector giving consideration to road vehicle integration with current commercial and residential buildings and infrastructure.

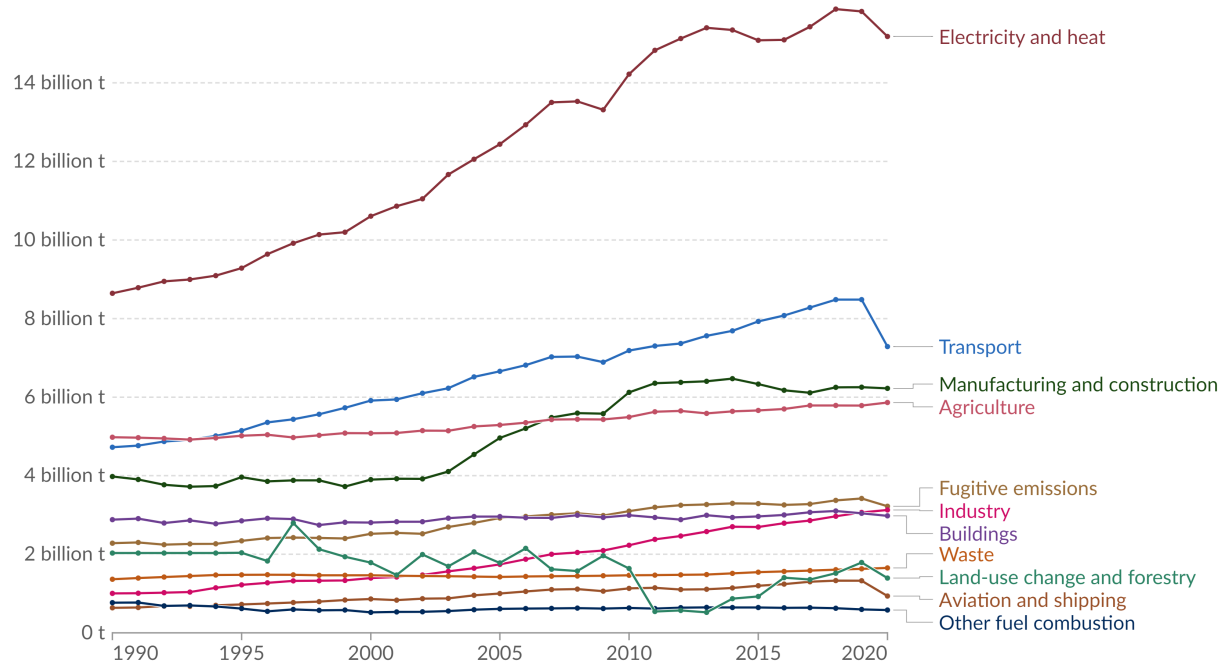

Figure 1.1: Global greenhouse gas emission by sector [6].

1.1.1 Energy/Electricity distribution grids

The rising number of EVs will lead to an increase in power demand from the distribution grid [7]. To facilitate the required increase in power delivery, power distribution networks require upgrades to handle the increased power transfer. By controlling charging events (charge scheduling), it is possible to manage the start time when charging events take place, effectively spreading the overall impact to the grid ensuring an overload is avoided [8]. Aiding the increase in EV power demand can be achieved using V2G chargers, where EV batteries are used to support grid operation by feeding power back intro the grid [9–11]. V2G benefit for the vehicles are less obvious, however the use of V2G and making use of energy prices leads to a reduction of charging cost by 13.6% [12]. Hence the use V2G can be mutually beneficial to both EV owners and the distribution grids by supporting increased adoption of renewable energy sources [13] and the control of EV charging demand and use of V2G contribute to more efficient system operation leading to lower cost and lower carbon emissions [14].

1.1.2 EV Adoption and Charging Infrastructure

From the global initiative down to the national level, different countries are setting their own targets to make their contribution in the net-zero initiative in a way that is more specific and realistic for their economy, policy and geography [15]. For instance the UK committing to net-zero targets by 2050, which recognises the nations previous targets need to be revisited to reach this end goal [16]. The transport sector being the largest-emitting sector in the UK, accounting for 23% of UK emissions [17]. As such the British government has brought forth the date to eradicate the sale of new petrol, diesel and hybrid cars and vans by 2035 or earlier if a faster transition appears feasible [18]. Furthermore, almost 600 thousand new

vehicles were registered in the UK during 2020 Q1 [19]. Legislation plays a big part in EV adoption as the solution needs to be feasible for the public to make the switch. This has been shown in countries such as Norway which enjoyed the largest EV market penetration due to financial incentives and tax benefits [20].

Considering all the information available, it is reasonable to conclude the UK will see an increase in Battery Electric Vehicles (BEVs), in order to facilitate this transition and make it feasible for the general public, charging solutions need to be developed and implemented to cater to users on a regular basis, be it over night or whilst at work in a car park.

Due to environmental and sustainability objectives, EVs are receiving more support in development and deployment. "To date, 17 countries have announced 100% zero-emission vehicle targets or the phase-out of internal combustion engine vehicles through 2050" [21]. As combustion engine vehicles are phased out, global EV sales are forecast to increase rapidly as electric vehicle stock is predicted to grow by 36% annually, reaching 245 million vehicles in 2030 [21].

Despite most nations (primarily Europe) being in recession which resulted in a reduction of car sales, EVs enjoyed a 55% increase in sales (Figure 1.2). Such growth indicates increasing acceptance and adoption rates for EVs and supporting technology. This highlights the success of purchasing incentives from local governments and introduces a requirement for more charging technology to support the increased uptake of EVs. While more powerful solutions are developed most vehicles gain sufficient where users plug-in overnight and while at work (Rapid charging: <43kW achieves 80% charge in 30-50min, ultra-rapid: <100kW) [22].

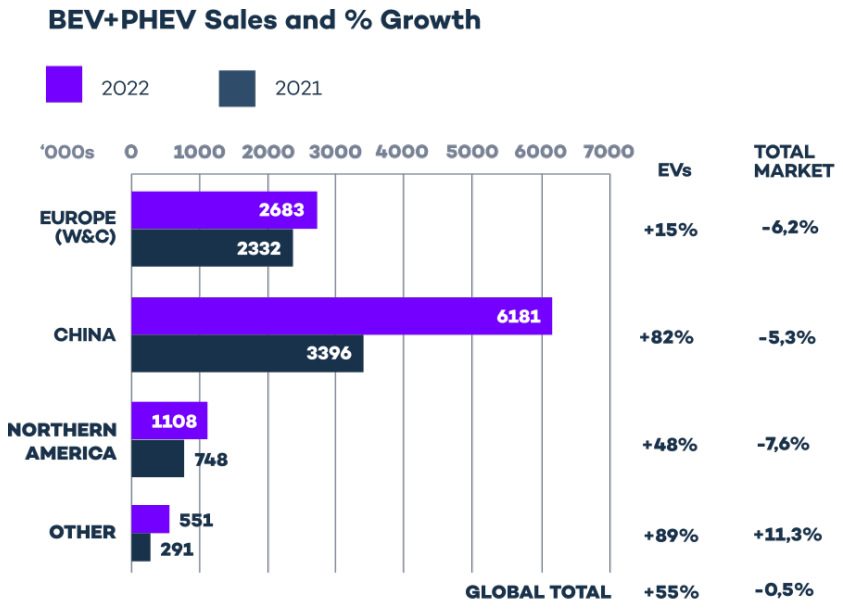

Figure 1.2: Global EV sale growth in 2022 [23]

Mode of charging is a way of classifying the power delivered by the charger. The IEC 61851 committee defined the four main charging modes which differ on the power capacity, protection devices and communication (see Tab 1.1). In practice the main reason for differentiation is the location of each charging mode. Mode 1 are early chargers intended for home use (hence single phase), normally mains connected; Mode 2 is a step up to include

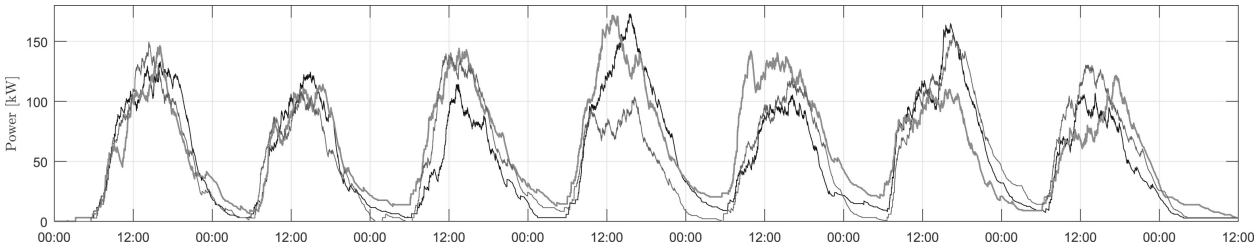

Figure 1.3: Three simulated load profiles over a week, based on empirical data from three German EV fleets [25].

up to 3-phase supplies and is the standard for public access chargers; Mode 3 requires additional upgrades to provide higher power but is still achievable with AC charging; Mode 4 broadly encompasses DC chargers which are the highest power rating of chargers and require a different connection interface (in-practical for home spaces).

Table 1.1: Charging modes and standards [24]

Charging Mode/Level	**Electrical Specification**	**Topology**	**Primary Locations**
Mode 1 (IEC 61851) / Level 1 (SAE J1772)	1ϕ AC, 230 V, 16 A, 3.7 kW	No active protection; relies on building-side RCD/MCB	Domestic
Mode 2 (IEC 61851) / Level 2 (SAE J1772)	1ϕ AC, 230 V, 32 A, 7.4 kW 3ϕ AC, 415 V, 32 A, 22 kW	On-board charger with in-cable protection (IC-CPD)	Semi-public
Mode 3 (IEC 61851)	3ϕ AC, 415 V, >32 A, >22 kW	On-board charger with dedicated EVSE	Public
Mode 4 (IEC 61851) / Level 3 (SAE J1772)	DC connection, 200–1000 V, >3.2 kW, >22 kW	Off-board charger (DC fast charging)	Public

Figure 1.3 the weekly power demand based on gathered data [25]. The results highlight a clear temporal pattern in EV charging behaviour, with relatively consistent demand during weekdays and a slight dip on Sunday. This trend reflects habitual use and is expected to scale with increasing EV adoption. As charging remains largely residential and occurs during predictable time windows, unless there are significant changes in charging infrastructure or user behaviour, this pattern is likely to persist. Consequently, the distribution grid will need to be reinforced to manage the higher and more temporally concentrated loads, especially in residential zones. Additionally, upfront costs associated with home charging installations may remain a barrier to adoption for some users.

1.2 Existing Chargers

Electric vehicle (EV) charging systems are categorized into four standardized modes, defined primarily by the IEC 61851 standard [26]. These modes vary in electrical characteristics, communication features, and safety mechanisms.

Mode 1:

Mode 1 charging is the most basic approach, involving direct connection of the vehicle to a standard AC socket using a simple cable, with no integrated protection or communication. Safety relies entirely on the building's circuit breakers or residual current devices. Due to the lack of protective measures, this mode is now prohibited in many regions [26].

Mode 2:

Mode 2 improves safety by integrating an In-Cable Control and Protection Device (IC-CPD) into the charging cable. This device supports limited communication (e.g., pilot signal) and basic protection functions such as ground fault detection and over-current protection. Mode 2 still uses standard socket outlets but ensures safer charging [27].

Mode 3:

Mode 3 charging uses dedicated EVSE permanently connected to the grid. It facilitates active communication with the EV and supports higher current levels through dedicated connectors (e.g., Type 2). It is widely used in residential and public charging infrastructures [26, 28].

Mode 4:

Mode 4 is used for DC fast charging. In this mode, the conversion from AC to DC takes place in an off-board charger, which supplies regulated DC directly to the vehicle's battery. It supports very high power levels and requires specific connectors such as CHAdeMO or CCS [26, 29, 30].

Wireless:

Wireless charging, also known as inductive charging, eliminates the need for physical connectors by transferring energy between a ground-mounted transmitter coil and a receiver coil installed in the vehicle. This method typically relies on magnetic resonance or inductive coupling to transmit power across a small air gap [31].

While current implementations are designed for stationary charging in controlled environments (e.g., residential garages, taxi ranks), wireless systems offer significant user convenience and mechanical durability. Challenges such as misalignment losses, electromagnetic interference, and lower overall efficiency still limit widespread deployment.

A promising extension of this technology is *Dynamic Wireless Power Transfer*, where vehicles receive power while in motion via embedded coils in the road surface. DWPT has the potential to reduce on-board battery size and increase vehicle uptime, especially for high-utilization fleets such as public transport [31]. However, high infrastructure costs and the need for international standardization remain major hurdles.

1.2.1 Dynamic Wireless Power Transfer (DWPT)

Previous case studies on the use of DWPT in Coventry showed that a high utilization rate is essential for the technology to be economically viable. Based on their findings, a guide was developed to assist in identifying suitable locations for deployment [32, 33]. As part of Coventry council's initiative to increase EV uptake and provide more charging solutions,

DWPT pairs well with their existing projects on autonomous vehicles and aims for public service/transport. One key point of their finding is the necessity for identification of potential use-cases based on certain factors. To make a case for the use of DWPT, the transmitter coils will need to have a high utilisation rate, hence will need to be in an area with high volume traffic, with vehicles suitable for the use of DWPT.

Before a charging event can occur using existing DWPT (primary) coils, several conditions must be met [32, 33]. First, the vehicle must be equipped with an inductive receiver coil and be in a state ready to receive power, based on its state of charge (State-of-Charge (SOC))—similar to other charging technologies. Second, a decision must be made on whether to initiate a charging event, considering the vehicle's journey, current SOC, and the cost or availability of alternative charging options (e.g., plug-in chargers). Finally, the power transfer rate is determined by multiple dynamic factors, including traffic density, available power, and user behaviour—primarily vehicle speed.

This illustrates that the practical application of DWPT is more complex than simply charging whenever a vehicle passes over a primary coil. In particular, the use of DWPT for public transport offers a more controlled and predictable environment, as vehicles typically have known routes and access to chargers at depots. In contrast, private vehicles present greater variability in destination and driving behaviour, which complicates system optimization.

To maintain grid stability at the location of the primary coils, power availability must be continuously considered and transfer rates adjusted accordingly. As DWPT systems scale, further studies will be required to understand and manage their impact on the distribution grid.

The power transferred to the vehicle is determined by the number of receiver coils installed, with each coil capable of delivering 25kW of output power. Given a system efficiency of 85%, the corresponding grid power demand per coil is approximately 29.4kW. The system implementation, uses multiple square coil transmitters, requiring switching control on/off while the vehicle moves from one coil to the next. This results is a fall in power transfer as coils are turned off, resulting in a mean system efficiency of 80%.

Grid impact is determined by the number of network connections (in this case only one main unit is grid connected, splitting power to the coils as required) and load management as the system consists of multiple coils rated at 25kW, the total power consumption depends on the utilisation of these coils at any given time. Furthermore the power quality and harmonic impact of the DWPT system is not yet know [32, 33].

The study also included scenario generation and vehicle demand modelling which feed into a business case analysis. The analysis considered the use of DWPT technology to various road types and number of suitable vehicles. The study summarised that the best case for DWPT are large fleets which frequent the same sections of motorway as this lowered the total estimated cost per kilowatt hour (£/kWh). Conversely the study showed urban areas for buses and coaches was the worst use case as the alternative for plug-in charging between journeys was cheaper alternative. Moreover, installations with traffic lights (allowing longer charging periods), almost doubled the cost effectiveness of the installation. It is therefore highlighted, the use case selection is crucial for economically viable deployments of DWPT.

Finally the study showed the impact of vehicle speed and the total power transferred by DWPT compared the power consumed by the vehicle. As can be expected, higher vehicle

speeds result in higher vehicle energy consumption, shorter duration of charging for DWPT and therefore a lower energy transfer. Interestingly, the study shows lower vehicle travel speeds are able to achieve higher charging power than power consumption ($P_{in} > Pout$). In theory, if a vehicle stays on a route where it is always connected to DWPT this would allow continuous travel. Up to around 35mph(56km/h) the total power transferred exceeds the total energy usage. This depends on vehicle type and use however serves as an example for future comparisons and business cases. As the study considered short sections of road, future case studies may considered either longer sections or multiple sections long a route which might find urban application at lower speed (30mph speed limits) to become a more suitable application.

Upcoming projects Several pilot and commercial projects have demonstrated the growing feasibility of DWPT across a range of use cases and environments.

Electreon in Europe Electreon, a leading industry player in wireless charging, has implemented DWPT systems in Sweden, Germany, and Italy. These projects focus on enabling dynamic charging for electric buses and freight vehicles. In Gotland, Sweden, a 1.6-kilometre road segment supports public bus routes with wireless power transfer up to 20 kW. Similar deployments in Karlsruhe, Germany and Brescia, Italy have tested the system's modularity, vehicle interoperability, and energy efficiency, reporting over a 90% energy transfer efficiency [34, 35].

Oslo, Norway In Norway, the city of Oslo is trailing wireless charging infrastructure at taxi stands to support electric taxi fleets. This quasi-dynamic configuration enables vehicles to charge while waiting for passengers, integrating clean energy targets with practical fleet operations. The project supports Oslo's goal of having all taxis be zero-emission by 2025 and represents a novel model for urban DWPT use [36].

Detroit, USA In the United States, a government-funded project led by the Michigan Department of Transportation (MDOT) and Electreon is deploying a DWPT pilot in Detroit. This initiative includes a quarter-mile test-bed embedded into public roads near Michigan Central Station. The $1.9 million pilot, launched in collaboration with Ford Motor Company and DTE Energy, seeks to evaluate infrastructure readiness and performance in North American urban conditions, ahead of the 2028 Olympics [37].

Tel Aviv, Israel In Israel, the world's first commercial DWPT terminal has been implemented in Tel Aviv. The system enables electric buses to wirelessly charge during scheduled stops at a bus depot, demonstrating readiness for real-world, high-frequency transit operations. This site serves as a proof of concept for integrating DWPT into permanent fleet infrastructure with minimal operational disruption [38].

These diverse implementations highlight not only the technical maturity of DWPT, but also the wide range of deployment strategies being explored globally. From urban taxi fleets to freight logistics and public transit, the evolving landscape of real-world pilots reflects growing confidence in the scalability and commercial viability of dynamic wireless charging

[39]. While these installations demonstrate growing global interest in DWPT, they currently remain niche applications. Broader adoption scenarios will require further study, though such developments are likely to emerge as the technology continues to advance.

1.3 Challenges

From the current landscape of charging technologies, funding allocations, and emerging deployment projects, it is evident that DWPT is receiving increased attention. However, the technology remains in its developmental phase and faces a number of technical and systemic challenges before it can be adopted at scale. Most academic research to date has focused on Static Wireless Power Transfer (SWPT), while practical implementation and evaluation of DWPT systems remain sparse and uneven across geographies [40, 41].

One of the foremost limitations is the lack of mature and validated simulation models that can accurately represent the behaviour of DWPT systems under dynamic conditions. Fast-moving vehicles introduce complex transient power phenomena—such as instantaneous current surges and sustained oscillations—that are not captured in conventional simulation frameworks [42]. This makes it difficult to model and test power delivery, circuit stability, and the control response to mutual inductance variations due to vehicle speed and alignment. Simulation studies that do exist often rely on computationally intensive methods like FEM and particle swarm optimization, with very long runtimes, limiting their practical use in iterative design processes [43].

Additionally, communication between vehicles and infrastructure is critical for safe and efficient DWPT operation. However, current systems face substantial issues in latency, synchronization, and reliability. Wireless signal interference, secure authentication, and the need for real-time feedback to enable coil activation—particularly at high speeds—remain key challenges for communication in dynamic wireless power transfer systems [44]. The lack of standardized protocols across vendors and jurisdictions compounds these issues. Communication failures can result in misalignment, interrupted charging, or even safety hazards, highlighting the need for robust, low-latency V2I and V2V communication strategies.

Grid integration introduces further complexity. Unlike SWPT stations, which can be easily co-located with stationary battery storage or renewable sources, DWPT systems involve multiple spatially distributed transmitters embedded in road infrastructure. This configuration presents significant challenges for power coordination, load balancing, and system protection. Research indicates that uncoordinated charging from high-traffic corridors can cause grid voltage fluctuations and increased power losses [39, 40]. Incorporating real-time grid awareness and potentially supporting bidirectional power flow for V2G applications may mitigate these issues, but these strategies are still largely theoretical at this stage.

Economic and practical deployment barriers also remain significant. Stakeholder concerns around installation cost, long-term maintenance, and road disruption must be addressed before widespread deployment can occur [39]. Public trust, regulatory frameworks, and interoperability are also critical for mass adoption. Many existing deployments are limited in scope—often pilots or test beds—and vary significantly in terms of vehicle types supported, power levels, and grid interaction capabilities [45, 46]. This fragmentation further limits the comparability of results and delays standardization.

In summary, although DWPT represents a promising path for continuous, efficient electric vehicle charging, several critical challenges must be overcome. These include improving simulation fidelity and scalability, developing secure and low-latency communication infrastructure, ensuring grid compatibility, and aligning economic incentives with deployment needs. Addressing these challenges will require a multidisciplinary approach, combining advances in power electronics, control theory, wireless communication, transportation policy, and infrastructure planning.

1.4 Objectives

While dynamic wireless power transfer (DWPT) has demonstrated technical feasibility in experimental deployments, simulation-based studies remain limited in scope, fidelity, and adaptability. Furthermore, there is a lack of unified modelling environments that can test control strategies, assess misalignment effects, or simulate vehicle-to-grid (V2G) integration. This thesis addresses these gaps through the development of a scalable, control-oriented simulation framework. The specific research objectives are as follows:

Obj 1.: To develop a MATLAB-based dynamic simulation model for Wireless Power Transfer (WPT) systems that captures coupling-dependent behaviour over time
Unlike current models that rely on static analysis, this work introduces a simulation approach that accounts for dynamic system behaviour, providing a more realistic and flexible tool for design and control development.

Obj 2.: Design and validate a dual-side control scheme for WPT that minimizes reliance on wireless communication
Many existing WPT systems assume continuous communication between the transmitter and receiver. This objective explores the design of autonomous dual-side control strategies that can maintain stable power transfer under dynamic conditions, reducing system complexity and increasing robustness.

Obj 3.: Develop a reduced-order average model to enable efficient large-scale simulation of dynamic wireless power transfer systems To support system-level analysis and reduce computational demands, the model will be simplified using average circuit modelling techniques. This allows for accurate simulation of dynamic charging scenarios, including grid interactions and multi-vehicle operation, with significantly reduced simulation time. The resulting framework enables realistic studies of DWPT performance under varying operating conditions, supporting practical design and deployment decisions.

Obj 4: Demonstrate the potential of dynamic WPT systems to deliver flexible bidirectional grid support (V2G), active/reactive power control, and continuous grid services—even without a vehicle—to enable fast response, peak shaving, and renewable energy integration.
The final objective is to evaluate how WPT systems — static or dynamic — can contribute to grid services. This includes modelling active and reactive power flows and simulating their effects with and without an EV connected, providing insight into possible roles of WPT in future smart grid infrastructure.

1.5 Outline and Contribution

Based on the objectives, Chapter 2 presents key findings from the literature to provide a comprehensive understanding of EV usage, advancements in charging technologies, and infrastructure developments. This analysis offers insights into current usage patterns, existing challenges, and potential avenues for future research. Chapter 3 elaborates on wireless charging technologies, specifically focusing on the modelling of wireless systems, with the intention of using this as a foundation for future research. In Chapter 4, control strategies for WPT are investigated, followed by the proposal of a new method for primary-side converter control. Building on these developments, Chapter 5 summarizes modelling techniques to create average models for the converter components, ensuring accurate average representations for grid and load integration. Finally, Chapter 6 explores the use of bidirectional charging technologies, elaborating on possible grid interactions of the developed systems and considerations for future research as technology evolves and EV penetration increases.

The work presented in this thesis successfully achieves the outlined objectives. Chapter 3 focuses on the development of the WPT model, which replicates previous research findings and provides a solid foundation for subsequent investigations, fulfilling Objective 1. Building upon this base model, Chapter 4 details the development of a control strategy for WPT, addressing Objective 2. In line with Objective 3, dynamic simulations are further enhanced in later chapters, incorporating advanced control strategies. This also includes an in-depth analysis of the system to reduce simulation time while maintaining an accurate representation of system dynamics. Chapter 6 looks into the V2G application of EVs to investigate the suitability of EV use for this purpose, inline with Objective 4.

The contributions are summarised as:

- Created new modelling technique for (dynamic) wireless charging.
  - Presented in Chapter 3.
  - Published in *2022 IEEE Compatibility in Power Electronics Conference* (Krzysztof Jakubiak, Jun Liang, and Liana Cipicgan, 2022).
  - Achieving Objective 1.
- Developed control strategy to remove communication requirements and expand analysis of wireless charging technologies.
  - Presented in Chapter 4.
  - Published in *EVI: Charging Ahead 2023* (Krzysztof Jakubiak, C. Li, J. Liang, and L. Cipicgan, 2023).
  - Achieving Objective 2.
- Furthered system analysis and modelling techniques to reduce simulation time.
  - Presented in Chapter 5.
  - Published in *Electronics, 13(21)* (Krzysztof Jakubiak, Jun Liang, Liana Cipicgan, Chuanyue Li, and Jingzhe Wu, 2024).

  - Achieving Objective 3.

- Demonstrated how a dynamic WPT system can provide grid support through active and reactive power control, enabling bidirectional operation (V2G).
  - Presented in Chapter 6.
  - Highlights practical control strategies for both charging and discharging modes, supporting fast response, peak shaving, and renewable integration.
  - Achieving Objective 4.

2 Literature Review

This chapter aims to introduce the motivation for research in sustainable technologies and more specifically EVs and surrounding systems. Following the broad introduction of global objectives, motivation and incentives, the focus is shifted first to energy systems before going into EV systems and supporting technology. The summary then provides a good basis to structure research objectives and summarise the resulting contributions.

Since the industrial revolution in 1850, the average global temperature has risen by over 1℃, with more recent studies showing the global average will almost certainly exceed 1.5℃ [47]. The continued increase in global temperature is expected to have adverse effects such increased frequency and intensity of extreme weather conditions, rising sea levels, habitat destruction and agricultural losses due to reduced crop yields and water shortages [48, 49]. These primarily environmental changes will in turn affect the global economy as damage caused by changes in sea level and weather will need to be repaired and prevented, increased difficulty in agriculture is expected to drive food prices up. With these effects it becomes abundantly clear this is a global issue which needs to be addressed. Some of the side effects have already been been observed with increased flooding [50], drought [51] and landslides [52] to name a few. Furthermore this is not an issue we can postpone as the change in temperature is showing exponential growth since 1850 [53]. To put this into perspective, in the period 1850-2015 global global average temperature average increased approximately 1℃ (Figure 2.1) and it is now expected to exceed 1.5℃ in the period 2023-2027.

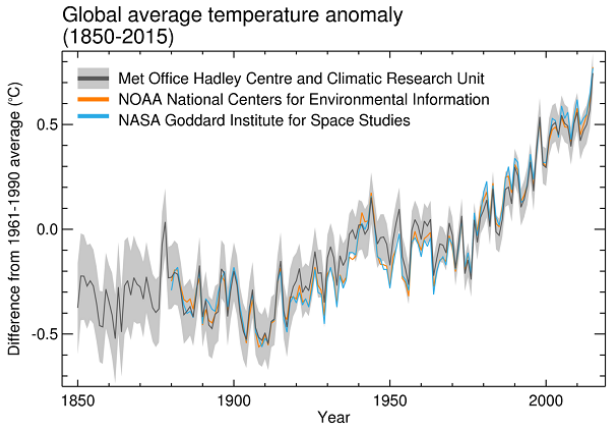

Figure 2.1: Rising global temperature from 1850 to 2015 [54].

The behaviour of users carries some variance but general trends can be seen due to working hours, this is further shown when compared to weekend power demand in Figure 2.2. Looking at four different countries it could be expected that there is variance based on population, EV penetration among others, it can be seen that power demand spikes around the start and end of the working day (9am and 5pm respectively) [55]. This places a demand on the grid to expand its peak power capabilities and is only sought to increase with EV penetration if charging facilities also expand.

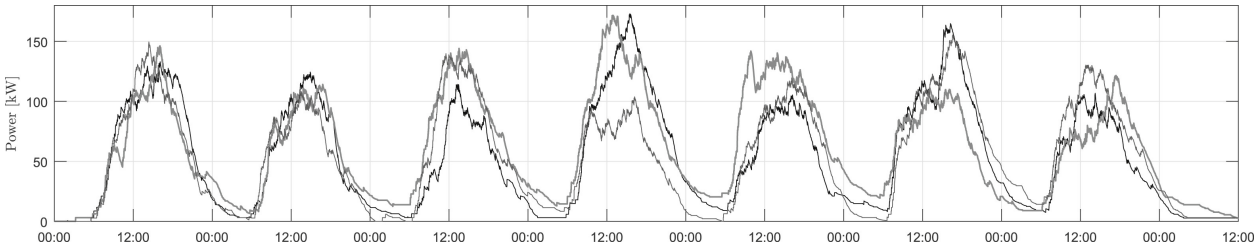

Figure 2.2: Three simulated load profiles over a week, based on empirical data from three German EV fleets [25].

2.1 Charging solutions

As EVs gain popularity, charging solutions have developed to decrease charging time and reduce range anxiety for drivers, hence charging modes developed with increasing power capacity reducing the time required to fully charge the vehicle or to charge enough to cover large trips. Table 2.1 shows the currently used charging interfaces for EV charging. Notably, no inductive (wireless) charging solution has been made commercially available, though several have been demonstrated or announced. Companies such as WiTricity [56], Electreon [57], and Momentum Dynamics [58] have showcased systems capable of transferring significant power, and Tesla has hinted at future wireless solutions [59]. As power capacity increases so does the amount of cables, going from single phase AC to three phase AC, contrasting to DC charging, uses large (cross section) cables to reduce power losses. As these solutions have a manual component to plug-in charge cables, robotic solutions have been developed to reduce effort and time [60]. Based on charging mode it is possible to reduce charging time, however automated charging solutions face a problem of standardisation, that is the different plugs/sockets associated with each charging mode. Moreover the position of charge inlets varies on different vehicles and to add to that issue, the final parking position will affect the position and orientation of the plug relative to the robot, hence current demonstrations of robotic chargers are in controlled environments to showcase the working solution.

2.1.1 Charging circuits explained

At it's core, the main purpose of EV charging solutions is to connect a power source (in this case the power grid) to the EV battery. For modern power grids, we will use an EV power source, while the EV power grid. Figure 2.3, shows a simplified representation of charging systems which consists of:

Grid connection AC power source, depending on circumstances, can be single-phase (1φ) or three-phase (3φ) at 120/240V, depending on the geographical operating area and available power rating.

Rectifier Changing Alternating Current (AC) to Direct Current (DC) power for subsequent circuit. Active rectification can be used to provide further functionality such as power factor correction.

Power Factor Correction (PFC) Ensures devices do not destabilise the grid. Note.:

Table 2.1: Conventional charger interfaces and standards

Charging interface	**Type of charging**	**Maximum charging power**	**Primary locations/markets**
SAE J1772 (Type 1)	AC	6.6kW	North America, Japan
IEC 62196-2 (Type 2)	AC	44kW	Europe
GB/T	AC/DC	22kW (AC) or 250kW	China
Tesla	AC/DC	43kW (AC) or 250kW	All markets (excluding Europe)
CCS1 (Type 1 & Type 4)	AC/DC	19.2kW(AC) or 80kW	North America
CCS2 (Type 2 & Type 4)	AC/DC	400kW	Europe
CHAdeMO	DC only	200kW	Japan

Some circuits combine the rectifier with PFC to reduce the number of components in the system.

DC/DC conversion (optional) Voltage level control which can be used to provide power control or adjust system efficiency based on application.

Power inversion Changing from DC to AC power, for the next circuit. Control depends on application and design, often the power inversion, galvanic isolation and rectification are designed together to provide efficient power transfer and required control for the application.

Galvanic isolation and compensation In conductive charging, a safety feature which removes direct conduction paths, meaning no direct current flow is possible. In the event of sudden current changes (such as short circuits), prevents fault propagation throughout the circuit. Most commonly this is a fixed core transformer which requires some compensation components (inductors and/or capacitors) to function efficiently (commonly in resonant mode) , furthermore the frequency for power transfer is often much higher than grid frequency as this allows for smaller converters.

Rectification Changing from AC to DC power, for the next circuit. Active rectification can be used to provide control at this stage.

DC/DC conversion (optional) Additional circuitry can be added to provide more direct control over output characteristics. In conductive charging solutions these are commonly removed as similar functionality can be achieved using the active rectifier or by controlling the inverter (sometimes both are used).

EV battery The primary function of the circuit is to supply DC power to the EV battery for charging. Although the battery pack is composed of many smaller cells with lower individual voltages, the overall pack voltage observed at this stage typically ranges from 400 to 1000 V.

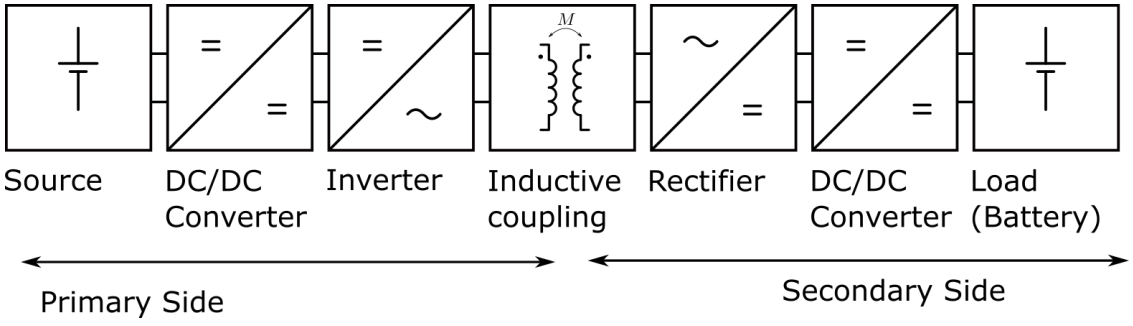

Figure 2.3: Full system schematic

The fundamental requirements for a charging circuit consist of an AC grid connection and an EV battery interface. However, given the high voltage levels typically involved (e.g., 230 V AC from the grid and 400 V DC at the battery), galvanic isolation is a critical safety requirement to electrically decouple the two systems.

Since the objective is to charge a DC battery from an AC source, the system must incorporate a rectification stage. In configurations where a DC distribution grid is available, this stage may be omitted or substituted with a suitable DC–DC converter to manage the power transfer between the source and the load.

To implement galvanic isolation, a transformer is generally used. However, transformers require AC operation, necessitating an inverter stage to convert the intermediate DC into high-frequency AC. The use of high-frequency operation is advantageous, as it reduces the size and cost of magnetic components.

As a result, the minimum practical architecture for a galvanically isolated charging system consists of six essential stages: a grid connection, an AC–DC rectifier, a high-frequency inverter, a high-frequency transformer providing galvanic isolation, a second rectification stage, and finally the DC battery interface.

Design choices explained Various design choices can be summarised by either voltage, current or efficiency control, this subsection will aim to present these decisions in a logical order to better understand how various circuits are selected and justify the differences in certain circuits.

Voltage control To enable battery charging, the applied voltage must exceed the battery's current terminal voltage. The grid typically provides $230\,\mathrm{V_{rms}}$ in single-phase systems or $415\,\mathrm{V_{rms}}$ in three-phase systems. To charge an EV battery with typical voltage range of 400-800 V DC, the voltage must be stepped-up and regulated/controlled.

One possible approach is to select a step-up transformer that simultaneously provides galvanic isolation. While this may suffice if the battery voltage were fixed, in practice, it varies significantly across different vehicle architectures. Moreover, the operating voltage of lithium-ion battery cells fluctuates by approximately $\pm 13\%$ around the nominal value, ranging from $3.2\,\mathrm{V}$ to $4.2\,\mathrm{V}$ with a typical nominal voltage of $3.7\,\mathrm{V}$ [61].

To further preserve battery longevity and safety, it is advisable to maintain the battery SOC within a range of 20–90% [62]. As a result, the system must be capable of dynamically adjusting the output voltage to accommodate both battery-specific requirements and operational variations. This necessitates the inclusion of additional power electronic stages capable of fine voltage regulation to ensure efficient and safe charging.

Inverter and/or rectifier control The simplest way to reduce or otherwise control the voltage is to used a simple rectifier control to (dis)connect power to raise and lower voltage. Alternatively this can be done at the inverter stage. More complicated implementations looks at the phase difference for both in order to maintain an efficient operating point.

DC/DC converters As rectifier control effectively utilises the rectifier switching components to provide a buck controller, instead this can be done by adding a full buck controller. Doing so gives the added benefit of not directly affecting the power transfer across the transformer. As this puts switching components nearest to the battery, ripple voltage can become an issue. A possible solution is applying the DC/DC converter before the inverter stage,

such that voltage ripples are smoothed out by subsequent components while also providing power control.

Power Factor Correction (PFC) The inclusion of various switching devices and reactive components (such as inductors and capacitors) leads to increased reactive power which has a negative impact on grid stability. PFC is used to control the reactive power drawn by the circuit at the grid connection point and is typically implemented at the grid-connected rectifier stage. For high power applications, PFC becomes a necessary component required by power grids.

2.1.2 Conductive charging

Providing power the vehicle is easier done with a physical cable connection. While the circuit topology remains the same as shown in Figure 2.3, there are differences in location and size of components in the circuit, in addition the power across the charging cable is also different based on these applications.

AC charging Covering the earliest connectors provided, AC charging solutions provide a direct grid connection to the vehicle, meaning AC voltage is connected across the charging cable and plug. Additionally the charging circuitry in Figure 2.3 is placed inside the vehicle. This is referred to at the OBC. As the charging components are inside the vehicle, their implementation falls onto the vehicle Original Equipment Manufacturer (OEM), where various design specifications and style choices, lead to minimizing the space allocated for the OBC which limits component size and therefore power rating.

Figure 2.4 shows the diagram of a commercially available OBC by onsemi, where a 3-phase connection is seen with PFC, and controlled inverter design, onsemi's product range cover 3.3-22kW OBCs.

As all charging components are present on the vehicle, a charging station is not required -apart from billing and protection purposes. Mode 1 charging allows a direct connection from a mains socket to vehicle. Mode 2 charging increases power from mode 1 adding protective gear and communication capabilities to control charging events. Mode 3 raises the power level again where 3-phase supplies are also seen, requiring additional safety measures and disconnection devices. What is commonly referred to as the EV charger only provides safety and communication, hence it is referred to as Electric Vehicle Support Equipment (EVSE).

Figure 2.5 shows the diagram of a typical EVSE provide by Bender GmbH. The diagram includes all components typically seen in a "wall-box" EVSE, where no switch gear is provided for power control. These components aim to provide a communication and authorisation for the charge network providers and ensure safety standards are upheld with current fault measuring and RCD safety components. These components are then linked to an OBC via an AC charging cable.

DC charging In contrast to AC charging, DC charging, maintains the same topology but moves the charging components off the vehicle and into the charger. Allowing for larger components to increase power rating, however more common is to stack multiple modules

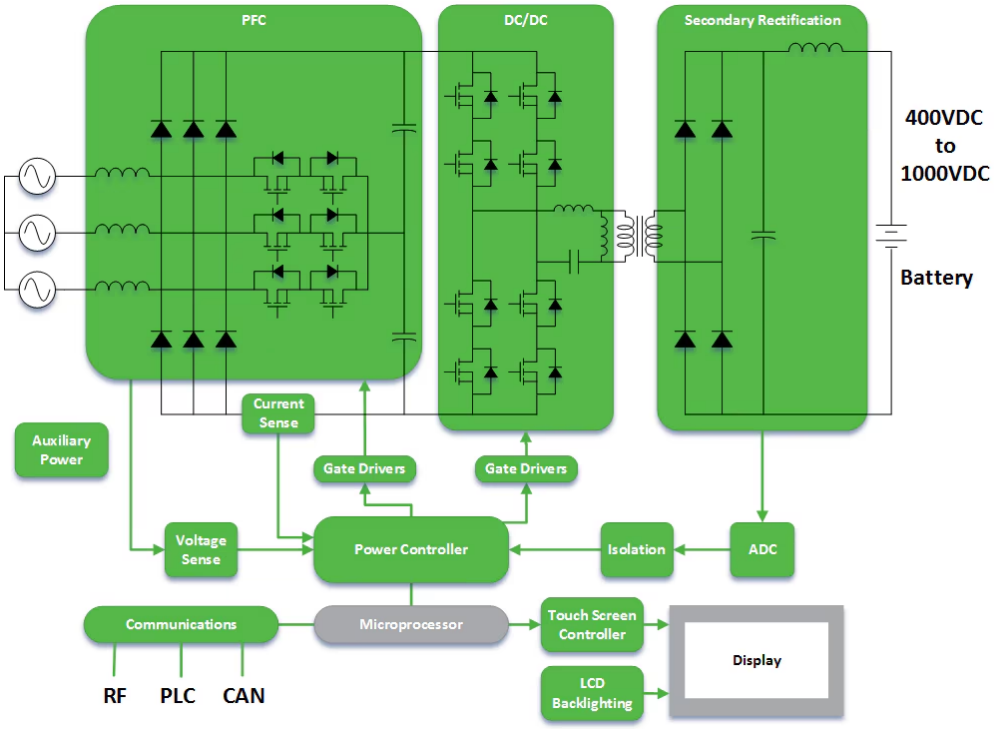

Figure 2.4: ON semiconductor's OBC diagram [63]

in parallel to increase total output power. Hence, DC chargers tend to have a larger form factor. Figure 2.6 shows an example DC charger schematic, where multiple identical modules can be connected in parallel. Note the near identical circuit layout to AC charging in Figure 2.4.

Additionally DC charging solutions transfer DC current across the cable (opposed to AC) at a higher power rating than previous AC solutions. As a result, the cables produce more heat and require heating at higher power ratings.

Removing components from the vehicle gives an additional benefit of reducing vehicle upfront cost, this however has not been fully utilised as most commercially available EVs with a DC charging capability, also offer an AC interface.

2.1.3 Wireless Power Transfer (WPT)

Following the adoption of conductive charging in different regions, multiple connector types emerged, resulting in interoperability issues for certain vehicles and chargers. A potential solution to this issue is wireless charging, which utilises EMF instead of conductive cables.

The application of WPT has been shown up to 1MW for rail systems with a total efficiency of 82.7% [66]. Using multiple pick up and transmitter coils the implementation for a high speed train offers similarities to road vehicle uses. Notably reliable high power transfer is achieved. An induced EMF on the rails is measured at 60V which is deemed safe for the application and shows the resulting magnetic fields at higher power can be safe and likely to also apply to road vehicle applications. However the application functions at a 50mm air gap and the coil misalignment is low (due to being a railway system, constrained in

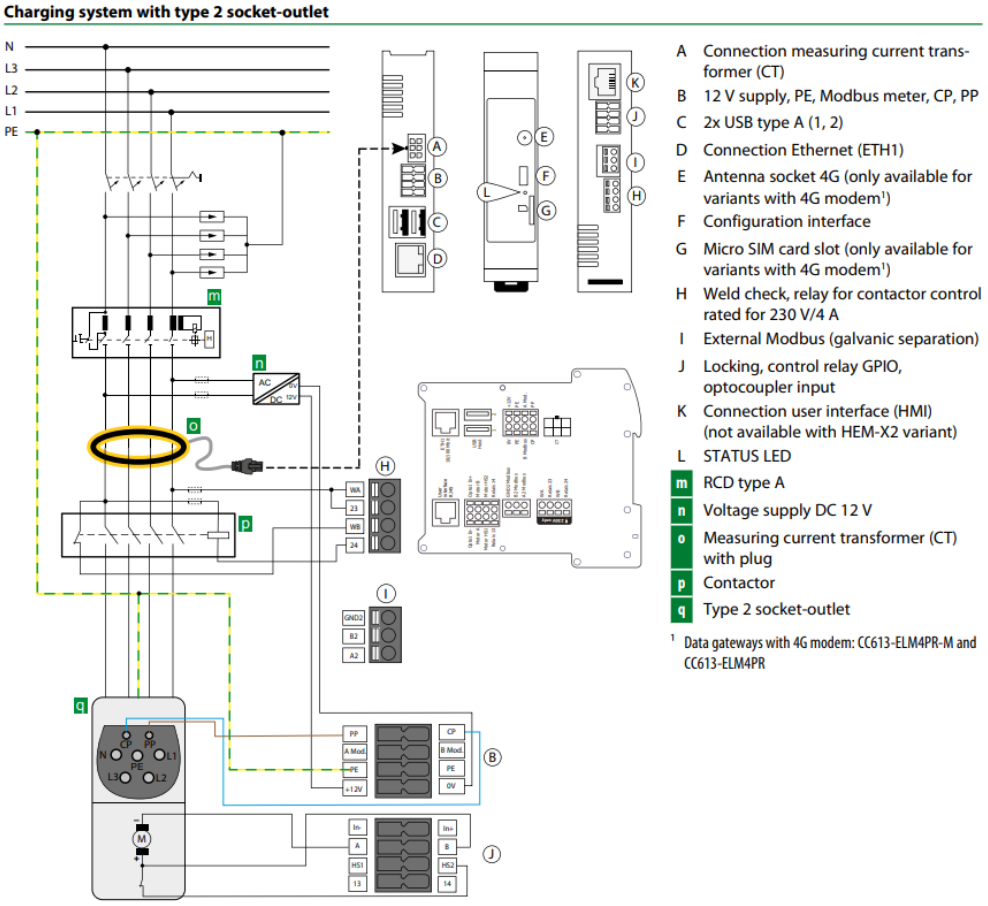

Figure 2.5: EVSE connection diagram from Bender GmbH [64].

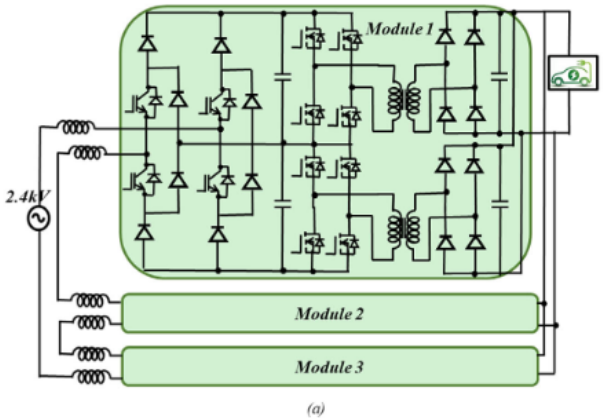

Figure 2.6: DC charging module example diagram [65].

lateral movement), applications for road vehicles need to cover an air gap of up to 200mm and account for the horizontal misalignment. Horizontal misalignment being one of the key concerns as power transfer decreases significantly [67]. It is important to consider the possible lateral misalignment as it will affect the ability to transfer power efficiently, meaning to

provide better efficiency for a wide range of vehicle alignment scenarios, a larger transmitter coil will be required. WPT can be achieved by either capacitive or inductive coupling systems, each having their own advantages for different applications.

Industry applications While no high-power inductive (wireless) charging system has yet reached full-scale commercial deployment, several promising technologies have been announced or demonstrated, indicating growing industry momentum.

WiTricity is a leading developer of magnetic resonance-based wireless charging and has partnered with OEMs such as Yutong to test systems for commercial EVs [56]. **Qualcomm** formerly led the field through its Halo platform before transferring the technology to WiTricity [68, 69].

Momentum Dynamics focuses on high-power wireless charging for fleets and public transport, with operational deployments at locations such as Kansas City Airport. Their systems support power transfer levels up to 200 kW [58].

Electreon specializes in dynamic wireless charging by embedding coils into roadways, enabling vehicles to charge while driving. This approach targets buses and delivery vehicles in pilot deployments [57].

Oak Ridge National Laboratory (ORNL) has achieved some of the highest performance in lab demonstrations, reporting up to 120 kW power transfer with 96% efficiency [70, 71].

Evatran (Plugless Power) was among the first to offer consumer-grade wireless EV chargers, targeting vehicles like the Nissan Leaf and Tesla Model S. These systems operated at lower power levels (3–7 kW) but helped demonstrate early user interest [72].

Tesla, though not yet offering a wireless charging solution commercially, has publicly acknowledged development in this area. The company recently teased a wireless charging pad concept as part of its next-gen home ecosystem, indicating serious intent to enter the market [59].

These efforts are increasingly accompanied by industry standardization initiatives and stakeholders are collaborating to ensure interoperability across vehicle platforms and infrastructure [73, 74].

Capacitive Power Transfer (CPT) CPT is a potential wireless solution which can be used at low air-gaps, have been deemed unsuitable for EV application [75, 76]. For EV charging, the air-gap of an average passenger car is 150-300mm, where inductive charging is better suited. Figure 2.7 shows a comparison of the output power achieved by IPT and CPT at various air gaps, showing the benefit of IPT at larger distances.

Inductive Power Transfer (IPT) Inductive power transfer, utilises a pair of inductive coils to transfer power and has become the standard means of delivering WPT. Offering an autonomous and hands free solution, inductive charging relies on generating a magnetic field using a coil on the ground, the magnetic field is the picked up by a similar receiving coil on the under-body of a vehicle where voltage is induced by the magnetic field and power transfer is achieved.

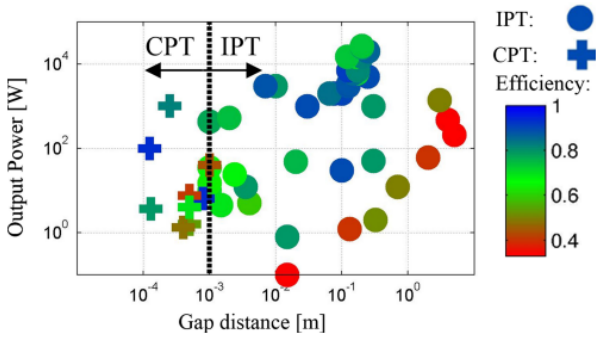

Figure 2.7: Comparing IPT and CPT output power at different air gaps [77]

Figure 2.8 shows a full circuit diagram with dual sided control for IPT, in this circuit the grid connection is changed to a DC power source, otherwise the circuit remains similar to the one presented in Figures 2.4 and 2.6. Table 2.2 outlines representative operating values for EV inductive charging systems.

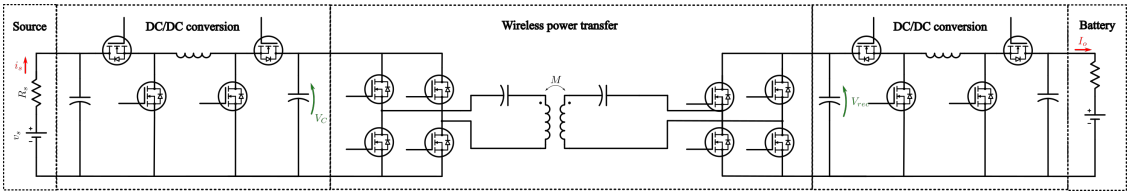

Figure 2.8: Full circuit for IPT.

2.1.4 Dynamic Wireless Power Transfer (DWPT)

Building on the existing IPT system, DWPT uses the same technology now allowing the movement of coils relative to each other, extending the possible applications of WPT to moving vehicles. In theory this technology could work similar to train pantographs, where power is continuously connected to a vehicle, allowing much longer journey (if not infinite) while connected to the DWPT systems. In practice, this technology is very expensive to implement due to high material costs and operation cost of installation (and maintenance). The potential application of this technology can aid to reduce EV battery size, saving on manufacturing cost, aid to reduce the number of EVSE installations while being utilised by a high number of participants. At present it is too early in the technologies life cycle to realise these benefits as they will only be seen at high adoption rates, to date only pilot studies and trials have been conducted.

Using the circuit shown in Figure 2.8, the movement of the coils causes the coupling factor (k) to vary. This is also the way fixed core transformers can be modelled, where a high coupling factor (approaching 1) tends toward a fixed core transformer. The coupling factor is a dimensionless constant between 0 and 1 that relates the mutual inductance M to the self-inductances of the primary and secondary coils, L_1 and L_2, respectively. It is defined by the expression $k = M/\sqrt{L_1 L_2}$. As for large coils, a large mutual inductance can

Table 2.2: Typical operating values for inductive coils in EV WPT research.

Parameter	**Value / Range**	**Notes**
Frequency	85 kHz (81 kHz to 90 kHz)	Recommended by SAE J2954 and widely adopted in EV IPT systems [78, 79].
Current	10–200 A	Up to 200 A in low-voltage/high-current systems [78].
Voltage	48–400 V (Rx); 400–800 V (Tx)	Low voltage on the receiver side (e.g., 48 V), and high voltage on the transmitter side [78].
Power Transfer	300 W–10 kW (typical); up to 20 kW+	Used in LEVs, AGVs, and higher power EV fast-charging [78].
Air Gap	100–300 mm	Common design range; affects magnetic coupling efficiency [78].
Coupling Coefficient (k)	0.1–0.3	Lower values due to misalignment, air gaps; compensated with tuning [78].
Quality Factor (Q)	$>$ 100 (desirable)	Higher Q enhances system efficiency; depends on coil and compensation design [78].

be expected, coupling factor is a standardised way to refer to system operation in a more relatable way (comparing circuits).

During DWPT, the mutual inductance between the transmitting and receiving coils varies as the vehicle moves, leading to fluctuations in system performance. If these fluctuations are not controlled, they can result in current ripple at the output, which may degrade the battery over time [80]. A common approach is to add a secondary side controller to provide either constant voltage [81], constant current or a combination of both [82]. Application of DWPT is commonly done with multiple transmitter coils along a stretch of road. As the vehicle moves over each pad, the coupling between coils—and consequently the power transferred—varies. Reducing output current ripple can be achieved by optimizing the primary pad design and control [83], as well as by minimizing the number of active coils and eliminating power losses in inactive segments. A flatter power transfer profile enables more consistent secondary-side control and helps maintain a constant current to the load, as fluctuations in transferred power can lead to load disturbances.

2.1.5 Automatic Connection Device (ACD)

A niche sector within EV charging, ACD refers to any autonomous device which facilitates the connection between EVSE and EV. As a core functionality, these devices do not need to alter the charging circuit's seen in Figures 2.4 and 2.6, hence they are an add-on service to charging technologies. To date, there are no commercially available ACD solutions.

Automatic Connection Device for vehicle Under-body connection (ACDU) In automated vehicle charging systems, it is no longer necessary to position the connector on the side of the vehicle. As a result, various ACD manufacturers have explored relocating the connection interface to the vehicle's underbody. This approach offers several advantages, including reduced clutter, improved aesthetics, and more efficient use of space in parking environments. Similar to WPT solutions, underbody ACDU systems benefit from simplified user interaction. However, they also retain the efficiency advantage of a direct conductive connection over wireless systems.

One of the key challenges in implementing underbody conductive charging is the integration of currently standardised EV connectors, which are often too large or geometrically unsuitable for unobstructed placement beneath the vehicle. Consequently, many manufacturers have developed bespoke connector systems tailored to their mechanical and electrical requirements. This, however, introduces compatibility issues, as these connectors are not standardized and cannot be used across different systems.

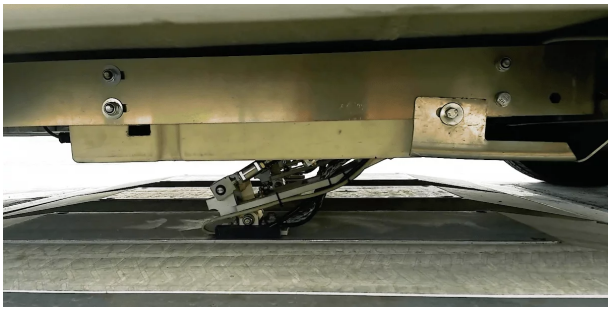

(a) Altsom bus ACDU trial [84].

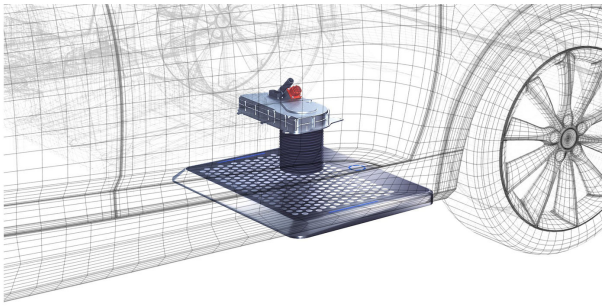

(b) Matrix Charging (MC) ACDU solution [85].

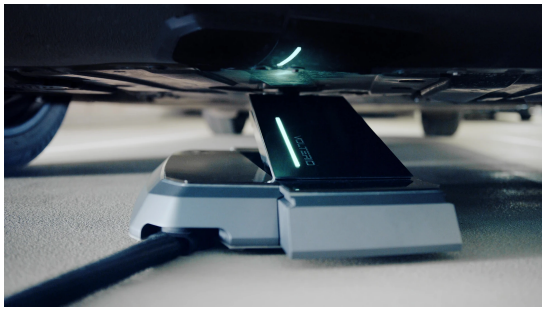

(c) VOLTERIO charging system [86]

(d) MOLE ACDU presented in depot trials at Ocado [87].

Figure 2.9: Examples of ACDU ongoing projects.

Figure 2.9 illustrates several prototype and commercial ACDU systems under development. For instance, Alstom's solution (Figure 2.9a) employs a mechanical arm that extends to contact a large exposed conductive pad beneath the vehicle. This configuration allows for moderate misalignment and has been deployed successfully in outdoor environments. Their implementation is capable of delivering up to 200 kW and has been tested on electric buses [84].

Matrix Charging's system (Figure 2.9b) follows a similar concept but includes a mag-

netic self-alignment mechanism, enhancing positional tolerance and contact reliability [85]. VOLTERIO's approach (Figure 2.9c) introduces a robotic solution that elevates a custom connector from the ground to interface with the underbody socket. The system relies on integrated sensors and actuators for alignment and connection [88]. While promising, the current prototype is bulky and must be custom-fitted to each vehicle, making it unsuitable for retrofit applications on existing BEVs. Development is currently focused on private environments such as garages, with plans to adapt the system for public deployment in the future [86].

VOLTERIO report that approximately 90% of EV charging occurs at home, which supports the viability of garage-based robotic charging solutions. Their existing system delivers 22 kW AC (Mode 2) power but is also designed to accommodate high-power DC (Mode 4) charging, indicating that robotic systems can be compatible with a broad range of charging modes and power levels.

In contrast to custom connector approaches, companies such as IPFT Fuels (developer of the MOLE system) aim to retain compatibility with existing vehicle-side connectors [87, 89]. This strategy allows easier retrofitting and reduces system complexity. In high-utilization fleet environments, such as logistics companies, there are operational costs associated with manual charging (e.g., plugging and unplugging). Furthermore, conventional chargers require additional space for equipment and cables. An automated underbody solution like MOLE could therefore provide both spatial and operational efficiency gains. However, as shown in Figure 2.9d, the MOLE system's above-ground configuration limits its suitability for vehicles with low ground clearance.

2.1.6 Vehicle-to-grid (V2G)

Enabling additional options for how users interact with the grid is rapidly evolving, and user behaviours are expected to shift accordingly as technologies mature [90]. Bidirectional chargers are a key enabler of this transition, offering multiple pathways for users to leverage the energy stored in their electric vehicles—not only for mobility but also as a distributed energy resource. Clearly defining and elaborating on these bidirectional use cases, such as Vehicle-to-home (V2H), Vehicle-to-building (V2B), and V2G, is essential for guiding future research, regulatory development, and system-level integration.

As the adoption of electric vehicles accelerates, particularly in urban and high-demand transport scenarios, the burden of supporting V2G capabilities may increasingly fall on DWPT systems. Unlike static chargers, DWPT has the potential to interact with the grid continuously and at scale, offering unique opportunities for real-time load balancing and energy redistribution. In scenarios where large fleets are constantly in motion—such as public buses, logistics vehicles, or ride-sharing fleets—DWPT could play a central role in enabling V2G at a system-wide level, provided it is designed to support bidirectional energy flow. Therefore, as DWPT deployment expands, its capacity to contribute to grid services and energy resilience should be considered a key design and policy priority.

To better understand the use of the V2X it is beneficial to compare the advantages and disadvantages of the technology. One of the main factors driving research is the added flexibility of batteries as energy storage, however the required infrastructure grows in complexity to implement this technology effectively. Starting from the lower scale of V2H, home electri-

cal system may need to be upgraded to utilise a V2H charger, in practice this is similar to the integration of home Photovoltaics (PV) [90]. Scaling up to V2G, again a standard compliant inverter will be required. With an increasing number of V2G chargers, a control and communication infrastructure also needs to be implemented to balance the grid effectively [9]. It is worth noting this also increases security risk for potential grid attacks.

Fast response Compared to conventional power generators and other forms of energy storage, batteries offer near-instantaneous response to changes in power demand or supply. This characteristic makes them highly effective for grid stability and efficiency, as they can rapidly switch between acting as a power source or a load, all while maintaining high operational efficiency. In contrast, generators often need to operate at suboptimal points to balance loads, reducing their efficiency.

V2X technology leverages this rapid response capability of vehicle batteries to not only assist in load management but also to help run other generators at more stable and optimal levels [91]. However, the frequent charge and discharge cycles associated with such usage do have an impact on battery longevity. Simulation studies indicate that regular participation in V2G could reduce battery lifespan by approximately 0.5 years, within the typical 6–8 year lifespan range [92].

Peak shaving The low inertia and rapid response of batteries make them ideal for managing fluctuations in power demand, particularly during periods of high usage—a process known as peak shaving. V2X can support the grid by smoothing out stochastic changes in load or assisting traditional generators that require longer times to reach optimal operating points. By maintaining these generators at steady outputs and using EV batteries to meet the variable portion of demand, overall system efficiency and stability are improved.

However, to effectively utilise EVs as a power source, their availability and usage patterns must be understood and forecasted. Uncertainty in vehicle behaviour, if unaccounted for, could disrupt base and peak power balancing and potentially lead to blackouts in parts of the distribution grid with limited supply capabilities. Research has shown that by analysing road congestion and user habits, the probability of vehicles being parked—and therefore available for V2X—can be estimated [93]. Historical data can also help predict power demand at charging stations, and fluctuations in capacity reveal how user behaviour varies by time of day [94]. These insights enable more accurate and reliable integration of V2X into grid operations.

Renewable energy uptake Renewable energy sources, while essential for sustainable power systems, present operational challenges due to their variability and dependency on uncontrollable environmental factors. Solar power is only available during daylight hours and is affected by cloud cover, while wind power generation can fluctuate dramatically from day to day. Expanding renewable generation often means adding more units—an approach that is not always practical or cost-effective.

In this context, battery storage plays a crucial role. It enables the grid to harvest and store surplus energy from renewable sources when production exceeds demand and later release it when generation is low. Vehicle batteries used in V2X systems are particularly

suited to this role due to their fast response and flexibility. They provide an opportunity to stabilize renewable energy integration, ensuring maximum utilization of green energy and reducing curtailment or efficiency losses in generation systems.

System complications One of the main concerns of current EV users, both domestic and commercial, is range anxiety. The users often plan or seek out charging stations to maintain high SOC for their vehicle. This follows onto a reluctance to participate in V2X as users view peek demand and grid stability as the grid operators concern not their own. For commercial uses, business also opt against the cost saving advantages in favour of reduced planning overheads and lower risk. Simply the vehicle's primary function of transportation is prioritised over the utilisation for monetary value.

Battery degradation Using a battery gradually degrades its capacity over time, and participation in V2X can accelerate this process by increasing the number of charge-discharge cycles. This degradation leads to reduced driving range and potentially more frequent battery replacements—an uncommon and costly practice that often prompts owners to sell their EV after a certain period. Despite these concerns, most BEV users do not fully deplete their battery between charges, leaving a portion of capacity underutilized. With thoughtful planning, this surplus energy can be used without significantly affecting battery health.

To address this, battery degradation models have been integrated into costing simulations to support cost-effective implementation of V2G. Research has explored bidirectional control strategies, including the modelling of bi-directional WPT systems [95]. However, challenges remain—particularly in the physical design of wireless systems. The transmitter coil is typically larger to ensure effective coupling and power transfer, which is impractical for passenger vehicles when discharging back into the grid. These hardware limitations indicate that further work is needed to optimize wireless V2G solutions for widespread use.

When managed properly, V2X participation can offer benefits to both the grid and the user, such as reduced charging costs and enhanced grid stability [96]. Additionally, BEVs can be used for home energy needs through V2H, further lowering electricity bills. For instance, V2H has demonstrated cost reductions of up to 57%, compared to only 12% from basic time-of-use charging [97].

Cost Participating in V2X involves a range of financial considerations. To begin with, vehicles require a compatible onboard charger, which is more complex and expensive than a conventional charger due to the need for additional power switches. Moreover, the vehicle must be connected to a V2X-compliant EVSE, which also carries a higher price point than standard units. For home applications, electrical systems may require upgrades to safely handle bidirectional power flow. These factors collectively contribute to a higher capital expenditure for the user.

Beyond hardware costs, economic viability depends on electricity tariffs. V2X transactions are often subject to similar pricing structures as residential photovoltaic systems, where electricity is typically purchased at a higher rate than it can be sold back to the grid. This pricing imbalance can discourage participation, especially when users can charge overnight at low rates and meet their daily driving needs without engaging in energy exports.

However, it's important to consider the potential for cost savings. For domestic users, improved system efficiency through V2X can translate into lower energy bills, particularly when employing solutions like V2H [97]. On a broader scale, increased efficiency reduces fuel consumption and operational demands on the grid, possibly lessening the need for additional generation infrastructure. While the initial infrastructure costs are significant, they are often viewed as long-term investments, especially as existing systems age and require replacement.

Summary of advantages and disadvantages It is quite clear the advantages of V2X primarily benefit the grid in distribution and power generation. The reluctance of users in participation is understandable as they carry a significant risk and cost with their vehicle which for many is a critical aspect of day-to-day life. At present the technology is at an early stage in it's product life cycle, as few vehicles and charge points are compatible. The cost association is a balancing act of capital and operational costs, which leads to the purchase decision making progress where users often favour lower upfront cost compared to other operates which often perform a system lifetime analysis considering both upfront and operational cost. As the technology develops and increases in use, it is likely to become a requirement to participate in V2X in some capacity as the small contribution of many users can be a significant factor for a large system such as the power distribution grid, in order for it to introduce more renewable sources and reduce fossil fuel generators.

Potential Applications Building on the preceding discussion, several practical applications of V2X technology are emerging. These span both grid-connected and off-grid contexts, each offering unique opportunities for enhancing energy flexibility, resilience, and efficiency.

Parking lots offer a compelling opportunity for deploying V2X technology, particularly in urban areas or near workplaces where vehicles remain parked for extended durations during peak power demand. With rising EV adoption, parking facilities are becoming critical hubs for charging infrastructure, which in turn increases overall power demand. These environments provide unique potential for numerous EV-grid interactions. By leveraging V2X, parking lots can mitigate the impact of stochastic charging events, reduce peak demand on the grid, and enhance energy management. This not only aids in grid stability but also presents financial incentives for vehicle owners [98]. Similar to V2B, Vehicle-to-parking (V2P) utilizes connected vehicles to offset the grid load during high-demand periods [9, 99]. As a result, parking lots are increasingly viewed as strategic assets in the broader EV energy ecosystem [99].

Off-grid applications EVs being a mobile energy storage unit, the energy stored in the battery can be used to provide power in remote locations. This can be useful for military applications which currently use diesel generators for their power demand [100]. Utilising large vehicle batteries to create micro grids for various applications and equipment, these use-cases are very specific and their financial feasibility maybe questionable but the utility enabled by bidirectional technology.

Static wireless power transfer For a wireless charging system to reverse power flow and provide V2X, it requires upgrading the secondary side of the charger from a passive rectifier to a full bridge inverter. This is not a difficult task as the system effectively becomes symmetrical and the control strategy effectively switches what is considered the source and load, both sides will have the same switching capability, so the main difference is the coils used. For identical coils this is then exactly the same, hence the key distinction is the coil sizes and compensation topologies. Coil size will determine the possible power transfer and efficiency as a larger coil will produce a larger magnetic field, hence for a static system the primary (transmitter) coil is often larger than the secondary (receiving) coil. The compensation topologies are often chosen for their power transfer characteristics, as asymmetrical compensation circuits (series-parallel, parallel-series or their complex counterparts with LCC or LCL circuits) provide different output characteristics for circuit design and control. Hence this needs to be considered and often results in additional switching components for compensation topology.

Dynamic wireless power transfer As EV adoption accelerates, there is growing demand for smart, flexible, and sustainable charging infrastructure. DWPT, when integrated with V2G capabilities, presents a promising solution to key challenges such as range anxiety, grid reliability, and renewable energy integration.

DWPT allows electric vehicles to charge while in motion, reducing the need for large batteries and alleviating range anxiety. This continuous charging approach minimizes downtime, enables lighter vehicle designs, and improves overall energy efficiency and cost-effectiveness [101, 102].

V2G functionality allows EVs to discharge stored energy back into the grid during periods of high demand or grid stress. When coupled with DWPT, this transforms roadways into distributed energy resources. Research indicates that such integration supports frequency regulation, peak load shaving, and stabilization of local grids, particularly when coordinated with renewable energy and storage systems [103, 104].

Recent developments in coil design, compensation networks, and power electronics have enhanced the feasibility of DWPT for both Grid-to-Vehicle (G2V) and V2G operations. Coil geometries like DDQ pads and the use of adaptive impedance matching networks enable high power transfer efficiency even under misalignment and variable driving conditions [105, 106]. Bidirectional converters and control schemes further ensure seamless and efficient energy flow between vehicles and the grid [103].

DWPT infrastructure, though initially capital-intensive, can become economically viable through optimized placement and smart energy management strategies. Studies show that the inclusion of V2G services improves the economic return for DWPT operators and reduces the overall cost of ownership for users by allowing energy arbitrage and ancillary services provisioning [102, 104]. Environmentally, enabling V2G via DWPT supports higher integration of renewables by acting as buffer storage [107].

As we progress toward smart cities, DWPT-enabled V2G systems fit naturally into the vision of an intelligent, connected transportation and energy ecosystem. Utilizing Internet of Vehicles (IoV) and V2X communication, vehicles can coordinate charging and discharging based on traffic, grid conditions, and user needs [108]. This convergence of mobility and

energy sectors underpins the future of sustainable urban development and aligns with the broader vision of smart, connected cities [108].

EV cluster control EV cluster control enables multiple vehicles to be managed as an aggregated unit, allowing for coordinated bidirectional power flow between the grid and the EV fleet in a V2G scheme. By grouping vehicles into clusters, the combined capacity can provide meaningful frequency support, improve grid stability, and make the control process more scalable and efficient compared to managing individual EVs.

Tube-based model prediction methods with a disturbance observer, designed to observe the magnitude of grid disturbance, and the previous value of frequency deviation is obtained with the lest control effort [192]. The simulation is verified with scenarios of both sufficient and insufficient generator capacity. Self-adaptive droop droop control for EV clusters and model predictive control is used for the energy storage system, parameters within the predictive control model were optimized using a genetic algorithm [193]. Hybrid fuzzy proportional integral (FPI)-linear active disturbance rejection control has successfully been implemented for frequency regulation [194]. Consideration of EV users, battery degradation and the economic of EV participation in frequency regulation has also been considered throughout research to develop better optimized control strategies for both EV users and power grids. EV user demand is considered to leave EVs with sufficient SOC for future journey [195]. Battery degradation and life cycle with EV cluster participation in auxiliary services such as V2G have also been studied to ensure the system as a whole is financially viable for future uses [196–198]. Battery degradation is summarized by the EV cluster power contribution as the impact of low and high frequency switching can be filtered out effectively. However current research focuses primarily on the grid (stability, voltage level, frequency deviation) while less attention is given to optimizing the EV cluster output power and contribution ratio.

2.2 Battery technology

A battery pack consists of multiple battery cells, for EVs the main battery used is located on the under-body of the vehicle and consists of thousands of cells connected in series/parallel to achieve specific voltage and power ratings between the battery terminals (For example a Tesla Model X battery consists of 7,256 cells). When using two identical batteries, stacking the batteries in series will double output voltage while maximum current they can output remains the same, if they are instead connected in parallel, the voltage remains the same but the pack would now be able to double it's maximum power output. The inner workings of a battery pack are managed by a Battery Management System (BMS), which is a controller connected to multiple sensors in the battery pack to monitor it's performance and facilitate safe usage. The BMS will send it's information onto various monitoring systems in the vehicle or charger which are used to lower the input power if necessary. State-of-Charge (SOC) describes the amount of power the battery is able to supply relative to it's maximum rating (expressed as a percentage). For charger development, it is important to control the voltage or current supplied to the battery as it's requirements might change depending on it's current SOC.

Current ripple can accelerate battery degradation by increasing internal impedance and promoting capacity fade, thereby reducing the battery's power capability. Studies have shown that high-frequency ripple currents can degrade battery performance up to ten times faster than conventional DC charging without any AC ripple components [109]. This accelerated degradation at higher frequencies is primarily attributed to increased internal heating, which promotes side reactions such as SEI (solid electrolyte interphase) layer growth [109]. However, smaller-scale experiments indicate that low-frequency ripple currents (e.g., below 100 Hz) can be similarly detrimental, causing only about 1% less degradation than high-frequency oscillations [110]. Further evidence from grid-tied battery storage systems shows that even 60 Hz ripple—typical of power electronic interfaces—can significantly increase internal resistance and shorten battery lifespan [111]. While the application context in [111] focuses on stationary storage, the power electronic converters in both systems operate at similar switching frequencies (typically in the tens to hundreds of kilohertz range). As a result, DWPT systems may expose EV batteries to ripple with comparable characteristics. This highlights the importance of incorporating appropriate control and filtering stages in WPT architectures to suppress ripple before it reaches the battery.

2.3 Inductive Power Transfer (IPT)

The misalignment of inductive power transfer coils affects the charging efficiency of the overall system. At an air gap of 14cm, the efficiency drops from 95.7% at 0cm misalignment to 91.5% at 20cm misalignment, further the angle between both coils further affect the system efficiency [112]. In order to become a more viable option for EV charging, the efficiency will need to be comparable to that of conductive (plug-in) charging, else the inefficiency amounts to cost which will be a main factor for larger applications such as car-parks. The angle and distance misalignment will be affected by user driving/parking ability and air gap will vary based on vehicle and laden or unladen load.

In comparison another study shows with air gaps of 100mm, 120mm and 140mm and power output of 3.3kW, the efficiency shows little change at 100mm and 120mm air gap, but importantly shows the adverse effects of increasing air gap which then drops the efficiency more as a function of misalignment [113]. These factors are important as the air-gap will vary based on type of vehicle which is an important factor for charging solution deployment.

Current research solutions for static wireless charging are able to provide 11kW charging with efficiency <90% at an air gap up to 180mm [114]. While the solution is slower than plug-in fast chargers (22kW+), the convenience of provided and lack of wires make it appealing to certain costumers for home charging and in the future potentially road side or car-park application which might require having the unit integrated into the road surface. Public transport applications using high-power on-route wireless charging systems (e.g., 200 kW) can enable effectively continuous vehicle operation by recharging during scheduled stops, allowing for near-unlimited driving range along fixed routes without the need for large battery capacities [115,116]. Such an accomplishment shows the technologies feasibility and aids the transition to EVs, which was considered difficult for public transport (buses in particular) due to larger battery capacity and power consumption. However Momentum Dynamics have shown the implementation of WPT technology to maintain 75% SOC which is excellent for its application and battery life span; Showing no interruption for environmental impacts (in-

cluding snow and ice). Furthermore they have also developed software for payment collection for different vehicles using their service [117], which could add another layer of convenience for users able to use the same charging points. Notably this application is static, charging while loading/offloading passengers. Dynamic charging options tend to compromise on some of their specifications; namely air gap, efficiency, power level and misalignment tolerance [118]. While design priorities vary across applications, WAVE (a provider of high-power wireless charging solutions) distinguishes itself by achieving 50 kW power transfer with 90% efficiency over an air gap as large as 254 mm [119]. With a larger air gap and misalignment tolerance, the solution proves viable for road applications, accounting for user misalignment and providing a high charging power, the application could solve a lot of range anxiety issues and bring WPT as a more mainstream means of charging, especially for heavy good vehicles or buses. Other high power solutions have been shown to provide up to 120kW [120]. While the power supplied rating is increased, the air gap decreases and coil size increases, which is part of the issues facing WPT system. To provide the convenience and compete with plug-in solutions, higher power is required for some applications, however this is driving up the dimensions and weight of coils as well as the cost, making them less attractive for use. Moreover the decreased air-gap limits the vehicles that can utilise the application, importantly vehicles which require the increased power rating, are ones which also have a higher air gap requirement (buses, vans, lorries). The common idea that DWPT will allow for smaller batteries has been disputed, in the interest of improving battery life [121]. With large batteries and now large receiver coils and power electronic components, the additional weight and size could cause issues for certain applications.

2.3.1 Coil design

Various coil designs have risen in literature, offering different advantages based on their application [106, 122–126]. Figure 2.10 shows some of the designs used for static wireless charging, these designs typically aim to improve the coil transfer characteristics to achieve better efficiency or reduce magnetic field leakage (reduce impact on surroundings). The same is also done for the case of DWPT where instead of a transmitter coil, a track is used along the centre of a driving lane. The track design features a narrower design (compared to static transmitter coils) to increase the magnetic field in the centre of the lane instead of spreading out more. In doing so, misalignment tolerance is increased as vehicles with larger misalignment (driving close to road markings), are still going to be over the transmitter rail as long as the vehicle is within the driving lane. Figure 2.11 shows the cross-section of DWPT track designs which are a better method for electrifying longer sections of road compared to increasing the size of static coil designs [106, 122, 123].

The comparison of coil designs is given in Table 2.3. For static WPT coil design where typically the design control extend to both the primary and secondary side of the circuit for interoperability, the coil shape can be chosen to best suit the design parameters. In the case of DWPT it is important to note the changing mutual inductance which in this case is summarised by misalignment, hence for DWPT rectangular coil would be best suited to allow for the change in misalignment. Note, the same is true for coils in Figure 2.10, where more intricate designs will have better performance for static charging but will have low misalignment tolerances.

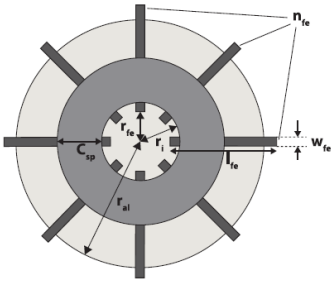

(a) Circular Coil [127]

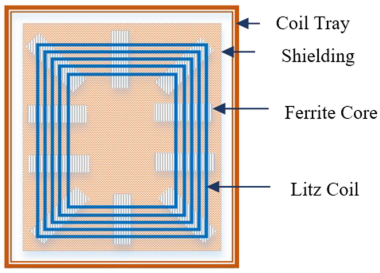

(b) Rectangular Coil [128]

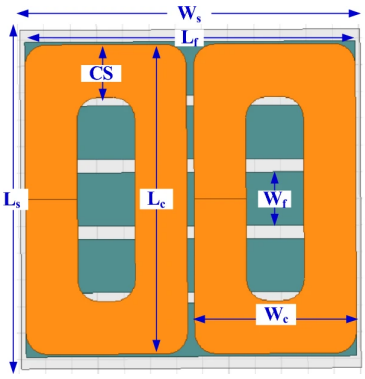

(c) Double D (DD) Coil [129]

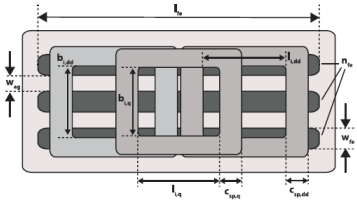

(d) Double D Quadrature (DDQ) Coil [127]

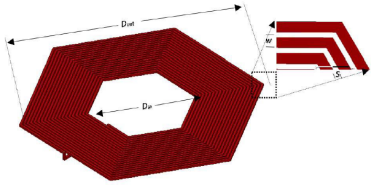

(e) Hexagonal Coil [130]

Figure 2.10: Diagrams of different coil structures used in wireless power transfer systems.

Table 2.3: Comparison of coil structures (as seen in Figure 2.10) in terms of coupling factor, manufacturing cost, and self-inductance.

Reference	**Coil Structure**	**Coupling Factor (k)**	**Self Inductance (μH)**	**Manufacturing Cost**	**Misalignment Tolerance**
[127, 131]	Circular	Medium	Medium	Medium: low copper, more ferrite	Good for rotation/vertical; poor lateral
[127, 132]	Rectangular	Medium-Low	Medium	Medium-High: less ferrite efficiency	High in one direction (longitudinal)
[133]	DD	High	Medium-Low	High: complex layout, ferrite precision	High in all directions
[127, 133]	DDQ	Very High	High	Very High: additional complexity	High; especially strong longitudinally
[130]	Hexagonal	Medium	Medium	Medium: modest ferrite use	Similar to circular; slightly better lateral

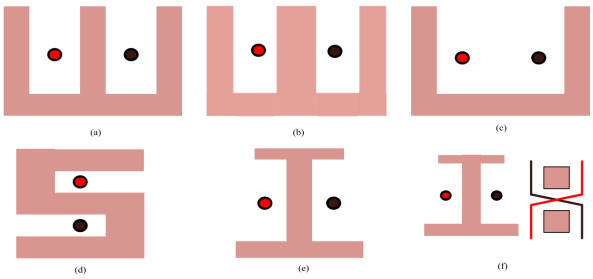

Figure 2.11: DWPT transmitter track cross-section designs [106], with positive (red) and negative (black) wires shown within ferrite cores of different shapes.

2.3.2 Compensation topologies

The main principle behind wireless inductive power system is operating at (or close to) the resonant frequency of the inductive coils on the primary and secondary sides of the system. Both sides consist of an LC circuit, running the system at high frequency allows for smaller components on both sides. In such systems the mutual inductance and quality factor where, mutual inductance affects the efficiency and quality factor affects the stability of the system [134].

To better control transfer characteristics of the inductive coils, compensation components are added on both the primary and secondary side. The connection of passive components (capacitor and inductor) in different ways [135], the differences be found in Table 2.4. Depending on the topology used, different control modes can be implemented [136, 137]. With higher order implementations achieving load independent control allows for simpler control implementation [137].

Figure 2.12 illustrates the fundamental compensation topologies commonly used in inductive power transfer (IPT) systems, while Table 2.4 compares their key characteristics. These topologies form the foundational resonant structures that enable efficient wireless power transfer by compensating for the reactive impedance in the system. Serving as a quick reference for understanding trade-offs between different topologies in terms of efficiency, control, output characteristics, and sensitivity to load or coupling variations.

Higher-order compensation topologies—such as LCL-S, LCC-S, and LCC-LCC—extend these basic configurations by adding additional reactive components (inductors and capacitors) to improve current shaping, enhance load regulation, and achieve nearly sinusoidal waveforms at the inverter input or output. These are typically used in low to medium power applications due to their complexity and increased component count. In contrast, the Series-Series (SS) topology is often preferred for high-power transfer scenarios because of its simplicity, robustness, and high efficiency under strong coupling conditions [123].

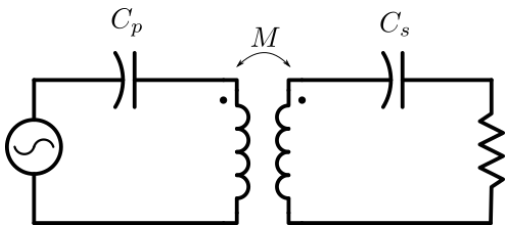

(a) Series-series

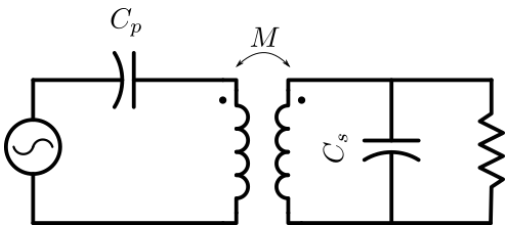

(b) Series-parallel

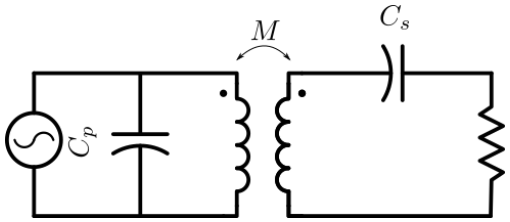

(c) Parallel-series

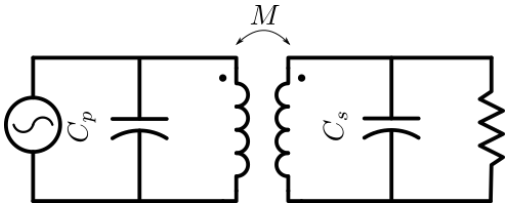

(d) Parallel-parallel

Figure 2.12: Compensation topologies for IPT.

Table 2.4: Quantified comparison of resonant compensation topologies [134, 138, 139].

Parameters	**Topologies**			
	SS	**SP**	**PS**	**PP**
Output	Current source	Voltage source	Voltage source	Current source
Dominant tuning component	Transmitter capacitance	Transmitter capacitance	Receiver capacitance	Receiver capacitance
Efficiency (%)	>90%	65–80%	70–85%	75–85%
Equivalent impedance	Minimum	Minimum	Maximum	Maximum
Output power	Up to 25 kW [138]	Up to 20 kW [139]	<1.5 kW (typical)	<1.5 kW (typical)
Control alternatives	Output current	Output voltage	Output voltage	Output current
Sensitivity to distance	Very sensitive	Very sensitive	Less sensitive	Less sensitive
PF @ distance	Unaffected	Unaffected	Increases with distance	Increases with distance
Dependent on Load	No	Yes	Yes	Yes
ZPA/ZVS capability	ZPA and ZVS achievable; stable	Difficult to maintain ZPA; needs tuning	ZPA with complexity; ZVS possible	Challenging ZPA and ZVS without tight control
Application suitability	EV charging (stationary and dynamic), industrial	High-power dynamic charging, variable loads	Biomedical, small electronics	Compact systems with limited space and power

Reducing the component count and weight on the vehicle side is desirable for cost reduction and improved system efficiency. One effective approach is to eliminate switching and sensing components from the secondary side by implementing control exclusively on the primary side. As shown in Table 2.4, certain compensation topologies—such as Series-Series (SS) and Parallel-Parallel (PP)—support output current control directly from the primary side, making them suitable candidates for this strategy. By measuring voltage and current at the primary coil, constant voltage (CV) or constant current (CC) charging can be achieved through appropriate control algorithms [140–142].

While this approach is effective in static charging scenarios, where coil alignment and coupling remain stable, it poses challenges for dynamic wireless power transfer systems. In such systems, variations in the coupling coefficient—caused by vehicle movement—lead to uncontrolled fluctuations in power transfer. Since secondary-side sensing is absent, these disturbances are not directly compensated. As a result, additional filtering or advanced control techniques on the primary side are necessary to maintain consistent output performance under dynamic conditions.

2.3.3 Foreign Object Detection

With the increased adoption of WPT systems in electric vehicles, ensuring operational safety is paramount. Two primary risks necessitate foreign object detection: the risk of EMF exposure to living beings and the safety and efficiency issues caused by conductive materials near the coils [143]. Foreign Object Detection (FOD) methods are commonly categorized by object type (metal or living), detection principle (electromagnetic, thermal, etc.), and implementation complexity [144]. Modern research explores machine learning approaches that maintain high accuracy even under coil misalignment conditions [143].

Metal Object Detection Metal Object Detection (MOD) focuses on identifying conductive objects—such as coins, screws, or foil—that enter the wireless charging zone. These objects can distort the magnetic field, causing eddy current heating and degrading power transfer efficiency. MOD methods are categorized based on how they detect such disturbances and how they interact with the WPT system.

Parameter Based These methods detect metal presence by monitoring variations in system parameters such as impedance, voltage phase shift, resonance frequency, or quality factor. They are typically low-cost and easy to implement but struggle with sensitivity under misalignment and for small objects [145].

Sensor-Based Techniques using external sensors—thermal imaging, hyperspectral cameras, or radar—can offer high accuracy and object differentiation. However, they are sensitive to environmental conditions and are costly [146].

Coil-Based These methods use dedicated sensing coils to detect disturbances in the magnetic field. Passive systems rely on WPT field-induced voltages, whereas active methods use an external excitation source. Combined systems integrate both to improve coverage and reliability [147].

Living Object Detection Living Object Detection (LOD) aims to identify biological entities such as humans or animals that may enter the high-EMF region of a WPT system. Because such exposure can cause physiological harm, LOD is critical for compliance with safety regulations and for protecting users and bystanders.

Capacitive Detection Capacitive methods sense changes in dielectric properties near comb-shaped electrode structures. Living organisms significantly alter capacitance due to their biological composition, enabling reliable detection [148].

Thermal Detection Using infrared or temperature sensors, this approach identifies living organisms based on emitted heat. It provides reliable spatial detection but is less effective under variable ambient temperatures [149].

Movement Detection Advanced methods like image-based detection using YOLOv7 identify living beings through movement or visual characteristics. This approach achieves high precision and recall, particularly with annotated datasets and pre-trained deep learning models [149].

Challenges Developing high-accuracy FOD systems that function reliably across misalignment scenarios remains a challenge. Small object detection, environmental robustness, and integration with high-power WPT systems are also unresolved issues. The trade-off between sensitivity and false alarm rate, especially for LOD, is a critical area of ongoing research [150].

FOD technologies are essential for the safe deployment of EV wireless charging systems. MOD is relatively mature, with effective solutions across various modalities. In contrast, LOD continues to evolve, particularly with new sensing and machine learning techniques. The trend toward shared MOD/LOD systems and integrated detection strategies promises comprehensive, scalable safety frameworks for future WPT deployments [151].

2.3.4 Inductive Power Transfer (IPT) models and modelling techniques

Modelling wireless power transfer is most commonly done using either the T-equivalent circuit model, which represents magnetic coupling through coupled inductances as shown in Figure 2.13b, or via the induced EMF approach, as illustrated in Figure 2.13c. These two modelling approaches are mathematically equivalent and yield identical results. Mutual inductance between coils behaves similarly to a transformer, without a magnetic core, which significantly lowers the coupling coefficient. Therefore most research applies transformer modelling techniques to WPT systems as they provide accurate predictions for system operation.

Figure 2.13, shows how the mutual inductance can be modelled using the t-equivalent (Figure 2.13b) and induced emf models (2.13c). With zero mutual inductance $M = 0$, no power is transferred—clearly depicted in the EMF model where the induced voltage vanishes. In the T-model, this case appears as a decoupling of the two coils, representing the secondary side as a short circuit that reflects minimal impedance to the transmitter. This results in a high primary current, consistent with the behaviour of inrush current in short-circuit

conditions. On the other hand, as $M \to L_1$ or $M \to L_2$, the reflected impedance increases, and the equivalent coupling approaches an ideal transformer scenario. The EMF model has the advantage of clearly illustrating the lack of a physical connection between coils, relying solely on magnetic coupling. Where further coils can be added to the system by adding the resulting induced EMF to each coil in the system.

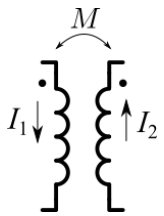

(a) Mutual inductance block diagram.

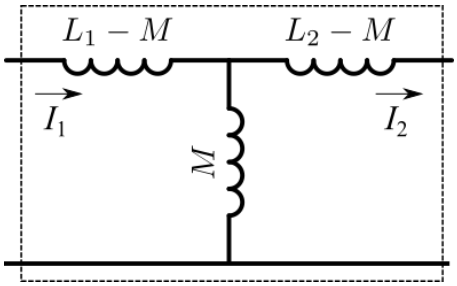

(b) T-equivalent model.

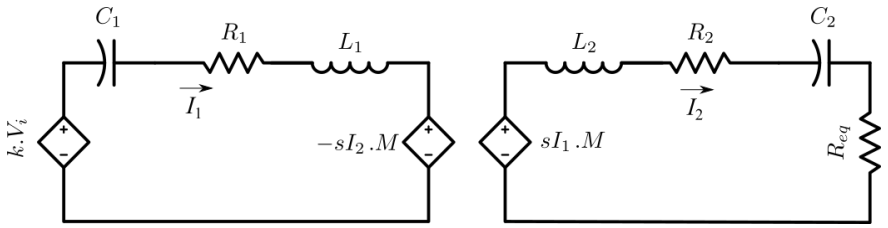

(c) Induced EMF model.

Figure 2.13: Mutual inductance equivalent models.

For multiple coil systems, mutual inductance terms expand to M_{ij} where i and j represent different coil pairs. This significantly increases the complexity of the T-equivalent model due to the need for many coupled inductances and changing interactions. In contrast, the EMF model scales more naturally, simply requiring the addition of more induced voltages based on coil positions and currents.

Current approaches in the literature predominantly rely on circuit-level steady-state analysis to design static charging systems and compare their performance. One common methodology is to derive power transfer efficiency as a function of mutual inductance [152–154]. This approach is attractive due to its simplicity but is often overly simplified as it is based purely on steady-state behaviour [152, 153]. While steady-state analysis is useful in static scenarios with long interaction times, it becomes insufficient in high-speed applications such as DWPT, where coupling durations are limited to milliseconds. In such cases, ignoring dy-

namic response and control limitations can lead to misleading conclusions and suboptimal controller design.

Additionally, some studies simulate a series of static offset cases [152, 155, 156], which are then used to imply dynamic system behaviour. Even when dynamic simulations are performed, they are often presented as a function of position rather than time, and typically involve low-speed operation to ease practical implementation [154], this is similar to gathering a series of steady state static system results. A broader sweep of mutual inductance values—corresponding to wider lateral and longitudinal misalignments—is essential for developing robust control strategies and investigating edge-case behaviours such as foreign object interference or coil failure.

Figure 2.14 shows an example of system efficiency as a function of displacement [154]. Although the general trend matches expectations—efficiency drops with increasing misalignment—the primary-side current is not reported, and efficiency values are truncated around 50%. This reflects static WPT behaviour where the system is tuned for minimal misalignment. In DWPT, however, interactions can begin under misaligned conditions with coupling coefficients still below 0.1. As k falls below this threshold, transmitter impedance drops, causing primary-side current to increase—an effect that models must accurately reflect, even if undesirable. Similar research articles demonstrate the circuit within a specific range, usually where coupling factor greater than 0.1 [156].

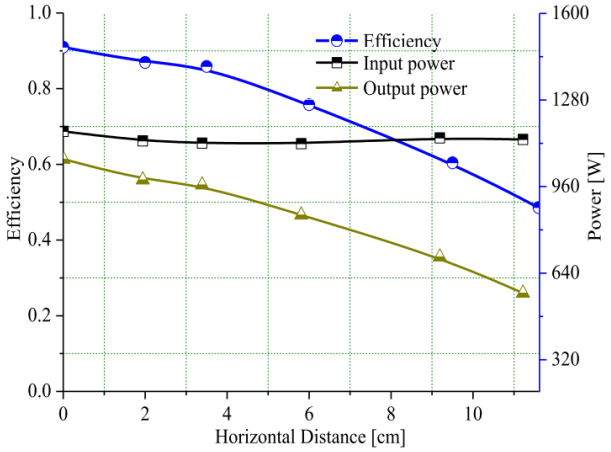

Figure 2.14: Transmission efficiency versus horizontal distance [154].

The common theme across literature is obtaining power transfer characteristics as a function of mutual inductance. Therefore, accurate and efficient modelling of mutual inductance is critical. Analytical approaches using Neumann's formula or Maxwell's equations can yield high-fidelity results [157], but are computationally intensive and often impractical in real-time simulations or iterative control design. Finite Element Analysis (FEA) methods, while highly accurate for coil design [155, 156], are similarly unsuitable for full-system simulation due to complexity and long runtimes. Instead, results from FEA are often extracted into parameterized models (e.g., to obtain L_1, L_2, M) for use in circuit-level simulations [155].

Extending mutual inductance modelling to multi-coil systems introduces the possibility of using coil arrays [158, 159]. For static charging, such arrays improve power density by

covering more ground with transmitter coils. On the receiver side, multiple coils can improve performance by capturing power from wider regions [156].

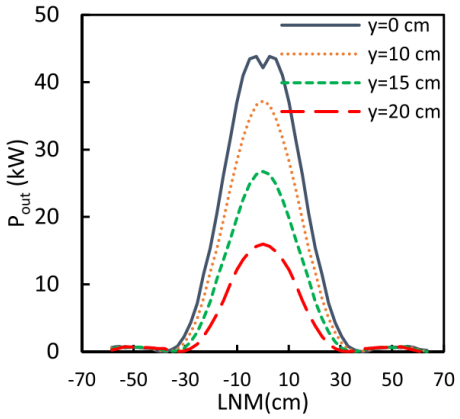

(a) Analysed power output over longitudinal misalignment (LNM) [160].

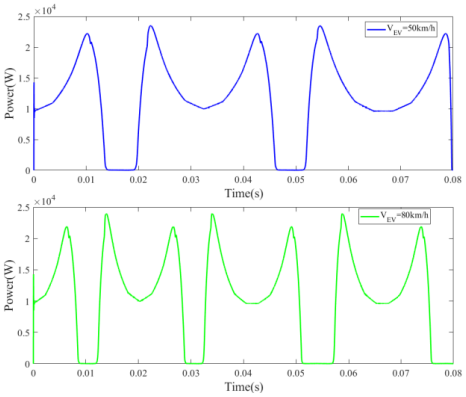

(b) Measured power output during practical operation [122].

Figure 2.15: Comparison of DWPT from analysis (a) and practical results (b). (a) Analysed power output of DWPT systems [160]. (b) Example power output for DWPT systems from practical results, obtained from the experimental setup described in [122].

Figure 2.15a shows the expected power transfer when using static analysis. Notably peak power transfer tends to occur at 0 misalignment, with symmetric behaviour around the peak—typical of static models. In contrast, the measured results in Figure 2.15b show an asymmetric and offset peak, demonstrating how dynamic operation and system interactions impact power delivery. The deviation from static predictions is evident. Despite this, power results are often omitted entirely in published dynamic studies, and no robust explanation is offered for the inconsistencies observed.

In summary, most modelling in DWPT focuses on circuit-level steady-state analysis for power transfer characteristics including power rating and efficiency. While this is suitable for design validation, it is insufficient for real-time control or transient behaviour modelling.

FEA remains essential for coil design but is impractical for full-system control analysis. Many studies avoid simulating low-coupling conditions ($k < 0.1$), but this region is critical for control systems that must detect vehicle presence, foreign objects, or activate coil handovers. Modelling multiple-coil or coil-array systems opens new possibilities for system scalability, multi-vehicle support, and extended electrified road segments, all of which are promising directions for future research.

2.3.5 System control

Achieving different control objectives can be done in different ways. In the context of DWPT, there are four possible control options and often multiple are used together to achieve desired control outcomes. Based on the circuit in Figure 2.8 which shows all four control circuits implemented into one circuit, this section will further expand on each circuit.

Primary Side Control To reduce secondary-side components, size, and complexity, primary-side control of WPT systems is of considerable interest. In most cases, the power provided by the primary coil is proportional to the power received at the secondary side, making it possible to regulate output power, current, or voltage from the primary side [136, 140, 161, 162]. Such systems have been effectively implemented in static environments, where coil alignment remains fixed during the charging process. However, in dynamic systems, movement causes fluctuations in the coupling coefficient, affecting power transfer, which in turn needs to be controlled. While primary-side control remains a promising approach, it may require supplementary secondary-side regulation to meet the precise demands of battery charging profiles.

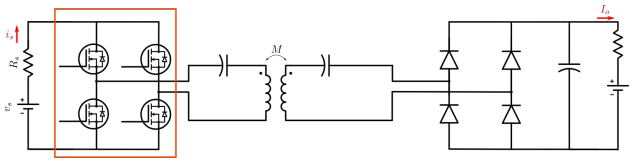

(a) Primary side inverter control.

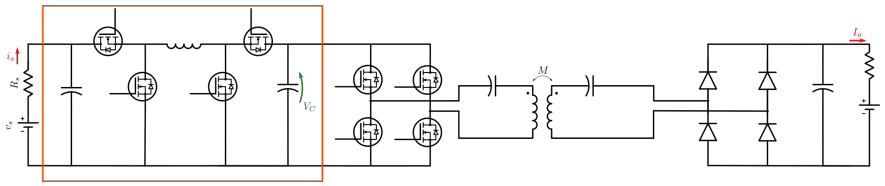

(b) Primary side control using DC/DC converter.

Figure 2.16: Primary side control circuits, highlighting area of control implementations.

Figure 2.16 shows two common options for implementing primary-side control. For inverter control (Figure 2.16a), the default operation generates a square wave at 85kHz with a 0.5 duty cycle to excite the WPT system at resonance. This baseline setup maximizes efficiency under ideal conditions. Further control is achieved by varying parameters such as modulation depth, duty cycle, switching frequency, or phase shift, enabling regulation of

output power. When system parameters are well-characterized and the mutual inductance remains within a predictable range, the control be achieved without explicit feedback from the secondary side [140, 161, 163]. Advanced implementations utilize phase-shift modulation and online load identification to support constant current (CC) and constant voltage (CV) charging operations while maintaining high efficiency and soft-switching conditions [136, 140].

Primary DC/DC converters (Figure 2.16b) are used to reduce the implementation complexity of frequency and phase-shift control (as used in inverter-based methods) by regulating the DC link voltage (V_c). This allows the inverter to operate at a constant frequency, improving system stability and reducing switching losses [136, 161]. Such converters are often implemented as buck or buck-boost topologies and are especially useful in systems aiming to maintain Zero Phase Angle (ZPA) conditions or soft switching throughout the charging cycle. While control inputs such as source current or primary coil current may vary, the essential control mechanism involves adjusting the DC supply voltage to the inverter.

Secondary side control Accounting for coil misalignment and adverse characteristics in dynamic charging systems can be used to stabilize the charging current supplied to the battery to prolong battery life and reduce design complexity of only primary side controlled systems [164]. Allowing for vehicles of different (coil) characteristics and alignment scenarios to use the same primary supply without further increasing system complexity, secondary control systems can also be used to improve the harmonics and reactive power of the system [165].

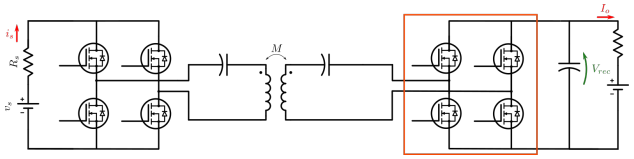

(a) Secondary side controlled rectifier.

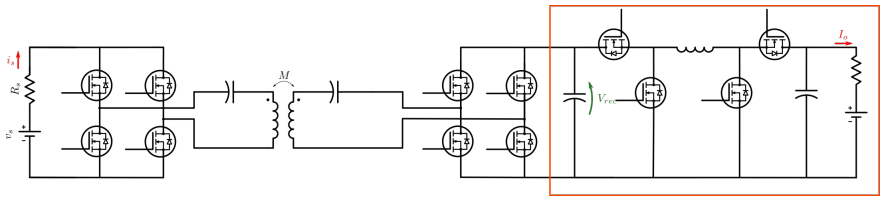

(b) Secondary side control using DC/DC converter.

Figure 2.17: Secondary side control circuits, highlighting area of control implementations.

A controlled rectifier (Figure 2.17a) is placed directly next to the output where previously used diodes are replaced with switching components. In doing so it is possible to achieve fast system response to alter output parameters such as voltage or current. A full bridge rectifier also has the advantage of enabling bidirectional capability as the circuit becomes symmetrical, provided symmetrical compensation topology is used. However the output ripple is often higher, hence LC filters are often used to reduce fluctuations.

The use of a secondary side DC/DC converter (Figure 2.17b), allows the simplest control implementation due to the circuits wide spread use and industry knowledge. Control over

the converter is well studied and reducing voltage/current ripple can be achieved by increasing frequency or increasing LC component Values. Compared to rectifier control, where changing LC values affects the power transfer directly, the DC/DC converter offers a stage of decoupling. Note.: for a constant output value, the output power will be lower than the power at the secondary DC link (V_{rec}). Hence if uncontrolled, the rectified voltage will rise and increase the output ripple.

Dual-sided control Combining aspects from both primary and secondary side control implements dual-sided control. Dual-sided reduces the system response time to control parameters, as the implementation allows a more direct control over the circuit. In essence, achieving output control can be done near the output with a controlled rectifier or a secondary DC/DC converter, compared to applying primary side control which has to propagate through the system before stabilising. This allows simultaneous control over source power consumption and output voltage/current characteristics [166–168].

2.4 Challenges in the Deployment and Operation of EV Charging Infrastructure

Road-side clutter Current BEVs and plug-in hybrid electric vehicles (PHEVs) use charge stations at designated locations or at home. These charge stations often stand out as features on sidewalks requiring more space per. Their inclusion onto road-side application in cities causes issues for pedestrians and loose cables from home to vehicle cause trip hazards

Charger location Providing charging stations to EV users is important, however optimal distribution of charge-points is difficult to achieve as typical charging behaviour can be shown to vary depending on events such as major holidays and working hours [169, 170]. However placing chargers in work places would cause a large spike in power demand at those locations, which will have an adverse effect on power quality in the area, hence requiring distribution grid upgrades (additional costs).

Demand management - Power quality As the number of EVs increases, demand for charge points and hence a demand for power networks to handle larger power demands at different times of day also increases. Excessive loading of a distribution grid can lead to degradation in power quality (e.g.: voltage drop and frequency degradation). "To safely integrate a high uptake of EVs into distribution networks, a combination of measures will need to be employed like charging EVs preferentially from renewable sources and smart management of EVs battery charging" [171]. While management strategies have been shown to reduce the impact of EV charging [172], the issues have been observed in residential distribution grid [173], and is expected to grow with market penetration. Furthermore, in larger applications such as fleet operations (for supermarket delivery and so on) or car-parks especially around major cities where a large power demand could be seen at specific times of the day. These demands will need to be planned for and managed accordingly to provide users with adequate charge over time without overloading the grid and putting a strain on resources.

Table 2.5: Control mode comparison

Control Type	**Control variable**	**Advantages**	**Disadvantages**
Primary-side inverter	I_p (I_o/V_o possible with communication)	• ZVS, ZPA capability • Fewest components	• Higher frequency requirement • Moderately complex
Primary-side DC/DC converter	V_c (I_o/V_o possible with communication)	• Easy implementation • Efficiency benefit	• Increased response time for output control
Secondary-side rectifier	V_{rec}	• Low number of components • Bidirectional capability	• Only buck functionality • Sensitive to phase difference
Secondary-side DC/DC converter	I_o or V_o	• Best output characteristics • Simple control • Decoupled from WPT	• Increased number of components on vehicle side
Dual-side control	Any of the above		• High number of switching components • More complicated control

Modelling techniques - Dynamic wireless power transfer With the increased interest in WPT technologies, system analysis and design techniques are crucial for accurate system control and grid load estimation. This is also true for DWPT applications, where current research often uses techniques developed for static WPT to design systems for DWPT, despite its different behaviour due to the system's dynamic nature. Further research and advanced modelling techniques are therefore required to more accurately represent system behaviour under varying conditions and to demonstrate the associated grid load impact.

2.5 Chapter summary

This section presented an overview of the overall EV charging landscape, including the currently used charging solutions and possible future solutions currently in development and testing. In general the conductive charging space has reached a maturity to a point where higher power chargers are niche installations for vehicles with large batteries (HGVs, buses, trucks, etc..), their deployment for passenger vehicles sees under-utilisation as vehicle OBCs are not able to make use of the full charging power. Additionally distribution network upgrades are required to add more charging solutions to most areas. Up to 22kW charging can be achieved with 3-phase AC solutions, beyond this point DC charging solutions are used, where increasing power is done by adding additional charging modules to the system, increasing charging cable diameter and providing adequate cooling.

V2G systems enable EVs to support grid functionality, helping to reduce the adverse effects of frequent charging events and increasing power demand on distribution networks. Often these come with integration of renewable energy source and are likely to be necessary in future deployment of EV charging solutions similar to the widespread use of PFC circuits.

Luxury add-on services such as ACDs present some opportunity for innovation in providing charging solutions, however their development moves more into the robotic space than electrical engineering, as majority of these systems incorporate established charging systems, only changing the means of connection.

Offering more research opportunities is wireless charging, as technology in an early development stage receiving research attention and few commercial trials. IPT has been identified as the preferred method of WPT due to it's high power capability at larger distances. Within IPT the research different on factors such as compensation topology, coil design and control implementation/design. Where the circuit topology and control is chosen to suit a specific design case and static IPT simulations achieve accurate results based on steady state analysis. The less developed area of this research is the DWPT system, as current research uses the same system design process as static WPT and report on the effects of moving the coils relative to each other. Few research articles feature FEA, which at an 85kHz operating frequency require long simulation times and are hard to scale up for multiple coil systems.

3 Modelling Wireless Power Transfer (WPT)

Building on the insights gained from the literature review, this chapter outlines the rationale behind the simulation model developed for this study. It details the design decisions related to circuit topologies, control strategies, and modelling techniques, with the aim of enabling consistent and meaningful analysis. These implementation choices reflect both the strengths and limitations observed in existing approaches and are tailored to address the specific objectives of this work.

Current implementations use static simulation techniques, where fixed coil parameters (including mutual inductance) are used to obtain steady-state values. These typically use mutual inductance blocks which are used to simulate transformer coils, and typically use either a T-equivalent circuit or an induced EMF model to link the power transfer between two coils. This implementation is good for early developments in WPT technologies however to obtain a more practical model for later use in DWPT or multiple coil systems, the simulation should use be able to easily vary the mutual inductance and have scalability considerations to incorporate multiple coil systems. To ensure consistency with existing approaches, the proposed system should reproduce the same voltage, current, and power transfer characteristics as established models under fixed mutual inductance conditions, effectively replicating static charging behaviour.

3.1 Circuit design choices

For EV charging applications, the proposed WPT solution should be competitive with existing technologies in terms of both power rating and efficiency. These factors are critical in selecting component power ratings and determining the appropriate compensation topology for effective power transfer.Furthermore, as this circuit is to form a baseline for future research, it should remain relatively simple to allow future exploration and complications to be added and compared easily.

Compensation topology Using the information in Table 2.4 the compensation topologies are narrowed down. Starting with high power (11-22kW for EV charging), narrows the choice down to series-series and series-parallel compensations. Further looking at their efficiencies, it is evident the series-series compensation is superior for this application and for this reason has been used in research.

Mutual inductance model Following the literature review, the EMF model is implemented with the aim of making the mutual inductance (M) a variable in the system. As demonstrated in the literature, this implementation has proven effective for static charging. If it can accurately model the system at position 'x' and at a slightly shifted position 'x+1', it follows that varying the mutual inductance should correspond to changes in position, thereby enabling a dynamic simulation.

In order to achieve a dynamic implementation, it is important to have a model describing the mutual inductance between two coils. Physical models of the coil shape and size are required to obtain mutual inductance, as coil shape, size and position will affect the result. Previous research has been carried out to summarise the interaction of two square coils [157],

which will be used for this research. Appendix 8.1 shows the equations used for coil self inductance and mutual inductance.

The remainder of the WPT system is built to represent the system based on coil parameters. Any changes in coil shape/size can be updated accordingly.

System topology An uncontrolled charging topology is chosen to first achieve power transfer and focus on the WPT, avoiding complications with increased number of control components. For inverter control, a sinusoidal reference is given at resonant frequency to match the WPT resonant frequency, a PWM signal is then generated to control the inverter.. Hence an uncontrolled rectifier is used with the addition a low-pass filter to reduce output. For battery output, a simple resistor and DC voltage source represent the battery internal resistance and nominal voltage respectively, these can later be updated to battery models with SOC estimations.

3.2 Circuit explanation

Figure 3.1 shows the circuit used for simulation, where the WPT is replaced controlled voltage sources to include the induced EMF. Note.:To avoid noise amplification, the differentiation function is implemented using an integrator - this is a common practice in simulations and the analysis will show how the approach approximates a derivative function as shown in Figure 3.1b. The remainder of the system is implemented using standard components. Circuit parameters used are given in Table 3.1

Figure 3.1 illustrates the circuit used for the simulation, where the WPT link is replaced with controlled voltage sources to emulate the induced EMF. The parameters used in the simulation are listed in Table 3.1. While the system analysis uses the derivative of current to obtain the EMF, differentiators are sensitive to noise and therefore the implementation approximates one by the use of an integrator. This approach reduces noise sensitivity and is often used in other simulation implementations such as PID controllers. Figure 3.2 shows the implementation of the voltage in the receiver coil as a function of the transmitter coil, with intermittent points labelled analysis of this diagram gives the following equations.

$$e(t) = I_1 - \frac{x(t)}{s} \tag{1}$$

$$x(t) = Ke(t) \tag{2}$$

$$V_2 = Mx(t) \tag{3}$$

Using (2) and (3):

$$x(t) = K\left(I_1 - \frac{x(t)}{s}\right) \tag{4}$$

$$x(t)\left(1 + \frac{K}{s}\right) = KI_1 \tag{5}$$

$$x(t)\left(\frac{1}{K} + \frac{1}{s}\right) = I_1 \tag{6}$$

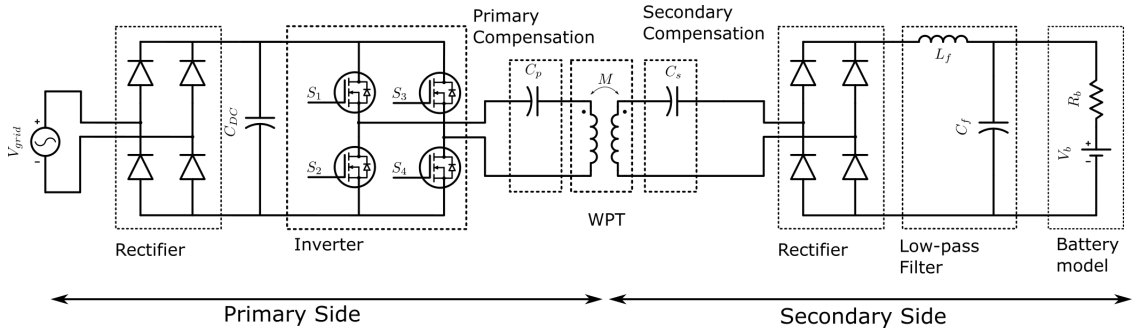

(a) Full circuit.

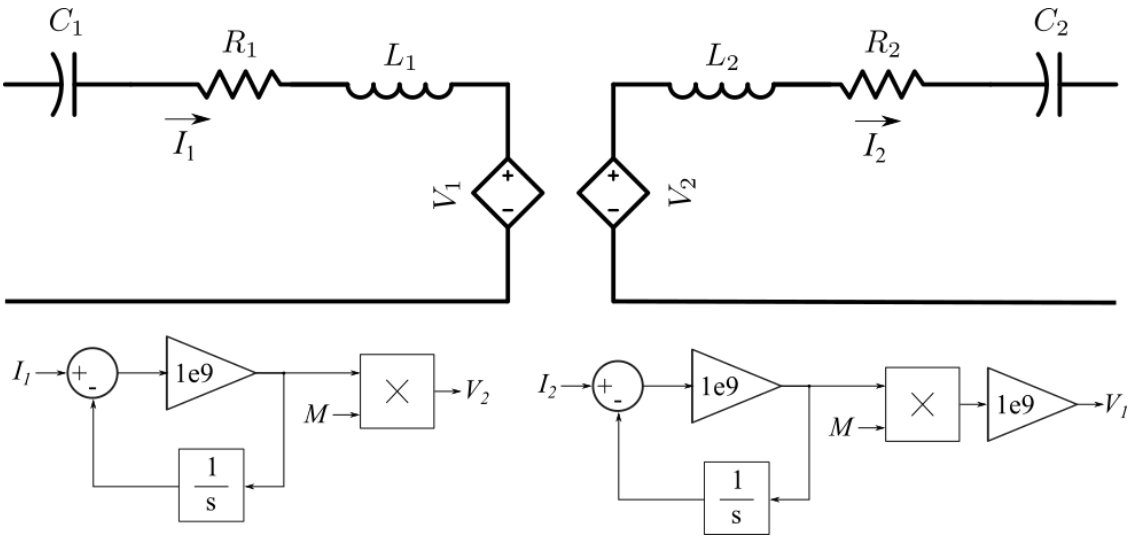

(b) WPT implementation.

Figure 3.1: Circuit used for validating WPT (3.1a) and the detailed implementation used for mutual inductance (3.1b).

As $K \to \infty$, $\frac{1}{K} \to 0$, therefore $x(t)\left(0 + \frac{1}{s}\right) = I_1$ and hence $x(t) \to sI_1$ then:

$$V_2 = sI_1.M \tag{7}$$

Based on experimental results presented in literature [122], the circuit should exhibit similar behaviour in power transfer as seen in Figure 3.3. Achieving this will show the system moving toward an accurate representation of DWPT modelling.

3.2.1 Wireless power transfer circuit analysis

Based on the circuit shown in Figure 3.1a, the WPT component of the circuit can be analysed by replacing the source and load connections—in this case, the inverter and rectifier, respectively. Figure 3.4 illustrates the WPT circuit used for further analysis. Here, R_{eq} denotes the equivalent resistance of the rectifier (related to the load resistance by $R_{\text{eq}} = \frac{8}{\pi^2} R_{\text{Load}}$), and V_i represents the primary-side DC bus voltage.

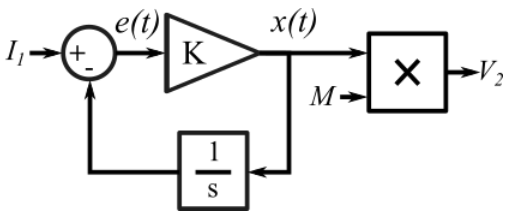

Figure 3.2: Derivative approximation used for EMF calculation.

Table 3.1: System specification for circuit in Figure 3.1a.

System	Label	Parameter	Value
Source	V_{grid}	Voltage	230 V, 3ϕ,50 Hz (415Vdc)
Inverter	f_{sw}	Switching frequency	1 MHz
	f_0	Fundamental frequency	82 kHz
Primary Side	C_p	Compensation capacitor	6.2969 nF
	L_p	Coil self-inductance	598.2 µH
	R_p	Coil resistance	177.8 mΩ
Secondary Side	C_s	Compensation capacitor	6.2297 nF
	L_s	Coil self-inductance	604.65 µH
	R_s	Coil resistance	192.6 mΩ
LPF	L_{f}	Inductor	1 mH
	C_{f}	Capacitor	10 µF
	f_c	Cut-off frequency	1.59 kHz
Battery Specifications	V_{b}	Nominal Voltage	400 V
		Capacity	75 A h

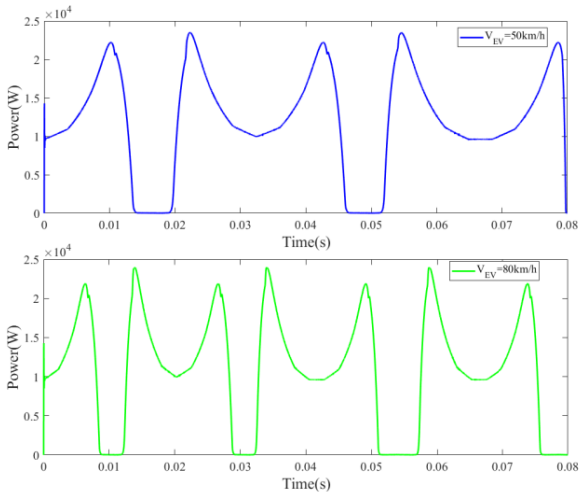

Figure 3.3: DWPT power transfer for multiple primary coil systems [122].

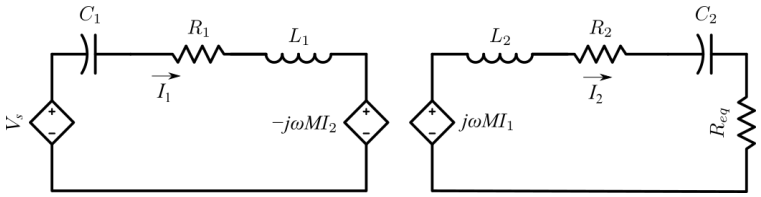

Figure 3.4: WPT equivalent circuit.

The mutual inductance M is defined as $M = k\sqrt{L_1 L_2}$, where k is a dimensionless coupling coefficient. Components L_1, R_1, and C_1 are the self-inductance, resistance, and compensation capacitance of the primary coil, respectively. Similarly, L_2, R_2, and C_2 represent the self-inductance, resistance, and compensation capacitance of the secondary coil. The primary and secondary coil currents are denoted as I_1 and I_2, respectively.

Practically the DC bus voltage serves as the positive and negative of the output square wave, sinusoidal waves are used for circuit analysis. As for a square wave the RMS value is equal to the amplitude, this should be accounted for before applying AC analysis. Additionally voltage drop due to converter efficiency can also be included at this stage by using $V_s \approx V_{DC}\eta\sqrt{2}$ where η denotes the inverter efficiency.

From Figure 3.4 the steady state values of the circuit can be obtained by analysing the circuit impedance at the operating frequency given by:

$$Z_1 = R_1 + j\omega L_1 + 1/j\omega C_1 \tag{8}$$

$$Z_2 = R_2 + j\omega L_2 + 1/j\omega C_2 + R_{eq} \tag{9}$$

where, Z_1 and Z_2 are the primary and secondary side impedance respectively. The angular frequency $\omega = 2\pi f$ where f is the operating frequency. Voltage analysis of the circuit in Figure 3.4 gives:

$$V_s = I_1 Z_1 + j\omega M I_2 \tag{10}$$
$$0 = j\omega M I_1 + Z_2 I_2 \tag{11}$$

hence,

$$I_1 = V_s/(Z_1 - \omega^2 M^2/Z_2) \tag{12}$$
$$I_2 = -j\omega M I_1/Z_2 \tag{13}$$

This analysis is for series-series compensated coils and relates the coil currents as a function of input voltage and output resistance, which can be related to output power. The analysis similar for other compensation topologies and has been discussed in Section 2.3.2, where the decision for series-series compensation is explained.

3.2.2 Coil Self-Inductance and Mutual Inductance

The inductance of coils, whether self- or mutual, depends on their geometry, orientation, and relative positioning. A general expression for calculating inductance between current-carrying conductors is given by Neumann's formula:

$$L = \frac{\mu_0}{4\pi} N_1 N_2 \oint_{\gamma_1} \oint_{\gamma_2} \frac{dl \cdot dl'}{r} \tag{14}$$

This double line integral computes the magnetic interaction between differential current elements dl and dl' along the contours γ_1 and γ_2, with r being the distance between them. The permeability of free space is denoted by μ_0. The winding numbers N_1 and N_2 refer to the number of turns in each coil.

- When $\gamma_1 = \gamma_2$, the equation describes self-inductance of a single coil.
- When $\gamma_1 \neq \gamma_2$, it evaluates the mutual inductance between two separate coils.

Figure 3.5 shows the configuration of two square coils with their geometric and positional parameters annotated. The coordinate system and key dimensions include the coil widths a_1, a_2, heights b_1, b_2, and displacements c, e, h in the x, y, z directions, respectively. The equivalent radii r_1 and r_2 represent the average coil radii based on turn count and cross-sectional area.

Self-Inductance For a rectangular coil, a closed-form approximation derived from Neumann's general formula yields the self-inductance:

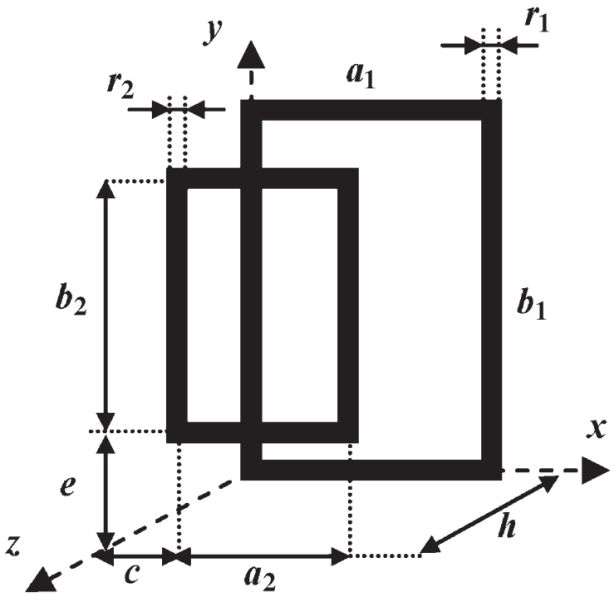

Figure 3.5: Square coil design parameters and relative position [157].

$$L_i = \frac{\mu_0}{\pi} N_i^2 \left[a_i \cdot \ln\left(\frac{2a_i b_i}{r_i \left(a_i + \sqrt{a_i^2 + b_i^2} \right)} \right) + b_i \cdot \ln\left(\frac{2a_i b_i}{r_i \left(b_i + \sqrt{a_i^2 + b_i^2} \right)} \right) - 2\left(a_i + b_i - \sqrt{a_i^2 + b_i^2} \right) + 0.25(a_i + b_i) \right] \tag{15}$$

The equivalent coil radius is approximated as:

$$r_i = \sqrt{\frac{N_i S_i}{\pi}} \tag{16}$$

And the winding resistance, assuming copper conductors, is:

$$R_i = \rho_{\mathrm{Cu}} N_i \frac{2(a_i + b_i)}{S_i} \tag{17}$$

Mutual Inductance Mutual inductance between two coils, given by the same general formula (14), now uses different path integrals:

$$M = \frac{\mu_0}{4\pi} N_1 N_2 \oint_{\gamma_1} \oint_{\gamma_2} \frac{dl \cdot dl'}{r} \tag{18}$$

Here, γ_1 and γ_2 correspond to the contours of the primary and secondary coils. This formulation accounts purely for the physical geometry and relative placement of the coils. Hence, models or simulations assuming fixed M are valid as long as the physical configuration remains unchanged.

The expanded analytical form of this integral for rectangular windings is provided in Appendix 8.1.

3.3 Practical system

Following theoretical system development, the next step is to build a practical system and compare the accuracy of results and explore overlooked issues. Figure 3.6 shows the lab setup using which is the minimum circuit for WPT where a single inverter and rectifier are used to power a resistive load. A scaled-down version of the system is used to investigate its behaviour during DWPT. When scaling the system up, similar transient behaviours are expected to occur, albeit at higher power levels.

For testing, two pairs of coils were made, one using strands of insulated copper wire, the other using litz wire. Litz wire is a thin multi-strand cable for high frequency AC signals, with the aim of reducing the skin effect on power transfer. Litz wire is more expensive, therefore the resulting coils were made smaller to remain within budget. Both coils are tested without ferrite cores and are held together using non-ferrous materials (plastic).

System Parameters First the coils were created based on available materials, their impedance is measured using an LCR meter. An operating frequency of 85kHz is chosen which determines the required compensation capacitors for series-series compensation. As the system input is an AC power source, rectification before high frequency inversion is required. Additionally a capacitor in parallel with a load resistance is used. System parameters for all components summarized in Table 3.2.

3.3.1 Results

System control signal A fixed frequency, fixed duty cycle control signal is generated from a dSpace control module which is fed to the inverter gate control seen in Figure 3.7.

Inverter output and rectifier input Based on the supplied control signal, inverter switching is controlled and results in a square wave output voltage from the inverter. The two coil types used have different characteristics and result in different power transfer characteristics when the same supply voltage is applied. Figure 3.8 shows the voltage waveforms for the litz wire coil setup where the square wave voltage applied is more distorted compared to the copper wire coil setup in Figure 3.9, this is due to the lower coil resistance of the primary litz coil, leading to the system having a lower damping factor - hence a larger inrush current during inverter switching. For both Figures 3.8 and 3.9, the minimum air gap is 10mm. An air gap of 0mm would imply the coils are in the same plane, which is physically impossible due to geometric intersection. The 10mm minimum is set by the thickness of the outer housing surrounding the coils.

Table 3.2: System parameters for laboratory setup.

Component	**Parameter**	**Value**
Copper Primary Coil	Self-inductance (L)	92.27 µH
	Resistance (R)	0.56 Ω
	Number of turns (N)	15
	Nominal voltage	50 V
	Nominal current	10 A
	Coil dimensions (H × W)	270 mm × 160 mm
Copper Secondary Coil	Self-inductance (L)	44.26 µH
	Resistance (R)	0.53 Ω
	Number of turns (N)	12
	Nominal voltage	24 V
	Nominal current	9 A
	Coil dimensions (H × W)	170 mm × 140 mm
Compensation Capacitor (Copper Primary)	Capacitance (C)	38.45 nF
Compensation Capacitor (Copper Secondary)	Capacitance (C)	83.98 nF
Litz Primary Coil	Self-inductance (L)	8.061 µH
	Resistance (R)	0.09 Ω
	Number of turns	8
	Nominal voltage	50 V
	Nominal current	13.5 A
	Coil dimensions (H × W)	90 mm × 90 mm
Litz Secondary Coil	Self-inductance (L)	5.695 µH
	Resistance (R)	0.32 Ω
	Number of turns	8
	Nominal voltage	12 V
	Nominal current	5 A
	Coil dimensions (H × W)	60 mm × 60 mm
Compensation Capacitor (Litz Primary)	Capacitance (C)	479.1 nF
Compensation Capacitor (Litz Secondary)	Capacitance (C)	736.2 nF
DC Capacitor	Capacitance	10 mF
Load	Resistance	3 Ω
	Capacitance	3 mF

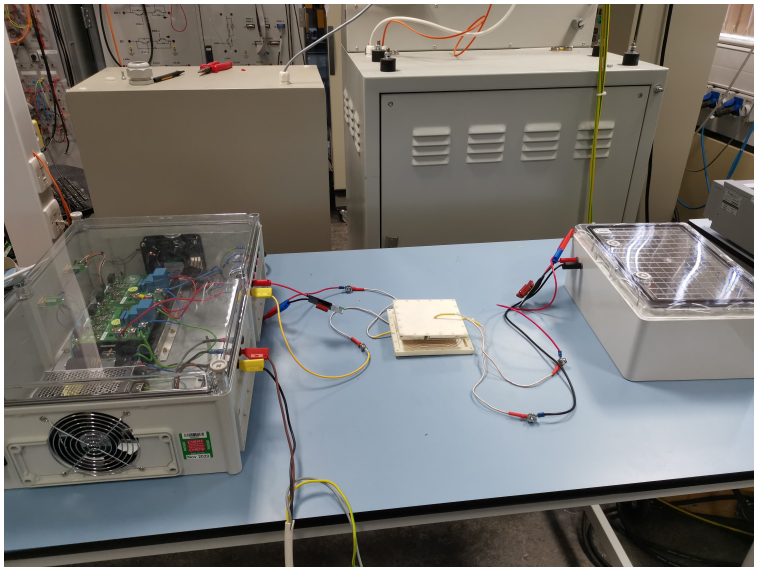

(a) Whole system setup with litz wire coils

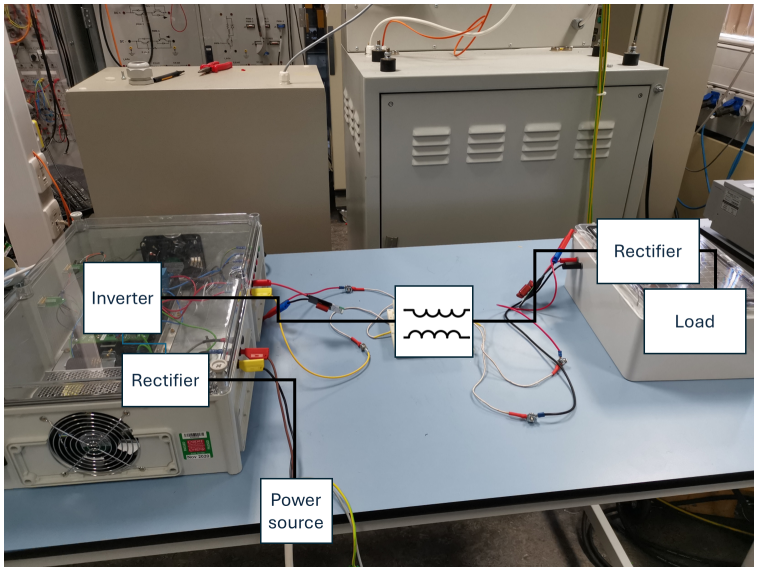

(b) Annotated system

Figure 3.6: Overview of the experimental setup.

Static charging variable changes First the system is tested in a static environment where a single parameter is changed each time, this is done for air gap (Figures 3.10 and 3.13), displacement (Figure 3.11 and 3.14) and supply voltage level (Figures 3.12 and 3.15). Efficiency measurements were obtained using a power analyser between the inverter output and the rectifier input.

The laboratory setup experiences several sources of power loss that contribute to reduced system efficiency. To minimize costs, the coil materials used are of lower quality than those typically found in industrial-grade WPT systems. Although both copper and Litz wire coils are employed, they are connected to the inverter and rectifier using standard wires

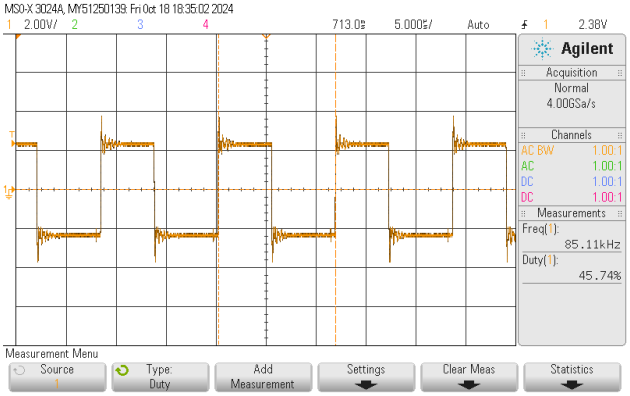

Figure 3.7: PWM control signal

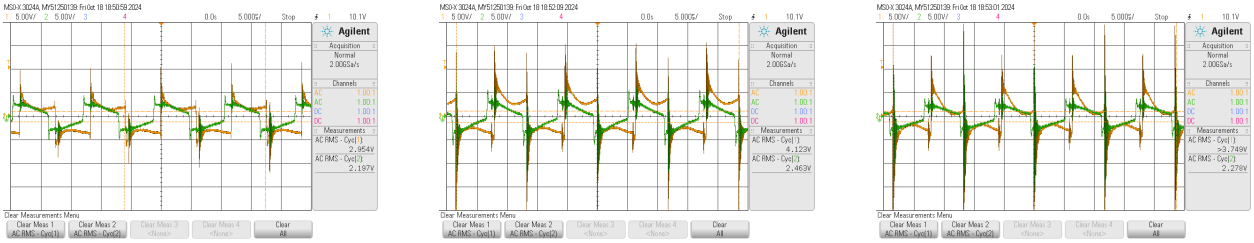

(a) 10mm air-gap (b) 20mm air-gap (c) 30mm air-gap

Figure 3.8: Inverter output voltage (yellow) and rectifier input voltage (green) at various air gaps, measured using a Litz wire coils and a 5V RMS power supply.

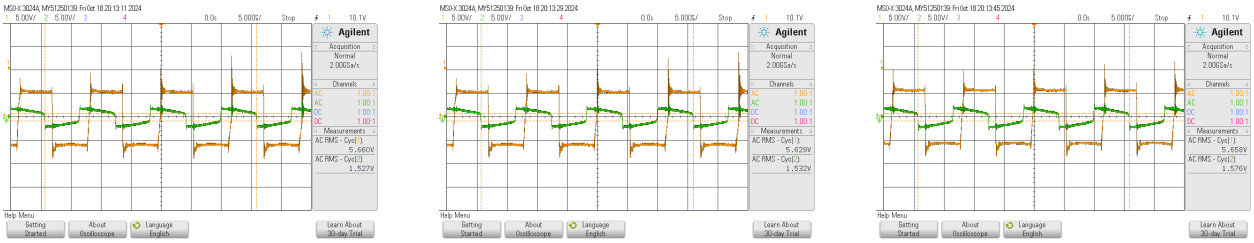

(a) 10mm air-gap (b) 20mm air-gap (c) 30mm air-gap

Figure 3.9: Inverter output voltage (yellow) and rectifier input voltage (green) at various air gaps, measured using a Copper wire coils and a 5V RMS power supply.

with banana clip connectors, which introduces additional resistance and potential contact losses. Furthermore, the integration of the power analyser requires extra wiring around the setup. Despite efforts to isolate the coils from surrounding components, electromagnetic interference from nearby wiring and hardware may still affect system performance during operation. Furthermore, the accuracy manufacture accuracy of system components such as the inductors and capacitors for resonant operation also add to the system inefficiency.

Copper wires experience a more pronounced skin effect at high frequencies, which restricts current flow to the surface of the conductor. As a result, the effective cross-sectional area available for conduction is reduced, leading to an increase in AC resistance. This behaviour is evident in Figure 3.12, where the efficiency of the copper coil decreases as the supply voltage increases, in contrast to the litz wire coil shown in Figure 3.15. As the voltage increases, the corresponding rise in current further amplifies resistive (I^2R) losses, resulting in greater heat dissipation and reduced power transfer efficiency.

By comparison, litz wire is engineered to counteract the skin effect through the use of many thin, individually insulated strands, woven so that current is distributed more uniformly across the entire conductor. This design maintains a lower effective resistance even at higher frequencies, thereby minimizing power losses and sustaining higher efficiency under similar voltage conditions. Consequently, increasing the supply voltage in copper coils leads to a more pronounced drop in efficiency than in litz wire coils, due to the combined effects of elevated current and frequency-dependent resistance.

Copper wire coils

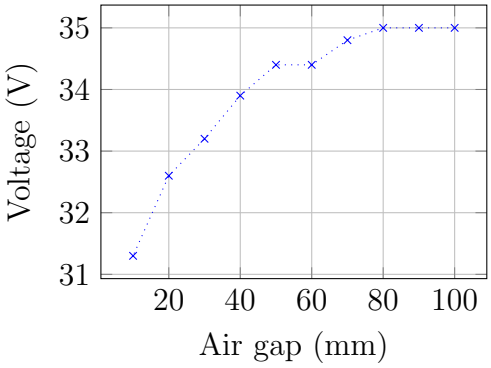

(a) Inverter RMS voltage

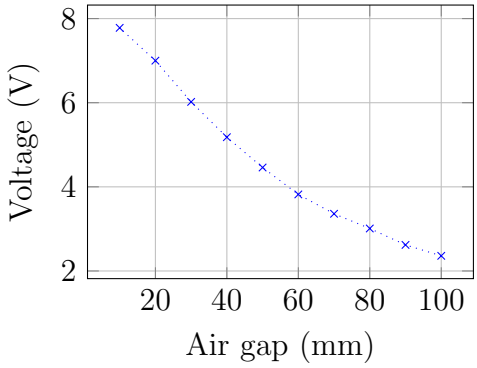

(b) Rectifier RMS voltage

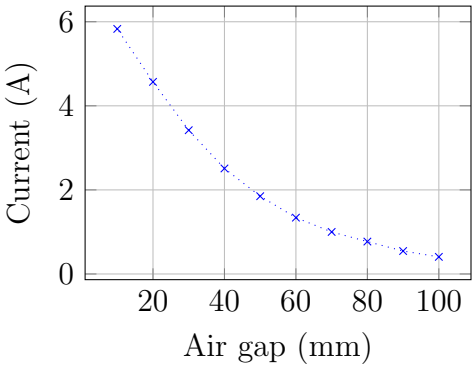

(c) Primary coil RMS current

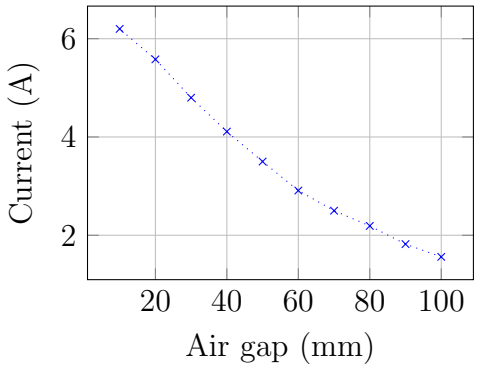

(d) Secondary coil RMS current

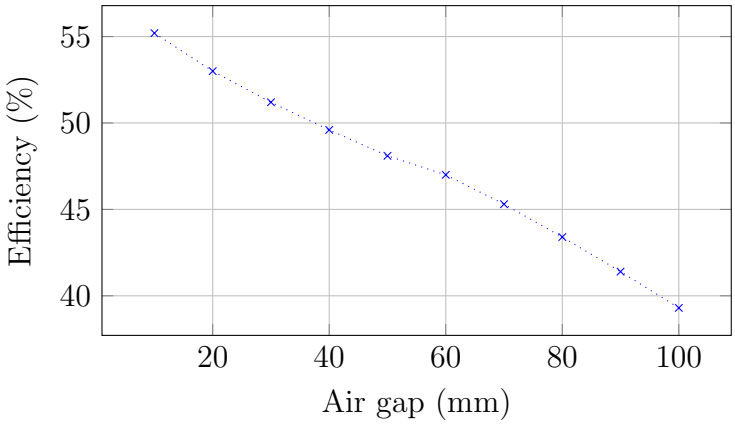

(e) Efficiency

Figure 3.10: Effect of varying air gap on voltages, currents, and efficiency for copper wire coils at $V_{DC1} = 50$V.

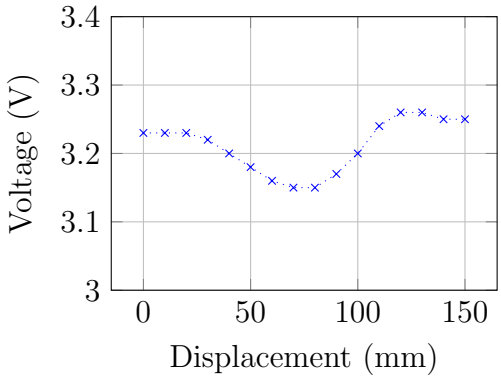

(a) Inverter RMS voltage

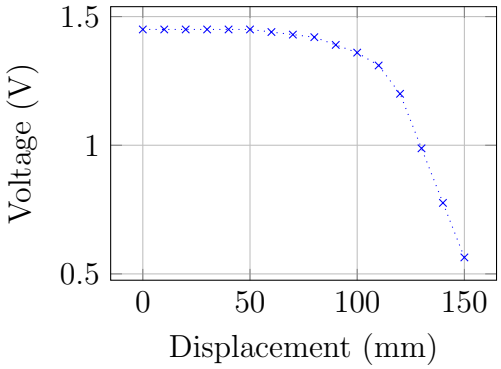

(b) Rectifier RMS voltage

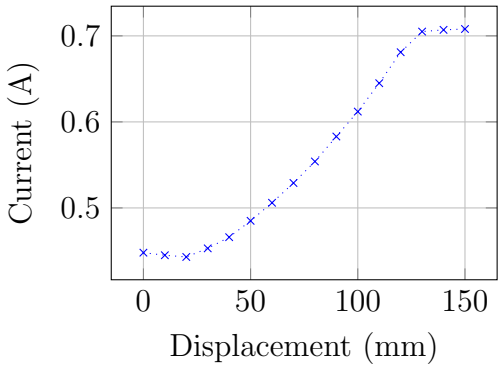

(c) Primary coil RMS current

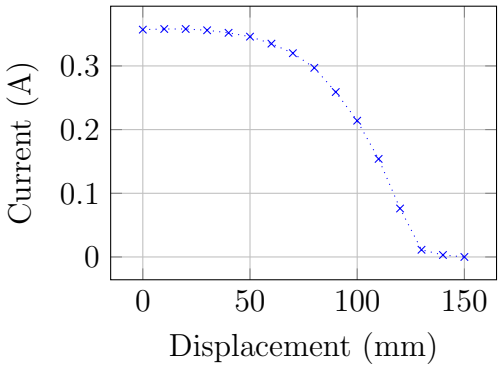

(d) Secondary coil RMS current

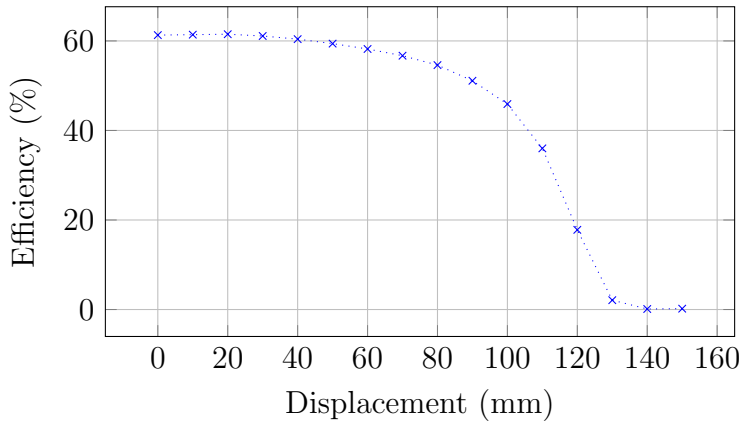

(e) Efficiency

Figure 3.11: Effect of varying displacement on voltages, currents, and efficiency for copper wire coils at $h = 100mm$.

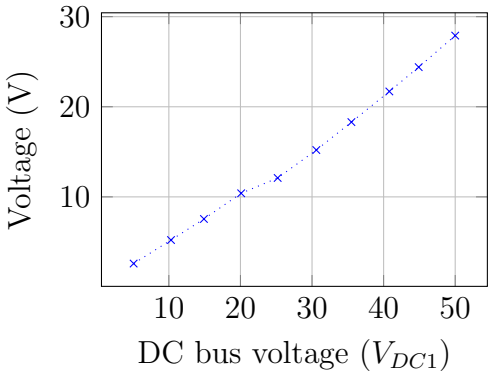

(a) Inverter RMS voltage

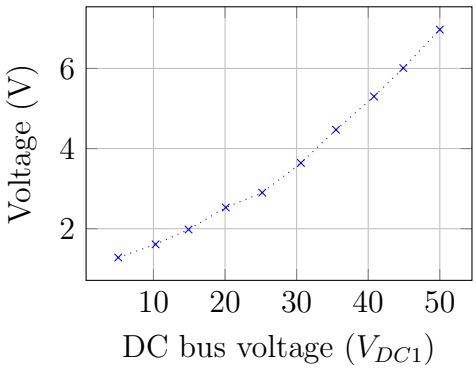

(b) Rectifier RMS voltage

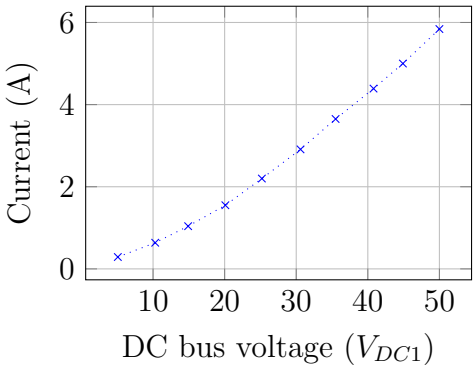

(c) Primary coil RMS current

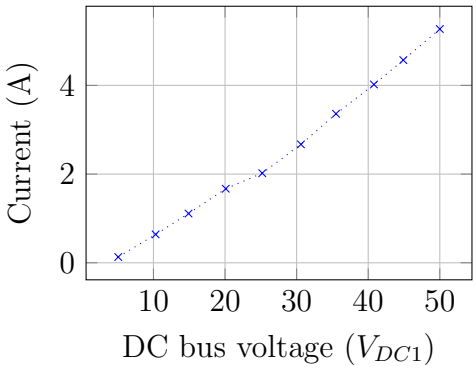

(d) Secondary coil RMS current

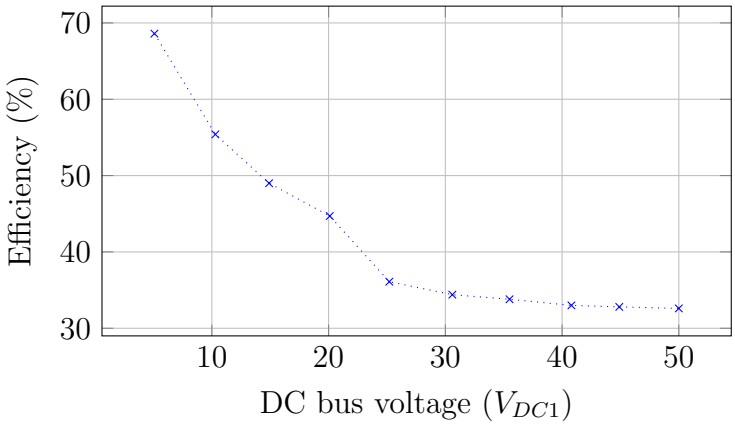

(e) Efficiency

Figure 3.12: Effect of varying input voltage (V_{DC1}) on voltages, currents, and efficiency for copper wire coils at $h = 100mm$.

Litz wire coils

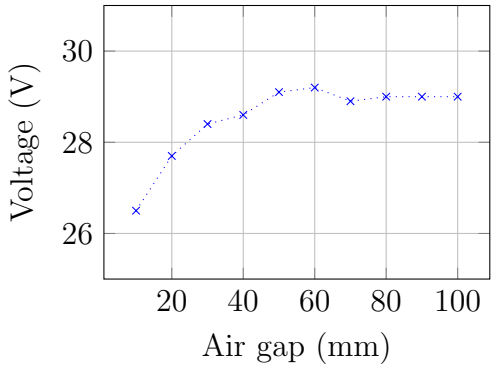

(a) Inverter RMS voltage

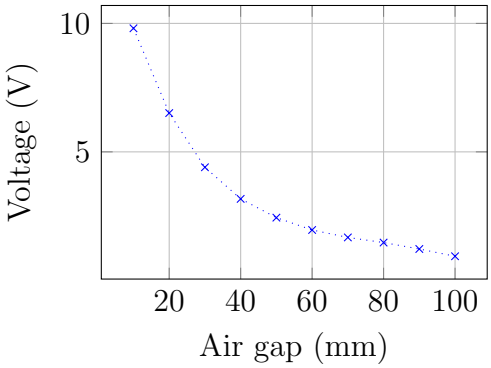

(b) Rectifier RMS voltage

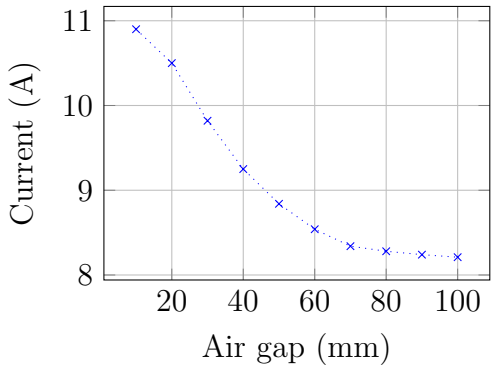

(c) Primary coil RMS current

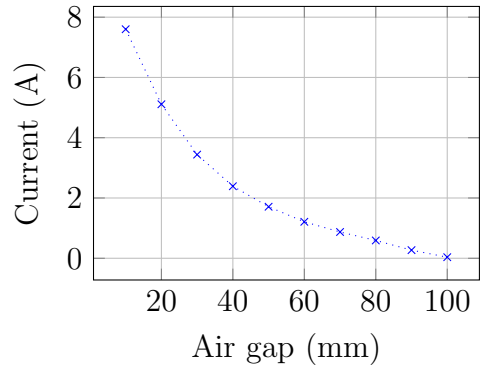

(d) Secondary coil RMS current

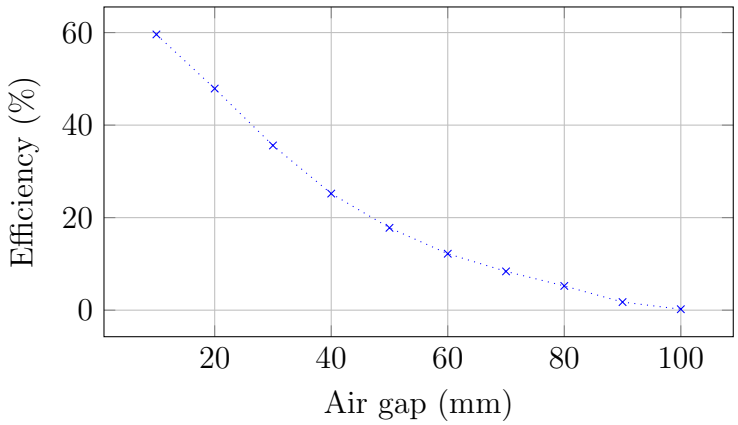

(e) Efficiency

Figure 3.13: Effect of varying air gap on voltages, currents, and efficiency for litz wire coils at $V_{DC1} = 50\text{V}$.

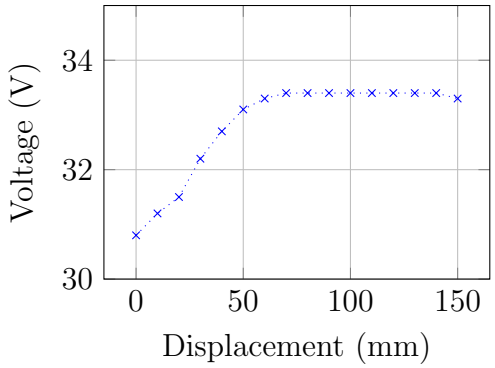

(a) Inverter RMS voltage

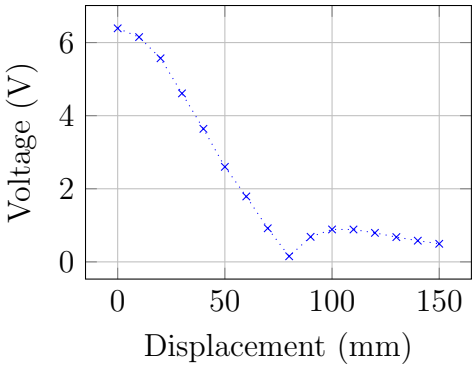

(b) Rectifier RMS voltage

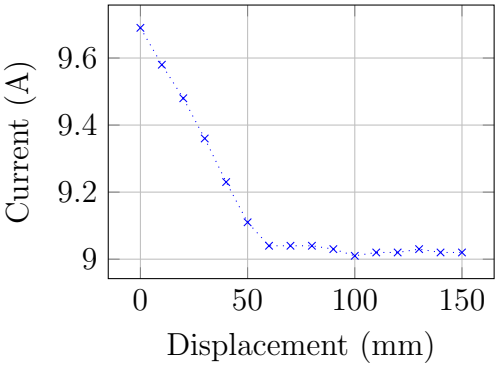

(c) Primary coil RMS current

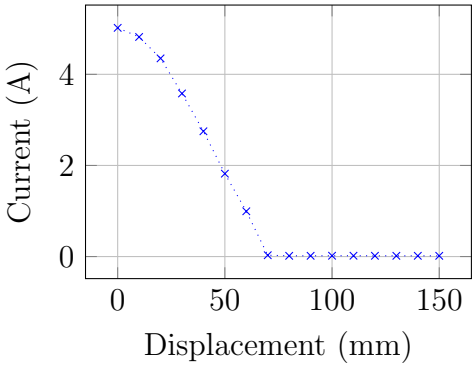

(d) Secondary coil RMS current

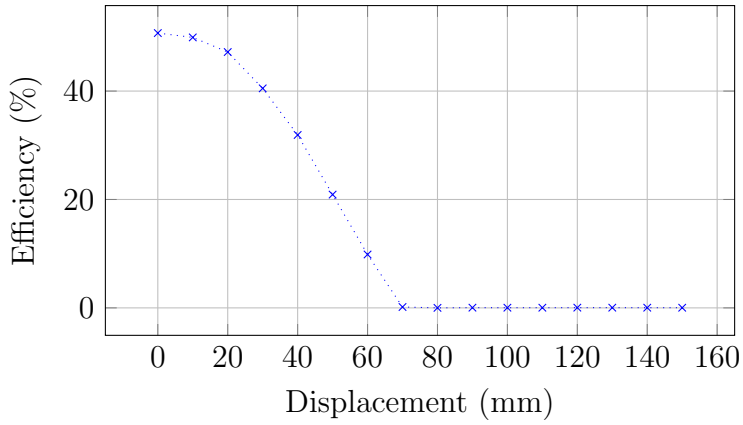

(e) Efficiency

Figure 3.14: Effect of varying displacement on voltages, currents, and efficiency for litz wire coils at $h = 10mm$.

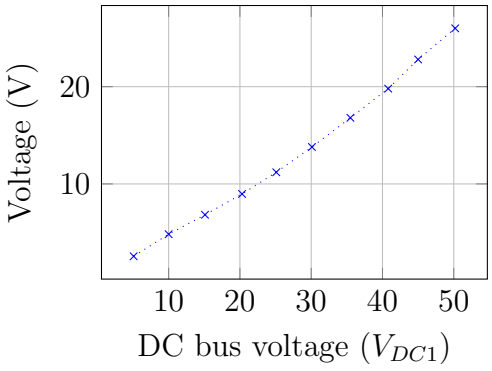

(a) Inverter RMS voltage

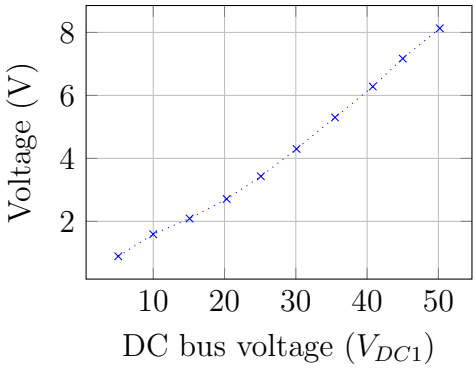

(b) Rectifier RMS voltage

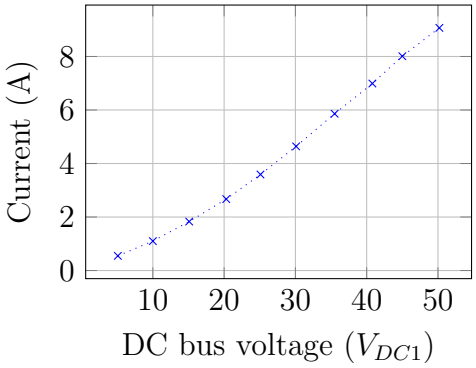

(c) Primary coil RMS current

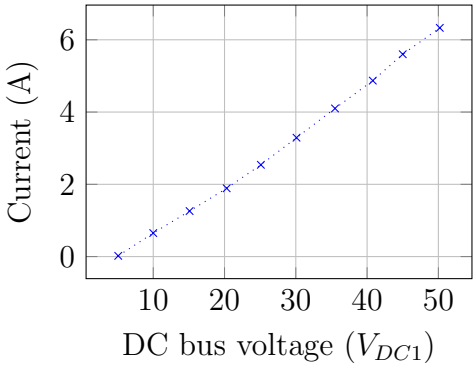

(d) Secondary coil RMS current

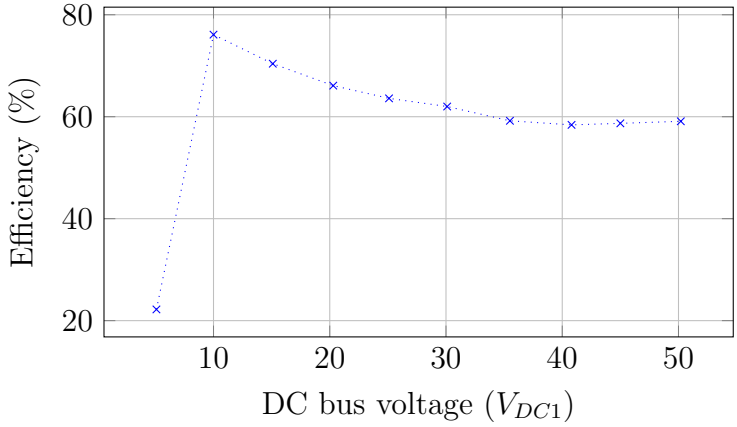

(e) Efficiency

Figure 3.15: Effect of varying input voltage (V_{DC1}) on voltages, currents, and efficiency for litz wire coils at $h = 10mm$.

Effect of Vehicle Speed on Dynamic Power Transfer Experiments were conducted to evaluate the influence of vehicle travel speed on power transfer characteristics. Although distinguishing the effects between slow (0.5m/s or 1mph) and fast (5m/s or 10mph) travel proved difficult due to the relatively small difference, minor variations in the primary-side current were observed at the moment power transfer began. Figure 3.18d shows approxi-

mately 5% variation in the peak current deviation, this is consistent with the later simulation in Figure 3.20 where approximately 5% peak difference is observed with 10mph difference. These observations align with simulation results, which predict that higher travel speeds produce a more pronounced initial power transfer peak. This behaviour highlights a key aspect of dynamic operation: faster speeds lead to shorter interaction times between the transmitter and receiver coils and higher instantaneous power demand but reduced overall energy transfer per coil.

Studying these dynamic effects is critical to understanding how DWPT systems behave under realistic conditions. Static analysis alone fails to capture important transient phenomena such as shifting mutual inductance, varying coupling efficiency, and fluctuating power demands. By experimentally validating these behaviours, the study contributes valuable insight into how to design and optimize DWPT systems for real-world deployment—enabling more efficient, scalable, and practical wireless charging infrastructure for electric vehicles.

Achieving a consistent and accurately controlled velocity during testing proved challenging, which limits the ability to draw precise quantitative comparisons between different travel speeds. However, the results shown in Figures 3.16 and 3.17 can be scaled along the time axis to align key events and enable a qualitative comparison of voltage and current amplitudes. To facilitate this, the time scale of Figure 3.17 is adjusted to overlay with the slower speed data in Figure 3.16. Figure 3.18d shows approximately 5% variation in the peak current deviation, this is consistent with the later simulation in Figure 3.20 where approximately 5% peak difference is observed with 10mph difference.

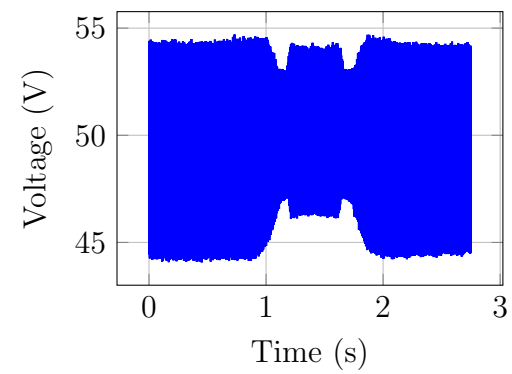

(a) Voltage V_{DC1}

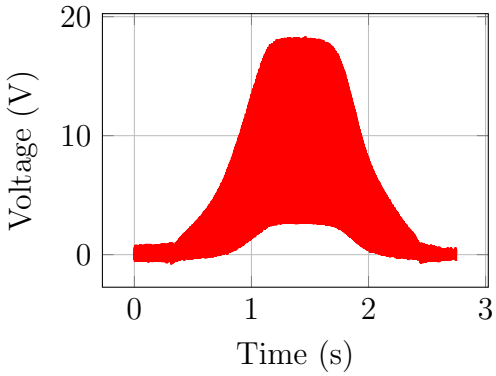

(b) Voltage V_{DC2}

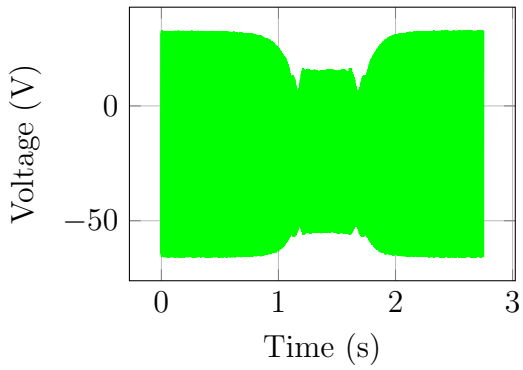

(c) Inverter Voltage V_p

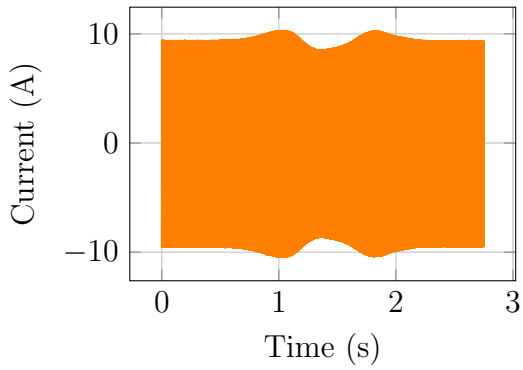

(d) Primary Current I_p

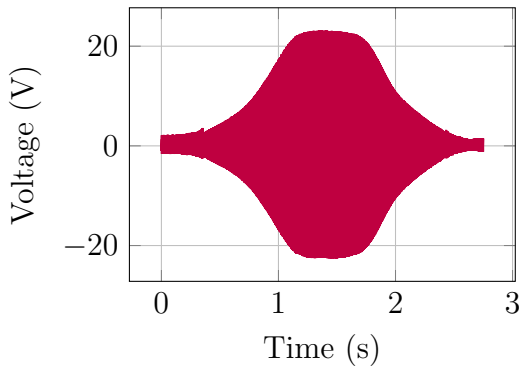

(e) Secondary Voltage V_s

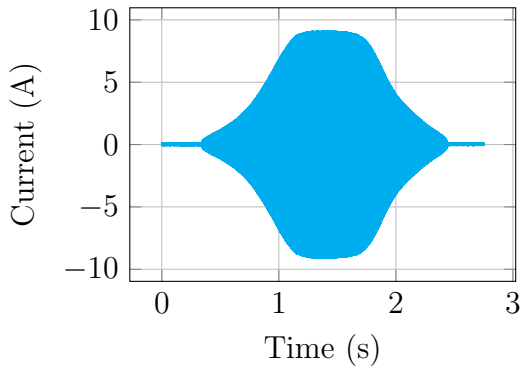

(f) Secondary Current I_s

Figure 3.16: Results for dynamic operation with copper wire coils.

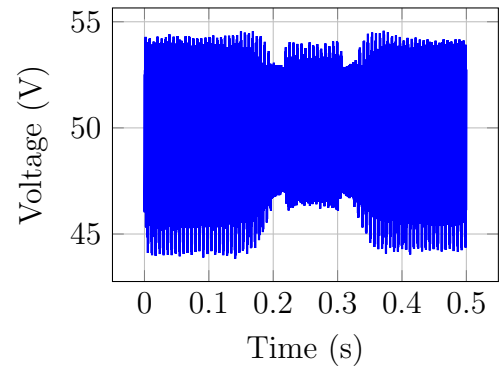

(a) Voltage V_{DC1}

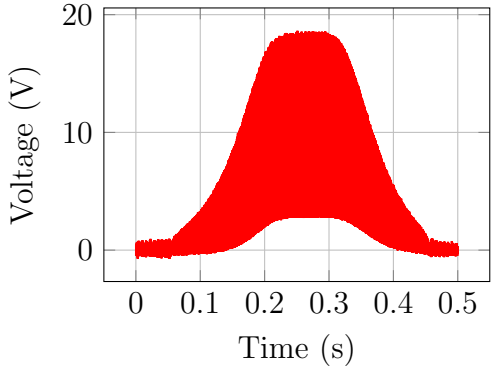

(b) Voltage V_{DC2}

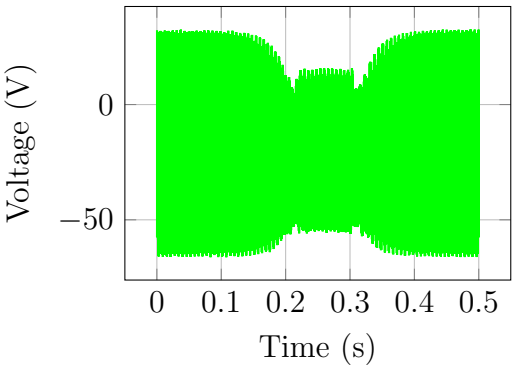

(c) Inverter Voltage V_p

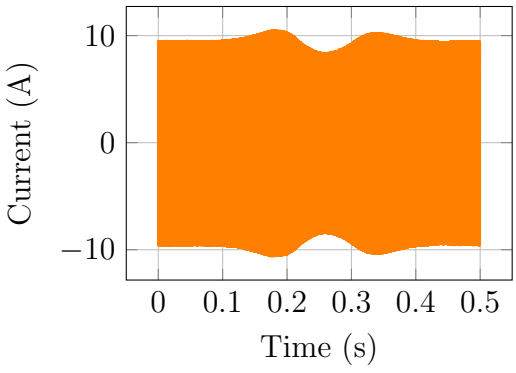

(d) Primary Current I_p

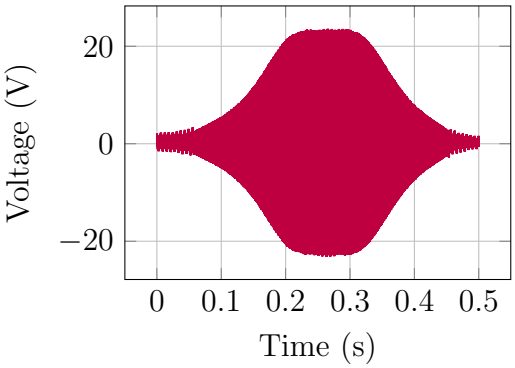

(e) Secondary Voltage V_s

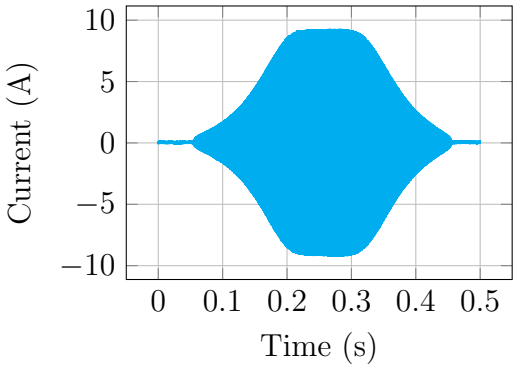

(f) Secondary Current I_s

Figure 3.17: Results for dynamic operation with copper wire coils at increased speed.

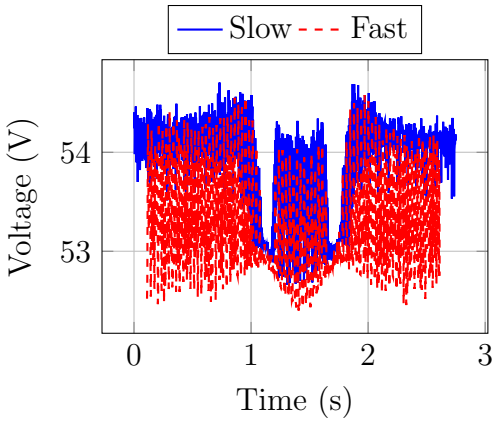

(a) Voltage $|V_{DC1}|$

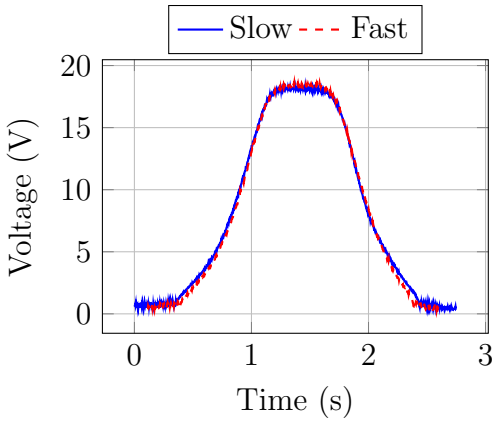

(b) Voltage $|V_{DC2}|$

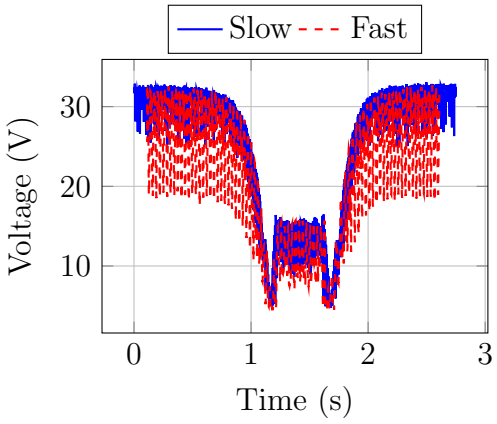

(c) Inverter Voltage $|V_p|$

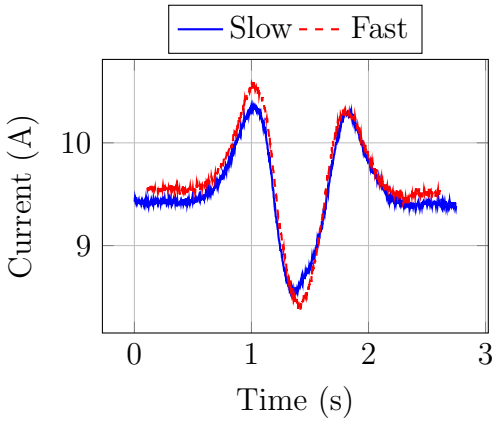

(d) Primary Current $|I_p|$

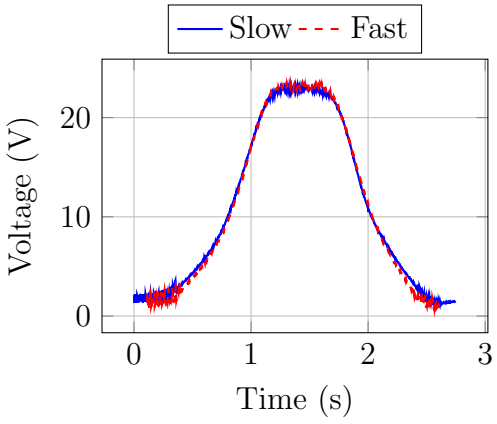

(e) Secondary Voltage $|V_s|$

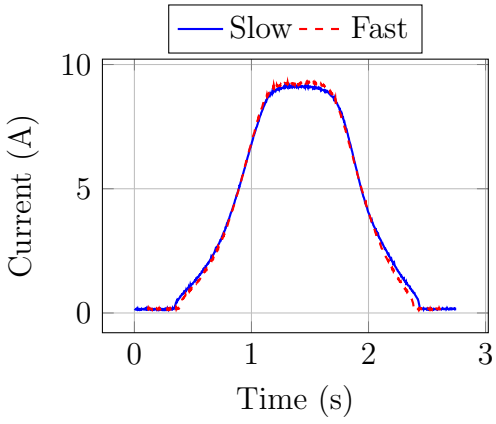

(f) Secondary Current $|I_s|$

Figure 3.18: Comparison of dynamic operation with copper wire coils: Slow vs. Fast travel speeds.

3.4 Simulation of Dynamic Wireless Power Transfer (DWPT)

Progressing onto the dynamic simulation of the system shown in Figure 3.19a requires modelling the mutual inductance as a time-varying parameter (this is shown in Figure 3.19b). In this context, the equations governing the mutual inductive coupling must be modified to reflect the time-varying mutual inductance $M(t)$. This accounts for the fact that, in a dynamic system, the mutual inductance is not constant but varies with the relative position of the coils:

$$v_s(t) = \frac{d}{dt}\left(M(t) * i_p(t)\right) \tag{19}$$

More generally, the voltages induced in each coil due to time-varying mutual inductance can be written as:

$$v_1(t) = \frac{d}{dt}\left(M(t) * i_2(t)\right), \quad v_2(t) = \frac{d}{dt}\left(M(t) * i_1(t)\right) \tag{20}$$

Here, $v_1(t)$ and $v_2(t)$ are the induced voltages in the primary and secondary coils, respectively, $i_1(t)$ and $i_2(t)$ are the currents in each coil, and $M(t)$ is the mutual inductance as a function of time.

Practically, the rate of change of mutual inductance is governed by the velocity of the secondary coil, which, in the case of a moving vehicle, can be approximated by typical highway speeds (e.g., 70 mph or approximately 31.3 m/s). This defines the mechanical time constant, τ_m, as the characteristic time it takes for the vehicle to traverse the effective coupling length (e.g., a 1-meter coil section), yielding:

$$\tau_m = \frac{L}{v} = \frac{1\,\text{m}}{31.3\,\text{m/s}} \approx 31.9\ \text{ms} \tag{21}$$

In contrast, the electrical system operates at a much higher frequency; for instance, an inverter switching at 85 kHz corresponds to an electrical time constant of:

$$\tau_e = \frac{1}{2\pi f} \approx \frac{1}{2\pi \cdot 85 \times 10^3} \approx 1.87\ \mu\text{s} \tag{22}$$

This large disparity in time scales, where $\tau_m \gg \tau_e$, implies that the mutual inductance changes very slowly relative to the fast electrical dynamics. Therefore the flux linkage can be approximated as a product of a slowly varying mutual inductance and the instantaneous current, effectively reducing the derivative of the product to:

$$\begin{aligned} v_1(t) &\approx M\frac{di_2(t)}{dt} \\ v_2(t) &\approx M\frac{di_1(t)}{dt} \end{aligned} \tag{23}$$

This simplification significantly reduces the computational complexity of the simulation while preserving accuracy over the relevant time scales.

Figure 3.20 shows the impact on transfer power at different travel speeds. The same result is shown in two ways to highlight the differences at different travel speeds and the lack of impact on mutual inductance, notice mutual inductance as a function of position remains

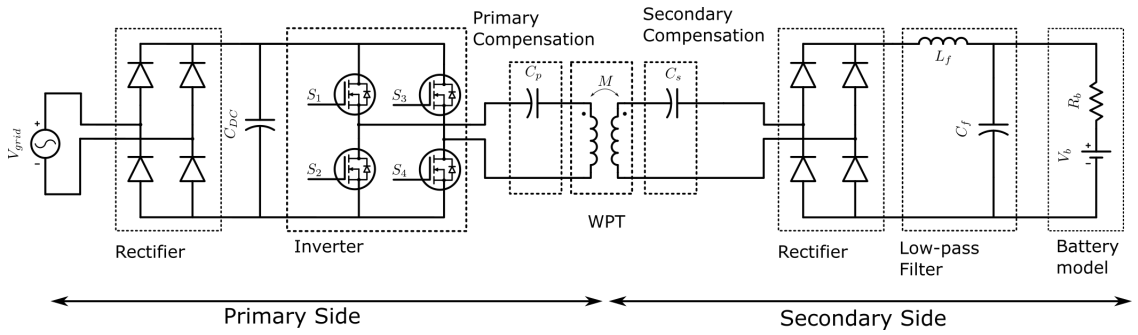

(a) Full circuit.

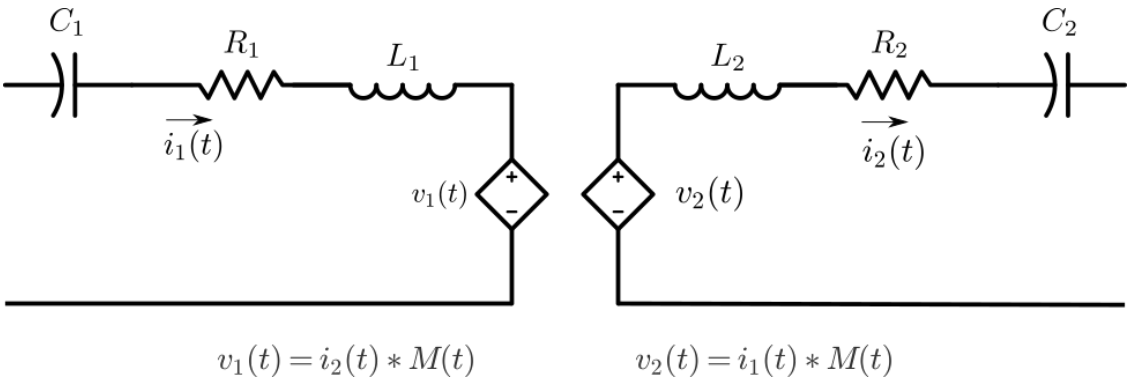

(b) WPT implementation.

Figure 3.19: Circuit used for validating WPT (3.1a) and the detailed implementation used for mutual inductance (3.23a).

the same. This is to be expected as the mutual inductance calculation is independent of travel speed.

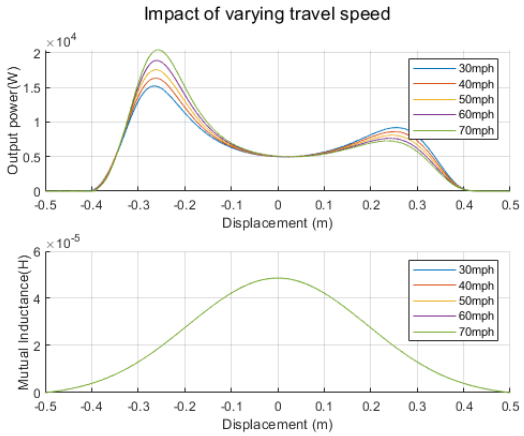

(a) Output power and mutual inductance over displacement for different travel speeds.

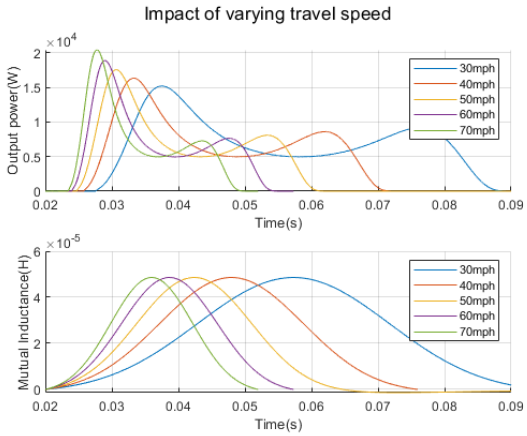

(b) Output power and mutual inductance over time for different travel speeds.

Figure 3.20: Impact of varying travel speed, presented over time and displacement [174].

Importantly, the result in Figure 3.20 resemble the behaviour seen in Figure 3.3, where high power is seen at the start and end of the coils. This is due to the rate of change of inductance in the system, as when $M = 0$ no power can be transferred between coils, at this time the primary coil current will also be high (due to low/zero impedance applied in addition to compensation capacitor and inductor coil). As mutual inductance increases, the high current across the primary coil is transferred to the secondary coil where the passive components charge up and begin reflecting power into the primary coil (as a result of the secondary coil current). As mutual inductance increases to it's peak, the reflected impedance also increases, altering the effective load seen by the primary side hence a reduction in the power transfer.

As the magnetic flux density is minimal at high displacement, peaks near zero displacement (maximum alignment), and decreases again as the vehicle moves away, travelling at higher speeds leads to a more rapid change in magnetic flux linkage. This results in a sharper, effectively producing a higher impulse of power delivery during the short window of strong coupling. Additionally higher travel speeds result in less time to achieve power transfer, hence less total energy will pass to the EV battery.

Once the system model is developed, it enables rapid investigation of parameter changes without the need to redevelop the entire system implementation. Figure 3.21 shows the impact of varying coil height (air gap), highlighting that the system response can differ significantly from what static analysis would suggest. For a planar coil (as modelled in this research), the magnetic field is at a minimum in the coil's plane (i.e., at the height of the coil itself) and increases along the vertical axis—normal to the coil surface—which is the direction of energy transfer. A lower air gap generally improves power transfer characteristics due to increased mutual inductance. This results in a higher peak power transfer and a narrower coupling window at lower air gaps, as shown in Figure 3.21.

However, at lower air gaps, coil misalignment has a more pronounced effect, a greater portion of the receiver coil moves out of the region of strong magnetic flux. In contrast, at higher air gaps, even though the magnetic field is weaker, a larger portion of the receiver coil remains within the field during misalignment, resulting in higher average power transfer in some conditions. This is shown by the mutual inductance between the two coils.

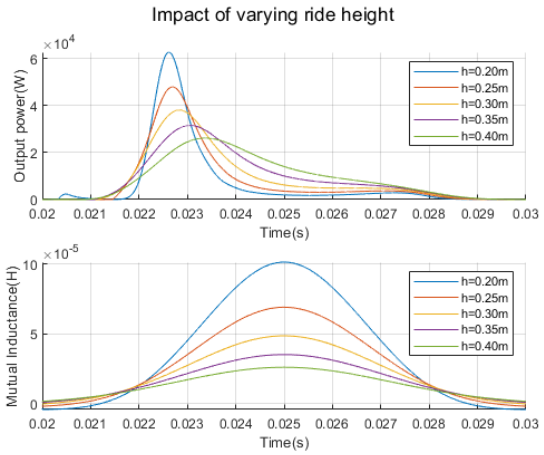

Figure 3.21: Output power and mutual inductance when changing ride height (h) [174].

Similarly, the system model can be used to investigate the impact of coil size on power transfer performance. Figures 3.22 and 3.23 show the effects of varying the dimensions of the primary and secondary coils, respectively. In each figure, subplots (a) and (b) illustrate the influence of changing the coil width and coil height. The mutual inductance is directly impacted by coil size, where a smaller coil leads to lower mutual inductance. This is to be expected as coil self inductance will also be lower. Notably, smaller coils tend to produce a more localized power response, often characterized by a single distinct peak. In contrast, increasing the coil width (perpendicular to the direction of travel) shows diminishing returns once the coil extends beyond the primary magnetic field region. This trend holds for both primary and secondary coils. On the other hand, extending the coil length in the direction of travel effectively increases the duration of coupling, thereby enhancing the total energy transferred. This type of analysis can be further extended to compare the performance of a single large coil versus multiple smaller coils, providing deeper insight into the overall power transfer characteristics of the DWPT system.

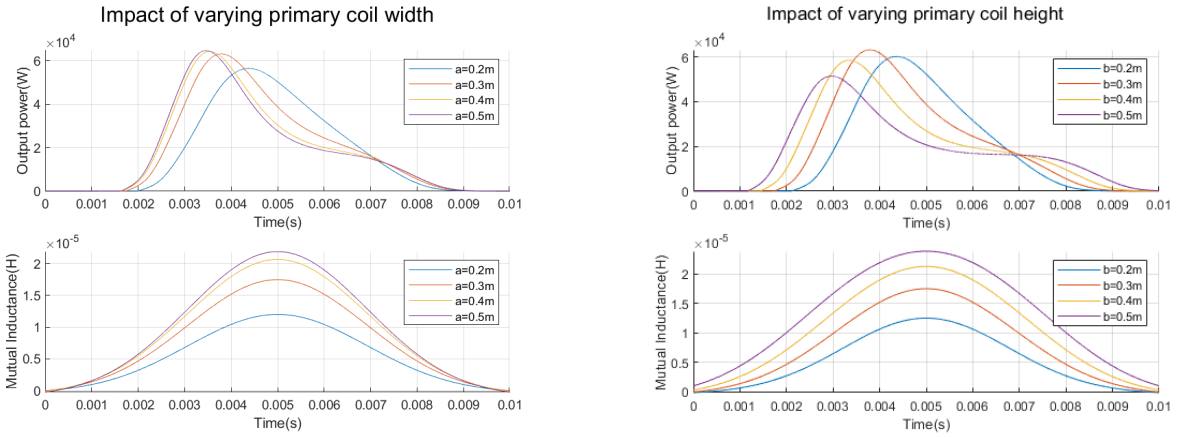

(a) Impact of varying primary coil width (a). (b) Impact of varying primary coil height (b).

Figure 3.22: Change in output power and mutual inductance as a result of varying primary coil dimensions [174]

3.5 Chapter Summary

The simulation of WPT has been achieved with the added benefit of extending the circuit to function for DWPT. Achieving identical results for static WPT compared to currently used research model, the system is used to obtain results for DWPT. Results for DWPT show similar behaviour to research giving confidence in the model. From here changing various system parameters gives insight into the behaviour of DWPT and highlights the need for such simulation models, as these system changes and their impact have not been discussed in previous research.

The lab results comparing copper and litz wire coils demonstrate the efficiency benefits of using litz wire. When using copper coils, increasing the amount of power transferred leads to higher power losses. In contrast, litz wire allows for more efficient energy transfer under

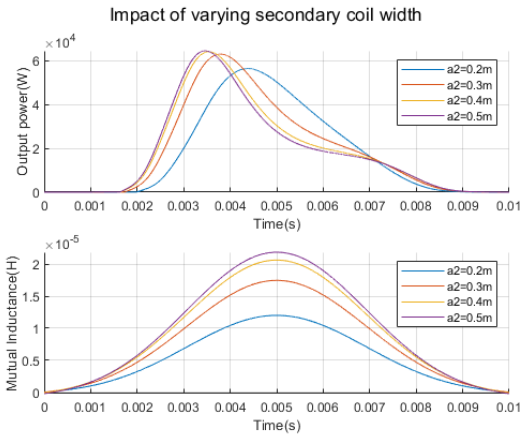

(a) Impact of varying secondary coil width (a2).

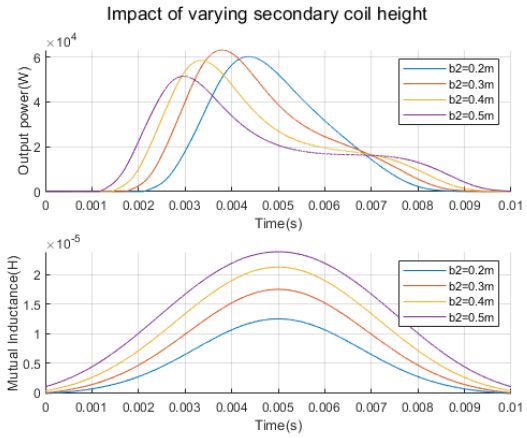

(b) Impact of varying secondary coil height (b2).

Figure 3.23: Change in output power and mutual inductance as a result of varying secondary coil dimensions [174]

similar conditions. Attempts to examine the impact of different travel speeds—specifically, a slow speed of approximately 0.5m/s (around 1mph) and a fast speed of 5m/s x (around 10mph)—proved challenging due to the relatively small difference between them. Nonetheless, a minor variation in the primary-side current was observed at the onset of power transfer. This observation aligns with simulation results, where the first peak of power transfer is notably higher at increased travel speeds.

The simulation of the DWPT system reveals several important behaviours that must be considered during the design process. An increase in travel speed leads to a higher instantaneous peak in power transfer but also shortens the duration over which power can be transferred. Therefore, operating at lower speeds is generally preferable, as it reduces peak power demand and allows more energy to be delivered over the same coil length. Another key factor is the coil height, or air-gap. As expected from SWPT systems, reducing the air-gap improves magnetic coupling, resulting in higher peak power. However, this also causes an overall decrease in the total amount of power transferred, demonstrating a trade-off that static analysis alone would not reveal.

Further investigation into coil geometry shows that increasing the coil size in the direction of travel tends to improve mutual inductance and extends the period during which power can be transferred. This leads to lower peak power demands and potentially more efficient system operation. On the other hand, increasing the coil dimensions perpendicular to the direction of travel yields diminishing returns. This is because the additional coil area lies in regions with weaker magnetic flux, offering limited benefit despite increases in inductance and mutual inductance.

These results collectively underscore the necessity of dynamic analysis in the design of DWPT systems. Static evaluations may suggest certain design choices—such as minimizing air-gap or maximizing coil dimensions—that could be suboptimal when dynamic behaviour is considered. The model used in this study provides a convenient way to explore critical system parameters such as coil dimensions, travel speed, and air-gap. Although not explored

in the current study, the model can also be extended to include the effects of lateral misalignment, variable velocity, and dynamic air-gap changes to better represent real-world driving behaviour. Furthermore, the model is flexible and can be adapted to accommodate different coil geometries by updating the mutual inductance formulation. It also supports multi-coil configurations by calculating the mutual inductance and induced voltages for each coil in the system.

Successful simulation can now be used as a starting point for further research in the field. It is recommended to consider presenting future results in terms of coupling factor (k) instead of mutual inductance (M) to better standardise results and more accurately compare the impact of various system changes.

4 Control of Dynamic Wireless Power Transfer (DWPT)

Building upon the WPT model presented in Chapter 3 and illustrated in Figure 3.1, this work now advances toward developing control strategies and exploring the system topologies to achieve the desired control objectives. The previous chapter showed the impact of varying system parameters on output power, these will remain fixed for this section as the main goal is now to explore the control implementation.

In the initial approach, the inverter control employed a high-frequency PWM signal using a 1MHz carrier wave and a reference signal operating 85kHz driving the circuit at resonance. This method aimed to reduce harmonic content and improve signal quality. However, it was observed that such a high switching frequency is not strictly necessary for achieving efficient power transfer. Operating at 1MHz introduces significant practical challenges, including the need for faster microcontrollers, more accurate sensing hardware, and higher-cost switching components, all while increasing Electromagnetic Interference (EMI).

To simplify the system and enhance practicality, the control strategy was revised. Instead of using high-frequency PWM, a square wave signal directly operating at the resonant frequency of 85kHz with a 50% duty cycle was adopted. This approach still ensures effective resonance in the circuit, making it a more efficient and cost-effective baseline configuration without compromising power transfer performance.

Table 2.5 presented a summary of advantages and disadvantages for control implementations. The system presented in this section features dual-sided control with two DC/DC converter and controlled rectifier, and no inverter control. An important factor in this development is the aim of achieving control DWPT which, based on the work presented in Figures 3.20-3.23, shows a small window of opportunity for control (for a 0.3x0.3m coil <10ms). This is important as research presented on the topic of control for WPT are static and focus on steady state values where charging events are orders of magnitude longer than the times for DWPT (charging events for WPT can be up to several hours for vehicle full charge).

Following the development of WPT taxi solutions, trialled in Nottingham [175], the charging system experienced issues with its detection and communication components, which failed to provide reliable readings. As a result, the charging process could not be initiated. To mitigate this, the charging bays were physically sectioned off and equipped with light gates to enhance vehicle detection and enable charging. These challenges highlight the importance of developing charging strategies that do not rely on a communication link between the primary and secondary sides of the system.

Inverter control was changed to a fixed 85kHz and 0.5 duty cycle (50% square wave at 85kHz), lowering the maximum switching frequency from 1MHz. Lower frequency operation offers more choice for manufacture and less expensive components, as high power, high frequency inversion is more expensive to implement. The impact of harmonic distortion on either grid or load (EV battery) can be improved by other circuit components in the whole system, especially when PFC and DC/DC converters operate at a lower frequency.

Furthermore, for the short duration and change in resonant frequency (as a result of changing inductance) seen in DWPT leads to complications in implementing frequency or phase shift based controls. It is also more practical to maximise the power transferred between primary and secondary DC buses (before inverter and after rectifier), and allow

secondary conversion circuits to manage battery charging with constant voltage/current controls. It is also highly likely, manufacturers will insist on using the OBC to ensure any charging components meet their requirements.

Secondary DC/DC converter is used to directly manage the load charging characteristics. A buck converter allows a low ripple current to be obtained (compared to buck-boost and boost converters), provides a relatively simple control scheme and it's characteristics can be tuned by changing circuit parameters, without affecting the DWPT components. Secondary DC bus voltage (rectified voltage V_{rec}) needs to be monitored as it can continue to rise while output control is set constant, maintaining a self voltage is achieved by using a controlled rectifier. It is possible to include this control into the DC/DC converter, however that will directly affect output characteristics and is therefore inadvisable.

Controlled rectifier is used to control secondary bus voltage. For this function only two of the four switches are used to provide a return path for current, effectively disconnecting power flow to the secondary DC bus. This solves the issue of rising capacitor voltage, any excess power will now be present in the WPT circuit where it is damped through passive and switching components. The voltage control can be adjusted based on system design parameters, especially if larger voltages are tolerable for the capacitor, it would allow for more power to be transferred to the capacitor while the DWPT link is available.

When the rectifier disconnects the load, the WPT system is operating with a low impedance load (only switch resistances as load), leading to high current. Increased current leads to increased power losses in switching components components. The only remaining way to reduce this, is to introduce another converter to reduce the primary side DC bus voltage, which will in turn lower the current and power through the system. Commonly this is achieved with communication between primary and secondary sides of the converter [122], this section will later show this to not be necessary based on the propose control scheme.

Primary DC/DC converter is used to reduce the primary DC bus voltage which in turn regulates the converter power consumption. This converter can also be used to keep the power draw from the grid below a certain level to manage grid impact. Stable tuning for this converter is important as it will directly impact further converters and is the only converter with a more complex equivalent load.

Control sequence and parameters are selected based on several design objectives. The process begins with ensuring proper control of the output charging characteristics. As the system design evolves, additional topologies and control targets are introduced to improve the overall performance and efficiency of the converter.

The simplest form of the WPT system is illustrated in Figure 4.1. This configuration enables wireless power transfer to the load with minimal components and control complexity—requiring only the inverter to generate a square wave at the system's resonant frequency (85kHz).

To regulate the load's charging characteristics (such as constant voltage or constant current), a secondary DC/DC converter is introduced. This converter decouples the WPT sys-

tem from the load, effectively managing fluctuations caused by variations in WPT operation. However, this approach leaves the secondary DC voltage (V_{rec} in Figure 4.2) uncontrolled. Without regulation, the capacitor voltage can continue to rise, as there is no mechanism in place to reduce input power and prevent overcharging.

To address this, the next stage is to implement voltage control to maintain the rectified voltage at a set-point. This is achieved using a semi-controlled rectifier, which regulates power flow from the inductive coil to the DC-side capacitor.

With the rectified voltage and load charging characteristics now managed by the secondary-side circuitry, attention shifts to input power control. A significant mismatch between input and output power can result in increased losses. While adjusting the inverter to control power is possible, it adds considerable complexity. Instead, a primary-side DC/DC converter is introduced to regulate the DC bus voltage before the inverter. This approach effectively controls the power supplied by the primary circuit and can operate at a lower frequency than the WPT resonant frequency.

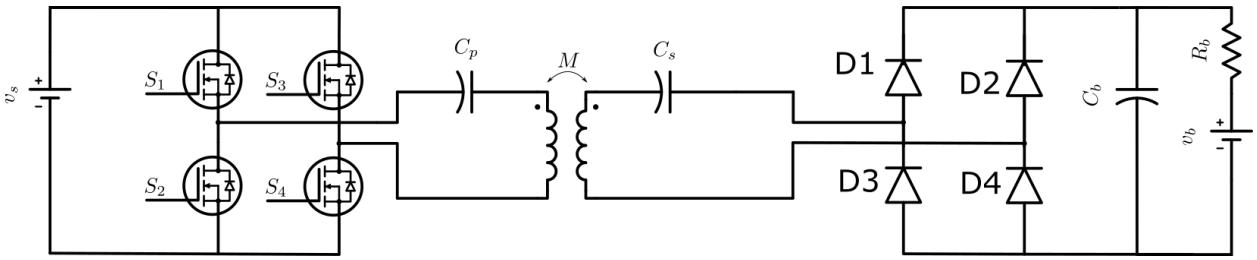

Figure 4.1: Base WPT system with fixed frequency and duty cycle inverter.

4.1 Methodology

Using equations (12) and (13), we obtain the expression for the secondary current:

$$i_2 = \frac{\omega M}{Z_2} \cdot \frac{V_\mathrm{s}}{Z_1 - \dfrac{\omega^2 M^2}{Z_2}} \tag{24}$$

$$= \frac{\omega M V_\mathrm{s}}{Z_2 \left(Z_1 - \dfrac{\omega^2 M^2}{Z_2} \right)} \tag{25}$$

Solving equation (25) for the input voltage V_s yields:

$$V_\mathrm{s} = \frac{Z_2}{\omega M} \cdot \left(Z_1 - \frac{\omega^2 M^2}{Z_2} \right) \cdot i_2 \tag{26}$$

Rather than assuming a fixed load resistance, we now consider the case of constant power consumption at the receiver. The load power is given by:

$$P_\mathrm{out} = |i_2|^2 R_\mathrm{eq} \quad \Rightarrow \quad |i_2| = \sqrt{\frac{P_\mathrm{out}}{R_\mathrm{eq}}} \tag{27}$$

Substituting equation (27) into equation (26), and taking magnitudes, the required transmitter-side input voltage becomes:

$$V_{\mathrm{s}} = \sqrt{\frac{P_{\mathrm{out}}}{R_{\mathrm{eq}}}} \cdot \left| \frac{Z_2}{\omega M} \left(Z_1 - \frac{\omega^2 M^2}{Z_2} \right) \right| \tag{28}$$

From equation (28), it is evident that the required input voltage V_{s} increases with the output power P_{out}.

Alternatively, using equation (13), the primary current can be expressed in terms of mutual inductance:

$$|i_1| = |i_2| \cdot \frac{|Z_2|}{\omega M} \tag{29}$$

This links the mutual inductance directly to the primary current. Since $|i_1|$ is proportional to the supply voltage in most converter topologies (e.g., full-bridge inverters), it follows that the required supply voltage can be reduced as M increases.

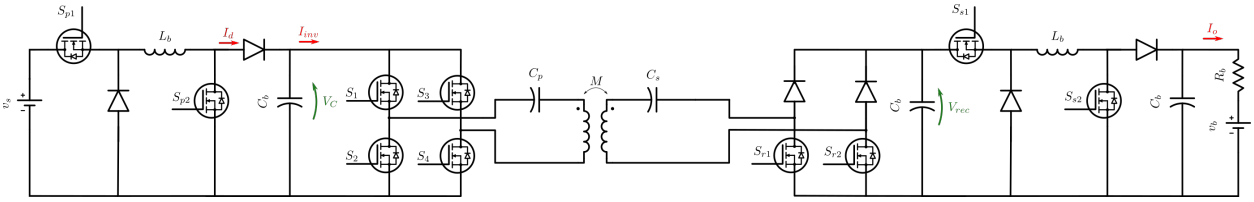

Figure 4.2: Circuit used for DWPT control modelling

Figure 4.2, shows the full circuit used to achieve DWPT, using the primary DC/DC converter as a buck-boost converter allowed better response time for raising or lowering V_C. Secondary DC/DC converter operation in buck mode allows for lower ripple current at the output. This section will first present circuit analysis for the converters used and WPT system before presenting an improve control strategy for the primary DC converter and discussing results.

4.1.1 DC/DC converter analysis

Figure 4.3 shows a configurable DC/DC converter. To achieve forward operation mode, $S_2 = S_4 = 0$ leaving S1 as the buck control switch and S3 the boost control switch, allowing the use of buck mode ($S_1 = PWM, S_3 = 0$), boost mode($S_1 = 1, S_3 = PWM$), or buck-boost mode ($S_1 = S_3 = PWM$). The same is possible for reverse operation mode where $S_1 = S_3 = 0$, buck mode ($S_4 = PWM, S_2 = 0$), boost mode($S_4 = 1, S_2 = PWM$), or buck-boost mode ($S_2 = S_4 = PWM$). As the circuit is symmetrical, analysis in forward mode is presented. Analysis will give state-space matrices and transfer functions (V_c/d, where d is the duty cycle) form using:

$$\dot{x} = Ax + Bu \tag{30}$$

$$y = Cx + Du \tag{31}$$

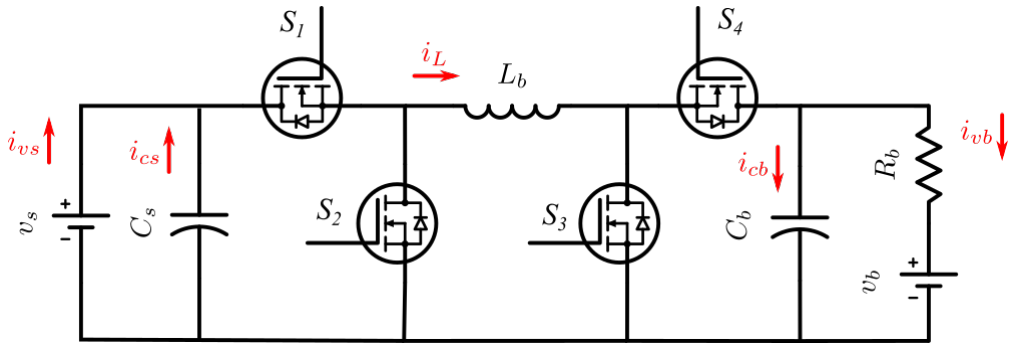

Figure 4.3: Configurable bidirectional DC/DC converter.

Where, **x** is the state vector, **y** is the output vector, **u** is the input (control) vector, **A** is the system state matrix, **B** is the input matrix, **C** is the output matrix, and **D** is the feed-forward matrix. For the buck-boost converter in forward operation mode, state variables are given by:

$$x = \begin{pmatrix} I_{Lb} \\ V_{cb} \end{pmatrix}, V_{cs} = V_{cs}$$

The analysis of the circuit is presented by operation mode to develop the system equations before summarising. Operating at a switching frequency f results in a switching period $T = 1/f$. The on-time, corresponding to the active conduction interval, is given by $t_{\text{on}} = dT$, where d is the duty cycle. The off-time occupies the remainder of the cycle, $t_{\text{off}} = (1-d)T$. The system behaviour during these intervals is modelled separately and then combined to form an averaged model over one period. This averaged model is then used to analyse the dynamic behaviour of the converter.

Buck mode

$$S_1 = PWM \tag{32}$$
$$S_2 = 0 \tag{33}$$
$$S_3 = 0 \tag{34}$$
$$S_4 = 0 \tag{35}$$

On state Shown in Figure 4.4.

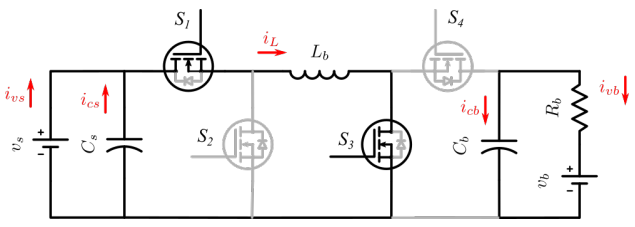

Figure 4.4: Buck converter forward mode showing current paths in the on state.

$$\frac{dI_{Lb}}{dt} = \frac{V_{cs} - V_{cb}}{L_b} \tag{36}$$

$$C_b \frac{dv_{cb}}{dt} = I_{Lb} - I_{vb} \tag{37}$$

$$I_{vb} = \frac{V_{cb}}{R_b} \tag{38}$$

Off state Shown in Figure 4.5.

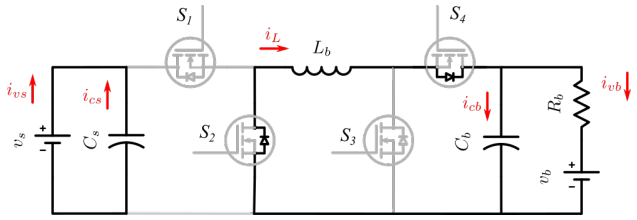

Figure 4.5: Buck converter forward mode showing current paths in the off state.

$$\frac{dI_{Lb}}{dt} = \frac{-V_{cb}}{L_b} \tag{39}$$

$$C_b \frac{dv_{cb}}{dt} = I_{Lb} - I_{vb} \tag{40}$$

$$I_{vb} = \frac{V_{cb}}{R_b} \tag{41}$$

Combined equations Averaging the on/off equations over a switching period with duty cycle d, the averaged equations become:

$$\frac{dI_{Lb}}{dt} = d\frac{V_{cs}}{L_b} - \frac{V_{cb}}{L_b} \tag{42}$$

$$C_b \frac{dV_{cb}}{dt} = I_{Lb} - \frac{V_{cb}}{R_b} \tag{43}$$

Small-Signal Linearisation To analyse the dynamic behaviour of the system, we perform small-signal linearisation by replacing all time-varying variables with the sum of a steady-state value and a small perturbation, denoted by tilde variables:

$$I_{Lb} \to I_{Lb} + \tilde{I}_{Lb} \tag{44}$$

$$V_{cb} \to V_{cb} + \tilde{V}_{cb} \tag{45}$$

$$d \to d + \tilde{d} \tag{46}$$

Note that $V_{cs} = V_s$ is a fixed voltage source and is therefore treated as a constant.

Substitute into Equation 42:

$$\frac{d(I_{Lb} + \tilde{I}_{Lb})}{dt} = (d + \tilde{d})\frac{V_{cs}}{L_b} - \frac{V_{cb} + \tilde{V}_{cb}}{L_b} \tag{47}$$

$$= d\frac{V_{cs}}{L_b} + \frac{V_{cs}}{L_b}\tilde{d} - \frac{V_{cb}}{L_b} - \frac{\tilde{V}_{cb}}{L_b} \tag{48}$$

In this analysis, steady-state terms such as $d\frac{V_{cs}}{L_b}$ and $\frac{V_{cb}}{L_b}$ are constant and do not affect the small-signal dynamics. Since we are linearising around the steady-state operating point, these terms are cancelled, isolating only the perturbation components. This yields the small-signal current equation:

$$\frac{d\tilde{I}_{Lb}}{dt} = \frac{V_{cs}}{L_b}\tilde{d} - \frac{1}{L_b}\tilde{V}_{cb} \tag{49}$$

Now apply the same process to Equation 43:

$$C_b\frac{d(V_{cb} + \tilde{V}_{cb})}{dt} = I_{Lb} + \tilde{I}_{Lb} - \frac{V_{cb} + \tilde{V}_{cb}}{R_b} \tag{50}$$

$$= \left(I_{Lb} - \frac{V_{cb}}{R_b}\right) + \tilde{I}_{Lb} - \frac{\tilde{V}_{cb}}{R_b} \tag{51}$$

Cancelling the steady-state terms yields the small-signal voltage equation:

$$C_b\frac{d\tilde{V}_{cb}}{dt} = \tilde{I}_{Lb} - \frac{1}{R_b}\tilde{V}_{cb} \tag{52}$$

Finally, taking the Laplace transform ($\frac{d}{dt} \to s$) gives the small-signal equations in the frequency domain:

$$s\tilde{I}_{Lb}(s) = \frac{V_{cs}}{L_b}\tilde{d}(s) - \frac{1}{L_b}\tilde{V}_{cb}(s) \tag{53}$$

$$s\tilde{V}_{cb}(s) = \frac{1}{C_b}\tilde{I}_{Lb}(s) - \frac{1}{R_bC_b}\tilde{V}_{cb}(s) \tag{54}$$

State-Space Equations The system can be expressed in state-space form using the duty cycle (d) as the control input. Define the state vector, output, and input as:

$$x = \begin{pmatrix} I_{Lb} \\ V_{cb} \end{pmatrix}, \quad y = V_{cb}, \quad u = d \tag{55}$$

The linearised state-space equations become:

$$\dot{x} = \begin{pmatrix} 0 & -\frac{1}{L_b} \\ \frac{1}{C_b} & -\frac{1}{R_bC_b} \end{pmatrix} x + \begin{pmatrix} \frac{V_{cs}}{L_b} \\ 0 \end{pmatrix} u \tag{56}$$

$$y = \begin{pmatrix} 0 & 1 \end{pmatrix} x + 0 \cdot u \tag{57}$$

Transfer Function The system transfer function can be obtained from the Laplace domain equations to give:

$$\frac{\tilde{V}_{cb}}{\tilde{d}} = \frac{V_{cs}}{L_b C_b s^2 + \left(\frac{L_b}{R_b}\right) s + 1} \tag{58}$$

Buck-Boost mode

$$S_1 = S_3 = PWM \tag{59}$$
$$S_2 = 0 \tag{60}$$
$$S_4 = 0 \tag{61}$$

On state Figure 4.6.

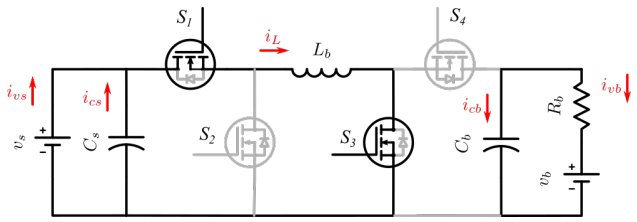

Figure 4.6: Buck-boost converter forward mode showing current paths in the on state.

$$L_b \frac{dI_{Lb}}{dt} = V_s \tag{62}$$
$$C_b \frac{dV_{Cb}}{dt} = \frac{-V_{Cb}}{R_b} \tag{63}$$

Off state Figure 4.7.

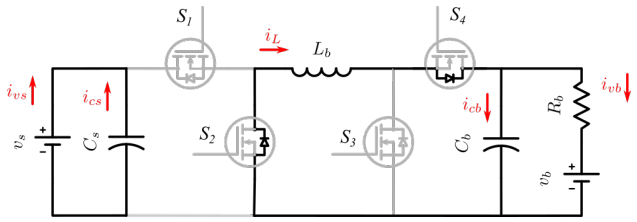

Figure 4.7: Buck-boost converter forward mode showing current paths in the off state.

$$L_b \frac{dI_{Lb}}{dt} = -V_{cb} \tag{64}$$
$$C_b \frac{dV_{Cb}}{dt} = i_{Lb} - \frac{V_{Cb}}{R_b} \tag{65}$$

Combined equations

$$L_b \frac{dI_{Lb}}{dt} = dV_s - (1-d)V_{cb} \tag{66}$$

$$C_b \frac{dV_{Cb}}{dt} = (1-d)I_{Lb} - \frac{V_{Cb}}{R_b} \tag{67}$$

Small-signal linearisation

$$s\tilde{I}_{Lb}L_b = \tilde{d}V_s - \tilde{V}_{Cb} + \tilde{d}V_C + d\tilde{V}_{Cb} \tag{68}$$

$$s\tilde{V}_{Cb}C_b = \tilde{I}_{Lb} - \tilde{d}I_{Lb} - \tilde{I}_{Lb}d - \frac{\tilde{V}_{Cb}}{R_b} \tag{69}$$

$$s\tilde{I}_{Lb} = \frac{-(1-d)}{L_b}\tilde{V}_{Cb} + \frac{V_s + V_c}{L_b}\tilde{d} \tag{70}$$

$$s\tilde{V}_C Cb = \frac{1-d}{C_b}\tilde{I}_{Lb} - \frac{1}{C_b R_b} - \frac{I_L}{C_b}\tilde{d} \tag{71}$$

State space equation

$$x = \begin{pmatrix} I_{Lb} \\ V_{cb} \end{pmatrix}, y = V_{Cb}, u = d \tag{72}$$

$$\dot{x} = \begin{pmatrix} 0 & -\frac{(1-d)}{L_b} \\ \frac{(1-d)}{C_b} & -\frac{1}{R_b C_b} \end{pmatrix} x + \begin{pmatrix} \frac{V_s+V_c}{L_b} \\ -\frac{I_L}{C_b} \end{pmatrix} u \tag{73}$$

$$y = \begin{pmatrix} 0 & 1 \end{pmatrix} x + (0)u \tag{74}$$

Where $V_c = V_s * d/(1-d)$ and $I_L = V_c/R_b/(1-d)$

Transfer function

$$\frac{\tilde{V}_c}{\tilde{d}} = -\frac{sL_b i_l - d'V_c}{s^2 L_b C_b + s\frac{L_b}{R_b} + d^2} \tag{75}$$

Boost mode

$$S_1 = 1 \tag{76}$$

$$S_2 = 0 \tag{77}$$

$$S_3 = PWM \tag{78}$$

$$S_4 = 0 \tag{79}$$

On state Figure 4.8.

$$L_b \frac{dI_{Lb}}{dt} = V_s \tag{80}$$

$$C_b \frac{dV_{Cb}}{dt} = \frac{-V_{Cb}}{R_b} \tag{81}$$

$$L_b \frac{dI_{Lb}}{dt} = V_s \tag{82}$$

$$C_b \frac{dV_{Cb}}{dt} = \frac{-V_{Cb}}{R_b} \tag{83}$$

Off state Figure 4.9.

$$L_b \frac{dI_{Lb}}{dt} = V_s - V_{cb} \tag{84}$$

$$C_b \frac{dV_{Cb}}{dt} = i_{Lb} - \frac{V_{Cb}}{R_b} \tag{85}$$

Combined equations

$$L_b \frac{dI_{Lb}}{dt} = V_s - (1-d)V_{cb} \tag{86}$$

$$C_b \frac{dV_{Cb}}{dt} = (1-d)I_{Lb} - \frac{V_{Cb}}{R_b} \tag{87}$$

Small-signal linearisation

$$s\tilde{I}_{Lb}L_b = -\tilde{V}_{Cb} + \tilde{d}V_C + D\tilde{V}_{Cb} \tag{88}$$

$$s\tilde{V}_{Cb}C_b = \tilde{I}_{Lb} - \tilde{d}I_{Lb} - \tilde{I}_{Lb}d - \frac{\tilde{V}_{Cb}}{R_b} \tag{89}$$

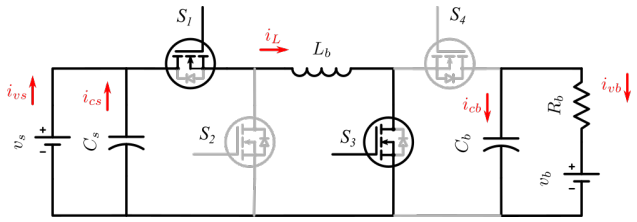

Figure 4.8: Boost converter forward mode showing current paths in the on state.

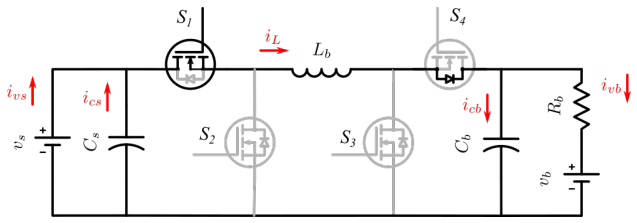

Figure 4.9: Boost converter forward mode showing current paths in the off state.

$$s\tilde{I}_{Lb} = \frac{-(1-d)}{L_b}\tilde{V}_{Cb} + \frac{V_c}{L_b}\tilde{d} \tag{90}$$

$$s\tilde{V}_C Cb = \frac{1-d}{C_b}\tilde{I}_{Lb} - \frac{1}{C_b R_b} - \frac{I_L}{C_b}\tilde{d} \tag{91}$$

State space equation

$$x = \begin{pmatrix} I_{Lb} \\ V_{cb} \end{pmatrix}, y = V_{Cb}, u = d \tag{92}$$

$$\dot{x} = \begin{pmatrix} 0 & -\frac{(1-d)}{L_b} \\ \frac{(1-d)}{C_b} & -\frac{1}{R_b C_b} \end{pmatrix} x + \begin{pmatrix} \frac{V_c}{L_b} \\ -\frac{I_L}{C_b} \end{pmatrix} u \tag{93}$$

$$y = \begin{pmatrix} 0 & 1 \end{pmatrix} x + (0)u \tag{94}$$

Where $V_c = V_s/(1-d)$ and $I_L = V_c/R_b * d/(1-d)$

Transfer function

$$\frac{\tilde{V}_c}{\tilde{d}} = -\frac{v_s\left(s\frac{dL_b}{d'^2 R_b} - 1\right)}{s^2 L_b C_b + s\frac{L_b}{R_b} + d'^2} \tag{95}$$

System transfer functions summarised Based on the analysis provided, the denominators of all converter transfer functions conform to the standard form for second-order systems. These systems can be expressed either without or with a zero in the numerator.

- **Without a zero (e.g., Buck converter):**

$$G(s) = \frac{K\omega_n^2}{s^2 + 2\zeta\omega_n s + \omega_n^2} \tag{96}$$

- **With a single zero (e.g., Boost and Buck-Boost converters):**

$$G(s) = \frac{K(s-z)\omega_n^2}{s^2 + 2\zeta\omega_n s + \omega_n^2} \tag{97}$$

Here ω_n is the natural frequency of the system, ζ its damping ratio, z represents the zero location and K is a gain constant that scales the magnitude response but does not affect system dynamics (pole or zero locations).

This general structure allows a unified framework for analysing converter dynamics and designing control strategies. The presence of a zero alters the transient and frequency response, especially affecting phase and overshoot, while K influences steady-state gain.

PI controller implementation

Table 4.1: Summary of Buck, Boost, and Buck-Boost converter control parameters in standard second-order form.

Mode	V_o	L_b	$\tilde{V}_c/\tilde{d}$	ω_n	ζ	Zero Location
Buck	dV_s	$\frac{V_s(1-d)Td}{\Delta i_l}$	$\frac{V_s \cdot \omega_n^2}{s^2 + 2\zeta\omega_n s + \omega_n^2}$	$\frac{1}{\sqrt{L_b C_b}}$	$\frac{1}{2R_b}\sqrt{\frac{C_b}{L_b}}$	–
Boost	$\frac{V_s}{1-d}$	$\frac{V_s Td}{\Delta i_l}$	$-V_s\left(\frac{dL_b}{d'^2 R_b}\right) \cdot \frac{\left(s - \frac{d'^2 R_b}{dL_b}\right)\omega_n^2}{s^2 + 2\zeta\omega_n s + \omega_n^2}$	$\frac{d'}{\sqrt{L_b C_b}}$	$\frac{1}{2R_b}\sqrt{\frac{C_b}{L_b}}$	$\frac{d'^2 R_b}{dL_b}$
Buck-Boost	$\frac{V_s d}{1-d}$	$\frac{V_s Td}{\Delta i_l}$	$-\left(\frac{L_b i_l}{d^2}\right) \cdot \frac{\left(s - \frac{d'V_o}{L_b i_l}\right)\omega_n^2}{s^2 + 2\zeta\omega_n s + \omega_n^2}$	$\frac{d}{\sqrt{L_b C_b}}$	$\frac{1}{2R_b}\sqrt{\frac{C_b}{L_b}}$	$\frac{d'V_o}{L_b i_l}$

General Approach For a PI controller, the transfer function is denoted as $G_c(s) = K_p + \frac{K_i}{s}$, where K_p and K_i are the proportional and integral gains, respectively. For a known system (Gp) in a closed loop set up, the overall transfer function is denoted is given by:

$$T(s) = \frac{1}{\frac{1}{G_p(s)G_c(s)} + 1} \tag{98}$$

This can be simplified and rearranged into a rational polynomial form, enabling the use of pole placement techniques to design the controller. Pole placement involves choosing desired closed-loop pole locations—typically to achieve specified damping, natural frequency, and response time—and solving for controller parameters that place the system poles at those locations.

Pole Placement: Motivation and Limitations

Pole placement provides an intuitive, model-based way to tailor dynamic behaviour such as overshoot, settling time, and stability margins [176]. However, it has several important drawbacks:

- **Model Sensitivity:** Controller gains depend on accurate knowledge of system parameters (L, C, R, V_s). Any mismatch (due to ageing, tolerance, or load variation) can degrade performance.
- **Lack of Robustness:** Unlike robust or adaptive methods, pole placement does not account for parameter uncertainty or disturbance rejection unless explicitly extended.
- **Integral Action Trade-off:** Although the integral term ensures zero steady-state error, it introduces an additional pole at the origin. If not carefully placed, this pole can lead to sluggish response or even compromise system stability.
- **Bandwidth Limitation in Non-Minimum Phase Systems:** Boost and buck-boost converters contain right-half-plane (RHP) zeros, which inherently limit achievable control bandwidth and make aggressive pole placement impractical.

Despite these limitations, pole placement is an effective and appropriate method for designing PI controllers for buck, boost, and buck-boost converters—particularly under nominal, continuous conduction mode (CCM) operation—because the plant dynamics are relatively well-understood and can be linearized into low-order systems amenable to analytical control design.

Buck mode

$$T = \frac{\frac{1}{a}\left(K_p s + K_i\right)}{s^3 + \left(\frac{b}{a}\right)s^2 + \left(\frac{c+K_p}{a}\right)s + \frac{K_i}{a}} \tag{99}$$

Where $a = R_b L_b C_b / V_s, b = L_b / V_s, c = R_b / V_s$. As the transfer function is a 3rd order system, we expect 3 poles, 2 symmetrical and another real pole at a value of α. We can therefore use pole placement for controller design.

$$s^3 + \left(\frac{b}{a}\right)s^2 + \left(\frac{c+K_p}{a}\right)s + \frac{K_i}{a} = (s+\alpha)(s^2 + 2\zeta\omega_n s + \omega_n^2) \tag{100}$$

$$\equiv s^3 + s^2\left(2\zeta\omega_n + \alpha\right) + s\left(\omega_n^2 + 2\alpha\zeta\omega_n\right) + \alpha\omega_n^2 \tag{101}$$

Equating coefficients:

$$\frac{b}{a} = 2\zeta\omega_n + \alpha \tag{102}$$

$$\frac{c+K_p}{a} = \omega_n^2 + 2\alpha\zeta\omega_n \tag{103}$$

$$\frac{K_i}{a} = \alpha\omega_n^2 \tag{104}$$

The settling time of a second-order system is typically defined as the time required for the system's response to remain within a specified percentage band around its final steady-state value. This band, known as the settling criterion, is selected based on the acceptable deviation from the final value. The settling time can be found using the settling criterion as:

$$t_s = \frac{-\ln(\delta)}{\zeta\omega_n} \tag{105}$$

For a 1.5% settling criterion, the response must remain within ±1.5% of the steady-state value. Substituting $\delta = 0.015$ into (105), the natural frequency ω_n can be related to the damping ratio ζ and the desired response time t_r as:

$$\omega_n = \frac{4.25}{\zeta t_r} \tag{106}$$

From here, the PI values can be found by:

$$K_p = \left(2\alpha\zeta\omega_n^1 + \omega_n^2\right)a - c \tag{107}$$

$$K_i = a\alpha\omega_n^2\alpha = \frac{b}{a} - 2\zeta\omega_n \tag{108}$$

Buck-boost mode

$$\tilde{i}_o = -\frac{v_s\left(s\frac{DL_b}{D'^2R_b}-1\right)}{s^2L_bC_bR_b+sL_b+R_bD'^2}\tilde{D} \tag{109}$$

$$G_c = K_p + \frac{K_i}{s} \tag{110}$$

$$T = \frac{1}{\frac{1}{G_pG_c}+1} = \frac{v_s\left(s\frac{DL_b}{D'^2R_b}-1\right)(K_p+\frac{K_i}{s})}{s^2L_bC_bR_b+sL_b+R_bD'^2 - v_s\left(s\frac{DL_b}{D'^2R_b}-1\right)(K_p+\frac{K_i}{s})} \tag{111}$$

$$T = \frac{v_s\left(s^2\frac{DL_b}{D'^2R_b}-s\right)(sK_p+K_i)}{s^3L_bC_bR_b+s^2\left(L_bR_b+\frac{DL_b}{D'^2R_b}v_sK_p\right)+s(R_bD'^2-\frac{DL_b}{D'^2R_b}v_sK_i+v_sK_p)+(v_sK_i)} \tag{112}$$

$$T = \frac{V_s(K_i+K_p*s)*(R_bD'^2-D*L_b*s)}{(D'^2R_b)} \tag{113}$$

$$T = \frac{V_s(K_i+K_p*s)*(R_bD'^2-D*L_b*s)}{s^3L_bC_b+s^2\left(L_b+\frac{DL_bv_sK_p}{D'^2R_b}\right)+s\left(R_bD'^2-\frac{DL_bv_sK_i}{D'^2R_b}+v_sK_p\right)+(v_sK_i)} \tag{114}$$

Boost mode

$$\tilde{i}_o = -\frac{1}{R_bs^2LC+s\frac{L}{R}+D'^2}\left(sLi_l - D'v_o\right)\tilde{D} \tag{115}$$

$$\frac{1}{C_bR_b} - \frac{I_LK_p}{C_bR_b} = 2\zeta\omega_n + \alpha \tag{116}$$

$$\frac{D'^2}{C_bL_b} + \frac{V_cR_bD'}{C_bL_bR_b} - \frac{I_LK_i}{C_bR_b} = \omega_n^2 + 2\alpha\zeta\omega_n \tag{117}$$

$$\frac{D'v_oK_i}{C_bL_bR_b} = \alpha\omega_n^2 \tag{118}$$

For a settling criterion of 1.5

$$\omega_n = \frac{4.25}{\zeta t_r} \tag{119}$$

$$\alpha = \frac{D'V_o\left(I_LR_bD'^2 - 2\zeta\omega_nC_bR_bVD' + V_cD' - C_bI_LL_bR_b\omega_n^2\right)}{C_bR_b\left(D'^2V_o^2 + 2\zeta\omega_nD'I_LL_bV_c + I_L^2L_b^2\omega_n^2\right)} \tag{120}$$

$$K_i = \frac{C_bL_bR_b\alpha\omega_n^2}{D'V_c} \tag{121}$$

$$K_p = \frac{-C_bR_b\alpha + 2C_bR_b\omega_n\zeta}{I_L} \tag{122}$$

4.1.2 Wireless Power Transfer (WPT) system analysis

Applying the same analysis to the WPT circuit can be done between the inverter and rectifier. Following the same approach for state space modelling, only with more state variables gives the mathematical representation of the system.

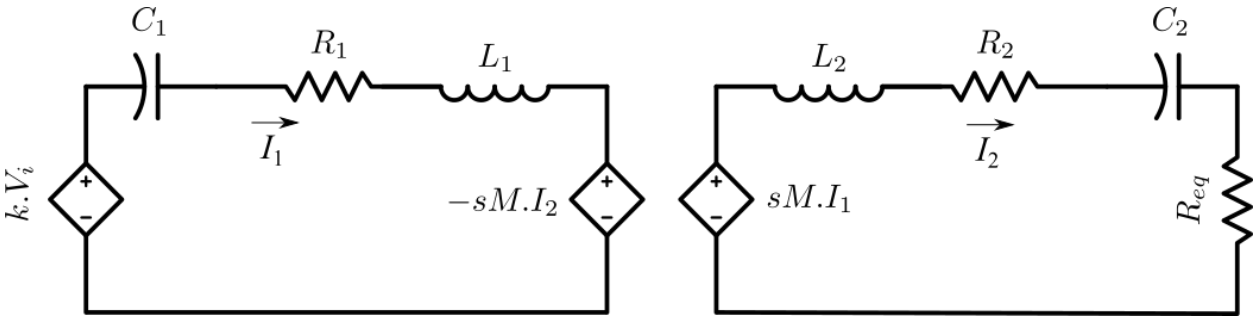

Figure 4.10: Equivalent WPT circuit between inverter and rectifier rectifier.

Where R_1&R_2 are the internal resistances of primary and secondary coil respectively. Using the induced EMF model for DWPT system modelling, it is appropriate to treat the mutual inductance M as a variable parameter, since it is directly affected by the relative position and alignment of the primary and secondary coils. However, in practical scenarios, changes in (M) are governed by the mechanical dynamics of the vehicle or moving platform carrying the secondary coil. These mechanical movements—such as lateral misalignment or coil height variation—occur at a much slower rate compared to the dynamics of the electrical subsystem. This is due to the significantly larger time constant of the mechanical system when compared to the electrical system. As a result, while M is variable in theory, it can often be considered quasi-static during short-term electrical analysis and control. A more detailed discussion of the time-scale separation between the mechanical and electrical subsystems, and its implications on the modelling of M, is provided in Section 3.4.

$$x = \begin{bmatrix} x_1 & x_2 & x_3 & x_4 & x_5 \end{bmatrix}^T \tag{123}$$

$$x = \begin{bmatrix} v_{C1} & i_1 & i_M & i_2 & v_{C2} \end{bmatrix}^T \tag{124}$$

$$\dot{x_1} = \frac{1}{C_1} x_2 \tag{125}$$

$$\dot{x_2} = \frac{1}{L_1 - M}(kV_i - x_1 - R_1 x_2 - M\dot{x_3}) \tag{126}$$

$$\dot{x_3} = \dot{x_2} - \dot{x_4} \tag{127}$$

$$\dot{x_4} = \frac{1}{L_2 - M}(M\dot{x_3} - (R_2 + R_e q)x_4 - x_5) \tag{128}$$

$$\dot{x_5} = \frac{1}{C_2} x_4 \tag{129}$$

Re-arranging equations to give:

$$\dot{x_2} = \frac{1}{(L_1 - M) + M}(kV_i - x_1 - R_1 x_2 + M\dot{x_4}) \tag{130}$$

$$\dot{x_4} = \frac{1}{(L_2 - M) + M}(M\dot{x_2} - (R_2 + R_{eq})x_4 - x_5) \tag{131}$$

hence,

$$\dot{x_2} = \frac{1}{L_1 - \frac{M^2}{L_2}}(kV_i - x_1 - R_1 x_2 - \frac{M(R_2 + R_{eq})}{L_2}x_4 - \frac{M}{L_2}x_5) \tag{132}$$

$$\dot{x_4} = \frac{1}{L_2 - \frac{M^2}{L_1}}(\frac{MkV_i}{L_1} - \frac{M}{L_1}x_1 - \frac{MR_1}{L_1}x_2 - (R_2 + R_{eq})x_4 - x_5) \tag{133}$$

As $x_3 = x_2 - x_4$, it is a redundant state and can be removed to give:

$$x = \begin{bmatrix} x_1 & x_2 & x_3 & x_4 \end{bmatrix}^T \tag{134}$$

$$x = \begin{bmatrix} v_{C1} & i_1 & i_2 & v_{C2} \end{bmatrix}^T \tag{135}$$

Which gives the following state space equation:

$$A_T = \begin{bmatrix} 0 & \frac{1}{C1} & 0 & 0 \\ \frac{-1}{L_1 - \frac{M^2}{L_2}} & \frac{-R_1}{L_1 - \frac{M^2}{L_2}} & \frac{-M(R2+R_{\text{eq}})}{L_2(L_1 - \frac{M^2}{L_2})} & -\frac{M}{L_2(L_1 - \frac{M^2}{L_2})} \\ -\frac{M}{L_1(L_2 - \frac{M^2}{L_1})} & -\frac{MR_1}{L_1(L_2 - \frac{M^2}{L_1})} & \frac{-(R2+R_{\text{eq}})}{L_2 - \frac{M^2}{L_1}} & -\frac{1}{L_2 - \frac{M^2}{L_1}} \\ 0 & 0 & \frac{1}{C_2} & 0 \end{bmatrix}$$

$$B_T = \begin{bmatrix} 0 \\ \frac{1}{L1 - \frac{M^2}{L2}} \\ \frac{M}{L1(L2 - \frac{M^2}{L1})} \\ 0 \end{bmatrix} \quad C_T = \begin{bmatrix} 1 & 0 & 0 & 0 \\ 0 & 1 & 0 & 0 \\ 0 & 0 & 1 & 0 \\ 0 & 0 & 0 & 1 \end{bmatrix} \quad D_T = \begin{bmatrix} 0 \\ 0 \\ 0 \\ 0 \end{bmatrix}$$

4.1.3 Decoupled Dual-Sided Control

Following the implementation of the DC/DC converter and WPT system, the primary-side DC converter control is revisited to improve efficiency and modularity. Traditional methods often rely on detailed circuit analysis to determine the optimal operating point, requiring full knowledge of system parameters and sometimes communication between the primary and secondary sides. However, this dependency on real-time communication adds system complexity and cost.

In the proposed system, the secondary-side circuit regulates the rectified output voltage, and the output power is assumed to remain approximately constant due to load regulation. Under this condition, applying current-based constraints—such as those derived from Equation 29, which directly relates primary and secondary WPT coil currents—would over constrain the system. The analysis shows that output power consumption is reflected in

the secondary coil current. Since the primary and secondary currents are directly proportional, imposing control on the primary coil current introduces redundancy and unnecessarily constrains the system.

Instead, using Equation 28, which relates the input supply voltage to power transfer, allows the system to adapt current flow dynamically while maintaining power balance. This enables the use of voltage-based control on the primary side without requiring feedback from the secondary side.

Since the inverter is left uncontrolled, the reflected power from the secondary coil appears as a change in the current drawn from the primary-side DC bus. If the primary DC voltage V_C is set higher than necessary, the resulting excess power—due to a mismatch between inverter demand and converter supply—is dissipated as losses in the primary circuit. Conversely, if V_C is too low, the WPT system under delivers power, leading to voltage collapse at the output.

This behaviour creates a control opportunity: the difference between the primary converter output current I_d and the inverter input current I_{inv} becomes an indicator of system efficiency and power matching. A mismatch suggests over- or under-supply of energy. This is exploited in the control structure shown in Figure 4.11, where a multi-loop control architecture is employed:

- An inner current loop regulates the inductor current for fast dynamic response.
- An outer voltage loop tracks the DC bus voltage V_C using a PI controller.
- A power balancing loop compares the measured current ratio $|I_d|/|I_{\text{inv}}|$ to adjust the voltage reference V_{ref}, optimizing efficiency without needing communication from the secondary side.

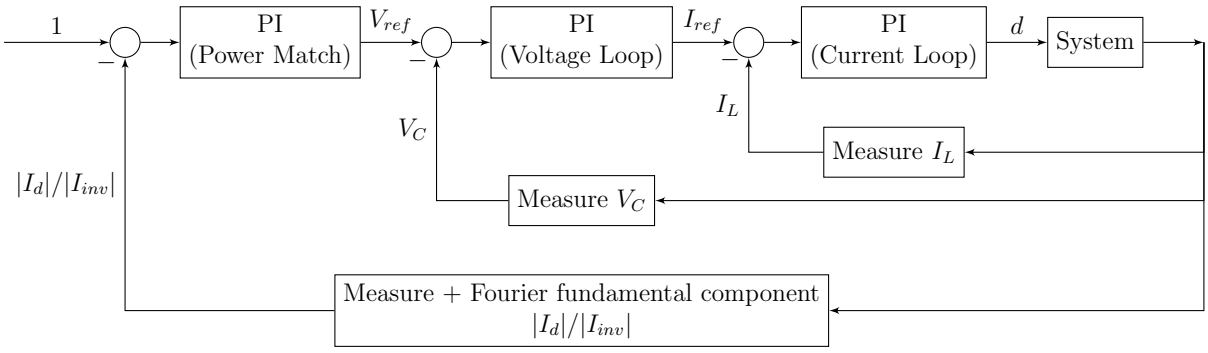

Figure 4.11: Primary DC/DC converter control loop

4.2 Results & Discussion

For the circuit depicted in Figure 4.2, the input power, output power, primary-side voltage (V_C), rectifier voltage (V_{rec}), and output current (I_o) are illustrated in Figure 4.12. This section presents a comparative evaluation of the proposed control strategy against a conventional step-based adjustment of the primary DC bus voltage (V_C). The goal is to validate the

controller's ability to regulate power flow, minimize input power consumption, and ensure stable output—all without requiring communication between the primary and secondary sides.

Figure 4.12c shows the response of the primary DC bus voltage. The step change method reflects a conventional control approach, where V_C is adjusted based on pre-calculated set points. In contrast, the proposed control scheme autonomously identifies the optimal operating point using only primary-side measurements. This data-driven approach demonstrates improved adaptability and responsiveness under varying load conditions.

The rectifier voltage (V_{rec}), presented in Figure 4.12d, remains exceptionally stable across both control schemes. The minimal ripple—less than 0.1%—underscores the robustness of the proposed controller, which maintains voltage stability despite the absence of secondary-side feedback. This affirms the system's ability to maintain functionality without communication while altering primary side operation.

Figure 4.12e illustrates the output current (I_{out}), which is regulated at 10 A in both scenarios, with minimal variation due to system changes. The observed ripple is primarily attributed to the design of the secondary-side DC/DC converter

The output power (P_{out}), shown in Figure 4.12b, remains virtually constant throughout the simulation for both methods, confirming that load demands are fully met. However, the input power behaviour—shown in Figure 4.12a—reveals a marked difference. The step-change method achieves a faster and more aggressive transition to a predefined reference voltage, while the proposed controller adapts to a more efficient operating point. This demonstrates the proposed control's capability to adapt to system fluctuations and parameter uncertainties, achieving efficient operation under real-world conditions.

The performance improvements are quantified in Table 4.2, which compares steady-state input power and system efficiency. The proposed controller achieves a higher efficiency of 93.5%, compared to 92.7% for the conventional method, while delivering the same output power. This clearly demonstrates the controller's capability to dynamically optimize the system's operating point, enhancing overall energy efficiency without any communication between the primary and secondary subsystems.

Table 4.2: Comparison of input power and efficiency for static control once in steady state.

Control mode	**Steady-state efficiency (η)**	**Input power (kW)**
V_C Step change	0.927	4.65
Proposed control	0.935	4.61

Figure 4.13 illustrates the performance of the proposed control strategy in a dynamic scenario, where the coils transition from a misaligned to an aligned state—as reflected in the increasing coupling factor. As the coupling improves, the system's power transfer capability increases accordingly, resulting in a noticeable reduction in input power consumption.

Compared to the static charging case, system fluctuations are more pronounced due to the varying magnetic coupling. Nevertheless, the proposed control effectively mitigates these

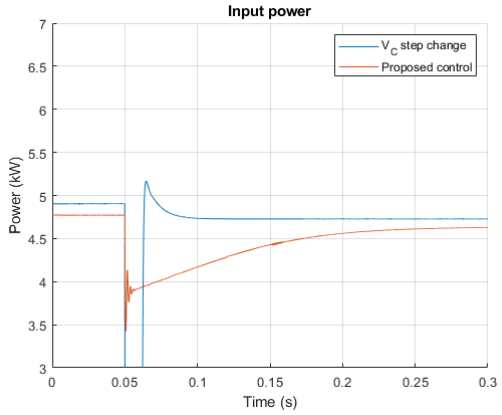

(a) Input power (P_{in}).

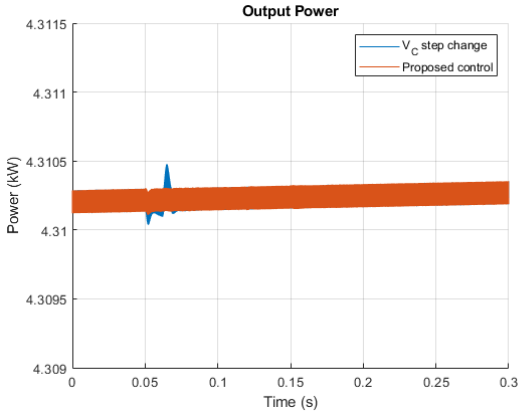

(b) Output power (P_{out}).

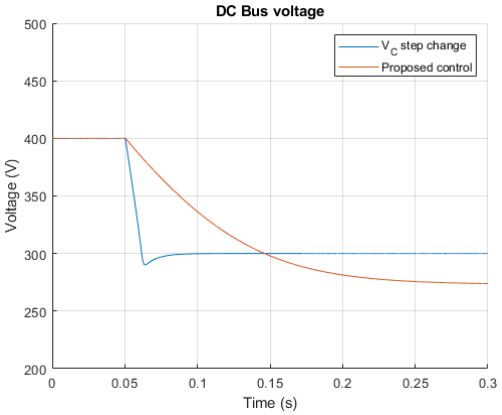

(c) Primary DC bus voltage (V_C).

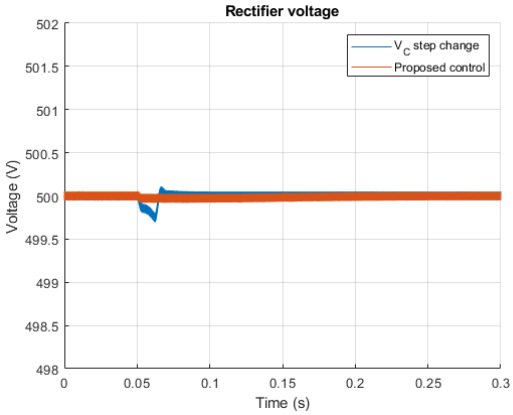

(d) Rectifier voltage (V_{Rec}).

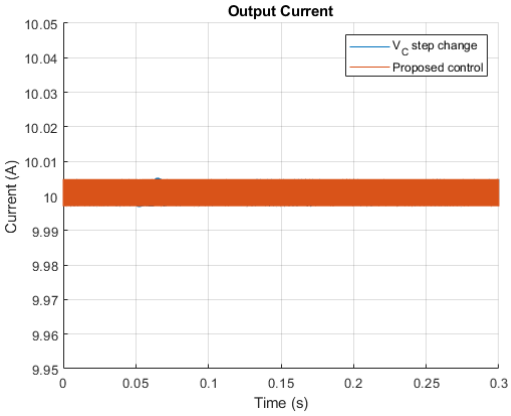

(e) Output current (I_{out}).

Figure 4.12: Comparison of proposed control strategy with V_C step change across key power system metrics.

disturbances. The rectifier voltage experiences only a modest deviation of approximately 0.5%, which is further attenuated by the secondary-side DC/DC converter, maintaining stable output voltage and current characteristics.

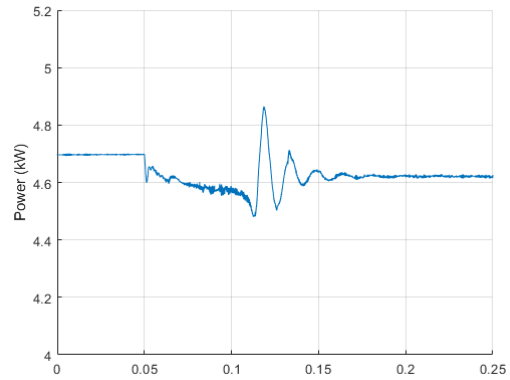

(a) Input power (P_{in})

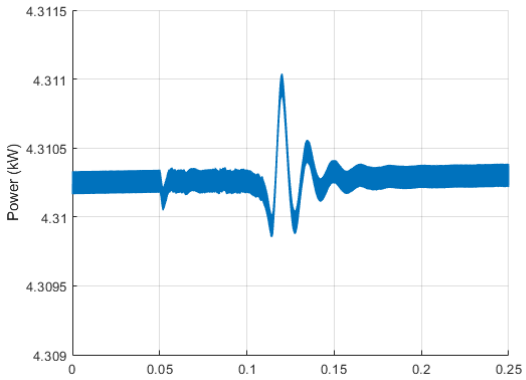

(b) Output power (P_{out})

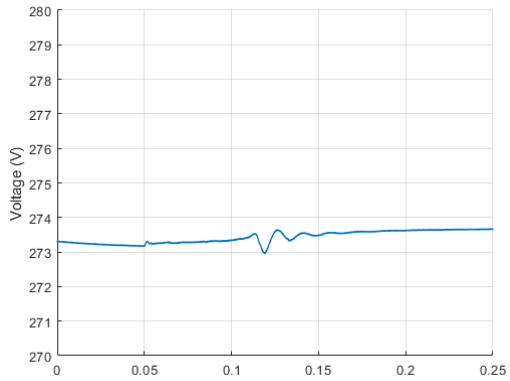

(c) Primary DC voltage (V_C)

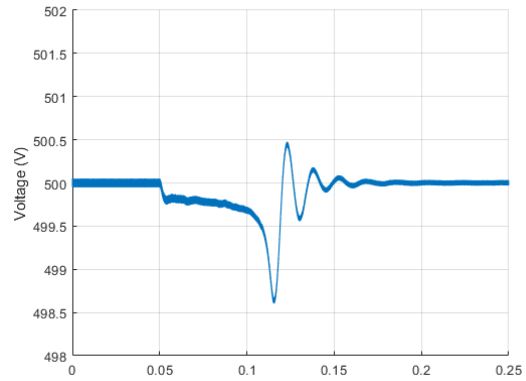

(d) Rectifier voltage (V_{Rec})

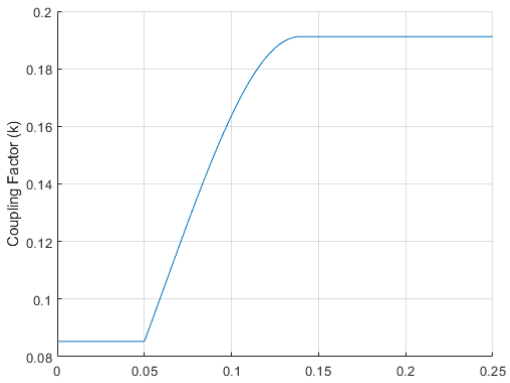

(e) Coupling factor (k)

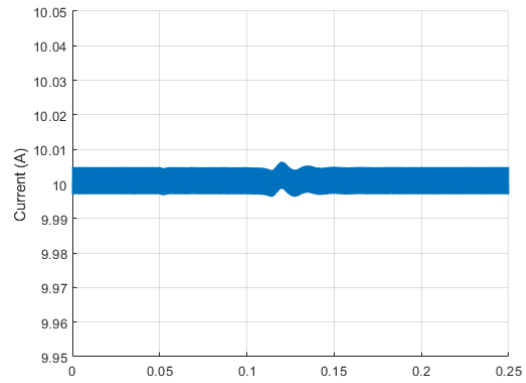

(f) Output current (I_{out})

Figure 4.13: Dynamic performance of the proposed control strategy under variable coupling conditions.

4.3 Chapter Summary

This work builds upon prior research that emphasizes the need for communication in dual-sided control of wireless power transfer systems [122]. In contrast, the proposed methodology

demonstrates that effective control of the secondary side—responsible for regulating output charging characteristics—can indirectly influence the primary side. As secondary-side load conditions change, the resulting variations in power consumption are reflected back to the primary, enabling the primary-side controller to adapt its operating point and reduce input power consumption—all without requiring direct communication between the two sides.

The implemented control strategy effectively suppresses system fluctuations and maintains stable output voltage and current—critical factors for battery health and long-term reliability. By eliminating the need for cross-side communication, the system architecture is significantly simplified, allowing for modular design and independent control tuning of each subsystem. This results in a practical, scalable, and implementation-friendly solution compared to more complex strategies reported in the literature.

Using the proposed control strategy, effective system control is achieved without introducing additional communication components which can incur connection issues due to the generate EMF for inductive charging. The modular design of the system allows for independent control for each sub-system, allowing the use of existing control and design strategies for each sub-system making it a more practical approach for system design and development in industrial applications.

The dynamic simulation scenario illustrates the controller's robustness under varying coupling conditions, where the mutual inductance changes to mimic coil misalignment and realignment. While the proposed control effectively manages these variations, certain limitations in the simulation setup must be acknowledged. Specifically, the step change in coupling occurs over a brief 10 ms window, during which the primary side remains continuously powered. In practical applications, it is more desirable to reduce or suspend power delivery during periods of low coupling to avoid unnecessary magnetic field generation and minimize energy loss. Once the system is powered up for active power transfer, the proposed controller can be utilized to regulate operation and achieve efficient, stable performance.

Moreover, if the objective is to maximize power transfer during short alignment intervals, dynamically adjusting the rectifier's reference voltage or output current could enhance energy throughput. This would allow the system to make more effective use of brief periods of optimal coupling, particularly in DWPT applications.

Another promising direction involves leveraging the primary-side DC/DC converter for grid-aware power management. By regulating input power to maintain a stable load profile at the grid interface, the system can contribute to grid stability while still fulfilling the desired constant-current/constant-voltage (CC/CV) charging profile for electric vehicles. Since the proposed control strategy has shown resilience in attenuating disturbances before they reach the output, it could also be extended to accommodate variability caused by DWPT transitions or fluctuating grid conditions.

5 Equivalent models and simulation time reduction for DWPT

DWPT systems exhibit significant modelling complexity, stemming from high-frequency switching, and the presence of numerous interacting electrical states. These detailed models are indispensable for accurate system-level analysis but pose considerable challenges for the development of control strategies due to their high computational burden.

With typical switching frequencies of 85 kHz, simulating the dynamic behaviour of WPT systems over extended durations becomes computationally intensive. However, for control design purposes, such high resolution is often unnecessary. In most cases, the principal concern lies in regulating the power transferred between the primary and secondary coils, rather than capturing every transient associated with switching events. As a result, full-resolution simulations are frequently inefficient and not well-suited to control-oriented modelling and design.

The high computational cost associated with full-resolution DWPT simulations presents a major barrier for several classes of applications. For instance, [177] highlights that the long simulation time of DWPT systems limits the feasibility of optimization approaches such as particle swarm optimization (PSO), particularly in dynamic or real-time scenarios. Similarly, [178] notes that while FEA-based modelling enables accurate design optimization, its use in multi-objective frameworks remains computationally intensive and requires considerable pre-processing and parameter tuning. At the system level, [179] discusses the challenges of incorporating full-scale DWPT models into grid interaction studies and traffic-dependent load forecasting, emphasizing that tools like PLECS and ANSYS are prohibitively slow for large-scale simulations. As an alternative, they propose generating time-dependent load profiles as a computationally efficient proxy for detailed electromagnetic modelling.

In light of these challenges, this work introduces a reduced-frequency average model of the DWPT system. By abstracting switching dynamics and focusing on average power flow, this model enables significantly faster simulation while preserving the system's dominant behaviour. This allows for efficient evaluation and design of control strategies without compromising key dynamic characteristics.

5.1 Methodology

5.1.1 Full circuit

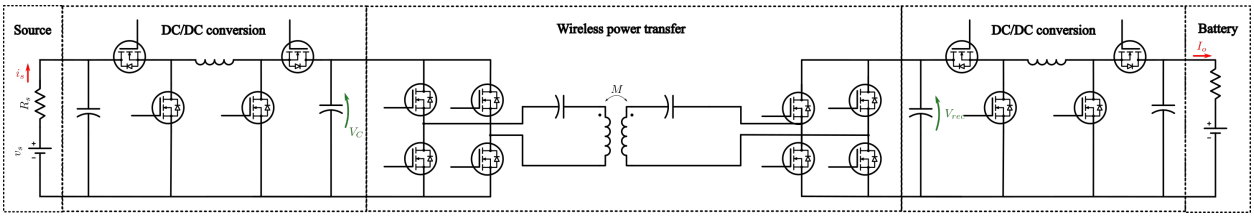

Figure 5.1: Full system schematic

The basic system required for WPT for EV charging the minimum circuit required consists of an inverter, rectifier and inductive coils and compensation capacitors. Adding primary and secondary DC/DC converters helps improve efficiency and control of the system by decouple both the source and load from fluctuations in the wireless power transfer system.

The base circuit used for comparison in this research is shown in Figure 5.1. The sub-circuit function aims to control either the voltage or current at intersection or connection points between subsystems. Primary side DC/DC converter controls the DC bus voltage which is supplied to the inverter; The inverter controls switching frequency for WPT, based on system parameters results in a secondary coil current; controlled rectifier using secondary coil current maintains a reference DC voltage; secondary DC converter can be set to constant current or voltage based on load requirements (for EVs this is based on SOC).

Note: The circuit is designed to be symmetrical around the inductive coils, hence can be configured to run in reverse mode for V2G applications

5.1.2 DC/DC converter

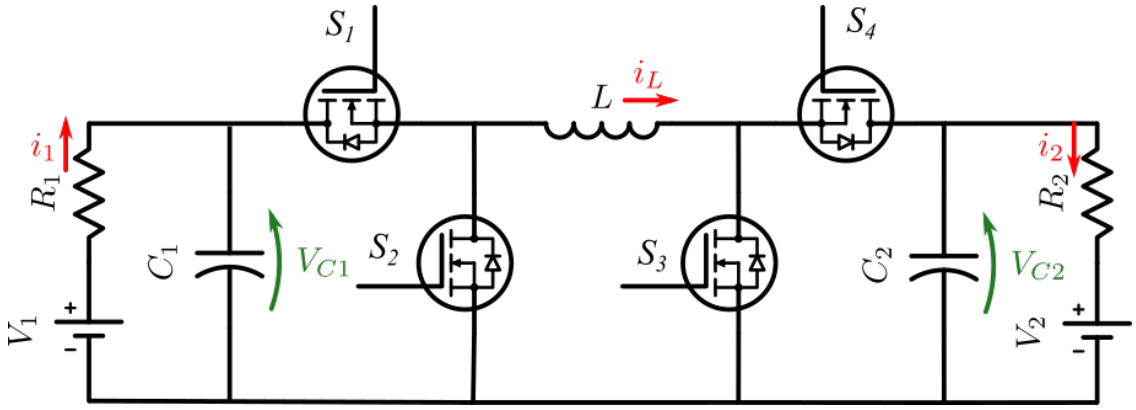

Figure 5.2: Configurable bidirectional DC/DC converter

For both primary and secondary side of the circuit in Figure 5.1, a configurable bidirectional DC/DC converter is used. Based on the used of switches S1-S4, the converter can set to Buck, Buck-Boost or Boost mode in either forward or reverse direction, the possible configurations are shown in Table 5.1, where a PWM signal is used to track a reference signal using a PI controller.

Table 5.1: DC/DC converter configurations. Tables should be placed in the main text near to the first time they are cited.

Mode	S1	S2	S3	S4
Buck	PWM	0	0	0
Buck-Boost	PWM	0	PWM	0
Boost	1	0	PWM	0
Reverse Buck	0	0	0	PWM
Reverse Buck-Boost	0	PWM	0	PWM
Reverse Boost	0	PWM	0	1

5.1.3 Inverter

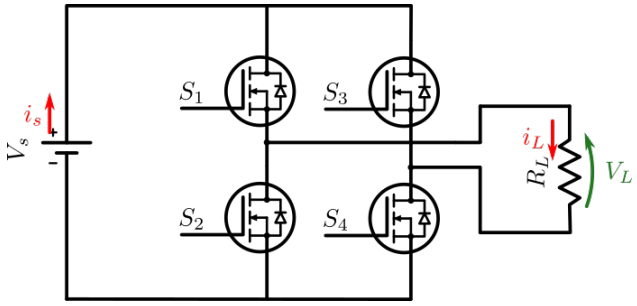

Figure 5.3: Inverter diagram

A fixed duty cycle inverter is used to drive the WPT circuit at resonant frequency. Figure 5.3 shows a basic implementation where a constant voltage sources and restive load are shown for circuit simplicity, these are later replaced with the circuits shown ins Figure 5.1.

5.1.4 Dynamic wireless power transfer

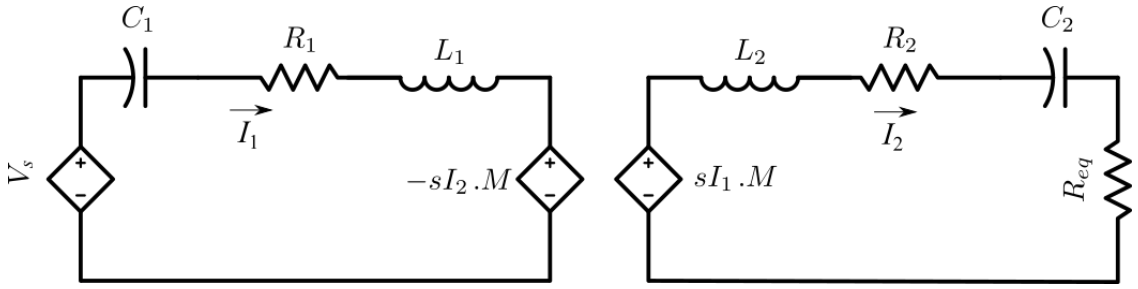

Figure 5.4: WPT model

The DWPT model, relates the two inductive coils using the induced voltage which is a function of mutual inductance. Same as other mutual inductance systems such as fixed core transformers use the same approach. The mutual inductance is a parameter which describes

the link between both primary and secondary sides, the coupling factor is a unit-less constant which describes the same relationship (coupling factor $k = M/\sqrt{L_1 L_2}$).

The remainder of the circuit (Figure 5.4) uses series-series connected compensation for resonant operation and an equivalent load resistance is used for the diagram. The DWPT model only requires measuring i_1 and i_2 to generate the induced voltages (shown as sMi_1 and $-sMi_2$). Hence the source and load can be connected to the full circuit without changing the DWPT.

Finally, dynamic modelling is achieved by varying the mutual inductance variable. As the mutual inductance is a function of displacement between the two coils, hence changing the mutual inductance will model the dynamic changes in the system. Previous research discusses this in more detail [174] including the model used for mutual inductance [157].

5.1.5 Semi-active rectifier

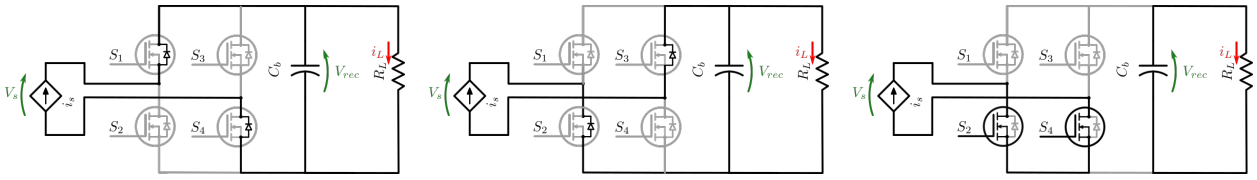

(a) Positive cycle (b) Negative cycle (c) Off state

Figure 5.5: Conduction paths for semi-active rectifier operation during operation.

Figure 5.5 illustrates the conduction paths for the semi-active rectifier under different switching states. In this configuration, only switches S2 and S4 are used to control power flow. When $S_2 = S_4 = 0$, the circuit functions as a passive rectifier, allowing maximum power transfer, as shown in Figures 5.5a and 5.5b. Conversely, when $S_2 = S_4 = 1$ (Figure 5.5c), the switches create a return path for the source current, effectively blocking power flow to the load.

The use of a semi-active rectifier circuit is recommended in scenarios where a secondary DC voltage source can otherwise continue rising to unsafe levels. This situation arises when the WPT system delivers more power than the load consumes, which is common in systems designed to maintain constant output characteristics. Rising voltage causes increase in voltage/current ripple and can compromise system safety. Semi-controlled rectifiers have been shown to manage power flow effectively, particularly by blocking conduction paths during critical intervals using controlled switches [180, 181]. However, relying on regulation solely from the primary side introduces a delay in response due to the decoupled nature of the primary and secondary converters via the WPT link. Although additional control strategies can be introduced—typically on the primary side—these are limited by the challenge of implementing reliable communication between the primary and secondary circuits [182]. Furthermore, passive components such as output filters are often necessary to mitigate ripple and stabilize voltage, especially under varying load conditions [183].

5.1.6 System control

The circuit used in Figure 5.1, is designed to have each sub system control variables within it's circuit using a PI controller for duty cycle which is then used to generate a PWM signal supplied to the switches as described in each sub-circuit section above. Hence, the primary DC/DC converter controls primary DC bus voltage; the inverter is fixed duty cycle (hence uncontrolled); rectifier control secondary DC bus voltage; secondary DC/DC converter controls load charging characteristics (constant current used in this paper).

5.1.7 Connection of subsystems and additional requirements

The interconnection of subsystems can be a challenge, as ideally these systems would connect directly to each other (similar to the switching circuit). However this is not always possible as each system is designed with ideal sources and loads, hence a solution can be achieved. Once multiple systems are chained together, the MATLAB Simulink solver has issues defining circuit parameters and views the system as a logic loop.

Primary DC/DC Converter The main function of this circuit is to convert the primary coil current from the WPT system to an equivalent DC current at the output of the DC/DC converter (acting as a load). The relationship between the magnitude of the primary coil peak current (I_p) and the RMS value is given by $I_{p_{\mathrm{RMS}}} = I_p/\sqrt{2}$.

To relate the load power consumption to the input power of the WPT circuit and account for inverter losses, we summarize the losses using the converter efficiency η_{inv}, where $P_{\mathrm{out}} = \eta P_{\mathrm{in}}$. As the inverter generates a square wave and that its RMS voltage equals the DC input voltage ($V_{DC1} = V_p$), the power relationship becomes:

$$P_{\mathrm{WPT1}} = \eta_{inv} P_{\mathrm{DC1}} \tag{136}$$

$$I_{p_{\mathrm{RMS}}} V_p = \eta_{inv} I_{2_{\mathrm{DC1}}} V_{DC1} \tag{137}$$

Substituting $V_{DC1} = V_p$, we obtain the current relationship:

$$I_{p_{\mathrm{RMS}}} = \eta_{inv} I_{2_{\mathrm{DC1}}} \tag{138}$$

$$I_{2_{\mathrm{DC1}}} = \frac{I_p}{\eta_{inv}\sqrt{2}} \tag{139}$$

Wireless power transfer First, the implementation for WPT assumes a sinusoidal input voltage, as the voltage applied in this study is a square wave the approximate value for input voltage is given by:

$$V_{in_{WPT}} \approx 1.27 V_{2_{DC1}} \tag{140}$$

The calculation of mutual inductance between he coils is given in Appendix 8.1 and the implementation of the implementation of the WPT system is given in Appendix 8.2.2. While

the equations are preserved, note the scale factor (sf) applied in the code to scale up the state space implementation response time.

Approximating the load resistance (secondary DC/DC converter) is achieved by approximating the converter's power consumption where:

$$P_o = \eta_{DC} P_{DC} \tag{141}$$
$$V_o I_o = \eta_{DC} V_{rec}^2 / R_{DC} \tag{142}$$
$$R_{DC} = \frac{\eta_{DC} V_{rec}^2}{V_o I_o} \tag{143}$$

$$P_{DC} = \eta_{rec} P_{WPT} \tag{144}$$
$$\frac{V_{rec}^2}{R_{DC}} = \eta_{rec} \frac{V_{sRMS}^2}{R_{eq}} \tag{145}$$
$$R_{eq} = \eta_{rec} \frac{V_{sRMS}^2}{V_{rec}^2} R_{DC} \tag{146}$$

$$R_L = \begin{cases} 4e3, & \text{if } k < 0 \\ R_{eq}, & \text{otherwise} \end{cases} \tag{147}$$

Where k is the coupling factor between the two coils.

Finally approximating rectifier voltage (V_{rec}) is done as a function of both the secondary coil current (I_s) converter equivalent resistance (R_{DCDC2}) such that:

$$C_{rec} \frac{dV_{rec}}{dt} = \sqrt{2} d_{rec} I_s - \frac{V_{rec}}{R_{DCDC2}} \tag{148}$$

Secondary DC/DC converter Once the considerations above are implemented, the circuit can be used the same as shown in analysis by applying rectifier voltage (V_{rec}).

5.2 Circuit equations and equivalent circuits

5.2.1 DC/DC converter

Fig 5.2 shows the bidirectional DC/DC converter. To achieve forward operation mode, $S_2 = S_4 = 0$ leaving S1 as the buck control switch and S3 the boost control switch, allowing the use of buck mode ($S_1 = PWM, S_3 = 0$), boost mode($S_1 = 1, S_3 = PWM$), or buck-boost mode ($S_1 = S_3 = PWM$). The same is possible for reverse operation mode where $S_1 = S_3 = 0$, buck mode ($S_4 = PWM, S_2 = 0$), boost mode($S_4 = 1, S_2 = PWM$), or buck-boost mode ($S_2 = S_4 = PWM$). Carrying out the circuit analysis gives the following:

Buck Mode

$$\frac{dv_{c1}}{dt} = \frac{i_1}{C_1} - d\frac{i_L}{C_1} \tag{149}$$
$$\frac{di_L}{dt} = d\frac{v_{c1}}{L} - \frac{v_{c2}}{L} \tag{150}$$
$$\frac{dv_{c2}}{dt} = \frac{i_L}{C_2} - \frac{i_2}{C_2} \tag{151}$$

Buck-boost Mode

$$\frac{dv_{c1}}{dt} = \frac{i_1}{C_1} - d\frac{i_L}{C_1} \tag{152}$$
$$\frac{di_L}{dt} = d\frac{v_{c1}}{L} - (1-d)\frac{v_{c2}}{L} \tag{153}$$
$$\frac{dv_{c2}}{dt} = (1-d)\frac{i_L}{C_2} - \frac{i_2}{C_2} \tag{154}$$

Boost Mode - Reverse

$$\frac{dv_{c1}}{dt} = \frac{i_1}{C_1} - \frac{i_L}{C_1} \tag{155}$$
$$\frac{di_L}{dt} = \frac{v_{c1}}{L} - (1-d)\frac{v_{c2}}{L} \tag{156}$$
$$\frac{dv_{c2}}{dt} = (1-d)\frac{i_L}{C_2} - \frac{i_2}{C_2} \tag{157}$$

Buck Mode - Reverse

$$\frac{dv_{c1}}{dt} = \frac{i_1}{C_1} - \frac{i_L}{C_1} \tag{158}$$
$$\frac{di_L}{dt} = \frac{v_{c1}}{L} - d\frac{v_{c2}}{L} \tag{159}$$
$$\frac{dv_{c2}}{dt} = d\frac{i_L}{C_2} - \frac{i_2}{C_2} \tag{160}$$

Buck-boost Mode - Reverse

$$\frac{dv_{c1}}{dt} = \frac{i_1}{C_1} - (1-d)\frac{i_L}{C_1} \tag{161}$$
$$\frac{di_L}{dt} = (1-d)\frac{v_{c1}}{L} - d\frac{v_{c2}}{L} \tag{162}$$
$$\frac{dv_{c2}}{dt} = d\frac{i_L}{C_2} - \frac{i_2}{C_2} \tag{163}$$

Boost Mode - Reverse

$$\frac{dv_{c1}}{dt} = \frac{i_1}{C_1} - (1-d)\frac{i_L}{C_1} \tag{164}$$

$$\frac{di_L}{dt} = (1-d)\frac{v_{c1}}{L} - \frac{v_{c2}}{L} \tag{165}$$

$$\frac{dv_{c2}}{dt} = \frac{i_L}{C_2} - \frac{i_2}{C_2} \tag{166}$$

The equivalent model of the DC/DC converter can be seen in Fig. 5.6 and it's Simulink implementation in Fig. 5.7

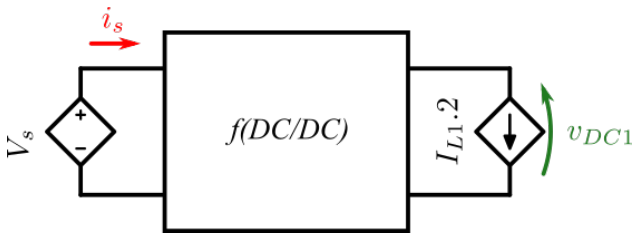

Figure 5.6: DCDC equivalent circuit

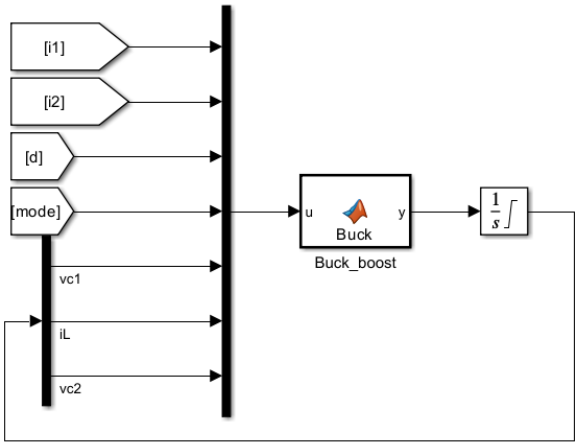

Figure 5.7: DC/CD converter Simulink implementation

5.2.2 Inverter

For the purpose of this research, a fixed duty cycle is used to generate a square wave with amplitude $\pm V_{DC}$. The supply voltage/current can hence be related to it's load voltage/current given by:

$$V_{source} = |V_{load} - 2R_{fet} * I_{load}| \tag{167}$$

$$I_{source} = |I_{Load}| \tag{168}$$

A more accurate representation takes into account MOSFET, practically this is <1% difference for analysis. Later this is connected to the WPT estimation which considers sinusoidal input instead of square hence:

$$V_{square} = \sqrt{2}V_{sine} \tag{169}$$

5.2.3 Dynamic wireless power transfer

To replace the WPT circuit, a power estimate from the secondary DC bus is used to estimate load resistance ($R_L = V_{rec}^2/P_{DC_2}$), to incorporate the rectifier an equivalent resistance is used to account for the rectified power consumption ($R_{eq} = 8R_L/\pi^2$). Like wise for inverter voltage, a sinusoidal input is assumed in AC analysis ($V_{in} = V_{DC}sin(f)$, where f is the operating frequency). The remaining variables represent compensation capacitors C1 and C2, coil inductance L1 and L2 and their resistance R1 and R2, the remaining parameter for mutual inductance links the primary and secondary sides. Note the mutual inductance is calculated from dimensionless parameter of coupling factor (k) where $k = M\sqrt{L_1L_2}$. With all of the above parameters, a steady state value can be estimated for both the input and output current using the impedance at operating frequency f for all passive components.

$$Z_1 = R_1 + j\omega L_1 + 1/j\omega C_1 \tag{170}$$
$$Z_2 = R_2 + j\omega L_2 + 1/j\omega C_2 + R_{eq} \tag{171}$$

Voltage analysis of both sides gives:

$$V_s = i_1 Z_1 + jw\omega M i_2 \tag{172}$$
$$j\omega M i_1 = Z_2 i_2 \tag{173}$$

Hence the input and output current can be obtained :

$$i_1 = V_s/(Z_1 - \omega^2 M^2/Z_2) \tag{174}$$
$$i_2 = j\omega M/Z_2 i_1 \tag{175}$$

For dynamic charging, the steady state values will need to change as system parameters (such as coupling factor changes), hence we are more interested in the peak values of voltage and current. To achieve this we can use the total impedance of the system for the following differential equations:

$$\frac{d(i_1)}{dt} = \frac{Vin - i_1 \Re Z_1 - wMi_2}{\Im Z_1} \tag{176}$$
$$\frac{d(i_2)}{dt} = \frac{wMi_1 - i_2 \Re Z_2}{\Im Z_2} \tag{177}$$

Hence we can relate primary and secondary DC buses, based on input voltage and output equivalent resistance. The full circuit features a dual active bridge, where the primary and secondary currents values can be converted to the equivalent DC currents before the inverter and after rectification for i1 and i2 respectively.

Hence the WPT equivalent circuit implementation is shown in Fig 5.8 and Fig. 5.9 MATLAB Simulink implementation code used to implement the aforementioned equations shown in annex 8.2.1 and annex 8.2.2.

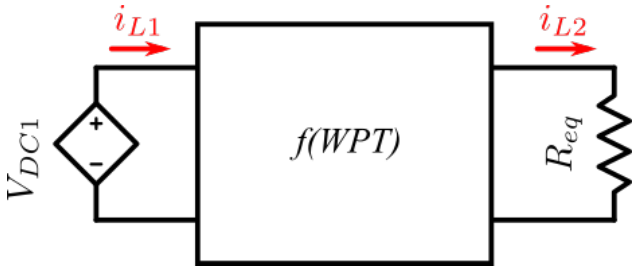

Figure 5.8: WPT equivalent circuit

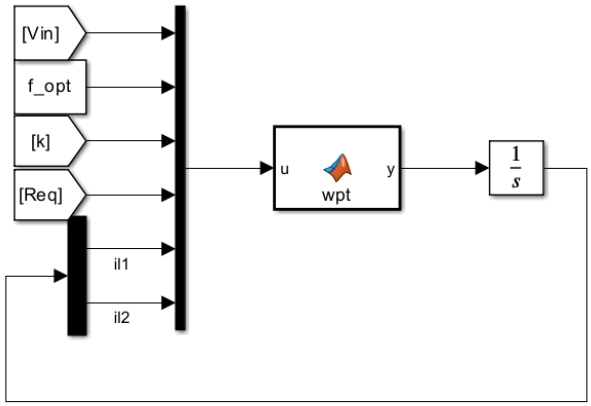

Figure 5.9: WPT Simulink implementation

5.2.4 Semi-controlled rectifier

A semi controlled rectifier is used to control rectifier voltage, switching off the input current from the WPT coil. For this function the two MOSFET's are controlled on to disconnect the power flow to the secondary DC converter.

Analysing the switching behaviour of the controlled rectifier, the voltage before the rectifier is a function of the secondary coil current, rectified voltage and rectifier diode/MOSFET on resistance such that:

$$d = 0 : V_s = V_{rec} * sign(I_s) + 2R_{fet}I_s \tag{178}$$
$$d = 1 : V_s = 2R_{fet}I_s \tag{179}$$

The current relationship is given by:

$$d = 0 : I_s = I_c + I_L \tag{180}$$
$$d = 1 : 0 = I_c + I_L \tag{181}$$

Note, d denotes the duty cycle of the switching signal for the semi-controlled rectifier. The approximation used for the proposed system is given by:

$$dI_s = I_c + I_L \tag{182}$$
$$V_s = I_L^2 R_L / I_S \tag{183}$$

5.3 Results & discussion

5.3.1 DC/DC converter

While the operation of DC/DC converters is well established, the key focus here is the system's bidirectional capability. To illustrate this functionality, a transition from forward to reverse buck-boost mode is presented, demonstrating the system's ability to switch power flow direction effectively.

The results presented in Fig. 5.10 show a comparison between the proposed model and switching model, where an accurate representation is achieved.

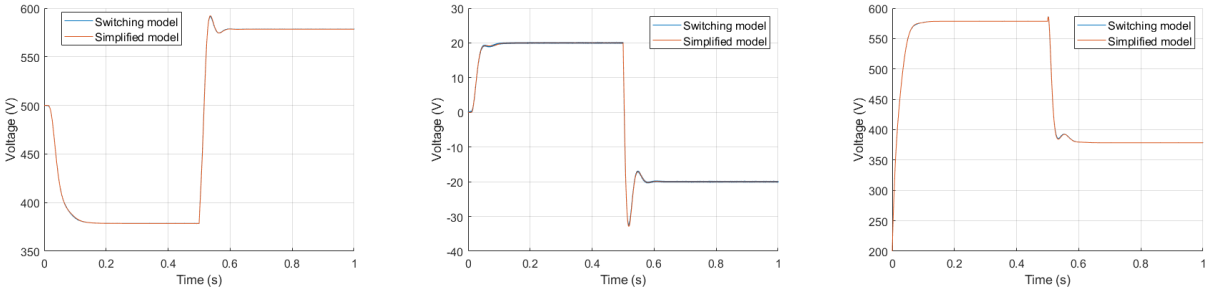

(a) Voltage (Vc1) comparison (b) Inductor current (IL) comparison (c) Voltage (Vc2) comparison

Figure 5.10: Bidirectional DC/DC converter switching from forward to reverse buck-boost mode at t=0.5s.

5.3.2 Wireless power transfer

Validation of the proposed WPT equivalent circuit is shown in Fig. 5.11. First the system operation is shown at steady state with a step change in coupling factor, then the direction of power flow is reversed and the step change is reverted to show the system operating in reverse mode. Notably, the proposed system gives the peak value of primary and secondary currents, which normally remain less than zero, here however the magnitude is given as negative, to indicated direction of power flow.

5.3.3 Dynamic wireless power transfer

Applying the WPT model to a dynamic scenario, Figure 5.12 shows the comparison of primary and secondary coil currents as a function of coupling factor where direction of power flow is switched at 50ms. The proposed system successfully estimates the magnitude of coil current which can than be used to connect to different sub systems (inverter and rectifier) for further analysis.

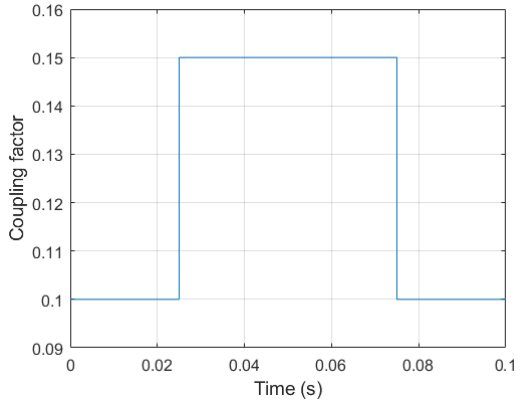

(a) Coupling Factor (k)

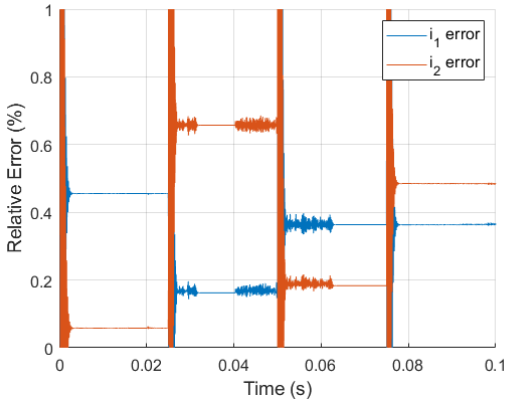

(b) Relative Error (%)

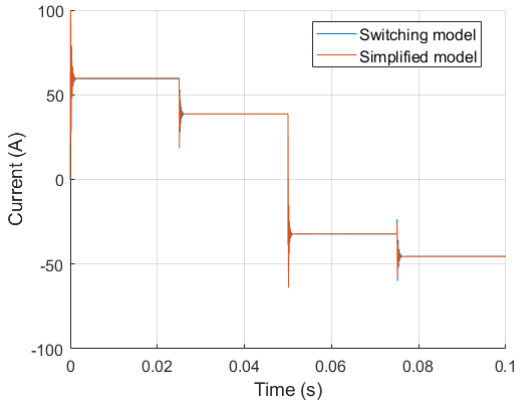

(c) Primary Current (i_1)

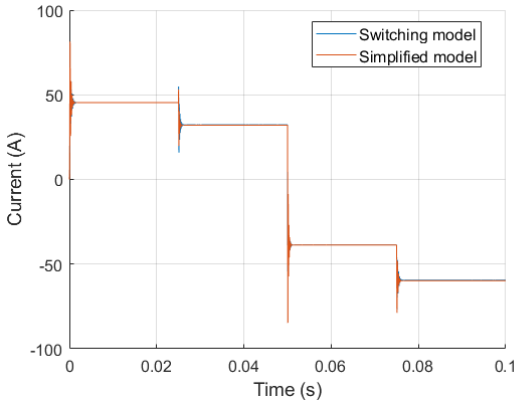

(d) Secondary Current (i_2)

Figure 5.11: Comparisons of primary and secondary currents for bidirectional WPT, switching direction at 50ms.

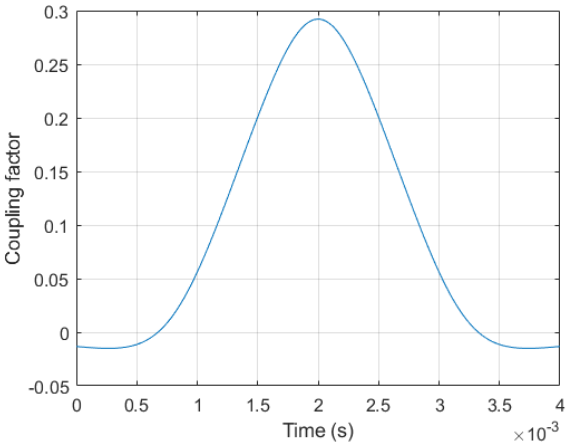

(a) Coupling factor (k)

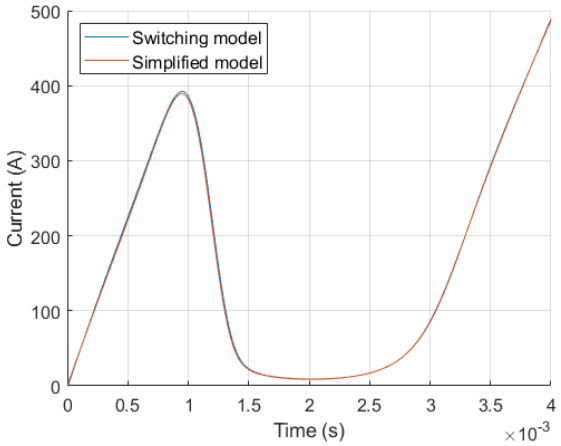

(b) Primary coil current amplitude ($|i_1|$)

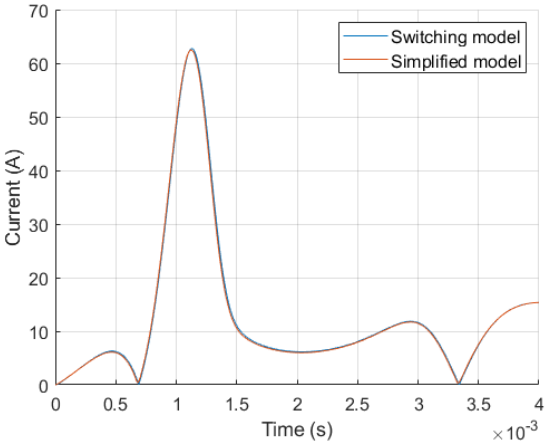

(c) Secondary coil current amplitude ($|i_2|$)

Figure 5.12: Comparisons of primary and secondary currents for DWPT with a restive load.

Table 5.2: Simulation system parameters.

Parameter	Symbol(s)	Value
Coil inductance	L1, L2	$132.410\mu H$
Coil internal resistance	R1, R2	$1.3\text{m}\Omega$
Compensation capacitance	C1, C2	$26.477\mu F$
DC/DC converter inductance	Lb	5mH
DC/DC converter capacitance	Cb	1.5mF
Inverter frequency	f_i	85kHz
DC/DC converter frequency	f_{dc}	2kHz

5.3.4 Full system

The main point of interest for the grid interaction simulations is the input (source) and output currents, which are shown in Figure 5.13. The proposed simulation captures the dynamic behaviour of the system in a much shorter simulation time, at the cost of slight inaccuracy at the start and end of the power transfer window. This is thought to be due to the behaviour of the controlled rectifier, as the voltage on the secondary circuit falls too low to forward bias the rectifier diodes. Consequently, the equivalent AC resistance seen by the circuit changes to the snubber resistance. This is further supported by the accuracy of the results within the main power transfer region, which show close correlation to the full circuit results.

To further explore the accuracy of the system, the DC bus voltages are also shown. Again, a similar response is observed, with the main reference voltages being achieved successfully. Note that the primary and secondary sides show very similar behaviour and response to changes in coupling. Notably, the primary-side DC voltage (v_{DC1}) shows a difference in the voltage rise and fall, indicating a potential inaccuracy in the load applied to the primary converter. While the results in Figure 5.10 show the DC converter modelling to be very accurate, this variation is thought to be linked to the AC equivalent resistance applied to the WPT system. As Figure 5.12 shows the DWPT system response with a resistive load, the key difference for the full system test is that the load resistance is calculated based on the power consumption by the secondary-side DC converter. This suggests that the modelling of the controlled rectifier should be revisited.

Overall, the results demonstrate the ability of the model to estimate not only the input and output currents based on the coupling factor but also the impact on other state variables, such as the primary and secondary voltages, which are controlled by PI controllers. Hence, the proposed model can be used to investigate different control schemes for DWPT.

As the main error occurs in the input power consumption, Figure 5.14 presents a comparison of the energy consumed at the source. A peak error of 5% is observed over the full simulation duration, highlighting the model's ability to closely replicate the behaviour of the full switching model throughout the simulation.

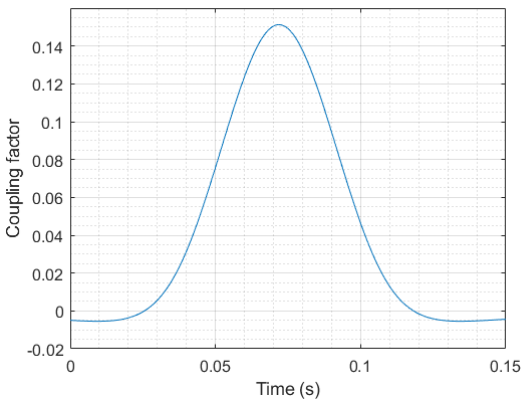

(a) Coupling factor (k)

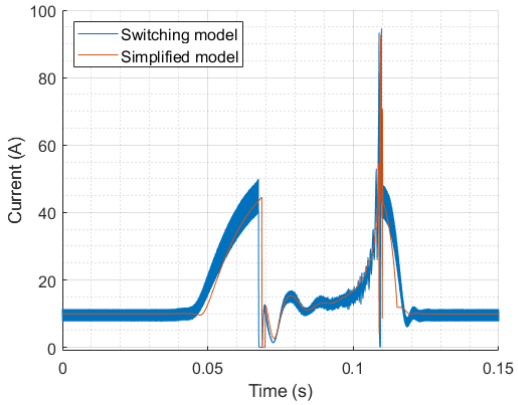

(b) Input current (i_{source})

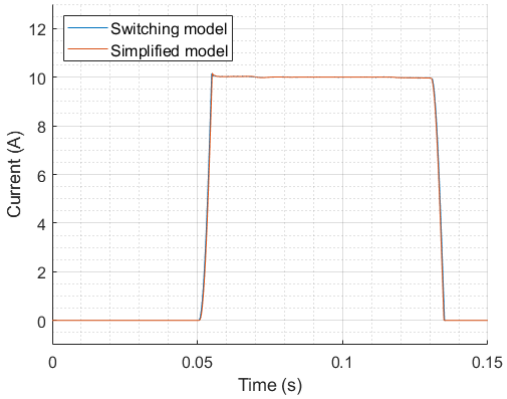

(c) Output current (i_o)

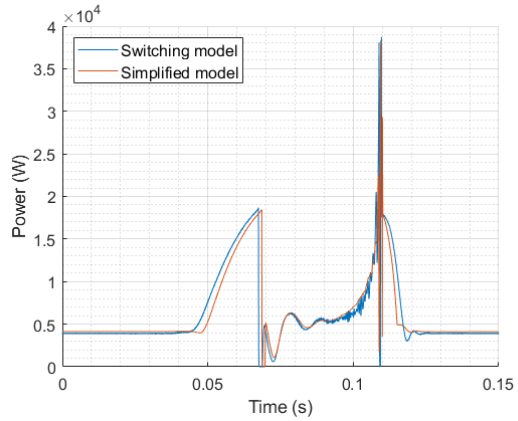

(d) System input power

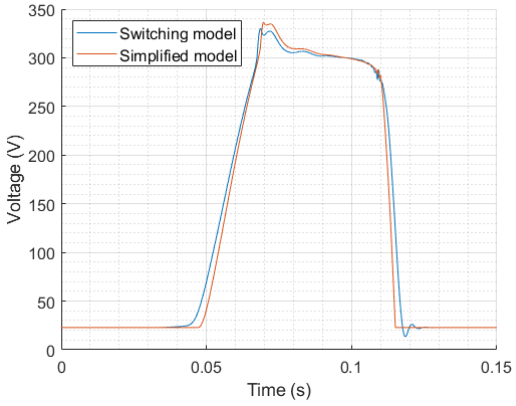

(e) Primary side DC voltage (v_{DC1})

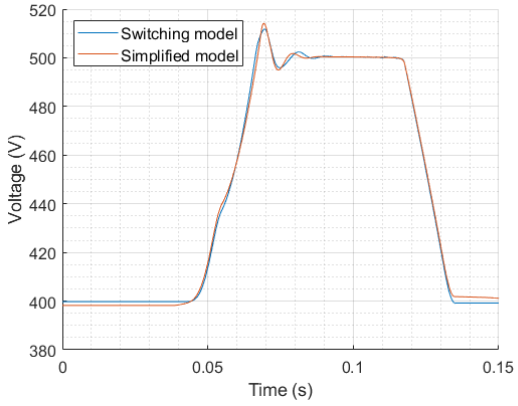

(f) Primary side DC voltage (v_{DC2})

Figure 5.13: Full system performance comparison between the switching a simplified model, comparing the obtained input and output currents and the system controlled DC voltage levels.

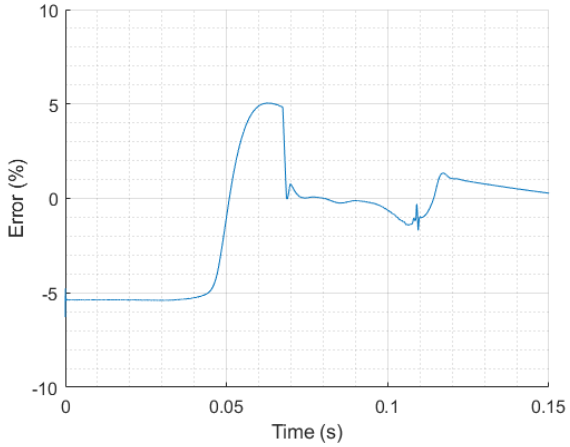

Figure 5.14: Cumulative error $\left(\frac{\int P_{\text{sw}}\,dt}{\int P_{\text{eq}}\,dt}\right)$

5.3.5 Simulation time

The system used for simulation has the following specifications: CPU - i7-6700 @3.40GHz; Memory - 16GB RAM; OS - Windows 11 64-bit (10.0 Build); Matlab - R2023a.

Table 5.3 shows a comparison of the simulation times for each circuit presented. Notably the main simulation showed $\approx$ 69x reduction in simulation time for the same simulation duration, confirming the effectiveness of the simulation techniques in reducing simulation time.

The increased simulation time is due the increased complexity of the full circuit model and computation required to obtain results. This is also true for the proposed equivalent circuit, however instantaneous values for voltage/current are omitted which in turn allows an increase in the required time step to obtain results.

Table 5.3: Comparison of simulation models.

Sub-system	Circuit	Time Step	Simulation Duration	Elapsed Time	Steady-State Error
DC-DC converter	Switching model	100 μs	1 s	2.54 s	0.03%
	Simplified model	100 μs	1 s	0.74 s	
DWPT	Switching circuit	117.65 ns	0.1 s	112.43 s	0.5%
	Simplified model	117.65 ns	0.1 s	4.00 s	
Full circuit	Switching circuit	117.65 ns	0.15 s	1391.76 s	5%
	Simplified model	117.65 ns	0.15 s	20.32 s	

5.4 Chapter Summary

The implemented average circuit models effectively reduced the maximum frequency required for simulation, resulting in over a 60-fold reduction in simulation time. This makes it feasible to accurately estimate DWPT system behaviour for scenarios such as grid interaction studies, which were previously impractical using detailed full-frequency models. By achieving this level of simulation efficiency, the approach directly addresses the challenges identified by Niu, Li, Lu, and Pan [177], who showed that particle-swarm-based parameter identification methods are too computationally intensive for dynamic, real-time applications. Similarly, it responds to the bottlenecks noted by Wang, Fu, Zhao, and Hu [178], who demonstrated that traditional FEM-based coil and magnetic component optimization can become prohibitively time-consuming for large-scale parametric sweeps.

In line with the system-level perspective of Newbolt *et al.* [179], the proposed modelling approach enables more practical long-duration and large-scale studies, such as assessing the voltage stability impacts of DWPT deployment under realistic traffic flows. The reduced-order average model also creates a robust foundation for future developments, including the integration of DWPT systems into digital twin frameworks and the investigation of multiple coil systems connected at different grid points.

Unlike previous approaches that rely on static load profiles derived from experimental setups to approximate DWPT dynamics, the developed model can be actively controlled using real-time vehicle speed and position inputs, and it returns the corresponding power consumption in response. This allows for realistic simulations of scenarios such as multiple transmitter pads at separate grid connection points, capturing how driving behaviour affects local power flow and grid stability. Furthermore, multiple vehicles with varying driving patterns can be modelled simultaneously to evaluate the broader benefits of DWPT adoption at

scale, including providing continuous power to different vehicles throughout the day. In doing so, the presented average modelling approach extends and improves upon prior methods, making detailed, realistic DWPT studies more feasible and accelerating the development of future dynamic charging technologies.

5.4.1 Future work

The main issue with the implementation is observed to be the interconnection of subsystems. In fact the issue of this interconnection is subsystem behaviour with low coupling factor (for WPT), this proved to be an issue with the controlled rectifier as at this time the power supplied to the output is approximately zero, meaning it's resistance - resulting in resistance calculations ($R = V^2/P$or $R = P/i^2$ tend to either 0 or infinity) causing issues with the power transferred. During this time the AC resistance connected corresponds to the Snubber resistance of the rectifier. Hence further modelling to the behaviour of the rectifier would further improve the accuracy of the simulation. When the rectifier is conducting in the main power transfer window, the results are closely linked and show an accurate representation of the system – further indicating the issue occurs at lower power transfer (low coupling).

Expanding the circuit to accommodate multiple coil systems, both primary and secondary, represents a significant advancement in research, as we move towards including multiple vehicles for charging and integrating multiple transmitter coils. This approach will allow for more comprehensive investigations into practical implementations of DWPT technology. Simulating multiple primary coils with a vehicle travelling between them is a logical next step, as it more accurately reflects future scenarios where road sections are electrified with several transmitter coils. This will also enhance the relevance of grid integration studies.

6 Vehicle-to-everything (V2X)

Vehicle-to-everything (V2X) summarises the bidirectional functionality of EV chargers where power from the EV battery is used to power other systems, by either using the DC power directly or creating it's own micro-grid. This technology encompasses a variety of use cases with to charge other vehicles (Vehicle-to-vehicle (V2V)), more broadly parking lots (V2P) or utilise the power to run home appliances (V2H) or more broadly buildings (V2B). Using the energy stored in the vehicle battery to run any electrical system is summarised in V2X.

Supporting distribution grids (V2G) with their operation is an area with increasing interest, as the market share and adoption rate of EV increase so will the demand on distribution grids. Needing to meet customer demands, distribution grids not only have to provide enough power to meet charging demands, but also manage grid stability with an increased rate of random high power events. Hence grid support technologies are of interest to help offset the adverse effects of increased EV charging events. Aiding grid operation can be achieved in the form of frequency or voltage stability (corresponding to active and reactive power).

This chapter focus on V2G capability of WPT to first show it's ability to participate in grid support and to show possible application with no vehicle present. Then frequency support of EVs is studied in more depth to show the benefit of utilising the quick response of battery technology. Bidirectional charging allows utilising the battery by both charging or discharging for various uses including load management, frequency control or supporting other vehicles. This chapter will first introduce the technology in-literature and previous uses before summarising the (dis)advantages and potential applications.

As the adoption of WPT systems grows alongside traditional conductive charging, it is important to recognise that the fundamental grid support requirements remain largely the same. Whether energy is transferred via cables or wirelessly, the principles of bidirectional power flow, grid stability support, and power quality compliance apply equally. In practice, this means that WPT systems intended for V2G must achieve high power transfer efficiency, low Total Harmonic Distortion (THD), and robust PFC, just like conductive chargers.

Recent studies demonstrate that with optimised resonant compensation, robust phase synchronisation, and advanced control strategies, wireless systems can reach power transfer efficiencies in the range of 90% to 96%, comparable to plug-in chargers. For example, Venkatesan et al. [184] report experimental efficiencies up to 90.1% for bidirectional operation using dual-phase shift PWM control, while Mohammad et al. [185] demonstrate grid-to-vehicle and vehicle-to-grid efficiencies exceeding 96% in a 20 kW LCC–LCC compensated system. Broader reviews and grid impact studies [186–190] further show that with well-designed compensation networks, robust control algorithms, and proper grid-side power factor correction, bidirectional WPT systems can match the grid-support performance of conventional conductive chargers. These results highlight that the grid impact and operational behaviour of efficient WPT can be effectively equivalent to wired solutions.

Therefore, as WPT infrastructure becomes more widespread—especially in dynamic or autonomous charging applications—its grid interaction role will increasingly mirror that of wired chargers. This includes not only supplying energy to EV batteries but also discharging stored energy back to the grid when needed to maintain frequency and voltage stability, respond to local demand fluctuations, or participate in ancillary services markets.

In this way, the integration of bidirectional WPT into distribution networks can help

realise the full potential of V2X services while preserving the flexibility and user convenience that make wireless charging attractive. The remainder of this chapter will review key enabling technologies, discuss state-of-the-art control and compensation strategies for reliable grid support, and summarise practical implications for large-scale deployment.

6.1 Grid support from WPT

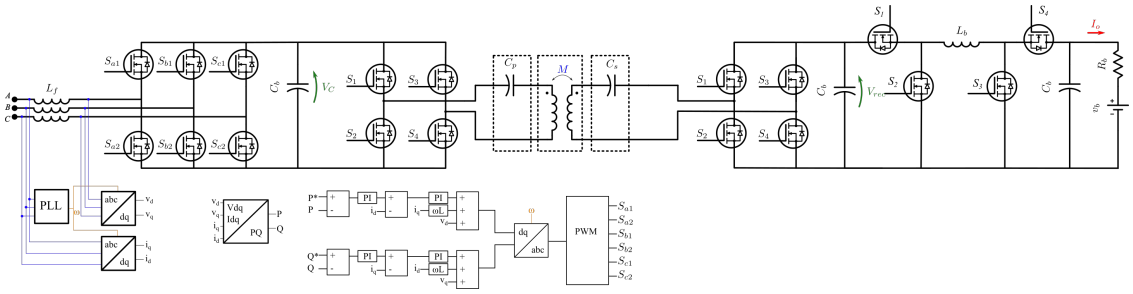

Figure 6.1: Wireless power transfer 3-phase connected system

To enable grid interaction between the WPT system, a 3-phase inverter/rectifier is connected before the primary side DC/DC converter shown in Figure 6.1. This allows active rectification for power factor correction, or later enabling reverse power flow by acting as an inverter for the system, shown in Figure 6.2.

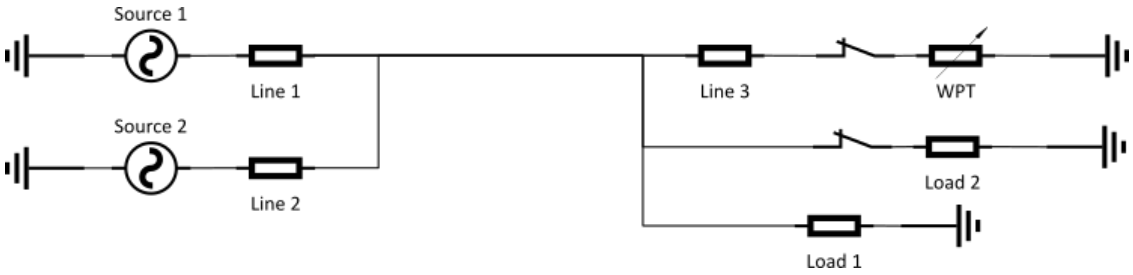

(a) Grid connection as variable load

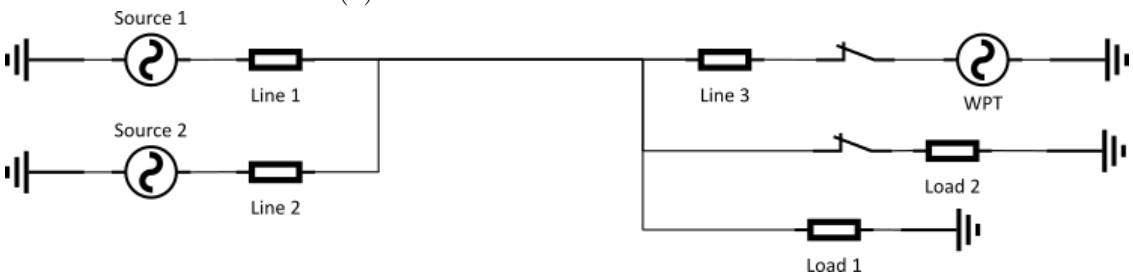

(b) Grid connection as variable source in V2G mode

Figure 6.2: Grid system with WPT system connected in forward mode (a) and reverse/V2G mode (b)

6.1.1 Active power control while charging

Figure 6.3 shows the system response to a step change in EV charging current. All results are shown in per-unit based on a nominal charging power of 22kw, 55A (DC) charging current, nominal grid voltage 400v (line-to-line RMS) and 22kVAr reactive power. In this case, only the output charging current (and therefore the output power) is varied, while other variables such as the DC bus voltages and reactive power control remain constant. As can be expected, an increase in output current leads to a higher power demand from the grid. This is because, for a battery load, the output power is approximately proportional to the output current as battery voltage remains approximately constant over the test duration. Consequently, the input power drawn from the grid is directly related to the output power through the system efficiency (η), according to $P_{in} = \frac{P_{out}}{\eta}$.

Since the system aims to maintain constant DC bus voltages and zero reactive power, any increase in output power must be met by an increase in active power drawn from the grid. As the entire WPT system electrically decouples the grid from the EV battery, there is an observable delay as the system adapts to the step change in output current. The resulting deviation in system parameters is minimised by the control system during the output power transition. By coordinating the various control stages, the impact on subsequent stages is reduced, allowing the system to continue operating normally.

Figure 6.4 how the active power can be increase by varying system parameters other than output current, effectively lowering system efficiency. This method maintains vehicle output current, allowing the EV to control it's charging characteristics independent of the grid impact control for active/reactive power. Decoupling both control systems is beneficial for the EV to reduce negative impact of high current switching events while providing grid support. The downside of this implementation is the lowered system efficiency resulting in power loss, hence if possible increasing output power is preferred.

6.1.2 Reactive power control

Figure 6.5 shows the impact of varying the inverter reactive power control. Effectively changing reactive power impacts the grid voltage level. In this operation mode, the system is able to maintain output characteristics and minimise fluctuations. This effectively functions the same as other charging technologies providing PFC the grid connection point.

6.1.3 Reverse power direction (V2G)

Reversing the direction of power flow is achieved by switching control signals between primary and secondary sides of the WPT system, allowing the inverter to act as a controlled rectifier and vice versa. In doing so, reverse power flow is achieved and the vehicle is used to feedback power into the grid. For active/reactive power control, the droop control can be applied to the inverter to synchronise the output with the grid and achieve desired control characteristics. Figure 6.6 shows the result of connecting the WPT system in reverse current flow, providing power to the gird. As grid voltage is maintained, increasing output current directly increases grid active power. Hence running the system in V2G mode is able to provide power to the grid for active or reactive power control.

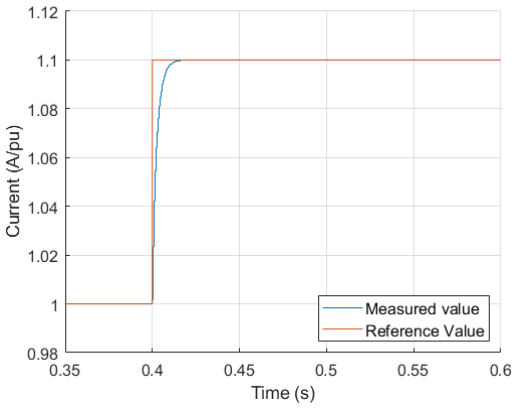

(a) EV charging current

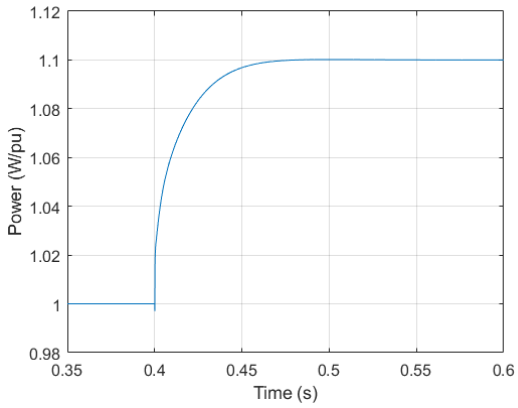

(b) Grid active power consumption

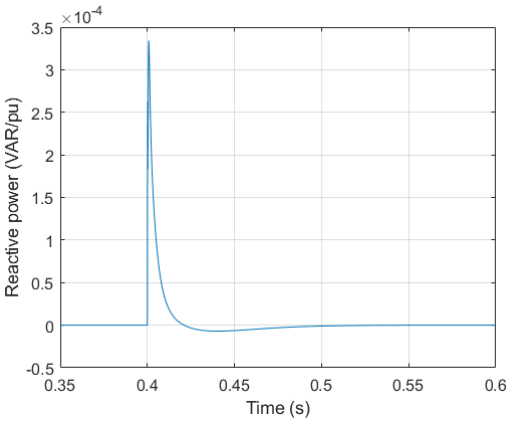

(c) Grid reactive power consumption

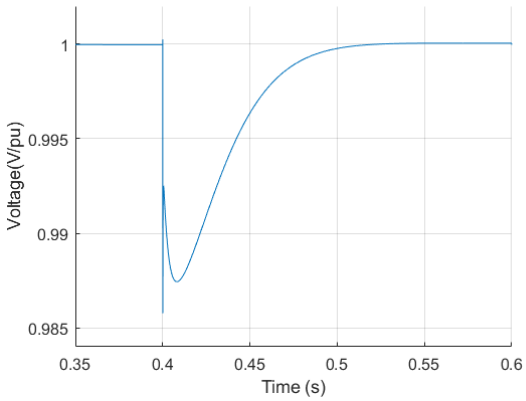

(d) Primary DC bus voltage

Figure 6.3: Grid interaction after EV charging current increase

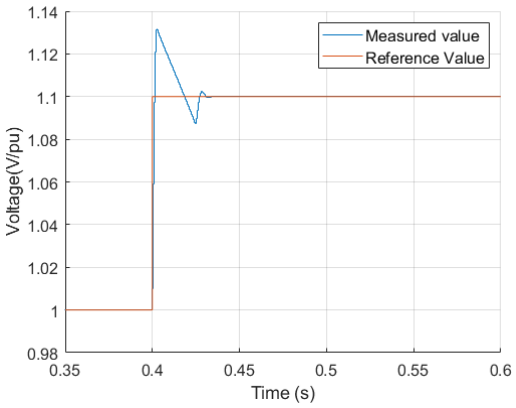

(a) Secondary DC bus voltage

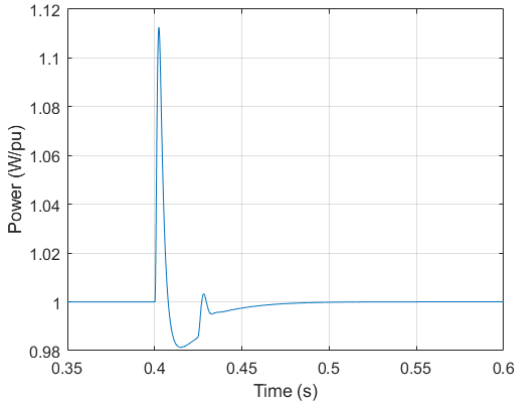

(b) Grid active power consumption

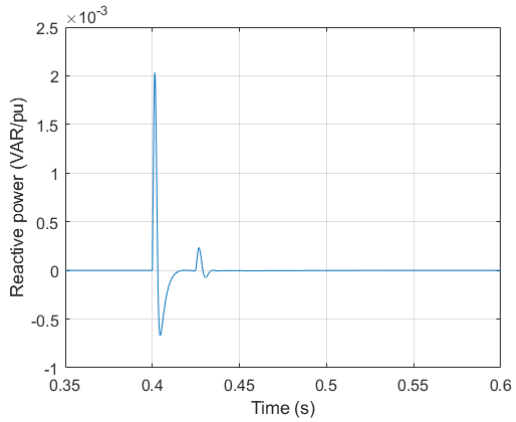

(c) Grid reactive power consumption

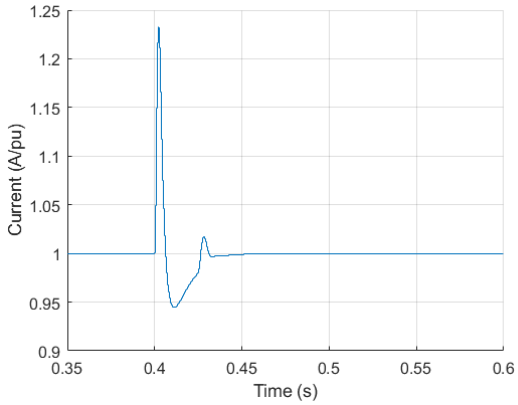

(d) EV charging current

Figure 6.4: Grid interaction after secondary DC bus voltage increase

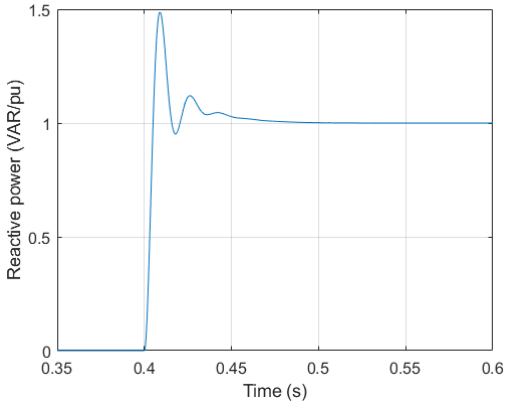

(a) Grid reactive power consumption

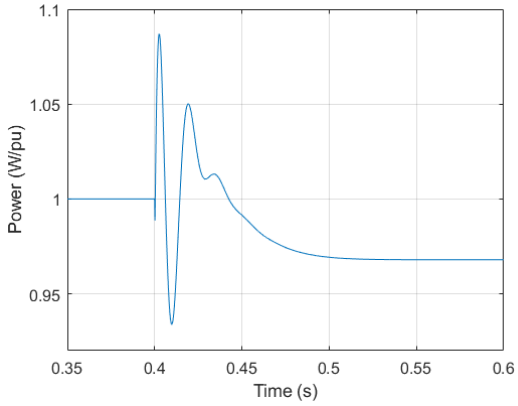

(b) Grid active power consumption

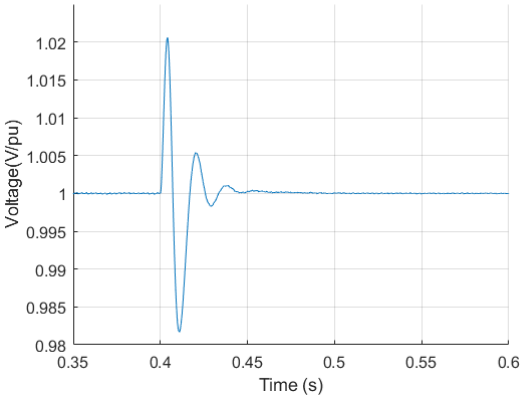

(c) Primary DC bus voltage

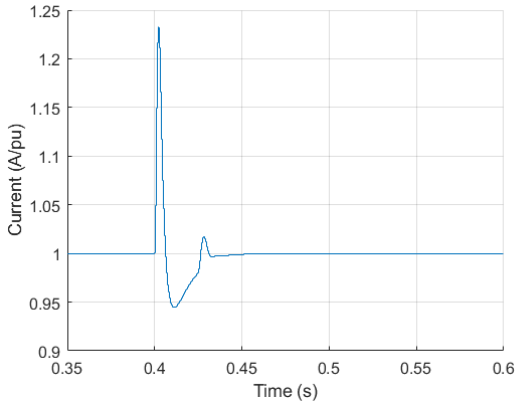

(d) Grid voltage level

Figure 6.5: Grid interaction after varying reactive power contribution.

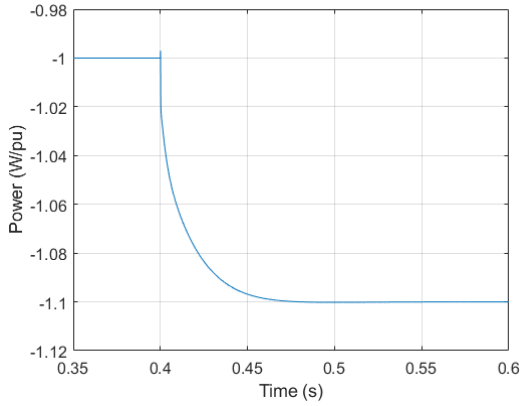

(a) Grid active power contribution

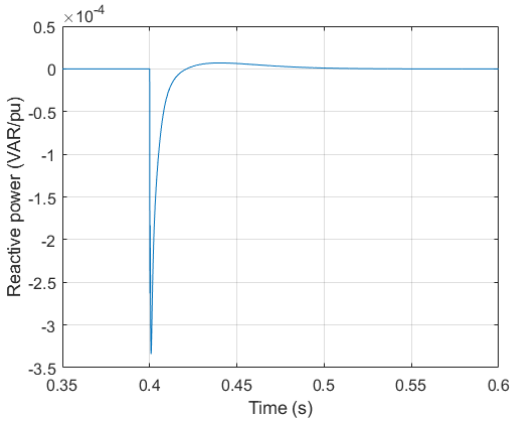

(b) Grid reactive power consumption

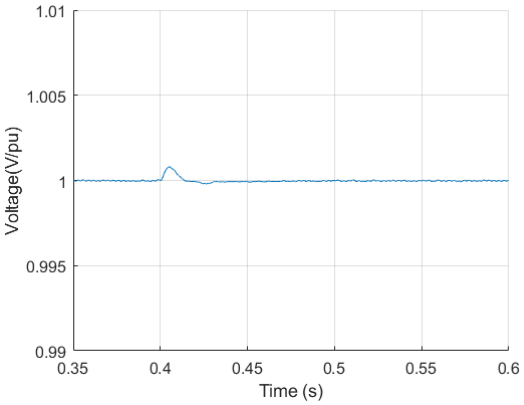

(c) Primary DC bus voltage

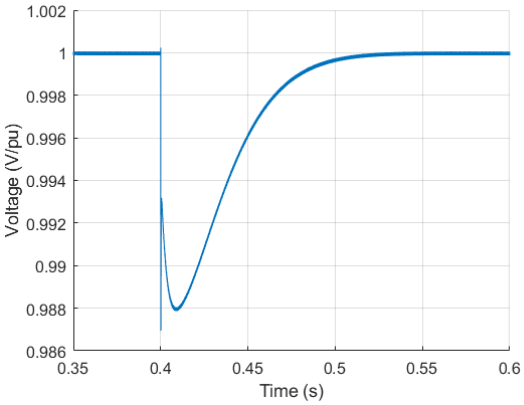

(d) Grid voltage level

Figure 6.6: Grid interaction in V2G mode after varying output current.

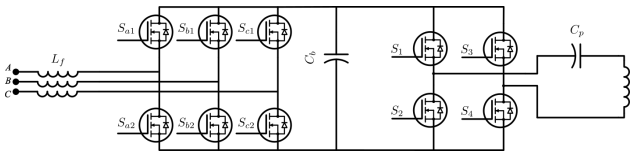

Figure 6.7: WPT system with no connected load (M=0).

6.1.4 Zero Mutual coupling - no vehicle present

With no vehicle present as the receiver, the mutual inductance $M = 0$, resulting in the inverter being connected to a series RLC circuit with low impedance. Since the inverter is limited to an operating frequency range of 81.39–90kHz based on standards SAEJ2954 and ISO19363, this restricts the obtainable impedance range and creates the problem of a low-impedance effective load for the DC/DC converter. This leads to operational issues, as the passive components are discharged too quickly, leaving negligible control authority over the system. For this zero-loading case, it is possible to switch to a different static load, which can be implemented by the front-end converter to maintain the operation of the remaining components while providing power factor correction and the active/reactive power control.

Figure 6.7, shows the equivalent circuit when there is no vehicle present for the WPT system. Coil and compensation capacitor values are $132, 4\mu H$ and $26.47nF$ (resonant frequency of 85kHz). Giving their total impedance:

$$Z_t = R_L + \omega(jL + \frac{1}{jC}) \tag{184}$$

For the frequency range of 80-90kHz, the impedance ranges from $Z_t = 1.3e^{-3} - 8.58j$ to $Z_t = 1.3e^{-3} + 8.08j$ with the resonant point having the lowest impedance of $Z_t = 1.3e^{-3} - 2.1e^{-3}j$. The control of the primary DC/DC converter can also be changed from voltage to current to better control the system. In theory this means the system can be used as a high power load, allowing it only to consume power from the grid. Since the connected system contains a controlled rectifier, it can also be used to alter it's reactive power consumption, similar the charging shown in Figures 6.3, 6.4 and 6.5. Varying inverter frequency changes the impedance of the connected load and can be used to alter between a net capacitive and net inductive load. Figure 6.8 shows the impact of varying primary coil current. Notably the impact of varying primary coil current is similar to increasing power consumption with a vehicle present, hence the same control schemes for active/reactive power could be applied.

6.1.5 Discussion

In general the WPT system can be equipped with a PFC circuit to manage it's reactive power impact to the connected grid. When a vehicle is connected, it is possible to alter both the active and reactive power control, the same as other systems. The only notable differences for the WPT system over wired EV charging, is the variance in mutual inductance and therefore it's efficiency and maximum power transfer. As most practical systems will have a primary (ground) coil larger than the receiver (EV) coil, it is more efficient to run the system in forward charging mode instead of V2G, hence changing charging power is a

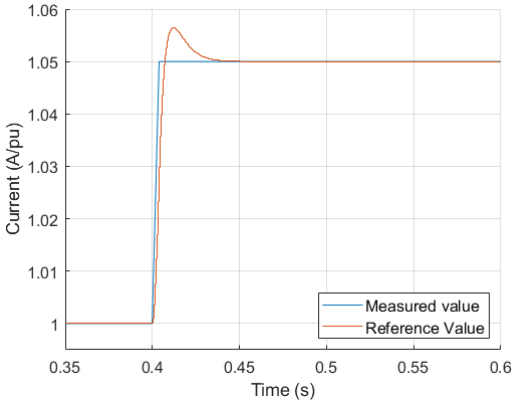

(a) Primary coil current

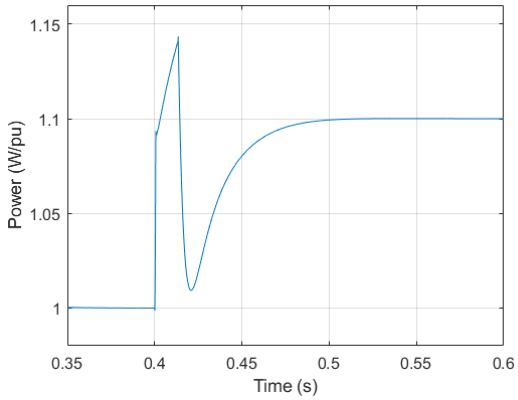

(b) Grid active power consumption

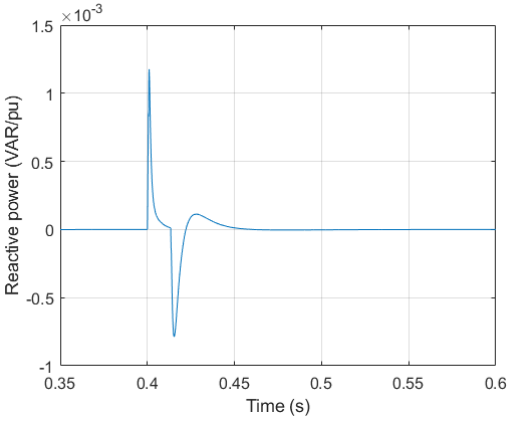

(c) Grid reactive power consumption

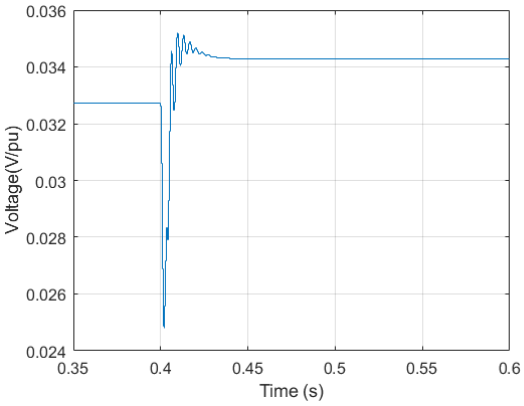

(d) Primary DC bus voltage

Figure 6.8: Grid interaction with no vehicle present (M=0) while varying primary coil current.

preferred method of power control. The WPT system has two DC bus capacitors (on primary and one secondary side) which can be charged to increase the power demand without altering output current (achieving constant voltage/current for EV charging).

Without a vehicle connected, the remaining circuit connected to the grid is a DC/DC converter and inverter with a low impedance load. Changing the operating frequency of the inverter allows a change in the total impedance of the connected LC circuit. The low impedance of the circuit leads to high current draw, which in turn depletes the primary side DC bus voltage. The current through the circuit can be controlled to offer some reactive power control, however this is significantly less than the capability with a vehicle connection, additionally the current will need to have an upper limit to mange the resulting magnetic field from the coil.

6.2 Frequency support

Increased integration of EVs into the power distribution grid with frequency regulation capability would result in excessive amount of energy discharge into the grid without a proper control and scheduling scheme. Where the system is not optimizing the use of connected generators and EVs. Current studies focus on the grid frequency stability without considering the power consumption from EV clusters. Hence a control strategy can be developed to more effectively manage the EV contribution for frequency stability. This section focuses on the proposed fuzzy-PI control scheme which optimizes the ratio of EV contribution from private cars, buses and taxis. The proposed control scheme is verified with a micro-grid frequency-regulation simulation.

The increase in EV adoption rate and continuing growth will result in more grid connected EVs which impacts grid stability as more high power (dis)charging events will take place. Throughout the day approximately 96% of EVs are not on the road and a large portion can be expected to be grid connected, additionally EVs can act as both a load and source for the grid presenting an opportunity to utilize V2G. Although the battery capacity of an EV is small compared to grid power levels, (dis)charging many vehicles is enough to support the grid power quality (peak-to-valley power demand, voltage shift, frequency instability, etc.). Utilization of EV clusters for frequency regulation in power systems has be a main focus of research in many articles.

6.2.1 EV Cluster participation system frequency regulation model

EV participation in grid frequency regulation consists of two main controllers, the primary frequency controller (PI controller) and electric vehicle aggregator (EVA) controller, shown in Figure 6.9. The implementation allows the PI controller to change generator output power based on grid frequency (including droop control), while the EVA controller affects the output power from available EVs. U_p and U_e are the output signals of the primary and EVA controllers respectively. T_g and T_t are the governor and prime mover time constants respectively, ΔP_v is the position change of the governor, ΔP_m is the mechanical power output of the generator, $\Delta P_{load}, \Delta P_{res}$ are load and renewable energy power changes respectively. M the inertia time constant, D is the load damping factor, Δf is the frequency deviation, finally S_1, S_k, S_n are the distribution ratios for cluster frequency regulation signals respectively.

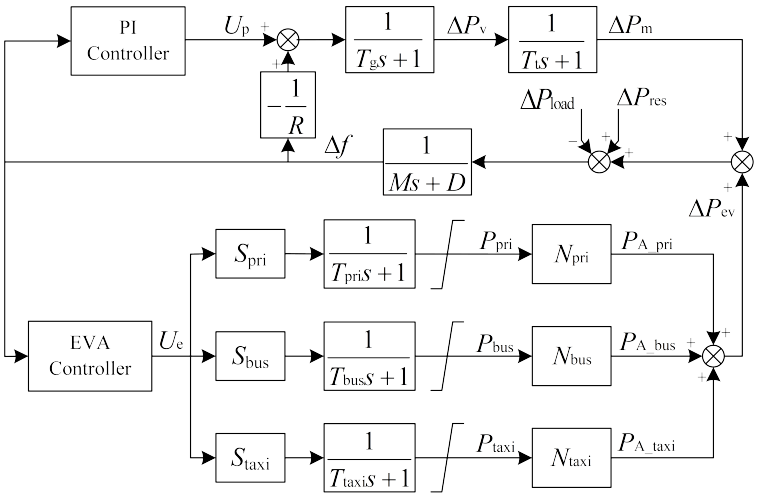

Figure 6.9: Single-area load frequency control system model with EV cluster participation [199].

The EV cluster model (Figure 6.10) shows how the EVA controller output (U_e) is used to regulate the EV output power for frequency regulation (ΔP_{ev}. $S_{pri}, S_{bus}, S_{taxi}$ are the allocation coefficients which are a ratio of the total maximum power of each vehicle type relative to the total maximum power of the cluster, these are calculated using equation 186. Which are used to obtain the power per vehicle $P_{pri}, P_{bus}, P_{taxi}$ which is kept within the limits of maximum and minimum power $P_{\text{pri}}^{\max}$, $P_{\text{bus}}^{\max}$, $P_{\text{taxi}}^{\max}$ and $P_{\text{pri}}^{\min}$, $P_{\text{bus}}^{\min}$, $P_{\text{taxi}}^{\min}$. Multiplied with the number of vehicles ($N_{pri}, N_{bus}, N_{taxi}$) to give the total power per vehicle type and sum to the total power output of the cluster ΔP_{ev}. Equations 185 - 188 describe the relation between parameters within the cluster participation model.

The implementation effectively responds to load disturbances and deviation in renewable energy sources to maintain grid frequency. When the total energy available from generators, renewable sources and EVs matches load power demand the overall system frequency will be stable (equation 188).

$$\begin{cases} P_{\text{pri}}^{\min} \leq P_{\text{pri}} \leq P_{\text{pri}}^{\max} \\ P_{\text{bus}}^{\min} \leq P_{\text{bus}} \leq P_{\text{bus}}^{\max} \\ P_{\text{taxi}}^{\min} \leq P_{\text{taxi}} \leq P_{\text{taxi}}^{\max} \end{cases} \tag{185}$$

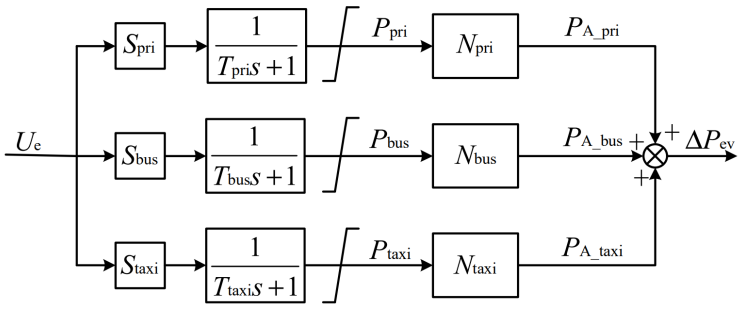

Figure 6.10: EV Cluster Model [199].

$$\begin{cases} S_{\text{pri}} = \dfrac{3P_{\text{pri}}^{\max}}{P_{\text{pri}}^{\max} + P_{\text{bus}}^{\max} + P_{\text{taxi}}^{\max}} \\ S_{\text{bus}} = \dfrac{3P_{\text{bus}}^{\max}}{P_{\text{pri}}^{\max} + P_{\text{bus}}^{\max} + P_{\text{taxi}}^{\max}} \\ S_{\text{taxi}} = \dfrac{3P_{\text{taxi}}^{\max}}{P_{\text{pri}}^{\max} + P_{\text{bus}}^{\max} + P_{\text{taxi}}^{\max}} \end{cases} \tag{186}$$

$$\begin{aligned} \Delta P_{\text{ev}} &= P_{\text{A\_pri}} + P_{\text{A\_bus}} + P_{\text{A\_taxi}} \\ &= P_{\text{pri}} N_{\text{pri}} + P_{\text{bus}} N_{\text{bus}} + P_{\text{taxi}} N_{\text{taxi}} \end{aligned} \tag{187}$$

$$\Delta P_{\text{m}} + \Delta P_{\text{ev}} - \Delta P_{\text{load}} + \Delta P_{\text{res}} = (MS + D)\Delta f \tag{188}$$

6.2.2 Control strategy

Utilization of the battery fast response time to providing energy for grid auxiliary support can be used to significantly and effectively reduce frequency deviation when a large number of EVs are connected. However large power consumption from the battery negatively impacts it's life cycle and performance degradation but also increases cost of grid frequency regulation. Previous implementation us the SMC for cluster control which has a chattering problem where the controller oscillates between modes frequently. Similarly the MPC is also complicated to implement with more control parameters. Hence a fuzzy PI controller is proposed to reduce implementation complexity and improve the performance by removing the controller chatter issue.

EV cluster output power should respond to grid frequency deviations. When the deviation is lower less power is required from the EVs, likewise when the deviation is high more power is required to stabilize the grid. The fuzzy-PI controller can help control the contribution of the EV cluster based on grid frequency deviation but also the rate of change of deviation (du/dt) as it is desirable to utilize EVs for high rate of change due to their fast response time compared to power generators. Figure 6.11 shows the implementation of the fuzzy controller where it's output (U_{fuzzy}) is passed through a first-order filter before combining with a PI controller.

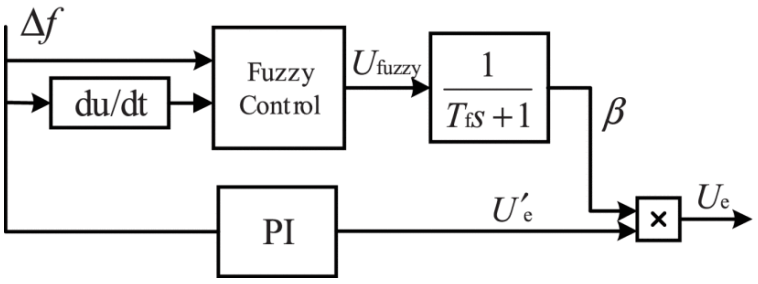

Figure 6.11: Block diagram of EV cluster control signals [199].

6.2.3 Optimization

During V2G contribution of EV clusters, the grid has to compensate customers for the use of their power for grid use. As this is an additional cost in grid operation, it is important to minimize the utilization of EV clusters while ensuring sufficient grid frequency regulation.

Objective function optimization For EV cluster participation in frequency regulation, it is import to consider both the system frequency deviation and the cost associated with providing this function. Hence the objective function F is established (equation 189). A lower F value indicates lower frequency deviation and therefore lower EV cluster output, vice versa is true for high F values. Hence optimization is carried out aiming to minimize F.

$$F = k_1 E + k_2 \Gamma \tag{189}$$

where k_1 and k_2 are weight coefficient, E is the output power of the EV cluster; Γ is the frequency stability index.

EV participation in grid frequency regulation, the amount of charging and discharging is surmised as E in equation 190.

$$E = \int_0^t \left|\Delta P_{\mathrm{ev(pu)}}\right| \, dt \tag{190}$$

where $P_{ev(pu)}$is the standardized sum of EV power for the three types considered (personal vehicles, buses and taxis).

Measuring the frequency stability index of the system, uses the integral of frequency deviation over time shown in equation 191

$$\Gamma = \int_0^t \left|\Delta f_{(\mathrm{pu})}\right| \, dt \tag{191}$$

Constraints Having defined objective functions for the system, it is important to limit the minimum and maximum values for EV contribution to ensure that the power exchanged by each EV remains technically feasible and operationally practical. The output power of an EV is constrained by the capabilities of both the EV and its charge point, while the minimum limit helps avoid inefficient low-power interactions that could increase switching frequency and system wear. To standardize this approach for different vehicle clusters, input

ratio parameters ($\alpha_{pri}, \alpha_{bus}, \alpha_{taxi}$) are used to proportionally allocate the total power among private cars, buses, and taxis.

Optimization Process Particle swam optimization is an easy to implement process with fast convergence, hence this is used to optimize equation 189. The optimization process is given as:

1. Establishing the model for the EV cluster participation in power system frequency regulation, and generating frequency fluctuation scenarios based on load fluctuations.
2. Initialize the particle swarm parameters, i.e., randomly generate N sets of particles that satisfy equation 192.
3. The N sets of particles are sequentially input to the model in MATLAB/Simulink to derive the Γ and E.
4. Calculate the objective function value F according to equation 189.
5. Update the individual optimal parameter values and global optimal parameter values of the particles according to the calculated objective function values.
6. Update the position and velocity parameter values of N sets of particles according to the individual optimal parameter values and the global optimal parameter values.
7. If the number of iterations is less than the maximum iteration value ($It_{\max}$), make the number of iterations $It = It + 1$, and then substitute the updated N sets of particle parameters in step f. into step c.; Otherwise, the obtained global optimal parameter value is the optimal input parameter value in the frequency regulation model, and the optimization ends.

$$\begin{cases} \alpha_{\text{pri}}^{\min} \leq \alpha_{\text{pri}} \leq \alpha_{\text{pri}}^{\max} \\ \alpha_{\text{bus}}^{\min} \leq \alpha_{\text{bus}} \leq \alpha_{\text{bus}}^{\max} \\ \alpha_{\text{taxi}}^{\min} \leq \alpha_{\text{taxi}} \leq \alpha_{\text{taxi}}^{\max} \end{cases} \tag{192}$$

6.2.4 Results and discussion

The grid capacity for this work is 300MW with a maximum (dis)charging power of 15kW for passenger cars and taxis, and 20kW for buses. PI controller parameters $k_p = 3$ $k_i = 25$ in the primary controller and $k_p = 0.01$, $k_i = 0.01$ in the EVA controller. System parameters are shown in Table 6.1.

Table 6.1: Parameter values used in the simulation.

Parameter	**Value**
Filter coefficient T_f	5
Governor time constant T_g	0.1 s
Governor time constant T_i	0.3 s
Regulation constant R	0.05 Hz/pu MW
Inertia constant of the generator M	10 pu MW/Hz
Damping coefficient of load D	1 pu MW/Hz
Private car and taxi time constant T_{pri}, T_{taxi}	0.35 s
Bus time constant R	0.05 Hz/pu MW

Number of accesses for different EV types To represent a realistic scenario, the study references the electric vehicle population in Zhengzhou City, Henan Province. As of July 2021, there were 10,854 licensed cruising taxis and significant numbers of new energy vehicles under active replacement plans. By the end of June 2020, Zhengzhou had registered a total of 84,133 new energy vehicles (including buses), with 77,817 cars and 6,316 buses owned by individuals or companies [200]. Based on the ratio of private cars, taxis, and buses in this fleet, the simulation assumes a representative EV cluster composed of 4,000 private cars, 1,500 taxis, and 600 buses. This example provides a practical reference point to demonstrate how the proposed control and optimization strategy can be applied to an actual urban EV fleet with diverse vehicle types and realistic availability for grid services.

Based on the number of vehicles present in the cluster and their typical travel behaviour, the vehicle grid connection availability is simulated and illustrated in Figure 6.12. The figure shows the variation in the total number of EVs connected to the grid over the test duration. This information is important because it directly affects the number of vehicles available to participate in frequency regulation at any given time. Accurately capturing these availability patterns ensures that the frequency control strategy realistically accounts for daily usage cycles, charging habits, and peak connection periods, which are critical for effective grid support.

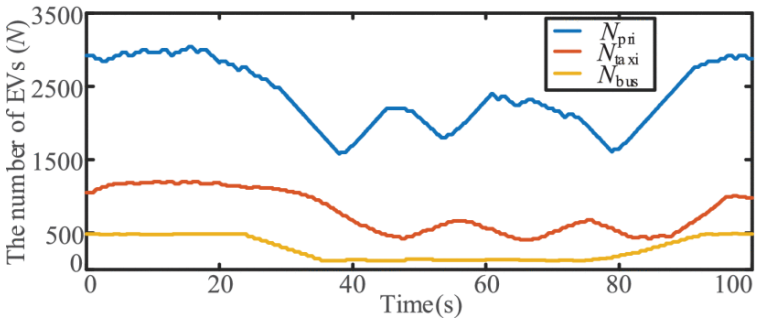

Figure 6.12: The change in the number of EVs connected to the grid [199].

Load disturbance A step load disturbance (shown in Figure 6.13)is used with a magnitude of 0.05pu at 30s and returns to 0pu at 70s, additionally the variation in renewable energy generation and random load disturbances overlap the main load disturbance. Random load and renewable energy disturbances are independent of the simulated load disturbance and can be expected to persist throughout the simulation as shown in Figure 6.13.

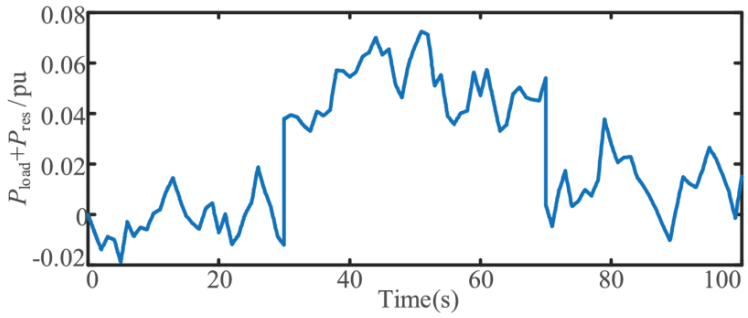

Figure 6.13: Total system disturbance [199].

Frequency response with EVs Comparing system frequency response with and without EV participation is shown in Figure 6.14. Due to the limited response time of generators, the step change in load disturbance takes the system longer to reduce frequency deviation, with EV participation this is reduced as EVs can respond quicker to the disturbance. This can be seen throughout the simulation but is most prevalant at the switching time for load disturbance (30s and 70s). Without EVs, the peak frequency deviation is 0.12Hz at both 30s and 70s, with the use of EVs the frequency deviation is lowered to 0.084Hz at 30s and 0.104Hz at 70s (30% and 13% reduction respectively).

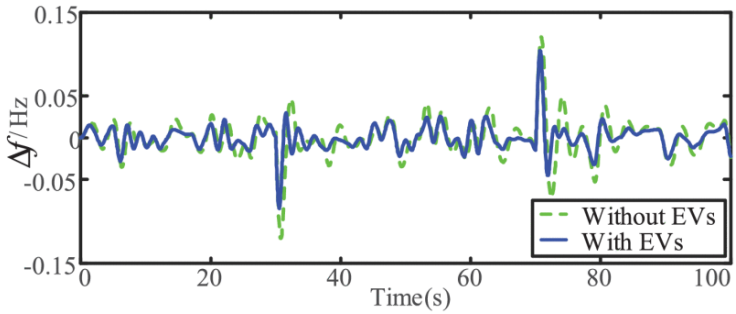

Figure 6.14: Frequency response with and without EV participation [199].

The peak frequency deviation is effectively reduced at 30s and 70s. Additionally throughout the simulation the frequency deviation is also reduced, to quantify this we can look at the frequency stability index in Table 6.2 which shows a 37.68% reduction. Showing the benefit of utilizing EVs in grid frequency stabilization.

Table 6.2: Comparison of frequency stability indexes [199].

	Without EVs	**With EVs**
Γ	0.03256	0.02029

Comparison of the generator and EV cluster output power both with and without the fuzzy control is shown in Figure 6.15. During the main disturbance steps, both generator and EV output power is increased/decreased accordingly. The main difference with the PI control is the prioritization of generator power to reduce total EV power demand. Table 6.3 shows there is a 36.78% power reduction from the EV cluster when utilizing the Fuzzy-PI control.

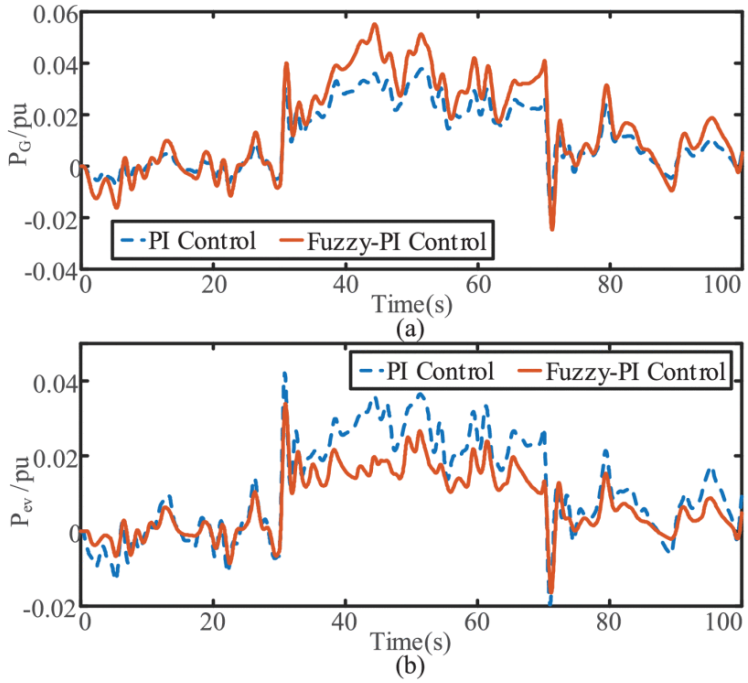

Figure 6.15: (a) Generator and (b) EV output change curves [199]. [199].

Table 6.3: Comparison of EV cluster output indexes [199].

	Without EVs	**With EVs**
E	1.38	0.8724

In summary, the Fuzzy-PI control can effectively utilize the advantage of battery fast response and effectively reduce the total power output of the EV cluster. Resulting in lower battery power consumption, degradation and reduce compensation costs of the grid to EV users.

Joint Optimization simulation Using particle swarm optimization algorithm, the input ratio parameters of the EV are set between 10% and 100% for α^{min} and α^{max} respectively.

Weights for the objective function, $k_1 = 7$ and $k_2 = 525$ are used. The obtained optimized input ratio for private cars is 79.6%, busts 80.5% and taxis 97.7%. The effect of optimization (before and after) is in Figure 6.16, shows no significant changes in frequency deviation. Additionally Figure 6.17 compares simulation results before and after optimization which overall show a 4.78% improvement in frequency stability index and a 9.36% reduction in EV cluster output (shown in Table 6.4). This shows the optimization effectively reduces the overall power demand from the EV cluster while providing similar functionality for frequency stabilisation.

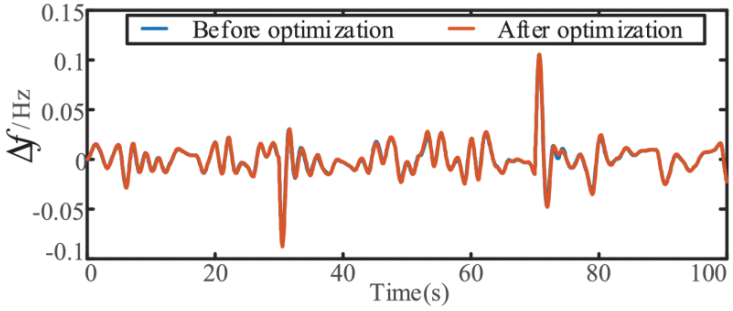

Figure 6.16: Variation of frequency before and after optimization [199].

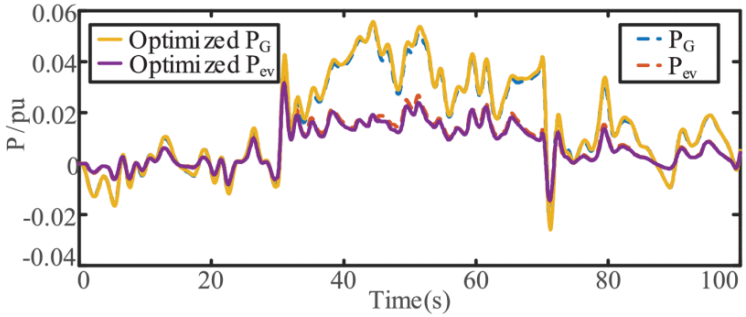

Figure 6.17: Variations of the power of generators and EVs before and after optimization [199].

Table 6.4: Comparison of indexes before and after optimization [199].

	Without EVs	**With EVs**
Γ	0.02029	0.02126
E	0.8724	0.7907

This research uses a particle swarm optimization algorithm to optimize the input ratio parameters of three kinds of EVs connected to the grid. Where each participation ratio is kept between 10% and 100%. For a weight of $k_1 = 7$ and $k_2 = 525$, the optimised input ratios are given by Figure 6.16 shows no significant changes in frequency deviation as a result of optimization, however Figure 6.17 shows a reduction in EV output power. Table 6.4 shows there is a 4.78% while reducing total energy consumption by 9.36%.

6.2.5 Discussion

The proposed control system load frequency control in micro-grids utilizes a Fuzzy-PI control regulate the EV participation in V2G. Controlling the power discharged from EVs the Fuzz-PI controller is able to significantly reduce the output power of EVs compared to the use of a regular PI controller. Simulation results for the Fuzzy-PI controller show an energy saving of 36.78% over the regular PI control. Successfully regulating the frequency and power output with a large number of EVs compared to the the massive output of the base scenario. The optimization of cars, buses and taxi participation in V2G resulted in 79.6%, 80.5% and 97.7% respectively, which successfully avoids the engagement of all EVs. Overall EV cluster output has been reduced by 9.36% while providing adequate frequency stabilization. This result shows the possibility to reduce the grid's compensation costs while also minimizing the loss of battery life seen by EVs.

Importantly, as global EV adoption continues to grow, the scale and impact of V2G services will also increase. Without advanced control strategies like the Fuzzy-PI controller, large-scale EV integration could pose challenges to battery health, and overall grid stability. Smart, optimized control can help address these challenges by ensuring that energy contributions are balanced, efficient, and only provided when truly beneficial to both the grid and the vehicle owner.

Furthermore, the growing interest in DWPT could expand these opportunities even further. While DWPT primarily aims to extend vehicle range and reduce the need for stationary charging stops, its widespread deployment could theoretically enable continuous, location-independent V2G participation if technical and efficiency barriers are overcome. This would allow EVs to provide frequency support or other ancillary services even while in transit, further increasing the flexibility and resilience of future smart grids.

Overall, these findings highlight the critical role of intelligent control and coordination in realizing the full potential of V2X technologies. Continued research in this area will be essential to develop practical, scalable solutions that can keep pace with increasing EV adoption and evolving grid demands.

6.3 Chapter Summary

V2X technology offers new opportunities for utilizing the energy stored in EV batteries to provide valuable ancillary services, such as frequency regulation. Among the possible use cases, frequency support is especially practical because it requires only small amounts of power from the vehicle battery compared to full active power support. This minimizes the impact on the vehicle's range and battery lifespan, which is crucial for maintaining user acceptance and ensuring that customers do not feel exploited as a means to fix grid issues. Therefore, strategies that intelligently manage the power contribution of EVs based on multiple factors, alongside dedicated grid support equipment, present a more viable approach.

The results of this work show that using an advanced control system, such as the proposed Fuzzy-PI controller, can significantly improve the efficiency and effectiveness of V2G operations. By optimizing the power output and participation of different vehicle types — including cars, buses, and taxis — the system reduces overall energy drawn from EVs while maintaining stable grid frequency, demonstrating a clear advantage over conventional PI

controllers. This directly addresses concerns about battery degradation and user willingness to participate in V2X schemes.

When it comes to implementation, the feasibility of V2X depends heavily on the type of charging technology used. While DC charging provides the most straightforward means for bidirectional energy flow due to its direct connection to the battery, AC charging and WPT face practical limitations. In particular, WPT systems, although technically capable of bidirectional power transfer, are more efficient in forward charging mode and less practical for V2X due to coil design constraints and mutual inductance variability. Moreover, in the absence of a connected vehicle, the capacity for reactive power support is minimal and must be carefully controlled to avoid excessive current draw and unwanted magnetic fields.

Overall, this study demonstrates that with the right control strategies and optimization of EV participation, V2X can provide effective and economically viable grid support while minimizing the impact on vehicle batteries. However, practical deployment will depend on selecting appropriate charging infrastructure, such as efficient DC charging, and ensuring that control systems can adapt to real-world operating conditions, including those unique to WPT installations. Coordinating these technical, economic, and user-focused aspects is essential to realizing the full potential of V2X within future smart grids.

7 Conclusion

The main contribution of this thesis is the comprehensive system analysis and modelling of DWPT. While average modelling techniques for DC converters and AC equivalent impedance analysis are individually well-established, their combined application to model DWPT systems represents a novel contribution. In this work, the resonant circuits of the DWPT system are first represented using their AC equivalent impedances, allowing the system to be characterized in terms of sinusoidal steady-state amplitude rather than time-domain switching waveforms. This transformation enables the use of average modelling techniques — similar to those applied in DC converter analysis — to compute the average power transfer and current amplitudes across the primary and secondary coils. As a result, the simulation avoids the need to resolve high-frequency switching behaviour, significantly reducing computational load and simulation time. Prior to this research, a detailed simulation framework capable of capturing both dynamic coil interactions and efficient average modelling for DWPT systems was largely absent from the literature. This thesis not only fills that gap but extends the framework to include grid integration studies, further supporting the practical deployment of DWPT technology.

Building on existing knowledge, the research first presented a review of the current state of charging technologies for EVs, identifying DWPT as an area of potential research with most research at the time focusing on static WPT. The technology was viewed as a newer development still in the early research stage which was backed up by the lack of commercially available WPT systems and ongoing trials for various systems. First, a simulation of WPT systems was created similar to the systems seen in current research. The preliminary simulation was able to successfully model WPT systems where research results could now be replicated as a start point for future developments, starting with investigating the different system topologies used for resonant (compensation) components and system control.

From the initial circuit and literature search, various control approaches were tested leading to the development of an autonomous primary side control for WPT systems. The proposed control scheme was successful in achieving an efficient operating without requiring primary-secondary side communication. This work gives insight into the functionality of the system with practical consideration for implementation based on perceived issues of wireless communication.

Building upon the initial WPT model, dynamic functionality has been incorporated to enable more accurate load estimation from a grid perspective. The developed model represents a pair of coils in three-dimensional space, allowing for realistic simulation of dynamic driving scenarios. To accurately capture the physical interactions during vehicle movement, variably mutual inductance has been integrated into the model, justified by its significantly slower rate of change compared to the electrical system's dynamic response. This consideration ensures that the inductive coupling is realistically modelled as vehicles travel at different speeds and positions relative to the transmitter coils. Consequently, the system exhibits dynamic behaviour, as supported by simulation results that reveal distinct operational characteristics across a range of driving speeds. This dynamic representation is essential for evaluating the practical feasibility and potential grid impacts of large-scale DWPT deployment, providing a robust foundation for future research into control strategies that optimise power transfer under real-world conditions.

The results demonstrate power demand trends consistent with those reported in the literature, but now achievable through simulation rather than through costly and time-intensive system development, deployment, and data collection. With this enhanced model, further investigation into practical DWPT implementations can be pursued by expanding the system to incorporate multiple coils for power transfer.

Extending the model to include multiple transmitter coils moves the concept closer to providing multiple points of access for DWPT, which can be strategically connected at various locations within the grid. This enables the exploration of the broader impacts that multiple DWPT connection points may have on grid stability, load distribution, and infrastructure planning. Furthermore, as more vehicles are introduced into the system, multiple secondary coils would naturally be present, capturing the increased complexity and variability of real-world traffic conditions and power demands. This extension allows for a more comprehensive analysis of the dynamic interactions between vehicles, the wireless charging infrastructure, and the wider power grid, supporting the development of scalable and resilient DWPT systems.

During development of simulations, the time per simulation became an issue as complexity of circuits increased. To reduce this time and enable an environment for faster development while maintaining result accuracy, work on reducing simulation frequency begun. Several methods and equivalent circuits were tested before arriving at the present solution. Replacing all high frequency switching components, the proposed solution was able to reduce the simulation time by a factor of 30, while incurring only a 6% accuracy penalty. This work brought insight into the modelling and behaviour, giving an accurate model of grid and load characteristics during charging.

Collaborative work on V2G demonstrated the potential of utilising EVs for grid frequency control by presenting an optimisation controller designed to determine the most effective use of EV participation within such schemes. This approach provided valuable insight into the operational benefits of integrating EVs as distributed energy resources, highlighting how coordinated charging and discharging strategies can support grid stability and reduce reliance on traditional balancing services. As the number of grid-connected EVs increases, the aggregated flexibility they provide becomes a critical asset for maintaining frequency and voltage levels, particularly under conditions of high renewable energy penetration.

Incorporating these capabilities into a unified framework opens opportunities for exploring how multiple charging points — static and dynamic — and multiple vehicles interact with the wider power system. This integration would allow for more comprehensive modelling of the impacts of large-scale EV adoption on grid infrastructure, power quality, and energy market dynamics. Ultimately, this work lays the groundwork for further research into optimised control strategies, multi-objective coordination, and the practical deployment of scalable solutions that leverage the synergies between V2G, DWPT, and smart grid technologies.

7.1 Future work

Following the main simulation work presented in Chapter 5, several avenues for future research have been identified to enhance the accuracy and practical relevance of the proposed WPT and DWPT models. One important next step is to refine the simulation and mod-

elling techniques to minimise errors and improve overall model fidelity. In particular, further investigation into the equivalent circuit representation of the WPT system could focus on directly modelling the secondary-side voltage rather than approximating it with an equivalent resistance could provide more accuracy in incorporating converter behaviour. Although the inclusion of a controlled rectifier proved challenging in the current work, exploring alternative modelling methods could help overcome these limitations. Similarly, integrating inverter control within the simulation will require further analysis of switching behaviour, modulation techniques, and control-loop interactions to ensure stable and efficient operation.

Expanding the system to include multiple transmitter and receiver coils is another significant area for further research. Modelling multiple coils would enable the simulation of realistic DWPT scenarios, where vehicles can charger from multiple coils as they travel along a roadway. This development would move the model towards a practical representation of real-world deployments and trial systems. Implementing such functionality will require scaling up the simulation environment and accurately defining the mutual inductance relationships between each pair of coils. As system complexity increases with each added coil, it will be essential to validate these models with practical experiments to identify any oversights or oversimplifications. Developing a small-scale test-bed with multiple transmitters and receivers would help confirm the accuracy of the simulations and provide valuable data for refining control strategies.

Furthermore, it would be beneficial to explore and compare different topologies and control schemes specifically tailored for DWPT. To date, many circuit and control design decisions are based on conclusions drawn from static WPT systems; however, the dynamic nature of DWPT introduces additional challenges and opportunities that merit dedicated analysis. Future studies should aim to quantify the trade-offs between different configurations, such as the use of multiple smaller coils versus fewer larger coils, and assess how these choices impact system performance, efficiency, cost, and ease of deployment. Investigating strategies for optimised coil activation, power flow management, and seamless handover between coils will also be crucial for ensuring reliable and efficient energy transfer under varying vehicle speeds and traffic conditions.

Another key area of future work involves assessing the broader grid impacts of large-scale DWPT deployment. Building up to a larger circuit model that includes multiple DWPT transmitters connected across a distribution network would allow for detailed studies of how these systems influence distribution bus voltages, power quality, and grid stability. This expanded model could be used to develop and test advanced control algorithms that coordinate the operation of DWPT systems with other grid assets, including renewable generation and V2G resources. Such research would provide deeper insights into how to integrate DWPT into existing infrastructure while maximising the potential benefits for grid flexibility and decarbonisation goals.

Finally, more focused analysis should be conducted to address the challenges associated with rectifier operation under varying coupling conditions. As highlighted during the modelling process, accuracy issues are most prevalent at low coupling levels or during low-power operation, when the converter may enter discontinuous conduction mode (DCM), causing the equivalent resistance of the WPT model to change dynamically. Developing more precise models will enhance the reliability and performance of future DWPT systems.

In summary, future research should aim to refine system accuracy, expand the scope

to multi-coil configurations, explore alternative topologies and control methods, investigate practical implementations, and quantify impacts on the wider grid. This work will help bridge the gap between simulation and real-world deployment, supporting the development of robust, efficient, and scalable DWPT solutions for the future of electric mobility.

8 Appendix

8.1 Mutual Inductance for a Pair of Square Coils

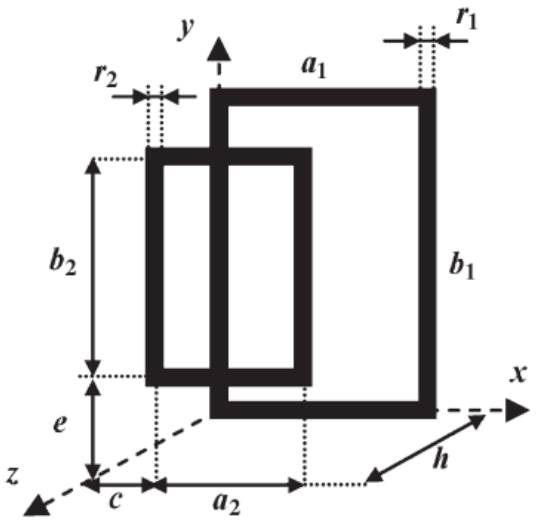

Figure 8.1: Rectangular coil relative position and parameters [157].

Figure 8.1 shows a visual representation of two square coils relative to each other. Based on the diagram, the coil self inductance (L_i) is given by:

$$L_i = \frac{\mu_0}{\pi} N_i^2 \left[a_i \cdot \ln\left(\frac{2a_i b_i}{r_i \left(a_i + \sqrt{a_i^2 + b_i^2} \right)} \right) + b_i \cdot \ln\left(\frac{2a_i b_i}{r_i \left(b_i + \sqrt{a_i^2 + b_i^2} \right)} \right) - 2\left(a_i + b_i - \sqrt{a_i^2 + b_i^2} \right) + 0.25(a_i + b_i) \right] \tag{193}$$

Now, for mutual inductance calculations, we define:

$$\begin{aligned} d &= a_1 - a_2 - c, & g &= a_1 - c, \\ m &= a_2 + c, & p &= b_1 - e, \\ q &= b_2 + e, & t &= b_1 - b_2 - e. \end{aligned}$$

The mutual inductance M is expressed as:

$$
\begin{aligned}
M = \frac{\mu_0}{4\pi} N_1 N_2 \Bigg[& \\
& \Bigg[d \ln \left(\frac{d + \sqrt{h^2 + (-t)^2 + d^2}}{d + \sqrt{h^2 + d^2 + q^2}} \right) \\
& + h \ln \left(\frac{g + \sqrt{h^2 + q^2 + g^2}}{g + \sqrt{h^2 + g^2 + (-t)^2}} \right) \\
& + c \ln \left(\frac{-c + \sqrt{h^2 + q^2 + c^2}}{-c + \sqrt{h^2 + c^2 + (-t)^2}} \right) \\
& + m \ln \left(\frac{-m + \sqrt{h^2 + (-t)^2 + m^2}}{-m + \sqrt{h^2 + m^2 + q^2}} \right) \\
& + \sqrt{h^2 + q^2 + d^2} - \sqrt{h^2 + q^2 + g^2} \\
& - \sqrt{h^2 + q^2 + m^2} + \sqrt{h^2 + q^2 + c^2} \\
& + \sqrt{h^2 + (-t)^2 + g^2} - \sqrt{h^2 + (-t)^2 + d^2} \\
& + \sqrt{h^2 + (-t)^2 + m^2} - \sqrt{h^2 + (-t)^2 + c^2} \Bigg] \\
& - \Bigg[d \ln \left(\frac{d + \sqrt{h^2 + (-p)^2 + d^2}}{d + \sqrt{h^2 + d^2 + e^2}} \right) \\
& + g \ln \left(\frac{h + \sqrt{h^2 + e^2 + g^2}}{g + \sqrt{h^2 + h^2 + (-p)^2}} \right) \\
& + c \ln \left(\frac{-c + \sqrt{h^2 + e^2 + c^2}}{-c + \sqrt{h^2 + c^2 + (-p)^2}} \right) \\
& + m \ln \left(\frac{-m + \sqrt{h^2 + (-p)^2 + m^2}}{-m + \sqrt{h^2 + m^2 + e^2}} \right) \\
& + \sqrt{h^2 + e^2 + d^2} - \sqrt{h^2 + e^2 + g^2} \\
& - \sqrt{h^2 + e^2 + m^2} + \sqrt{h^2 + e^2 + c^2} \\
& + \sqrt{h^2 + (-p)^2 + g^2} - \sqrt{h^2 + (-p)^2 + d^2} \\
& + \sqrt{h^2 + (-p)^2 + m^2} - \sqrt{h^2 + (-p)^2 + c^2} \Bigg]
\end{aligned}
$$

$$
\begin{aligned}
&+\left[t\ln\left(\frac{t+\sqrt{h^2+(-g)^2+t^2}}{t+\sqrt{h^2+t^2+c^2}}\right)\right.\\
&+p\ln\left(\frac{p+\sqrt{h^2+p^2+c^2}}{p+\sqrt{h^2+(-g)^2+p^2}}\right)\\
&+e\ln\left(\frac{-e+\sqrt{h^2+e^2+c^2}}{-e+\sqrt{h^2+e^2+(-g)^2}}\right)\\
&+q\ln\left(\frac{-q+\sqrt{h^2+(-q)^2+q^2}}{-q+\sqrt{h^2+c^2+q^2}}\right)\\
&+\sqrt{h^2+c^2+t^2}-\sqrt{h^2+c^2+p^2}\\
&-\sqrt{h^2+c^2+q^2}+\sqrt{h^2+e^2+c^2}\\
&+\sqrt{h^2+(-g)^2+p^2}-\sqrt{h^2+(-g)^2+t^2}\\
&\left.+\sqrt{h^2+(-g)^2+q^2}-\sqrt{h^2+(-g)^2+e^2}\right]\\
&-\left[t\ln\left(\frac{t+\sqrt{h^2+(-d)^2+t^2}}{t+\sqrt{h^2+t^2+m^2}}\right)\right.\\
&+p\ln\left(\frac{p+\sqrt{h^2+m^2+p^2}}{p+\sqrt{h^2+(-d)^2+p^2}}\right)\\
&+e\ln\left(\frac{-e+\sqrt{h^2+e^2+m^2}}{-e+\sqrt{h^2+e^2+(-d)^2}}\right)\\
&+q\ln\left(\frac{-q+\sqrt{h^2+(-d)^2+q^2}}{-q+\sqrt{h^2+m^2+q^2}}\right)\\
&+\sqrt{h^2+m^2+t^2}-\sqrt{h^2+m^2+p^2}\\
&-\sqrt{h^2+m^2+q^2}+\sqrt{h^2+e^2+m^2}\\
&+\sqrt{h^2+(-d)^2+p^2}-\sqrt{h^2+(-d)^2+t^2}\\
&\left.+\sqrt{h^2+(-d)^2+q^2}-\sqrt{h^2+(-d)^2+e^2}\right].
\end{aligned}
$$

8.2 Reduced frequency simulation code

8.2.1 DC/DC Converter Code

```
function y = Buck(u)
% Input signals
Vs = u(1);        % input voltage
i1 = u(2);    % input current
i2 = u(3);    % output current (measurement)
d = u(4);         % duty cycle
```

```
mode = u(5);        % switching frequency
vc1 = u(6);         % capacitor 1 voltage
iL = u(7);          % inductor current
vc2 = u(8);         % capcitor 2 voltage

% Circuit parameters
L= 0.005;          % inductance
C1 = 0.0015;       % output capacitance
C2 = 0.0015;       % output capacitance

%(iL*.05 + i2*.05) dampens the output using "on" resitance of components

switch mode
    case 1 %Buck
        dvc1 = (i1-d*iL)/C1;
        dil = (d*vc1-vc2 - (iL*.05 + i2*.05))/L;
        dvc2 = (iL-i2)/C2;

        if iL<0 %Diode forward bias
            if dil<0
                dil=0;
            end
        end

    case 2 %Buck-boost
        dvc1 = (i1-d*iL)/C1;
        dil = (d*vc1-vc2*(1-d)-(iL*.05 + i2*.05))/L;
        dvc2 = ((1-d)*iL-i2)/C2;

        if iL<0 %Diode forward bias
            if dil<0
                dil=0;
            end
        end

    case 3 %boost
        dvc1 = (i1-iL)/C1;
        dil = (vc1-vc2*(1-d)-(iL*.05 + i2*.05))/L;
        dvc2 = ((1-d)*iL-i2)/C2;

        if iL<0 %Diode forward bias
            if dil<0
                dil=0;
            end
        end
```

```
    case 4 %reverse buck
        dvc1 = (i1-iL)/C1;
        dil = (vc1-d*vc2 - (iL*.05 + i2*.05))/L;
        dvc2 = (d*iL-i2)/C2;

        if iL>0 %Diode forward bias
            if dil>0
                dil=0;
            end
        end

    case 5
        dvc1 = (i1-(1-d)*iL)/C1;
        dil = (vc1*(1-d)-d*vc2-(iL*.05 + i2*.05))/L;
        dvc2 = (d*iL-i2)/C2;

        if iL>0 %Diode forward bias
            if dil>0
                dil=0;
            end
        end

    case 6
        dvc1 = (i1-(1-d)*iL)/C1;
        dil = (vc1*(1-d)-vc2-(iL*.05 + i2*.05))/L;
        dvc2 = (iL-i2)/C2;

        if iL>0 %Diode forward bias
            if dil>0
                dil=0;
            end
        end

    otherwise
        disp('error');
        dvc1 =0;
        dil =0;
        dvc2 =0;
end

% Output results
y = [dvc1 dil dvc2];
```

8.2.2 WPT Converter Code

```
function y = fcn(u)
% Define inputs from mux.
mode = u(1);  %V2G mode
f = u(2); % frequency
k = u(3); % cooupling factor (k)
v1 = u(4); % Primary side DC voltage
i1 = u(5); % Priary DC current
v2 = u(6); % Secondary side DC voltage
i2 = u(7); % Secondary DC current
il1 = u(8); % Primary coil current
il2 = u(9); % Secondary coil current

eta = .90; %Rectifier efficiency

%RLC coils and compensation capcitors
L1 = 1.3241e-04;
L2 = 1.3241e-04;
C1 = 2.6477e-08;
C2 = 2.6477e-08;
R1 = 1.3e-3;
R2 = 1.3e-3;

M = k*sqrt(L1*L2);
w = 2*pi*f;



switch mode
    case 0 % forward mode
        R_load = abs(v2/i2)*eta;
        if R_load>1e2 %Limit to avoid infinity
            R_load = 1e2;
        end

        Z1 = R1 + 1j*w*(L1) + 1/(1j*w*C1);
        Z2 = R_load + R2 + 1j*w*(L2) + 1/(1j*w*C2);

        sf = 9.5;
        dil1 = (1.25*v1 - il1*real(Z1) - w*M*il2)/abs(imag(Z1)/sf);
        dil2 = (w*M*il1 - real(Z2)*il2)/abs(imag(Z2)/sf);
    otherwise %reverse mode
        R_load = abs(v1/i1)*eta;
        if R_load>1e2 %Limit to avoid infinity
            R_load = 1e2;
        end
```

```
        Z1 = R_load + R1 + 1j*w*(L1) + 1/(1j*w*C1);
        Z2 = R2 + 1j*w*(L2) + 1/(1j*w*C2);

        sf = 9.5;
        dil1 = (w*M*il2 - il1*real(Z1))/abs(imag(Z1)/sf);
        dil2 = (-1.25*v2 - w*M*il1 - real(Z2)*il2)/abs(imag(Z2)/sf);

end
y = [dil1, dil2];
```

9 References

References

[1] United Nations Framework Convention on Climate Change. The paris agreement — unfccc. https://unfccc.int/process-and-meetings/the-paris-agreement. (Accessed on 06/15/2023).

[2] United Nations Framework Convention on Climate Change. Race to zero campaign — unfccc. https://unfccc.int/climate-action/race-to-zero-campaign. (Accessed on 06/15/2023).

[3] Un-convened net-zero asset owner alliance – united nations environment – finance initiative. https://www.unepfi.org/net-zero-alliance/. (Accessed on 06/15/2023).

[4] European Comission. A european green deal. https://commission.europa.eu/strategy-and-policy/priorities-2019-2024/european-green-deal_en. (Accessed on 06/15/2023).

[5] The climate pledge — be the planet's turning point. https://www.theclimatepledge.com/#main-navigation. (Accessed on 06/15/2023).

[6] Our World in Data. Emissions by sector - our world in data. https://ourworldindata.org/emissions-by-sector. (Accessed on 06/15/2023).

[7] Tianjin Chen, Xiao-Ping Zhang, Jianji Wang, Jianing Li, Cong Wu, Mingzhu Hu, and Huiping Bian. A review on electric vehicle charging infrastructure development in the uk. *Journal of Modern Power Systems and Clean Energy*, 8(2):193–205, 2020.

[8] Junjie Hu, Shi You, Morten Lind, and Jacob Østergaard. Coordinated charging of electric vehicles for congestion prevention in the distribution grid. *IEEE Transactions on Smart Grid*, 5(2):703–711, 2013.

[9] Chau KT LIU C, D WU, et al. Opportunities and challenges of vehicle-to-home, vehicle-to-vehicle and vehicle-to-grid technologies [j]. *Proceedings of the IEEE*, 101(11):2409–2427, 2013.

[10] Jiuqing Cai, Changsong Chen, Peng Liu, and Shanxu Duan. Centralized control of parallel connected power conditioning system in electric vehicle charge-discharge and storage integration station. *Journal of Modern Power Systems and Clean Energy*, 3(2):269–276, 2015.

[11] Nuh Erdogan, Fatih Erden, and Mithat Kisacikoglu. A fast and efficient coordinated vehicle-to-grid discharging control scheme for peak shaving in power distribution system. *Journal of Modern Power Systems and Clean Energy*, 6(3):555–566, 2018.

[12] Mahdi Kiaee, Andrew Cruden, and Suleiman Sharkh. Estimation of cost savings from participation of electric vehicles in vehicle to grid (v2g) schemes. *Journal of Modern Power Systems and Clean Energy*, 3(2):249–258, 2015.

[13] Bijan Bibak and Hatice Tekiner-Moğulkoç. A comprehensive analysis of vehicle to grid (v2g) systems and scholarly literature on the application of such systems. *Renewable Energy Focus*, 36:1–20, 2021.

[14] Mahmoud M Gamil, Tomonobu Senjyu, Hasan Masrur, Hiroshi Takahashi, and Mohammed Elsayed Lotfy. Controlled v2gs and battery integration into residential microgrids: Economic and environmental impacts. *Energy conversion and management*, 253:115171, 2022.

[15] UK Government. Cop26: The negotiations explained, Nov 2021.

[16] UK Government. Uk becomes first major economy to pass net zero emissions law - gov.uk. `https://www.gov.uk/government/news/uk-becomes-first-major-economy-to-pass-net-zero-emissions-law`. (Accessed on 06/15/2023).

[17] Committee on Climate Change. 2022 progress report to parliament - climate change committee. `https://www.theccc.org.uk/publication/2022-progress-report-to-parliament/`. (Accessed on 06/15/2023).

[18] UK Government. Consulting on ending the sale of new petrol, diesel and hybrid cars and vans - gov.uk. `https://www.gov.uk/government/consultations/consulting-on-ending-the-sale-of-new-petrol-diesel-and-hybrid-cars-and-vans`. (Accessed on 06/15/2023).

[19] UK Government. Vehicle licensing statistics: 2022 - gov.uk. `https://www.gov.uk/government/statistics/vehicle-licensing-statistics-2022`. (Accessed on 06/15/2023).

[20] Francisco Carranza, Olivier Paturet, and Sebastian Salera. Norway, the most successful market for electric vehicles. In *2013 World Electric Vehicle Symposium and Exhibition (EVS27)*, pages 1–6, 2013.

[21] International Energy Agency. Global ev outlook 2023 – analysis - iea. `https://www.iea.org/reports/global-ev-outlook-2023`. (Accessed on 06/28/2023).

[22] How many electric vehicles are there in the uk - ev market statistics 2023. `https://www.zap-map.com/ev-stats/ev-market/`. (Accessed on 06/28/2023).

[23] Virta Global. The global electric vehicle market in 2023 – virta. `https://www.virta.global/en/global-electric-vehicle-market`. (Accessed on 06/28/2023).

[24] Maria Carmen Falvo, Danilo Sbordone, I. Safak Bayram, and Michael Devetsikiotis. Ev charging stations and modes: International standards. In *2014 International Symposium on Power Electronics, Electrical Drives, Automation and Motion*, pages 1134–1139, 2014.

[25] Johannes Schäuble, Thomas Kaschub, Axel Ensslen, Patrick Jochem, and Wolf Fichtner. Generating electric vehicle load profiles from empirical data of three ev fleets in southwest germany. *Journal of Cleaner Production*, 150:253–266, 2017.

[26] Iec 61851-1: Electric vehicle conductive charging system – part 1: General requirements, 2017.

[27] Iec 62752: In-cable control and protection device (ic-cpd) for mode 2 charging of electric road vehicles, 2016.

[28] Institution of Engineering and Technology. *Code of Practice for Electric Vehicle Charging Equipment Installation*. IET, 4th edition, 2022.

[29] Sae j1772: Electric vehicle and plug-in hybrid electric vehicle conductive charge coupler, 2020.

[30] CHAdeMO Association. Chademo protocol specification, 2018. Available at: `https://www.chademo.com/`.

[31] Kristien Clement-Nyns, Edwin Haesen, and Johan Driesen. A comprehensive review of electric vehicle charging technologies and infrastructure. *IEEE Transactions on Industrial Informatics*, 8(1):15–25, 2012.

[32] Tests show electreon's wireless electric road system is ready for large-scale deployment — electreon. `https://electreon.com/articles/tests-show-electreons-wireless-electric-road-system-is-ready-for-large-scale-deplo` (Accessed on 09/23/2024).

[33] National grid - dynamic charging of vehicles (dynacov). `https://www.nationalgrid.co.uk/innovation/projects/dynamic-charging-of-vehicles-dynacov`. (Accessed on 09/23/2024).

[34] Our wireless charging electric road projects — electreon. `https://electreon.com/projects`. (Accessed on 09/27/2024).

[35] Editorial staff. Electreon: wireless charging on its way from demo to commercial deployments. interview with head of global strategy charlie levine - sustainable bus, 5 2025. [Online; accessed 2025-06-11].

[36] Norway's wireless ev charging roads: A game changer - yocharge. `https://yocharge.com/news/norways-wireless-ev-charging-roads-a-game-changer/`. (Accessed on 09/27/2024).

[37] Mdot, city of detroit and electreon unveil nation's first public ev-charging roadway at michigan central — city of detroit. `https://detroitmi.gov/news/mdot-city-detroit-and-electreon-unveil-nations-first-public-ev-charging-roadway-mi` (Accessed on 09/27/2024).

[38] Electreon unveils the world's first commercial wireless charging terminal for buses in israel — electreon. https://electreon.com/articles/electreon-unveils-the-worlds-first-commercial-wireless-charging-terminal-for-buses-~:text=The%20commercial%20project%2C%20delivered%20to,in%20a%20distributed%20energy%20model. (Accessed on 09/27/2024).

[39] Shamala Gadgil, Karthikeyan Ekambaram, Huw Davies, Andrew Jones, and Stewart Birrell. Determining the social, economic, political and technical factors significant to the success of dynamic wireless charging systems through a process of stakeholder engagement. *Energies*, 15(3):930, 2022.

[40] Mohammad Rabih, Maen Takruri, Mohammad Al-Hattab, Amal A Alnuaimi, and Mouza R Bin Thaleth. Wireless charging for electric vehicles: A survey and comprehensive guide. *World Electric Vehicle Journal*, 15(3):118, 2024.

[41] Yuvaraja Shanmugam, R Narayanamoorthi, Pradeep Vishnuram, Mohit Bajaj, Kareem M AboRas, Padmanabh Thakur, et al. A systematic review of dynamic wireless charging system for electric transportation. *IEEE Access*, 10:133617–133642, 2022.

[42] Shunpan Liu, Junjie Xu, Yuhang Liu, Yong Li, Yeran Liu, and Zhengyou He. Phenomenon, modeling, and analysis of transient power impacts and oscillations in fast-moving dynamic wireless power transfer system. *IEEE Transactions on Industrial Electronics*, 2025.

[43] Deyu Wang, Chaowei Fu, Qinglin Zhao, and Ting Hu. A pso-based optimization design of w-type noncontact transformer for stable power transfer in dwpt system. *IEEE Transactions on Industry Applications*, 58(1):1211–1221, 2021.

[44] Xiang Ma, Yuan Zhou, Hanwen Zhang, Qun Wang, Haijian Sun, Hongjie Wang, and Rose Qingyang Hu. Exploring communication technologies, standards, and challenges in electrified vehicle charging. *arXiv preprint arXiv:2403.16830*, 2024.

[45] Hongjie Wang, Ujjwal Pratik, Aleksandar Jovicic, Nazmul Hasan, and Zeljko Pantic. Dynamic wireless charging of medium power and speed electric vehicles. *IEEE Transactions on Vehicular Technology*, 70(12):12552–12566, 2021.

[46] V Ravichandran, Gopinath Singaram, J Velmurugan, M Sivaramkrishnan, J Karthikeyan, and Neelam Sanjeev Kumar. A review of the challenges in ev wireless charging technology. In *2023 8th International Conference on Communication and Electronics Systems (ICCES)*, pages 263–269. IEEE, 2023.

[47] Met Office. New global temperature records on the horizon - met office. https://www.metoffice.gov.uk/about-us/press-office/news/weather-and-climate/2023/global-temperatures-set-to-reach-new-records-in-next-five-years. (Accessed on 06/14/2023).

[48] NASA. Effects — facts – climate change: Vital signs of the planet. https://climate.nasa.gov/effects/#:~:text=Earth%20Will%20Continue%

20to%20Warm,and%20rainfall%20from%20tropical%20cyclones. (Accessed on 06/14/2023).

[49] Met Office. Effects of climate change - met office. https://www.metoffice.gov.uk/weather/climate-change/effects-of-climate-change. (Accessed on 06/14/2023).

[50] Adeola Olufunke Kehinde. The effect of global warming in nigeria: Flood in perspective. *Studia Prawno-Ekonomiczne*, 124:39–58, 2022.

[51] Sergio M Vicente-Serrano, Steven M Quiring, Marina Pena-Gallardo, Shanshui Yuan, and Fernando Dominguez-Castro. A review of environmental droughts: Increased risk under global warming? *Earth-Science Reviews*, 201:102953, 2020.

[52] Ubydul Haque, Paula F. da Silva, Graziella Devoli, Jürgen Pilz, Bingxin Zhao, Asmaa Khaloua, Wahyu Wilopo, Peter Andersen, Ping Lu, Juneseok Lee, Taro Yamamoto, David Keellings, Jian-Hong Wu, and Gregory E. Glass. The human cost of global warming: Deadly landslides and their triggers (1995–2014). *Science of The Total Environment*, 682:673–684, 2019.

[53] F. Beugnet and K. Chalvet-Monfray. Impact of climate change in the epidemiology of vector-borne diseases in domestic carnivores. *Comparative Immunology, Microbiology and Infectious Diseases*, 36(6):559–566, 2013.

[54] Met Office. Global-average temperature records - met office. https://www.metoffice.gov.uk/weather/climate/science/global-temperature-records. (Accessed on 06/14/2023).

[55] Zhaoxi Liu and Qiuwei Wu. Ev charging analysis based on the national travel surveys of the nordic area. In *2014 IEEE PES General Meeting— Conference & Exposition*, pages 1–6. IEEE, 2014.

[56] Editorial Staff. Witricity tests wireless chargers with yutong, 2 2023. [Online; accessed 2025-05-20].

[57] Marilyn Burkley. Charged evs — electreon and xos to implement wireless charging for ups delivery vehicles in michigan - charged evs, 12 2024. [Online; accessed 2025-05-20].

[58] Editorial Staff. First airport with wireless e-bus charging in the world. us: Kansas airport turns to momentum dynamics, 1 2022. [Online; accessed 2025-05-20].

[59] Noah Jampol. Tesla announces highly anticipated new wireless charging tech — here's how it could transform the industry, 11 2024. [Online; accessed 2025-05-20].

[60] Bernhard Walzel, Christopher Sturm, Jurgen Fabian, and Mario Hirz. Automated robot-based charging system for electric vehicles. https://core.ac.uk/download/pdf/53025466.pdf. (Accessed on 06/28/2023).

[61] Ruifeng Zhang, Bizhong Xia, Baohua Li, Libo Cao, Yongzhi Lai, Weiwei Zheng, Huawen Wang, Wei Wang, and Mingwang Wang. A study on the open circuit voltage and state of charge characterization of high capacity lithium-ion battery under different temperature. *Energies*, 11(9):2408, 2018.

[62] Mohammad Kamrul Hasan, Md Mahmud, AKM Ahasan Habib, SMA Motakabber, and Shayla Islam. Review of electric vehicle energy storage and management system: Standards, issues, and challenges. *Journal of energy storage*, 41:102940, 2021.

[63] onsemi.com/powersolutions/content.do?id=19106. `https://www.onsemi.com/PowerSolutions/content.do?id=19106`. (Accessed on 09/17/2024).

[64] Cc613 charge controller. `https://www.bender-uk.com/products/charge-controller/cc613-charge-controller/`. (Accessed on 09/17/2024).

[65] Yameena Tahir, Irfan Khan, Syed Rahman, Muhammad Faisal Nadeem, Atif Iqbal, Yinliang Xu, and Mohammad Rafi. A state-of-the-art review on topologies and control techniques of solid-state transformers for electric vehicle extreme fast charging. *IET power electronics*, 14(9):1560–1576, 2021.

[66] Jae Hee Kim, Byung-Song Lee, Jun-Ho Lee, Seung-Hwan Lee, Chan-Bae Park, Shin-Myung Jung, Soo-Gil Lee, Kyung-Pyo Yi, and Jeihoon Baek. Development of 1-mw inductive power transfer system for a high-speed train. *IEEE Transactions on Industrial Electronics*, 62(10):6242–6250, 2015.

[67] Yabiao Gao, Antonio Ginart, Kathleen Blair Farley, and Zion Tsz Ho Tse. Misalignment effect on efficiency of wireless power transfer for electric vehicles. In *2016 IEEE Applied Power Electronics Conference and Exposition (APEC)*, pages 3526–3528, 2016.

[68] Dylan McGrath. Qualcomm sells off halo wireless ev charging technology - ee times, 2 2019. [Online; accessed 2025-05-20].

[69] Renault and qualcomm sign mou on wireless ev charging technology — global highways, 5 2025. [Online; accessed 2025-05-20].

[70] Lawrence Ulrich. Wireless ev charging: Oak ridge sets a new record - ieee spectrum, 7 2024. [Online; accessed 2025-05-20].

[71] By Chris Randall. Oak ridge researchers achieve wireless charging with 96% efficiency - electrive.com, 3 2024. [Online; accessed 2025-05-20].

[72] Charles Morris. Charged evs — evatran wireless ev charging system goes on sale with special promotional pricing - charged evs, 1 2014. [Online; accessed 2025-05-20].

[73] Web Team. Wireless ev charging leaders push for standard - electric & hybrid vehicle technology international, 11 2024. [Online; accessed 2025-05-20].

[74] InductEV. Two global leaders in wireless ev charging strike agreement to standardize technology's interoperability, 11 2024. [Online; accessed 2025-05-20].

[75] Ahmed AS Mohamed, Ahmed A Shaier, Hamid Metwally, and Sameh I Selem. Wireless charging technologies for electric vehicles: Inductive, capacitive, and magnetic gear. *IET Power Electronics*, 2023.

[76] Chang-Hua Lin, Mohammad Amir, Mohd Tariq, Mohd Shahvez, Basem Alamri, Ahmad Alahmadi, Mobashshir Siddiqui, and Abdul R Beig. Comprehensive analysis of ipt v/s cpt for wireless ev charging and effect of capacitor plate shape and foreign particle on cpt. *Processes*, 9(9):1619, 2021.

[77] Jiejian Dai and Daniel C Ludois. A survey of wireless power transfer and a critical comparison of inductive and capacitive coupling for small gap applications. *IEEE Transactions on Power Electronics*, 30(11):6017–6029, 2015.

[78] Manh Tuan Tran, Sarath Thekkan, Hakan Polat, Dai-Duong Tran, Mohamed El Baghdadi, and Omar Hegazy. Inductive wireless power transfer systems for low-voltage and high-current electric mobility applications: Review and design example. *Energies*, 16(7):2953, 2023.

[79] P Kašpar and P Ripka. Induction coils: voltage versus current output. In *Imeko World Congress*, volume 5, pages 55–60, 2000.

[80] Kotub Uddin, Andrew D Moore, Anup Barai, and James Marco. The effects of high frequency current ripple on electric vehicle battery performance. *Applied energy*, 178:142–154, 2016.

[81] Zhimeng Liu, Lifang Wang, Chengliang Yin, Yanjie Guo, and Chengxuan Tao. A research on constant voltage output characteristics of wireless power transfer system with a dc-dc converter. In *2019 IEEE 15th Brazilian Power Electronics Conference and 5th IEEE Southern Power Electronics Conference (COBEP/SPEC)*, pages 1–4. IEEE, 2019.

[82] Van-Binh Vu, Duc-Hung Tran, and Woojin Choi. Implementation of the constant current and constant voltage charge of inductive power transfer systems with the double-sided lcc compensation topology for electric vehicle battery charge applications. *IEEE Transactions on Power Electronics*, 33(9):7398–7410, 2017.

[83] Farzad Farajizadeh, D Mahinda Vilathgamuwa, Dejan Jovanovic, Prasad Jayathurathnage, Gerard Ledwich, and Udaya Madawala. Expandable n-legged converter to drive closely spaced multitransmitter wireless power transfer systems for dynamic charging. *IEEE Transactions on Power Electronics*, 35(4):3794–3806, 2019.

[84] Chris Randall. Alstom develops gound-based charging for electric buses - electrive.com. `https://www.electrive.com/2019/09/27/alstom-develops-conductive-charging-for-electric-buses/`. (Accessed on 06/28/2023).

[85] National chinese platform picks matrix charging for ev automated charging technology. `https://www.aftermarketnews.com/`

national-chinese-platform-picks-matrix-charging-for-ev-automated-charging-technolo
(Accessed on 09/18/2024).

[86] Hildegard Suntinger. Wireless charging stations with robotic technology for e-cars. https://innovationorigins.com/en/start-up-of-the-day-wireless-charging-stations-with-robotic-technology-for-e-cars/ (Accessed on 06/28/2023).

[87] Automated vehicle charging – energy – motion. http://www.ipft.co.uk/automated-vehicle-charging/. (Accessed on 09/18/2024).

[88] VOLTERIO. Volterio — automatic electric vehicle charging. https://www.volterio.com/. (Accessed on 06/28/2023).

[89] Trl — mole trials of conductive ev charging. https://www.trl.co.uk/projects/mole-trials-of-conductive-ev-charging. (Accessed on 09/18/2024).

[90] J Svarc. Bidirectional ev charging explained - v2g, v2h & v2l — clean energy reviews. https://www.cleanenergyreviews.info/blog/bidirectional-ev-charging-v2g-v2h-v2l#:~:text=For%20V2H%20to%20operate%2C%20it,to%20and%20from%20the%20grid. (Accessed on 07/19/2024).

[91] Yin Yao, Wenzhong Gao, and James Momoh. Performance optimization and evaluation of v2g in regulated and deregulated microgrid. In *2017 IEEE Conference on Energy Internet and Energy System Integration (EI2)*, pages 1–6. IEEE, 2017.

[92] Dai Wang, Jonathan Coignard, Teng Zeng, Cong Zhang, and Samveg Saxena. Quantifying electric vehicle battery degradation from driving vs. vehicle-to-grid services. *Journal of Power Sources*, 332:193–203, 2016.

[93] Lav Agarwal, Wang Peng, and Lalit Goel. Probabilistic estimation of aggregated power capacity of evs for vehicle-to-grid application. In *2014 International Conference on Probabilistic Methods Applied to Power Systems (PMAPS)*, pages 1–6, 2014.

[94] Songyu Huang, Chengjin Ye, Yi Ding, Bo Zou, Chenjin Xu, Kun Wang, and Lei Wang. Estimation of ev charging profiles based on the diffusion estimator. In *2019 IEEE Sustainable Power and Energy Conference (iSPEC)*, pages 2293–2297, 2019.

[95] Manoj Hans and Pritam Deshmukh. Bidirectional wireless power transfer system for electric vehicles-overview and implementation. In *2020 International Conference on Smart Electronics and Communication (ICOSEC)*, pages 1062–1065. IEEE, 2020.

[96] Sourav Das, Aniruddha Bhattacharya, and Parimal Acharjee. Charging scheduling of electric vehicles (ev) in probabilistic scenario considering grid-to-vehicle (g2v) and vehicle-to-grid (v2g). In *2020 IEEE Calcutta Conference (CALCON)*, pages 467–472, 2020.

[97] Reza Hemmati, Hasan Mehrjerdi, Nasser A Al-Emadi, and Elyas Rakhshani. Mutual vehicle-to-home and vehicle-to-grid operation considering solar-load uncertainty. In *2019 2nd International Conference on Smart Grid and Renewable Energy (SGRE)*, pages 1–4, 2019.

[98] Bunyamin Yagcitekin, Mehmet Uzunoglu, Arif Karakas, and Mucahit Vurgun. Assessment of a car park with electric vehicles. In *4th International Conference on Power Engineering, Energy and Electrical Drives*, pages 961–964, 2013.

[99] Saeed Rezaee, Ebrahim Farjah, and Benyamin Khorramdel. Probabilistic analysis of plug-in electric vehicles impact on electrical grid through homes and parking lots. *IEEE Transactions on Sustainable Energy*, 4(4):1024–1033, 2013.

[100] M. Abul Masrur, Annette G. Skowronska, Janie Hancock, Steven W. Kolhoff, Dean Z. McGrew, James C. Vandiver, and Jim Gatherer. Military-based vehicle-to-grid and vehicle-to-vehicle microgrid—system architecture and implementation. *IEEE Transactions on Transportation Electrification*, 4(1):157–171, 2018.

[101] Yuvaraja Shanmugam, R Narayanamoorthi, Pradeep Vishnuram, et al. A systematic review of dynamic wireless charging system for electric transportation. *IEEE Access*, 10:133617–133642, 2022.

[102] Chuanyue Li, Xue Dong, Liana M Cipcigan, et al. Economic viability of dynamic wireless charging technology for private evs. *IEEE Transactions on Transportation Electrification*, 9(1):1845–1861, 2023.

[103] Lei Wang, Udaya K Madawala, and Man-Chung Wong. A wireless vehicle-to-grid-to-home power interface with an adaptive dc link. *IEEE Journal of Emerging and Selected Topics in Power Electronics*, 9(2):2373–2386, 2021.

[104] Shiyao Zhang and James J. Q. Yu. Electric vehicle dynamic wireless charging system: Optimal placement and vehicle-to-grid scheduling. *IEEE Internet of Things Journal*, 9(8):6047–6060, 2022.

[105] J Rahulkumar, R Narayanamoorthi, Mohit Bajaj, et al. An empirical survey on wireless inductive power pad and resonant magnetic field coupling for in-motion ev charging system. *IEEE Access*, 11:4660–4678, 2023.

[106] Aganti Mahesh, Bharatiraja Chokkalingam, and Lucian Mihet-Popa. Inductive wireless power transfer charging for electric vehicles–a review. *IEEE Access*, 9:137667–137713, 2021.

[107] Yuechuan Tao, Jing Qiu, Shuying Lai, et al. Coordinated planning of dynamic wireless charging systems and electricity networks considering range anxiety of electric vehicles. *IEEE Transactions on Smart Grid*, 15(4):3876–3890, 2024.

[108] Tasneim Aldhanhani, Anuj Abraham, Wassim Hamidouche, and Mostafa Shaaban. Future trends in smart green iov: Vehicle-to-everything in the era of electric vehicles. *IEEE Open Journal of Vehicular Technology*, 5:278–296, 2024.

[109] Kotub Uddin, Andrew D. Moore, Anup Barai, and James Marco. The effects of high frequency current ripple on electric vehicle battery performance. *Applied Energy*, 178:142–154, 2016.

[110] Martin Johannes Brand, Markus Hans Hofmann, Simon S Schuster, Peter Keil, and Andreas Jossen. The influence of current ripples on the lifetime of lithium-ion batteries. *IEEE Transactions on Vehicular Technology*, 67(11):10438–10445, 2018.

[111] Ishaan Puranik, Lei Zhang, and Jiangchao Qin. Impact of low-frequency ripple on lifetime of battery in mmc-based battery storage systems. In *2018 IEEE Energy Conversion Congress and Exposition (ECCE)*, pages 2748–2752. IEEE, 2018.

[112] Yeran Liu, Udaya Kumara Madawala, Ruikun Mai, and Zhengyou He. Zero-phase-angle controlled bidirectional wireless ev charging systems for large coil misalignments. *IEEE Transactions on Power Electronics*, 35(5):5343–5353, 2019.

[113] Lei Zhao, Duleepa J Thrimawithana, and Udaya K Madawala. Hybrid bidirectional wireless ev charging system tolerant to pad misalignment. *IEEE Transactions on Industrial Electronics*, 64(9):7079–7086, 2017.

[114] WiTricity. Automotive solutions. `https://witricity.com/products/automotive-solutions/`. (Accessed on 07/06/2023).

[115] Chris Randall. Momentum dynamics presents inductive charging system with two power classes - electrive.com. `https://www.electrive.com/2022/05/06/momentum-dynamics-presents-inductive-charging-system-with-two-power-classes/`. (Accessed on 07/06/2023).

[116] Bruno Dalla Chiara, Giovanni Pede, Francesco Deflorio, and Marco Zanini. Electrifying buses for public transport: Boundaries with a performance analysis based on method and experience. *Sustainability*, 15(19):14082, 2023.

[117] Taylor M Fisher, Kathleen Blair Farley, Yabiao Gao, Hua Bai, and Zion Tsz Ho Tse. Electric vehicle wireless charging technology: a state-of-the-art review of magnetic coupling systems. *Wireless Power Transfer*, 1(2):87–96, 2014.

[118] Devendra Patil, Matthew K McDonough, John M Miller, Babak Fahimi, and Poras T Balsara. Wireless power transfer for vehicular applications: Overview and challenges. *IEEE Transactions on Transportation Electrification*, 4(1):3–37, 2017.

[119] WAVE. No limits. no cables. no range anxiety. `https://waveipt.com/`. (Accessed on 07/06/2023).

[120] Hao Feng, Reza Tavakoli, Omer C Onar, and Zeljko Pantic. Advances in high-power wireless charging systems: Overview and design considerations. *IEEE Transactions on Transportation Electrification*, 6(3):886–919, 2020.

[121] Seungmin Jeong, Young Jae Jang, Dongsuk Kum, and Min Seok Lee. Charging automation for electric vehicles: Is a smaller battery good for the wireless charging electric vehicles? *IEEE Transactions on Automation Science and Engineering*, 16(1):486–497, 2018.

[122] Milad Behnamfar, Temitayo O. Olowu, Mohd Tariq, and Arif Sarwat. Comprehensive review on power pulsation in dynamic wireless charging of electric vehicles. *IEEE Access*, 12:66858–66882, 2024.

[123] Benitto Albert Rayan, Umashankar Subramaniam, and S. Balamurugan. Wireless power transfer in electric vehicles: A review on compensation topologies, coil structures, and safety aspects. *Energies*, 16(7), 2023.

[124] Chunhua Liu, Chaoqiang Jiang, and Chun Qiu. Overview of coil designs for wireless charging of electric vehicle. In *2017 IEEE PELS Workshop on Emerging Technologies: Wireless Power Transfer (WoW)*, pages 1–6, 2017.

[125] Saeid Ghazizadeh, Saad Mekhilef, Mehdi Seyedmahmoudian, Jaideep Chandran, and Alex Stojcevski. Performance evaluation of coil design in inductive power transfer for electric vehicles. *IEEE Access*, 12:108201–108223, 2024.

[126] Venkatesan Ramakrishnan, Dominic Savio A, Balaji C, Narayanamoorthi Rajamanickam, Hossam Kotb, Ali Elrashidi, and Waleed Nureldeen. A comprehensive review on efficiency enhancement of wireless charging system for the electric vehicles applications. *IEEE Access*, 12:46967–46994, 2024.

[127] S. Bandyopadhyay, P. Venugopal, J. Dong, and P. Bauer. Comparison of magnetic couplers for ipt-based ev charging using multi-objective optimization. *IEEE Transactions on Vehicular Technology*, 68(6):5416–5429, 2019.

[128] J Rahulkumar, R Narayanamoorthi, Pradeep Vishnuram, C Balaji, Tomas Gono, Tomas Dockal, Radomir Gono, and Petr Krejci. A review on resonant inductive coupling pad design for wireless electric vehicle charging application. *Energy Reports*, 10:2047–2079, 2023.

[129] Ahmed A Shaier, Ahmed AS Mohamed, Hamid Metwally, and Sameh I Selem. A new hollow solenoid receiver compatible with the global double-d transmitter for ev inductive charging. *Scientific Reports*, 13(1):11925, 2023.

[130] I. U. Castillo-Zamora, P. S. Huynh, D. Vincent, F. J. Perez-Pinal, M. A. Rodriguez-Licea, and S. S. Williamson. Hexagonal geometry coil for a wpt high-power fast charging application. *IEEE Transactions on Transportation Electrification*, 5(4):946–956, 2019.

[131] Mickel Budhia, Grant A. Covic, and John T. Boys. Design and optimization of circular magnetic structures for lumped inductive power transfer systems. *IEEE Transactions on Power Electronics*, 26(11):3096–3108, 2011.

[132] S. Ghazizadeh, K. Ahmed, M. Seyedmahmoudian, S. Mekhilef, J. Chandran, and A. Stojcevski. Critical analysis of simulation of misalignment in wireless charging of electric vehicles batteries. *Batteries*, 9(2):106, 2023.

[133] M. Budhia, J. T. Boys, G. A. Covic, and C.-Y. Huang. Development of a single-sided flux magnetic coupler for electric vehicle ipt charging systems. *IEEE Transactions on Industrial Electronics*, 60(1):318–328, 2013.

[134] KN Mude and K Aditya. Comprehensive review and analysis of two-element resonant compensation topologies for wireless inductive power transfer systems. *Chinese Journal of Electrical Engineering*, 5(2):14–31, 2019.

[135] Zhen Zhang, Hongliang Pang, Apostolos Georgiadis, and Carlo Cecati. Wireless power transfer—an overview. *IEEE transactions on industrial electronics*, 66(2):1044–1058, 2018.

[136] Van-Binh Vu, Duc-Hung Tran, and Woojin Choi. Implementation of the constant current and constant voltage charge of inductive power transfer systems with the double-sided lcc compensation topology for electric vehicle battery charge applications. *IEEE Transactions on Power Electronics*, 33(9):7398–7410, 2017.

[137] Xiaohui Qu, Yanyan Jing, Hongdou Han, Siu-Chung Wong, and K Tse Chi. Higher order compensation for inductive-power-transfer converters with constant-voltage or constant-current output combating transformer parameter constraints. *IEEE Transactions on Power Electronics*, 32(1):394–405, 2016.

[138] Mariusz Bojarski, Erdem Asa, Kerim Colak, and Dariusz Czarkowski. A 25 kw industrial prototype wireless electric vehicle charger. In *2016 IEEE Applied Power Electronics Conference and Exposition (APEC)*, pages 1756–1761, 2016.

[139] Xin Liu, Fei Gao, Huanjun Niu, Guodong Sun, Tianfeng Wang, and Hua Wang. A series–parallel transformer-based wpt system for 400-v and 800-v electric vehicles with z1 or z2 class. *IEEE Transactions on Power Electronics*, 39(1):1749–1761, 2023.

[140] Kai Song, Zhenjie Li, Jinhai Jiang, and Chunbo Zhu. Constant current/voltage charging operation for series–series and series–parallel compensated wireless power transfer systems employing primary-side controller. *IEEE Transactions on Power Electronics*, 33(9):8065–8080, 2017.

[141] Junnosuke Nohara, Hideki Omori, Aoto Yamamoto, Noriyuki Kimura, and Toshimitsu Morizane. A miniaturized single-ended wireless ev charger with new high power-factor drive and natural cooling structure. In *2018 IEEE International Power Electronics and Application Conference and Exposition (PEAC)*, pages 1–6. IEEE, 2018.

[142] Ryota Maeno, Hideki Omori, Hisato Michikoshi, Noriyuki Kimura, and Toshimitsu Morizane. A 3kw single-ended wireless ev charger with a newly developed sic-vmosfet. In *2018 7th International Conference on Renewable Energy Research and Applications (ICRERA)*, pages 1–6. IEEE, 2018.

[143] Masaya Ote, Soyeon Jeong, and Manos M Tentzeris. Foreign object detection for wireless power transfer based on machine learning. In *2020 IEEE Wireless Power Transfer Conference (WPTC)*, pages 476–479. IEEE, 2020.

[144] Javier Stillig, Martin Edviken, and Nejila Parspour. Overview and aspects of foreign object detection in wireless power transfer applications. In *2020 IEEE Wireless Power Transfer Conference (WPTC)*, pages 380–383. IEEE, 2020.

[145] Yong Tian, Wenhui Guan, Guang Li, Kamyar Mehran, Jindong Tian, and Lijuan Xiang. A review on foreign object detection for magnetic coupling-based electric vehicle wireless charging. *Green Energy and Intelligent Transportation*, 1:100007, 2022.

[146] Tao Meng, Linlin Tan, Ruying Zhong, Huiru Xie, and Xueliang Huang. Research on metal foreign object detection of electric vehicle wireless charging system based on detection coil. *World Electric Vehicle Journal*, 12(4):203, 2021.

[147] Yingyao Zheng, Yicheng Zhou, Ronghuan Xie, Xingkui Mao, Xiaoying Chen, Xiangpeng Cheng, and Yiming Zhang. A self-resonant foreign object detection system for metal and living object detection in electric vehicle wireless charging systems. *IEEE Transactions on Power Electronics*, 40(5):6459–6463, 2025.

[148] Shengkun Cai, Zhizhen Liu, Xueqing Luo, Zhuoqun Shi, Yuxin Xie, Jintao Wang, Xianglin Li, Siyu Hou, and Qingyun Zhao. Research on metal and living foreign object detection method for electric vehicle wireless charging system. *World Electric Vehicle Journal*, 15(1):34, 2024.

[149] Yusuf Ahmed Khan, Syed Imaduddin, Aqueel Ahmad, and Yasser Rafat. Image-based foreign object detection using yolo v7 algorithm for electric vehicle wireless charging applications. In *2023 5th International Conference on Power, Control & Embedded Systems (ICPCES)*, pages 1–6, 2023.

[150] Yong Tian, Wenhui Guan, Guang Li, Kamyar Mehran, Jindong Tian, and Lijuan Xiang. A review on foreign object detection for magnetic coupling-based electric vehicle wireless charging. *Green Energy and Intelligent Transportation*, 1:100007, 2022.

[151] Chenyang Xia, Chenhao Lu, Shuze Zhao, Ziyue Yang, Yuheng Cao, Fuqian Liu, and Yuxiang Gao. Planar double-winding foreign object detection for the ev wireless charging system based on time-division multiplexing. *IEEE Transactions on Power Electronics*, 39(10):13988–13994, 2024.

[152] Naoui Mohamed, Flah Aymen, Turki E. A. Alharbi, Claude Ziad El-Bayeh, Sbita Lassaad, Sherif S. M. Ghoneim, and Ursula Eicker. A comprehensive analysis of wireless charging systems for electric vehicles. *IEEE Access*, 10:43865–43881, 2022.

[153] Aqueel Ahmad, Mohammad Saad Alam, and Rakan Chabaan. A comprehensive review of wireless charging technologies for electric vehicles. *IEEE Transactions on Transportation Electrification*, 4(1):38–63, 2018.

[154] Changsong Cai, Junhua Wang, Zhijian Fang, Pengcheng Zhang, Meilin Hu, Junkun Zhang, Liang Li, and Zhongzheng Lin. Design and optimization of load-independent magnetic resonant wireless charging system for electric vehicles. *IEEE Access*, 6:17264–17274, 2018.

[155] Md Rakib Raihan Razu, Sultan Mahmud, Mohammad Jalal Uddin, Sikder Sunbeam Islam, Badariah Bais, Norbahiah Misran, and Mohammad Tariqul Islam. Wireless charging of electric vehicle while driving. *IEEE Access*, 9:157973–157983, 2021.

[156] Jutturit Thongpron, Wuttikai Tammawan, Teerasak Somsak, Wiwat Tippachon, Kosol Oranpiroj, Ekkachai Chaidee, and Anon Namin. A 10 kw inductive wireless power transfer prototype for ev charging in thailand. *ECTI Transactions on Electrical Engineering, Electronics, and Communications*, 20(1):83–95, 2022.

[157] Jesús Sallán, Juan L Villa, Andrés Llombart, and José Fco Sanz. Optimal design of icpt systems applied to electric vehicle battery charge. *IEEE Transactions on Industrial Electronics*, 56(6):2140–2149, 2009.

[158] Glauber de Freitas Lima and Ruben Barros Godoy. Modeling and prototype of a dynamic wireless charging system using lsps compensation topology. In *2017 Brazilian Power Electronics Conference (COBEP)*, pages 1–6, 2017.

[159] Rong Zeng, Veda Prakash Galigekere, Omer C. Onar, and Burak Ozpineci. Grid integration and impact analysis of high-power dynamic wireless charging system in distribution network. *IEEE Access*, 9:6746–6755, 2021.

[160] Reza Tavakoli and Zeljko Pantic. Analysis, design, and demonstration of a 25-kw dynamic wireless charging system for roadway electric vehicles. *IEEE Journal of Emerging and Selected Topics in Power Electronics*, 6(3):1378–1393, 2018.

[161] Huanjie Zhu, Bo Zhang, and Lihao Wu. Output power stabilization for wireless power transfer system employing primary-side-only control. *IEEE Access*, 8:63735–63747, 2020.

[162] Jinhai Jiang, Kai Song, Zhenjie Li, Chunbo Zhu, and Qianfan Zhang. System modeling and switching control strategy of wireless power transfer system. *IEEE Journal of Emerging and Selected Topics in Power Electronics*, 6(3):1295–1305, 2018.

[163] Kang Sun and Wangqiang Niu. Spwm inverter control for wireless constant current and voltage charging. *World Electric Vehicle Journal*, 14(4):111, 2023.

[164] Katsuhiro Hata, Takehiro Imura, and Yoichi Hori. Dynamic wireless power transfer system for electric vehicles to simplify ground facilities-power control and efficiency maximization on the secondary side. In *2016 IEEE applied power electronics conference and exposition (APEC)*, pages 1731–1736. IEEE, 2016.

[165] Febry Pandu Wijaya, Takuya Shimotsu, Tatsuhito Saito, and Keiichiro Kondo. A simple active power control for a high-power wireless power transmission system considering coil misalignment and its design method. *IEEE Transactions on Power Electronics*, 33(11):9989–10002, 2018.

[166] Qiang Zhao, Anna Wang, Jinglu Liu, and Xingyu Wang. The load estimation and power tracking integrated control strategy for dual-sides controlled lcc compensated wireless charging system. *IEEE Access*, 7:75749–75761, 2019.

[167] Kai Song, Ruizhi Wei, Guang Yang, Hang Zhang, Zhenjie Li, Xiaoliang Huang, Jinhai Jiang, Chunbo Zhu, and Zhijiang Du. Constant current charging and maximum system efficiency tracking for wireless charging systems employing dual-side control. *IEEE Transactions on Industry Applications*, 56(1):622–634, 2020.

[168] Min Wu, Xu Yang, Wenjie Chen, Laili Wang, Yongbin Jiang, Chenxu Zhao, and Zhengchao Yan. A dual-sided control strategy based on mode switching for efficiency optimization in wireless power transfer system. *IEEE Transactions on Power Electronics*, 36(8):8835–8848, 2021.

[169] Zeming Jiang, Hao Tian, Mohammed J. Beshir, Ruslan Sibagatullin, and Ali Mazloomzadeh. Statistical analysis of electric vehicles charging, station usage and impact on the grid. In *2016 IEEE Power & Energy Society Innovative Smart Grid Technologies Conference (ISGT)*, pages 1–5, 2016.

[170] M. Caruso, P. Livreri, R. Miceli, Fabio Viola, and M. Martino. Ev charging station at university campus. In *2017 IEEE International Telecommunications Energy Conference (INTELEC)*, pages 615–623, 2017.

[171] Noraidah Binti Mohd Shariff, Mohammed Al Essa, and Liana Cipcigan. Probabilistic analysis of electric vehicles charging load impact on residential distributions networks. In *2016 IEEE international energy conference (ENERGYCON)*, pages 1–6. IEEE, 2016.

[172] AA Eajal, Mostafa F Shaaban, EF El-Saadany, and Kumaraswamy Ponnambalam. Fuzzy logic-based charging strategy for electric vehicles plugged into a smart grid. *International Journal of Process Systems Engineering*, 4(2-3):119–137, 2017.

[173] Hassanien Ramadan, Abdelfatah Ali, and Csaba Farkas. Assessment of plug-in electric vehicles charging impacts on residential low voltage distribution grid in hungary. In *2018 6th International Istanbul Smart Grids and Cities Congress and Fair (ICSG)*, pages 105–109. IEEE, 2018.

[174] Krzysztof Jakubiak, Jun Liang, and Liana Cipcigan. Modelling of inductive wireless charging for electric vehicles. In *2022 IEEE 16th International Conference on Compatibility, Power Electronics, and Power Engineering (CPE-POWERENG)*, pages 1–7, 2022.

[175] Wireless charging electric taxi trial goes live in nottingham - electrive.com. https://www.electrive.com/2022/10/13/wireless-charging-electric-taxi-trial-goes-live-in-nottingham/. (Accessed on 09/21/2024).

[176] Karl Johan Åström. Control system design lecture notes for me 155a. *Department of Mechanical and Environmental Engineering University of California Santa Barbara*, 333, 2002.

[177] Haowei Niu, Guocun Li, Jinghang Lu, and Xuewei Pan. Parameter identification method with dynamic impedance modulation for the dwpt system. *IEEE Journal of Emerging and Selected Topics in Power Electronics*, 10(5):6332–6344, 2022.

[178] Deyu Wang, Chaowei Fu, Qinglin Zhao, and Ting Hu. A pso-based optimization design of w-type noncontact transformer for stable power transfer in dwpt system. *IEEE Transactions on Industry Applications*, 58(1):1211–1221, 2021.

[179] Travis Newbolt, Paras Mandal, Hongjie Wang, and Regan Zane. Dwpt-integrated microscopic traffic flow for distribution grid voltage stability analysis. In *2024 56th North American Power Symposium (NAPS)*, pages 1–6. IEEE, 2024.

[180] Mahashree Tamta, Mayank Chaturvedi, et al. Experimental analysis of power quality of semi controlled rectifier system. In *2019 Women Institute of Technology Conference on Electrical and Computer Engineering (WITCON ECE)*, pages 54–59. IEEE, 2019.

[181] Md Inzamamul Haq, Abdul Hadi Hanan, Jerin Tasnim Humayra, Shahria Tanzil, and Mahmuda Rahman. Design and simulation of a semi controlled full bridge and its control circuit. In *2021 IEEE Conference of Russian Young Researchers in Electrical and Electronic Engineering (ElConRus)*, pages 1425–1428. IEEE, 2021.

[182] Demercil S Oliveira, Mônica M Reis, Carlos EA Silva, Luiz HS Colado Barreto, Fernando LM Antunes, and Bruno L Soares. A three-phase high-frequency semicontrolled rectifier for pm wecs. *IEEE Transactions on Power Electronics*, 25(3):677–685, 2009.

[183] Georges Rizk, Stéphanie Salameh, Hadi Y Kanaan, and Elias A Rachid. Design of passive power filters for a three-phase semi-controlled rectifier with typical loads. In *2014 9th IEEE Conference on Industrial Electronics and Applications*, pages 590–595. IEEE, 2014.

[184] Murugan Venkatesan, R Narayanamoorthi, Kareem M AboRas, and Ahmed Emara. Efficient bidirectional wireless power transfer system control using dual phase shift pwm technique for electric vehicle applications. *IEEE Access*, 12:27739–27755, 2024.

[185] Mostak Mohammad, Omer C Onar, Gui-Jia Su, Jason Pries, Veda Prakash Galigekere, Saeed Anwar, Erdem Asa, Jonathan Wilkins, Randy Wiles, Cliff P White, et al. Bidirectional lcc–lcc-compensated 20-kw wireless power transfer system for medium-duty vehicle charging. *IEEE Transactions on Transportation Electrification*, 7(3):1205–1218, 2021.

[186] Murugan Venkatesan, Narayanamoorthi Rajamanickam, Pradeep Vishnuram, Mohit Bajaj, Vojtech Blazek, Lukas Prokop, and Stanislav Misak. A review of compensation topologies and control techniques of bidirectional wireless power transfer systems for electric vehicle applications. *Energies*, 15(20):7816, 2022.

[187] Subia Meraj, Saad Mekhilef, Marizan Mubin, Hari Krishnan Ramiah, Mehdi Seyedmahmoudian, and Alex Stojcevski. Bidirectional wireless charging system for electric vehicles: A review of power converters and control techniques in v2g application. *IEEE Access*, 2025.

[188] Jalaj Kumar and Suvendu Samanta. A single-stage universal input wireless inductive power transfer system with v2g capability. *IEEE Journal of Emerging and Selected Topics in Industrial Electronics*, 2024.

[189] Irfan Hussain, Saad Mekhilef, Mehdi Seyedmahmoudian, Tey Kok Soon, Hazlie Mokhlis, Kafeel Ahmed, Ahmed Elsanabary, and Alex Stojcevski. A phase-synchronization control of bidirectional wireless power transfer system for g2v and v2g operation modes. *IEEE Transactions on Transportation Electrification*, 2025.

[190] Rong Zeng, Veda Prakash Galigekere, Omer C Onar, and Burak Ozpineci. Grid integration and impact analysis of high-power dynamic wireless charging system in distribution network. *IEEE Access*, 9:6746–6755, 2021.

[191] C. Mu, W. Liu, and W. Xu. Hierarchically adaptive frequency control for an ev-integrated smart grid with renewable energy. *IEEE Transactions on Industrial Informatics*, 14(9):4254–4263, Sep. 2018.

[192] A. Oshnoei, M. Kheradmandi, S. M. Muyeen, and N. D. Hatziargyriou. Disturbance observer and tube-based model predictive controlled electric vehicles for frequency regulation of an isolated power grid. *IEEE Transactions on Smart Grid*, 12(5):4351–4362, Sep. 2021.

[193] M. U. Jan, A. Xin, H. U. Rehman, M. A. Abdelbaky, S. Iqbal, and M. Aurangzeb. Frequency regulation of an isolated microgrid with electric vehicles and energy storage system integration using adaptive and model predictive controllers. *IEEE Access*, 9:14958–14970, 2021.

[194] P. Sharma, A. Mishra, A. Saxena, and R. Shankar. A novel hybridized fuzzy pi-ladrc based improved frequency regulation for restructured power system integrating renewable energy and electric vehicles. *IEEE Access*, 9, 2021.

[195] H. Liu, Z. Hu, Y. Song, J. Wang, and X. Xie. Vehicle-to-grid control for supplementary frequency regulation considering charging demands. *IEEE Transactions on Power Systems*, 30(6):3110–3119, Nov. 2015.

[196] O. Kolawole and I. Al-Anbagi. Electric vehicles battery wear cost optimization for frequency regulation support. *IEEE Access*, 7:130388–130398, 2019.

[197] S. A. Amamra and J. Marco. Vehicle-to-grid aggregator to support power grid and reduce electric vehicle charging cost. *IEEE Access*, 7:178528–178538, 2019.

[198] H. Farzin, M. Fotuhi-Firuzabad, and M. Moeini-Aghtaie. A practical scheme to involve degradation cost of lithium-ion batteries in vehicle-to-grid applications. *IEEE Transactions on Sustainable Energy*, 7(4):1730–1738, Oct. 2016.

[199] Erbo Wu, Krzysztof Jakubiak, Yaoqiang Wang, and Jun Liang. Optimizing ev cluster contribution for vehicle-to-grid (v2g) frequency regulation. In *2022 57th International Universities Power Engineering Conference (UPEC)*, pages 1–6. IEEE, 2022.

[200] Zhengzhou Audit Bureau. No. 62 of 2020 (total no. 299) announcement of findings of special audit on the construction, management and use of new energy vehicle charging infrastructure in zhengzhou city, 2020. [EB/OL].